UNIVERSITAT DE BARCELONA

Universitat de Barcelona
Departament d'Estructura i Constituents de la Matèria
Programa de doctorat de Física Avançada
Bienni 2003–05

Shapes in Cells.

Dynamic instabilities, morphology, and curvature in biological membranes

Memòria de la tesi presentada el novembre de 2008 per
Fèlix Campelo i Aubarell
per optar al títol de Doctor en Física
dirigida per la Dra. Aurora Hernández-Machado

Fèlix Campelo i Aubarell
Departament d'Estructura i Constituents de la Matèria,
Facultat de Física, Universitat de Barcelona
e-mail: campelo@ecm.ub.es

FRONT COVER: *Mathematical Form, Surface, 0004 Onduloid: a surface of revolution with constant non zero mean curvature*, from the series *Conceptual Forms*, gelatin-silver print, 2004. © Hiroshi Sugimoto (http://www.sugimotohiroshi.com). We superimposed, in orange, the mathematical function corresponding to the artist's work, as we found by fitting an onduloid.
BACK COVER: Three-dimensional plot of the mathematically defined unduloid, corresponding to the photograph on the front cover, performed by the designated Wolfram *Mathematica* software.

Typeset by the author, adapted from a WILEY-VCH Verlag GmbH & Co. KGaA, Weinheim LaTeXclass.

Índex

Acknowledgments

Theses are not the individual work of one person, but an amalgam of different influences, advises, and pieces of knowledge shared by other people and captured in a manuscript. This thesis is not an exception, and in these lines I will try to give credit to those who contributed in one way or another to get my thesis done.

Abans de res, vull agrair a la meva directora de tesi, l'Aurora Hernández-Machado, el fet d'haver-me permès realitzar una tesi doctoral sota la seva tutela. No va dubtar ni un instant en permetre'm treballar en el camp de la biofísica, en el qual jo estava interessat al començar la tesi, tot i que jo no en tenia gaire coneixements. A més a més, el seu entusiasme per la ciència ha estat un gran suport durant tots aquests anys i tot un exemple a seguir.

En este sentido, querría también agradecer a Joel Stavans por haberme introducido en el campo de las membranas biológicas. Su visita a Barcelona justo en el inicio de mi tesis fue lo que nos decidió a estudiar los fenómenos dinámicos y las inestabilidades de forma en membranas. También agradecerle sus comentarios y críticas constructivas a nuestros artículos sobre inestabilidades dinámicas, haciéndolos más comprensibles y precisos.

Je voudrais vraiment remercier Martine Ben Amar et Jean-Marc Allain pour leur accueille au Laboratoire de Physique Statistique de l'École Normale Supérieure de Paris. Ce fut un grand plaisir de travailler avec eux, et d'apprendre differentes méthodes analytiques et numériques pour résoudre les équations de forme.

Visiting Tel Aviv University was an incredible opportunity I could enjoy for a year. I would like to express my deepest gratitude to Misha Kozlov for all the effort and patience he put on me, for showing me some of the intricate points of membrane elasticity, and for always having a moment to discuss on scientific or non-scientific issues. My acknowledgments also for Harvey McMahon, from Cambridge University, who collaborates with us with his group's great experimental results on membrane curvature generation by proteins. I have to thank Tom Shemesh, Andreas Papadopulos, Ran Shneor, and Adi Pick from

Tel Aviv University for their great help in finding accommodation and making me feel like home far away from home.

També vull agrair molt sincerament a l'Ignacio Pagonabarraga la seva ajuda i disponibilitat com a tutor d'un dels dos treballs de D.E.A. Del grup de física no lineal de l'UPC, vull agrair a l'Ana Lacasta per cedir-me el seu codi de resolució de models de camp de fase, i al Blas Echebarría pels seus consells i ajuda sobre aquest tipus de models.

During his visits to Barcelona, it was very interesting to discuss on phase-field topics with Rui Travasso, now at the University of Coimbra. His calculations on the Gaussian curvature in a phase-field approach were really useful, and we expect to get some insights on these issues with them.

I would like to acknowledge the Spanish and Catalan governments for economical support, as well as to the European Union Marie Curie Research Training Network "Flippases".

No puc deixar de mencionar tots els companys i amics que han fet del meu pas per la Universitat de Barcelona una experiència inoblidable. A ells els agraeixo molt sincerament la seva companyia als diferents despatxos, durant els dinars, als congressos i també en les estades a l'estranger on vam coincidir amb alguns d'ells, així com les discussions científiques cafè en mà. Els comentaris sobre versions preliminars d'aquest manuscrit del Rodrigo Ledesma i el Marc Pradas han estat de gran ajuda, així com els consells del Jaume López sobre el processador LaTeX. També vull agrair a la Montserrat Badia la seva ajuda en la correcció lingüística del resum en català.

I, evidentment, també vull agrair el suport incondicional dels meus pares i la meva germana, que m'ha permès arribar fins aquí. Per últim, la Marta m'ha ajudat en tot moment amb els seus ànims, la seva paciència i per fer-ho tot senzill. Moltes gràcies.

Vilafranca del Penedès, September 2008 *Fèlix Campelo i Aubarell*

1
General introduction

1.1
Shapes in nature

The possibility of explaining the shapes occurring in living matter by physical considerations, and assume that they are subject to the physical laws is the main hypothesis we have to make to achieve some knowledge on shapes in cells. Thus, we might assert that objects in nature are not shaped by chance, independently of its role. It is important to note that equal shapes appear in completely different scenarios, meaning that some common principle regarding their functionality has to be underlying [247]. Nature shapes, therefore, are not an evolutionary caprice, but they respond to an optimal design for a specific function of the object itself. In this thesis, we theoretically study from a physical perspective some aspects on cellular morphology [160].

If we ask ourselves for the reason that something has a definite shape and not another, we will enter into a loose discussion. Let's then reformulate the question in another manner: how something acquires a definite shape and not another? When we formulate the question in that way, we are asking about a mechanism leading to that very shape. This is a question a physicist can answer, or at least ask. In biology, the question could even be reformulated differently: which are the benefits this object has by being shaped in a specific form? Evolution can be a part of the answer. A deep enough comprehension of the biological function is also of great help. To understand the function that a part of a living organism has, as well as the mechanisms by which it carries it out, are the first steps in that direction.

For instance, let's take probably the most ubiquitous shape in nature, the sphere. As it is well known the sphere is the shape with the smallest surface area among all shapes enclosing a given volume. In other words, it is the optimal shape to enclose a given volume by having the minimum surface area in contact with the external environment. This happens, for instance, with soap films [53, 198]. It is known from microscopic models that such a system can be energetically described by a surface tension term. Area creation increases

the system energy, and therefore the equilibrium configuration corresponds to the minimal energy configuration, i.e. the minimal surface area shape given the external system constraints[1]. However, this is *a* mechanism leading to spherical shapes, but it does not mean that it is *the* only possible mechanism for that. Spheres have other peculiarities, like the fact that they are isotropic, that is, they are uniform in all directions. This is the reason why most orbiting astronomical objects are almost spherical. There are plenty of other beautiful examples of spheres in nature [247, 253].

Contrarely to spheres, when the surface area enclosing a given volume has to be, due to some reason, maximum instead of minimum, a ramified geometry has to appear. This is the case of fractals [82, 163]. There are other recurrent shapes in nature. Morphology, the study of which physical mechanisms create the shapes and structures of living entities, is of a primary importance. Further connection between forms and functions has to be studied as well, a task where morphology (shapes) and physiology (functions) have to be interwoven.

1.2 Physics in life sciences

The fragmentation of natural sciences into academic disciplines resulted in the existence of boundary topics between these disciplines which did not belong clearly to any of them. Although in the history of science there have been people dealing with these topics, the benefits of sharing knowledge between sciences have not been fully exploited. In particular, while speaking about physics and life sciences, the interconnexion is clear regarding to the instrumentation developed using physical principles (X-ray imaging, microscopy, and other visualization techniques), and used in life sciences (discovery of DNA structure, medical equipments).

Recently, the terms *multidisciplinarity* and *interdisciplinarity* are listened at a daily basis in the scientific field, becoming the hallmark of contemporary research. In this sense, the growing interest in biophysical research is clear. However, there are still two different kinds of biophysics, that is, biophysics made by biologists, and biophysics made by physicists. Physicists should not only bring their mathematical skills to model biological problems. In addition, biologists, as Karl Pearson said more than hundred years ago in a letter to *Nature* [194]:

> I believe the day must come when the biologist will -without being a mathematician- not hesitate to use mathematical analysis when he requires it.

1) Such a shape is usually called a minimal surface [185].

1.3 Cells, membranes, and lipid bilayers

Cells are the structural and functional unit of living organisms. It is important to remark the fact of the uniqueness of a cell, that is, a cell is defined as an individual entity, something which has some independence, albeit its interactions with other surrounding entities like it. Here, a question arises: how does this structure keep its unity? The answer is that there has to be some frontier defining the limits of a cell as an individual, and keeping its fluidlike internal medium bound. This boundary is the membrane, a thin layer mainly consisting of a lipid bilayer with associated proteins which encloses the cell and separates the intracellular components from the extracellular medium. In the next Chapter of the thesis introduction, we review some general aspects on biological membranes, like their composition and phase behavior.

At this point, one might ask why physicists might be interested in studying biological membranes. As Erich Sackmann wrote in the first chapter of *Structure and Dynamics of Membranes* [160], membranes are very attractive to physicists for several reasons:

(i) They are examples of two-dimensional colloidal systems exhibiting various novel physical properties (e.g., non-classical elastic properties) which are simultaneously essential for their biological function.

(ii) Their composition involves about a hundred components and thus poses a real challenge for the development of new concepts of the physical basis of self-organization of multicomponent systems.

(iii) Despite their complexity they allow us to explore the interplay between biochemical modulations of the physical properties of biomaterials and the control of biological functions (e.g., in the course of signal transduction processes).

(iv) By reconstitution of model membranes from a few lipids and membrane proteins, specific membrane function can be studied on a molecular level.

(v) Studies of biomembranes yield direct insight into the possible role of universal physical properties for the behavior and function of biological materials (such as scaling laws or logarithmic laws typical for two-dimensional systems).

1.4 Thesis aims and structure

The main aims of this thesis are to understand the formation and dynamics of membrane shapes from a physical point of view, and relate it biological experimental observations. In order to achieve this goal, it is important to identify the basic physical principles describing membranes. This is the reason why, in our analyses, the complexity of cell membranes is reduced to a simple model system, lipid bilayers closed to form monocomponent lipid vesicles. Further complexity is introduced sequentially in order to understand which consequences every new ingredient has on the system.

In order to set the proper conceptual context, this thesis starts with this general introduction, and it is followed by two other introductory Chapters on the biological and physical properties of membranes.

Our original research is then structured in three separate parts. The first and most extensive one deals with the study of dynamic instabilities in biological membranes. In particular, we study shape changes occurring in model membranes when an destabilizing agent is introduced in the system. In this context, these instabilities are not as usual hydrodynamic instabilities [46] where the response of the system is usually characterized by non-bound growing modes. Our instabilities correspond to the type where a stable membrane geometry turns unstable by the addition of some polymeric molecules, which act on the membrane by changing its geometric properties. Thus, this destabilizing agents induce a dynamic shape transition into a new geometry.

For this purpose, and motivated by the experimental results on the topic by the group of Joel Stavans at the Weizmann Institute [249], we derived a dynamic model for dealing with the bending energies which describe fluid membranes as elastic surfaces [44, 109], reviewed in Ch. 3. This dynamic model is of the kind of phase-field models, explained in Ch. 4. Thus, in Ch. 5, we present the derivation of a phase-field for dynamically dealing with membrane energies. We derive as well a dynamic equation describing the time evolution of the membrane shape. This model is numerically solved in Ch. 6 in the simplest case possible, when no unstabilizing agents are introduced in the system. This lets us find the stationary shapes of fluid vesicles, that is, the shape a closed membrane acquires as a result of minimizing its bending energy. There, the membrane is assumed to be homogeneous and symmetric. The resulting shape only depends on the ratio between the area and the inner volume of the vesicle, which are constant. Thus, given a value of this ratio, a shape which minimizes the bending energy can be found, and therefore one can trace a shape diagram. These results agree with the shape diagrams found by other non-dynamic means.

However, biological membranes are not simple lipid vesicle, but much more complex entities, containing several types of lipids and proteins. In addition,

during cell life, membrane shapes are constantly evolving. Membrane lipids and proteins are synthesized inside the cell. In order to reach the plasma membrane they have to be transported from the endoplasmic reticulum and the Golgi apparatus [3]. Also, internal membrane trafficking is ubiquitous in cell's life, and includes membrane remodelling and recycling, as well as membrane fussion and fission events. It is clear thus, that in biomembranes there have to be agents responsible for such trafficking events. In this thesis we study the role proteins have in shaping membranes. In this first Part we study the dynamic instabilities induced by membrane proteins. In particular, a curvature-induced pearling instability is analyzed theoretically in Ch. 7, and a polymer-driven tubulation phenomenon is studied in Ch. 8.

A polymer containing hydrophobic groups anchor the membrane and acts as a wedge inducing local curvature to the membrane. This mechanism mimics the way some proteins insert hydrophobic domains in the bilayer (something we study in the third Part of this thesis). Thus, the system consisting of a fluid lipid vesicle with anchored polymers is a model system, simple enough to let a good control on the experiments and an easy enough modelization, but complex enough to grasp some of the much more complex processes occurring *in vivo*. Among these, the shape transformation of long cylindrical membrane tubes into a peristaltic tube formed by almost spherical pearls connected through a narrow neck, known as pearling instability, is studied from a theoretical point of view in Ch. 7. Such morphological instabilities are often found in nature. The Rayleigh-Plateau instability is an example in the field of hydrodynamics. This occurs when a cylindrical fluid jet becomes unstable due to surface tension, and modes deforming the cylinder in a sinusoidal manner along the axial direction grow, eventually breaking the tube to form small droplets. Actually, these kind of surface tension pearling instabilities can also be found in membrane literature, where tension induced in a lipid tube triggers a surface tension instability to form pearls in a tube-like vesicle. However, the experiments we are interested in deal study a pearling instability produced under a completely different mechanism, as they are curvature-induced.

The curvature-induced pearling instability might occur by the anchorage of proteins or polymers in a lipid tubelike vesicle. Due to their shape or to the depth of insertion, these anchored groups may induce spontaneous curvature to the membrane. The vesicle, in turn, responds to this change by adopting a new shape which minimizes the overall bending energy of the vesicle. The point is that, the dynamics of this shape transition consists, as seen in the experiments [251], by a subsequent formation of pearls starting from the tip of the tube. Using the phase-field model derived in Ch. 5, we observe the dynamics of this instability, in agreement with the experiments. Further, we study the instability depending on the polymer concentration. Thus, we find

that depending on the concentration, the pearl size changes from a homogeneous distribution to an inhomogeneous one.

Besides, in Ch. 8 we drive our attention to the formation of membrane tubes from vesicles. These tubulation processes are of an outstanding importance in cell biology since they are the basis of intracellular transport [3]. There are different mechanisms which lead to such transformations, most of which are associated with a force that pulls tubes. The one we address in this thesis is due to membrane curvature, and most specifically, due to an inhomogeneous distribution of potential membrane-curving molecules in the bulk outside a lipid vesicle. In accordance with the experiments in Ref. [250], we study theoretically such phenomenon. We see that a tube can be extracted from a vesicle by means of no force directly acting on the bilayer. Our analyses are both analytical, using a simplified geometrical scheme, and numerical, using the curvature phase-field model derived in Ch. 5.

In the second Part of the thesis, we are interested in multicomponent vesicles. In the first Part, all the lipid membranes under consideration are formed by only one type of lipids in a fluid state. However, in actual biological systems, the richness in membrane composition is much higher. In addition of having different lipid components, vesicles may contain phase-separated domains. In the next Chapter of this introduction, we detail the composition of biological membranes, as well as the different phases lipid membranes can adopt.

Thus, understanding the mechanical behavior of lipid domains of different phases and compositions, and thus of different elastic parameters, is of primary importance for a deep understanding of cell processes. In Ch. 9 we study a specific lipid mixture, formed by two kinds of phospholipid molecules and cholesterol. Such a system phase separates when the conditions are suitable into two different phases: a liquid disordered phase, and a more rigid liquid ordered phase. These two phases have different elastic properties, and the interface between them introduces new energy terms. This line tension term penalizes the interface formation, since there is a mismatch between the lipids in the two phases. However, in experiments by Tobias Baumgart and coauthors [14], the existence of long membrane tubes formed by a periodic alternate disposition of these two phases was observed. In order to understand these experiments, we minimize the bending energy of such a membrane tube, taking into account both the bending terms (with different elasticities for each phase) and the line tension between phases. Within this context, we use an Euler-Lagrange scheme to find the differential equation for the vesicle shape. This non-linear equation is treated both analytically, in its linearized version, and numerically. Further energy minimization depending on the phase wavelength and on the area fraction between both phases gives rise to the existence

of periodic lipid membrane tubes under certain circumstances that we explain in Ch. 9.

Afterwards, in Ch. (10), we study multicomponent systems, not in three-dimensions as in Ch. (9) but in two-dimensions. In fact, we study lipid monolayers at the air-water interface. Such a simple model is a very interesting playground for studying intermolecular interactions between lipid molecules, or even between lipids and proteins. We focus ourselves in understanding the formation of non-circular shapes, as starfish shapes or ellipses, due to the competition between line tension and a dipole-dipole interaction between lipid molecules [8, 131]. Using an approximation due to Iwamoto and Zhongcan [125], that model can be mapped into a two-dimensional bending model with an effective line tension which does not need to be positive. Using the bending phase-field model derived in Ch. (5), we are able to find the dynamic evolution leading to such shapes, in a very good qualitative agreement with experimentally reported observations [131, 152].

Finally, in the third Part of the thesis we focus on the way proteins generate membrane curvature [171, 263]. Just as in the first Part of this thesis we assume that proteins asymmetrically anchored in a bilayer generate a certain curvature which in turn shapes vesicles accordingly, in the third Part we study the mechanism by which these proteins induce such curvature. In order to do so, we need to go beyond the classical curvature models used in the first two Parts, and derive a microscopic model taking into account the internal strains and stresses of the lipid matrix. In this way we can study how high concentrations of shallowly inserted protein domains create the large curvatures observed *in vivo*. In the introductory Ch. 11 of this Part, we review some of the biologically relevant mechanisms of membrane curvature generation known to date. In Ch. 12, we study a specific mechanism, due to proteins. Actually, the so-called hydrophobic insertion mechanism of membrane curvature generation by proteins happens because of the introduction of relatively small hydrophobic domains into the membrane matrix. The wedge effect these inserted domains has on the bilayer is what we study both qualitatively and quantitatively by means of an elastic model. This elastic model consists on the equilibrium equation of an anisotropic elastic medium with the considerations needed to account for laterally fluid membranes. In order to solve such a model, consisting in a set of coupled non-linear partial differential equations, we use a numerical method, the finite element method.

Besides of generating and/or stabilizing membrane curvature, membrane proteins can also act as sensors of curvature. This means, in gross terms, that a protein might have a different affinity of binding to highly curved membranes or to almost flat membranes. In the framework of our elastic microscopic model for thick membranes, we study this issue in Ch. 13.

Last, we present a separated concluding Part of the thesis, containing general conclusions, and future perspectives to continue studying how different shapes appear in cells, under which mechanisms they appear, and to see if we can get a further understanding of the intracellular world by setting together biological and physical tools.

2
Biological membranes: from molecular components to fluid vesicles.

2.1
Molecular components of biological membranes: the membrane building blocks

Lipid bilayers are the common principle which guarantee a stable but flexible surrounding for cells and cell organelles. However, it is biologically necessary to provide every one of these membrane-enclosed entities with very specific structural and functional properties. Thus, the biochemical composition of, say, an eukariotic cell membrane, has to be rather complex [243] (see Fig. 2.1), and differ from membrane to membrane. The basic components of a cell membrane include several kinds of lipids, some of which form the lipid bilayer, and some others control its fluid behavior. Besides, proteins involved in both functional and structural matters have to be forming the membrane. Regardless of the polymer networks which join some cell membranes, like the cytoskeleton [119], or the glycocalyx [220], biomembranes are basically composed by lipids and proteins.

2.1.1
Lipids

Among the high diversity of existent lipid molecules, only some types are involved in the formation of animal cell membranes [70]. These membrane lipids generally constitute about one half of the cell membrane's mass. Most membrane lipids are roughly cylindrical in shape, their typical length and cross-section area being $\sim 2\,\text{nm}$, and $\sim 0.6\,\text{nm}^2$, respectively [196]. This means that there are of the order of $\sim 10^9$ lipids in the plasma membrane of a usual animal cell [3].

Lipid molecules consist of two chemically differentiated parts, one being polar (or hydrophilic, that is, water-loving); and the other being non-polar (or hydrophobic, that is, water-avoiding). This dual nature of lipids is called amphiphilicity (or amphipathicity). Lipids are only one kind of amphiphilic

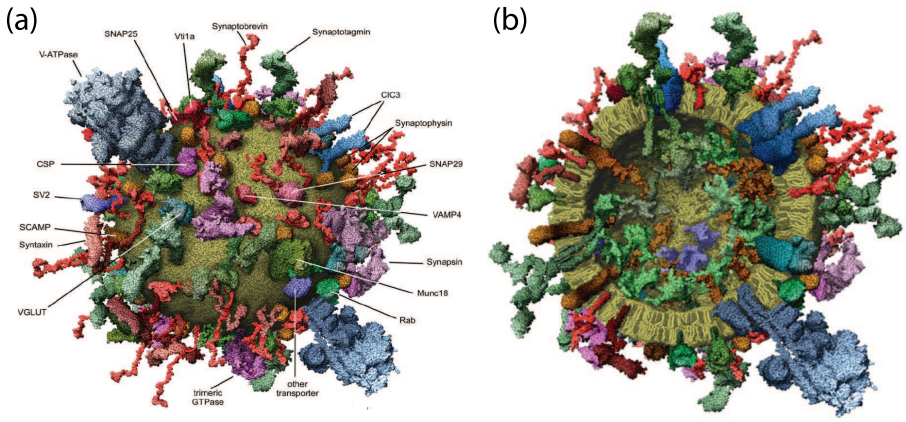

Figure 2.1 Molecular model of a typical synaptic vesicle (from Ref. [243]). (a) Outside view of the vesicle, and (b) view of the vesicle sectioned in the middle. For details on the membrane proteins present in the vesicle, see [243].

molecules (or amphiphiles). Surfactants, like detergents or soaps (e.g. sodium stearate, the common soap), among other molecules, are also amphiphiles. As we will see in the next Section, this amphiphilicity is crucial for the lipids to form a bilayer structure. Thus, one might say that lipid molecules are essential for the formation of a thin and soft, albeit resistant, boundary to enclose and define individual functional entities, as cells are.

Besides, lipids are structurally characterized, from a physical point of view, by the size and length of their polar and non-polar parts; by the electric properties of the polar moiety; and by the nature of the chemical bonds of the non-polar part, mainly [160]. Next, we describe the main properties of the major subgroups of membrane lipids: phosphoglycerides, sphingolipids, glycolipids, and cholesterol.

- **Phosphoglycerides.** Phospholipids are the most abundant lipid components in cell membranes. Like all membrane lipids, they are amphiphilic molecules. They are derived from an alcohol molecule, either from glycerol (a three-carbon alcohol), or from sphingosine (a more complex alcohol) [18, 155]. The ones formed from a glycerol backbone are known as phosphoglycerides. The three carbon atoms of the glycerol are linked to the rest of the phospholipid: two hydrophobic fatty acid chains linked to two of these carbon atoms; and the third one connects to a hydrophilic esterified phosphate ligand, which in turn links to a hydrophilic head group (see Fig. 2.2a).

  The fatty acid chains can either be saturated or not, unsaturated chains containing one or more double bonds between two of their carbon atoms. Double bonds are rigid, so they create a kink in the chain, al-

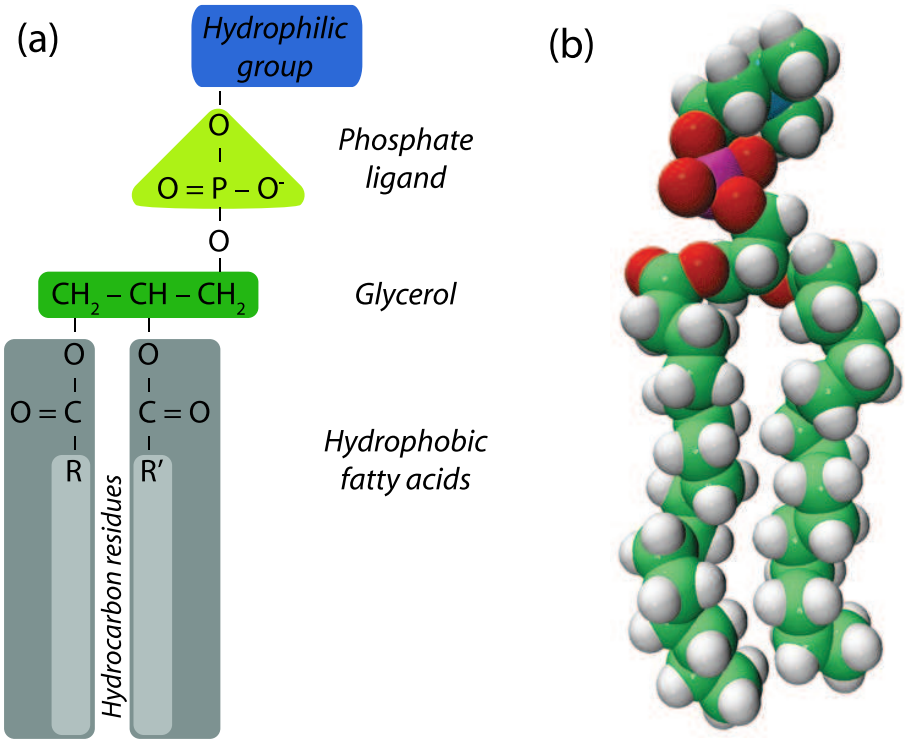

Figure 2.2 Phosphoglyceride structure. (a) The chemical formula of a general phosphoglyceride is shown. The hydrophilic group, the phosphate ligand, and the glycerol backbone are shown in blue, yellow, and green, respectively, and correspond to the hydrophilic part of the molecule. The hydrophobic part, consisting of two fatty acid chains (with a common COO- structure linked to two different hydrocarbon residues, R, and R') is shown in gray. (b) Three-dimensional space-filling model of a common phospholipid, dipalmitoylphosphatidylcholine (DPPC), having a choline headgroup and two equal saturated fatty acids (palmitic acid).

though the rest of the chain continues being able to rotate about the other C – C single bonds. Typically, fatty acids in membrane lipids contain an even number of carbon atoms, usually between 14 and 24, the 16– and 18– being the most common. In chemical notation, a saturated fatty acid of n carbons can be represented by

$$CH_3\,(CH_2)_{n-2} - COOH.$$

Palmitic acid, stearic acid, and arachidic acid, correspond to chains with $n = 16$, $n = 18$, and $n = 20$, carbons, respectively (see Fig. 2.2b). Unsaturated fatty acids depend not only on the number of carbon atoms, but also on the location of the double bond. For example, oleic acid has 18 carbon atoms (thus being a monounsaturated form of stearic acid), and a double bond in the *cis*-9 position (i.e. in the $n - 9$ position, thus

belonging to the $\omega - 9$ fatty acid class [7]). Unsaturated lipids are less packable than saturated lipids, thus having a lower gel transition temperature (see Sec. 2.3 below).

On the other hand, the small hydrophilic group linked to the phosphate ligand is normally negatively charged, and define the properties of the polar moiety of the molecule. Usual headgroups found in membrane lipids are choline, ethanolamine, or serine, chemically represented by

$$\begin{array}{ll} \textit{Choline} & -CH_2 - CH_2 - N^+(CH_3)_3, \\ \textit{Ethanolamine} & -CH_2 - CH_2 - N^+H_3, \\ \textit{Serine} & -CH_2 - CH \left\langle \begin{array}{l} N^+H_3 \\ COO^- \end{array} \right. . \end{array}$$

Phosphoglycerides are named by the headgroup they contain. Phosphatidylcholine (PC), phosphatidylethanolamine (PE), and phosphatidylserine (PS) are formed by the previously mentioned polar headgroups, respectively. In red blood cells, they constitute, $\sim$ 17%, $\sim$ 18%, and $\sim$ 7%, respectively [3]. However, these are phospholipid classes, since they are just named after the polar headgroup they contain, independently of which fatty acid chains they are bound to. Just to mention two common examples of membrane lipids called after both their polar headgroup and their fatty acid chains, dioleoylphosphatidylcholine (DOPC) is a monounsaturated lipid formed by two oleic acid chains; and dipalmitoylphosphatidylcholine (DPPC), formed by two saturated palmitic acid chains (see Fig. 2.2b).

- **Sphingolipids.** These are phospholipids that, contrarely to phosphoglycerides, lack the glycerol backbone. Instead, they contain sphingosine, an aliphatic amino alcohol derived from serine with a long unsaturated hydrocarbon chain. The sphingosine backbone is also linked to a polar headgroup like phospholipids. Sphingomyelins are the most common sphingolipids in human cells ($\sim$ 85% of all sphingolipids). Their phosphate-containing headgroup (see Fig. 2.3a) can either be phosphocholine or phosphoethanolamine. In red blood cells, sphingolipids count $\sim$ 18% of plasma membrane lipids composition [3].

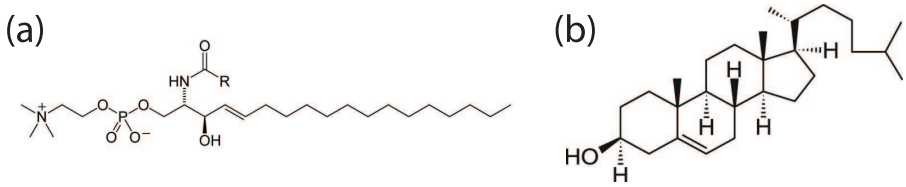

Figure 2.3 Membrane lipids. (a) Chemical formula of a general sphingomyelin. (b) Chemical formula of cholesterol molecule.

- **Glycolipids.** Carbohydrates are found in membranes forming the so-called glycocalyx, a network of polysaccharides that project from cellular surfaces [3]. They are covalently bound to the membrane, to either membrane proteins, or directly to membrane lipids, forming glycolipids. Structurally, glycolipids, like phospholipids, are composed of two hydrophobic hydrocarbon chains and a polar region. In this case, the polar region contains one or more sugar residues and no phosphate. Glycolipids are found in red blood cell membranes at a low concentration, $\sim$ 3% of lipid weight percentage [3].

- **Cholesterol.** It belongs to the steroid class of lipids (as testosterone does), being by far the most common of them in cell membranes. It constitutes $\sim$ 23% of the lipid composition in red blood cell's membrane [3]. Cholesterol structure differs from phospholipids and sphingolipids. The basic structure of steroids is a four-ring aromatic hydrocarbon backbone. Cholesterol has a single hydroxyl group constituting the polar part of the molecule. It is therefore an amphiphilic molecule (see Fig. 2.3b).

  Cholesterol molecules are about half long as usual phospholipids. This property, together with the small size of their polar head, makes cholesterol molecules position parallelly to phospholipids, with the cholesterol polar head aligned with the phospholipid glycerol backbone. Since cholesterol aromatic rings are stiff, small concentrations rigidify phospholipid chains, thus diminishing the fluidity of the bilayer. However, at high concentrations, cholesterol prevents the hydrocarbon chains from crystallizing, inhibiting possible phase transitions [135, 183].

2.1.2 Proteins

While lipids confer cell membranes their basic structural and geometric properties in order to be suitable cell frontiers, proteins account for membrane functionality [1]. Proteins are somehow swimming into a two-dimensional lipid pool, the bilayer, and generally contribute to membrane's weight as much as lipids. However, lipid molecules are much lighter than membrane proteins, meaning that for a typical plasma membrane there are $\sim$ 50 lipids for each protein.

There are several ways by which membrane proteins associate with the lipid bilayer. According to the nature of this membrane-protein interaction, membrane proteins can be broadly classified in two main categories: integral and peripheral proteins.

1) They also play a role in membrane structure, as we study in the third Part of this thesis.

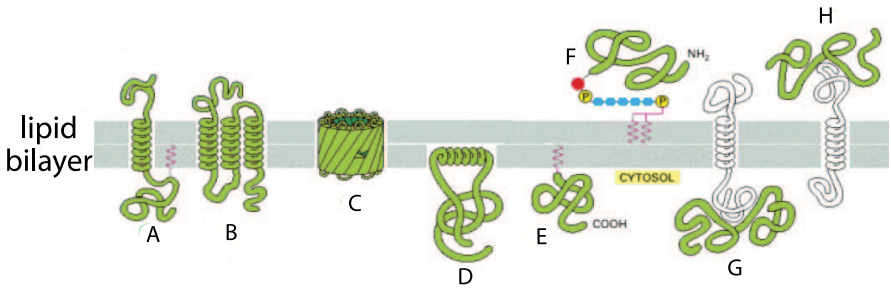

Figure 2.4 Membrane protein association with the lipid bilayer. Transmembrane proteins (A-C) span across the whole bilayer thickness as a single (A) or several (B) α-helices; or as a β-barrel (C). Integral monotopic proteins (D-F) anchor to a part of the entire membrane by insertion of the hydrophobic residues of an α-helix (D), or by attaching the bilayer through a lipid intermediate by a covalent bond (E), or by a oligosaccharide linker (F). Noncovalent interaction of a protein with another protein link peripheral membrane proteins to any side of the bilayer (G,H). Adapted from Ref. [3].

- **Integral proteins.** They are permanently attached to the membrane, requiring some apolar solvent (like a detergent) to be removed. According to how they anchor to the membrane, they can be subclassified as transmembrane proteins or integral monotopic proteins.

  Transmembrane proteins span the entire membrane, crossing it at least once (see 2.4A) (or weave it several times (see 2.4B)). Like lipids, these are also amphiphilic molecules. Their hydrophobic parts insert into the hydrophobic core of the bilayer, while their hydrophilic domains are exposed to either the inner or the outer aqueous media. Among transmembrane proteins, we may cite α-helical proteins (see 2.4A,B), and β-barrels (see 2.4C).

  Integral monotopic proteins are permanently attached to the membrane by one side. They might contain an amphipathic α-helical domain which anchors one leaflet of the bilayer (see 2.4D). They can also directly attach lipid chains by covalent bonds (see 2.4E), or via an oligosaccharide linker (see 2.4F).

- **Peripheral proteins.** Other membrane proteins do not span over the entire thickness of the bilayer membrane, not reaching its hydrophobic region. These proteins are noncovalently bound to other proteins in either face of the bilayer (see 2.4G,H). Extraction of these proteins is easier than for integral proteins, for instance by adding a solution of extreme pH or salt concentration, which affects on the protein-protein interactions, but not on the stability of the lipid bilayer.

In the third Part of this thesis we are devoted to understand a mechanism of curvature generation by membrane proteins, particularly, by the partial insertion of amphiphilic α-helices into the membrane.

2.2 Self-assembly

We have just seen the amphiphilic nature of lipid molecules. What happens when we put a certain number of amphiphilic molecules in water solution? The hydrophilic moiety of the amphiphiles is energetically favored by being in contact with the water environment, contrarely to what occurs to the hydrophobic moiety. An answer, in terms of reducing the free energy of the amphiphiles, comes from the fact that the energy cost of these hydrocarbon-water interfaces can be lowered by creating aggregates, in expenses of reducing the entropy of the system. If the overall free energy is lower in such a configuration, we say that the system has self-assembled or self-organized. Quoting S. Camazine *et al.*'s book [35]:

> Self-organization is a process in which pattern at the global level of a system emerges solely from numerouse interactions among the lower-level components of the system. Moreover, the rules specifying interactions among the system's components are executed using only local information, without reference to the global pattern.

It is, lipid-lipid and lipid-water interactions arrange the amphiphiles in a geometrically constrained pattern which minimizes the total free energy of the system.

2.2.1 Thermodynamics of self-assembly

Let us study the thermodynamics of a system consisting of molecular aggregates. An aggregate of size N, in this sense, is an association of N molecules (monomers). Thermodynamical equilibrium requires that the chemical potential of all identical molecules in aggregates of different size be equal [123, 245]. This chemical potential can be expressed as follows [123],

$$\mu_N = \mu_N^0 + \frac{1}{N} k_B T \log\left(\frac{X_N}{N}\right) = \text{constant}, \quad N = 1, 2, 3, \ldots, \tag{2.1}$$

where μ_N is the mean chemical potential of a molecule in an aggregate of size N; μ_N^0 is its mean interaction free energy per molecule; $k_B T$ is the product of the Boltzmann constant and the absolute temperature; and X_N is the concen-

tration of molecules in N-sized aggregates. It can be rewritten in the following equivalent form

$$X_N = N \left[X_1 \exp\left(\frac{\mu_1^0 - \mu_N^0}{k_B T} \right) \right]^N, \tag{2.2}$$

which, together with the conservation relation for the total solute concentration, C,

$$C = \sum_{N=1}^{\infty} X_N, \tag{2.3}$$

completely defines the system. We notice, from Eq. (2.2), that the way μ_N^0 changes with N describes the formation of large aggregates. Thus, for μ_N^0 increasing with N, or even independent of it, large aggregates form at very low concentrations (remind that $X_1 \leq 1$). The necessary condition for the formation of large aggregates is then that the mean interaction free energy per particle, μ_N^0, decreases with the aggregate size, N.

2.2.2 Amphiphile self-assembly

Let us now focus on the self-assembly of amphiphilic molecules. From the general thermodynamic theory in the previous Section, one can see that a theory describing the interaction free energy is needed in order to further proceed. Self-assembly of amphiphiles is mainly governed by two kinds of forces.

First, the hydrophobic attraction at the hydrocarbon-water interface. Due to the energy cost of exposing the lipid acyl chains, the size of this interface tends to shrink, creating an effective attractive force between lipid molecules. Typical interfacial free energies per unit area for membrane lipids are $\gamma \approx 20 - 50\ \mathrm{mJ\,m^{-2}}$ [123,193]. Thus, this contribution to the interaction free energy can simply be written as

$$\mu_{N,\mathrm{att}}^0 = \gamma a, \tag{2.4}$$

where a is the surface area occupied per headgroup [2].

Second, the hydrophilic, ionic, or steric repulsion of the headgroups generates an opposite repulsive interaction between these polar heads. In spite of the complexity of this interaction, we can give a first order approximation.

2) Sometime the attractive free energy is written as

$$\mu_{N,\mathrm{att}}^0 = \gamma(a - a^*),$$

but this only changes the zero of energy, so it has no effect on further analyses.

If we expand the energy in terms of the inverse of the surface area per headgroup,

$$\mu^0_{N,\text{rep}} = \mu^0_{N,\text{rep}}\left(\frac{1}{a}\right) = A + K/a + K'/a^2 + \ldots, \tag{2.5}$$

which, up to the first relevant order, and neglecting the constant term in the expansion, can be rewritten as

$$\mu^0_{N,\text{rep}} = \frac{K}{a}. \tag{2.6}$$

The total interaction energy is then the sum of Eq. (2.4) and Eq. (2.6),

$$\mu^0_N = \gamma a + \frac{K}{a}. \tag{2.7}$$

The optimal headgroup area, a_0, is found after minimization of the interaction energy Eq. (2.7) (see Fig. 2.5),

$$\left.\frac{\partial \mu^0_N}{\partial a}\right|_{a=a_0} = 0 \quad \Rightarrow \quad a_0 = \sqrt{\frac{K}{\gamma}}. \tag{2.8}$$

Using this in Eq. (2.7), we can eliminate the unknown constant K, and then write the interaction free energy in terms of measurable physical parameters,

$$\mu^0_N = 2\gamma a_0 + \gamma\frac{(a-a_0)^2}{a}. \tag{2.9}$$

It has to be noted that in this simplified description important effects have been disregarded, such as specific interactions between polar heads or between non-polar chains or curvature effects [123].

2.2.3 Shape of aggregates: geometric packing parameter

The interaction free energy Eq. (2.9) is almost independent on the aggregation number N. In this case, as we argued from Eq. (2.2), entropy favors the structure with the lowest aggregation number. However, energy considerations impose that the area per headgroup, a, keeps its optimal value a_0. The shape of aggregates is thus dictated by geometric considerations, as follows.

Assume that we define a molecular geometry based on the packing properties of the molecule itself. The area per molecule remains in its optimal value, a_0. The volume of the hydrophobic core, v, is also kept constant because of the incompressibility of the fluid. The other parameter is the so-called critical chain length, l_c, which sets a limit in the length of the chains. From these three

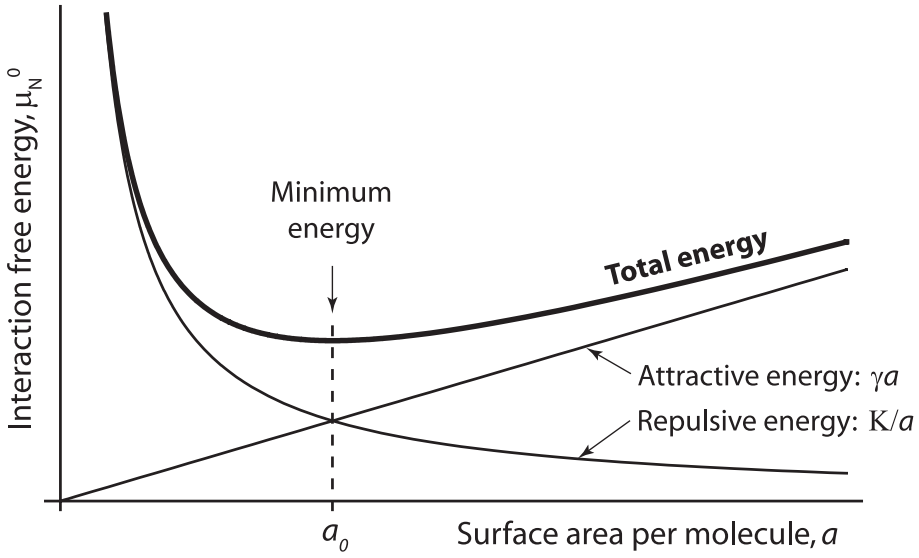

Figure 2.5 Qualitative plot of the interaction free energy, μ_N^0, as a function of the surface area per molecule, a. Both the attractive and the repulsive parts of the total energy are shown. The optimal headgroup area, a_0, is found by minimizing the total energy with respect to the surface area per molecule, and corresponds to the crossing point of the attractive and repulsive energies.

geometric parameters we can define a dimensionless quantity, the packing parameter, or shape factor, p, as

$$p = \frac{v}{a_0 l_c}, \tag{2.10}$$

such as $p < 1$ for conelike or truncated conelike structures, $p = 1$ for cylinders, and $p > 1$ for inverted conelike geometries (see Fig. 2.6). The value of this parameter, i.e. the effective packing shape of the amphiphile, determines in which structure the amphiphiles self-assemble [124]:

- **Spherical micelles.** Consider a spherical micelle of radius R, formed by the aggregation of M amphiphiles of area a_0, volume v, and maximum chain length l_c (see Fig. 2.6). The total surface area and the micelle volume are, respectively,

$$A_{\text{sph}} = 4\pi R^2 = M a_0, \tag{2.11}$$

$$V_{\text{sph}} = \frac{4}{3}\pi R^3 = M v, \tag{2.12}$$

from where, eliminating M, we get that

$$R = \frac{3v}{a_0}, \tag{2.13}$$

and since the radius of the micelle has to be smaller than the maximum chain length, $R \leq l_c$, and using Eq. (2.10), we get the following geometrical constraint on the formation of spherical micelles,

$$p_{\text{sph}} \leq \frac{1}{3}. \tag{2.14}$$

Lysolipids (lipids lacking one of the two hydrocarbon chains) with large headgroup areas usually fall under this regime of being micelle-forming lipids.

- **Cylindrical micelles.** For packing parameters $p > 1/3$, spherical micelles cannot be formed by geometric considerations, altough they would be the most suitable structures in entropic terms. Let us check in which regime of the packing parameter cylindrical micelles of radius R and length L can be formed [3]. As previously we calculate the area and volume of such a micelle, which respectively are

$$A_{\text{cyl}} = 2\pi RL = Ma_0, \tag{2.15}$$

$$V_{\text{cyl}} = \pi R^2 L = Mv. \tag{2.16}$$

Again, since $R \leq l_c$, we get the following condition for the packing parameter,

$$\frac{1}{3} < p_{\text{cyl}} \leq \frac{1}{2}. \tag{2.17}$$

Single-chained lipids with small headgroup areas, like lysolecithin, fit in this regime of values of the lipid packing factor.

- **Vesicles and bilayers.** For larger packing parameters, micelles cannot be formed, and then vesicles or bilayers are formed (see Fig. 2.6). The area and volume of a piece of bilayer, of area A_{bil}, and thickness $2h$, are, respectively,

$$A_{\text{bil}} = Ma_0, \tag{2.18}$$

$$V_{\text{bil}} = \frac{A_{\text{bil}}}{2} 2h = Mv, \tag{2.19}$$

and, since $h \leq l_c$, we have that

$$p_{\text{bil}} \leq 1. \tag{2.20}$$

3) This length has to be finite, therefore leaving free edges which are energetically unfavorable, and they have to pack into hemispherical caps which do not fall under the range of permitted packing parameter, thus adding an energy cost to the total micellar free energy (see Ref. [123] for a more detailed discussion on this issue).

Most common phospholipids are bilayer-forming lipids. Depending on the relative size of their headgroups and acyl chains, their packing factor gets closer to the unity.

- **Inverted micelles.** When the packing factor exceeds the unity, $p > 1$, inverted micelles come into play. In this situation, amphiphiles are not soluble in water anymore, and form inverted structures with crystalline order (such as inverted hexagonal or inverted cubic phases) at high amphiphile concentration. Double-chained lipids with small headgroup area and unsaturated hydrocarbon chains at high temperature may form inverse structures.

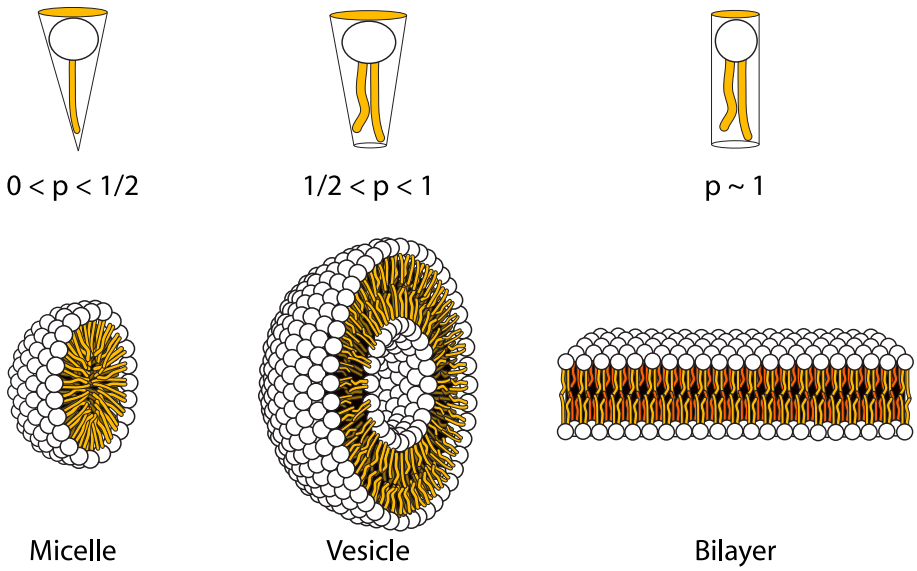

Figure 2.6 Lipid self-assembly. Depending on the value of the lipid packing factor, p, different structures are formed. From left to right, a micelle, a vesicle, and a bilayer are shown. In the upper line, the mean lipid geometry is shown, and under which range of packing factor values each structure is formed.

Summarizing, depending on the geometric properties of amphiphiles, different kinds of structures are formed by self-assembly. In particular, single-chained lipids (surfactants like common soap), tend to adopt packing factors $p \lesssim 1/2$, whereas double-chained lipids have packing factors $p \gtrsim 1/2$, thus favoring the formation of bilayers, or, turning the tables, bilayers can be formed by double-chained lipids, as it is known to happen in cells.

2.3 Phase behavior of cell membranes

Lipid bilayers present different phases depending on their composition, temperature, or lateral pressure. Simple single-component model bilayers already present a rich polymorphism (see Ref. [139] for a review on phosphatidylcholine lipid phases); while more complex bilayer mixtures (containing phosphoglycerides, sphingolipids, and cholesterol) might indeed form phase-separated domains within the lipid bilayer, the so-called lipid rafts [234] (see also Part II of this thesis). These topics are of a great interest and they are subject of extensive studies. However, at this point, we will only introduce the basic concepts of lipid phase polymorphism, focusing ourselves in lamellar bilayer lipid phases (for further information on lipid polymorphism, cfr. Chapter 3 in [160], and for polymorphism in lipid monolayers, Chapter 4 *ibid*.).

Phospholipid bilayers are generally, at physiological temperatures, in a fluid state. More precisely, in a lamellar fluid state, where lipids are free to move along the bilayer plane (the diffusion coefficient of a lipid being $D \sim 10^{-8}$ cm^2/s, that is, they have a fast diffusion), and the acyl chains are highly disordered accounting for a large entropy level. Such a phase is called liquid-crystalline or *liquid-disordered phase*, and represented by l_d, or L_α (L for lamellar, and α for liquid-like chain conformation) (see Fig. 2.7a).

When the temperature of the bilayer decreases under a certain temperature, T_m, the melting temperature, characteristic of each lipid, phospholipid bilayers go into a 'frozen' state. This phase is the ordered *gel phase*, or solid-ordered phase, and it is represented as L_β (β for ordered gel-like chains). It corresponds to a slow lipid diffusion along the membrane plane (the diffusion coefficient of a lipid being $D \sim 10^{-10}$ cm^2/s, two orders of magnitude slower than in the L_α phase). In addition, gel phase can be subdivided according to the mean orientation of the lipid chains. If they are oriented along the bilayer normal, we say that the bilayer is in an *untilted* gel phase, L_β (see Fig. 2.7b). Otherwise, when the lipids are tilted a certain angle with respect to the bilayer normal, the bilayer is in a *tilted* gel phase, $L_{\beta'}$ (see Fig. 2.7c). However, the gel phase does not appear to exist in biological membranes, except for unusual cases [192].

Phase coexistence of L_α and L_β phases has been experimentally observed by confocal microscopy and fluorescence spectroscopy in model pluricomponent vesicles [137]. In these membranes, the presence of cholesterol acts as a chain rigidifier (see Sec. 2.1.1), and a new liquid phase can be observed, the so-called *liquid-ordered* phase (see Fig. 2.7d). In this phase, lipid chains acquire their maximum length, like in the gel phase, thickening the bilayer from $\sim$ 4 nm to $\sim$ 5 nm. However, lipids have still a relatively large lateral mobility (the

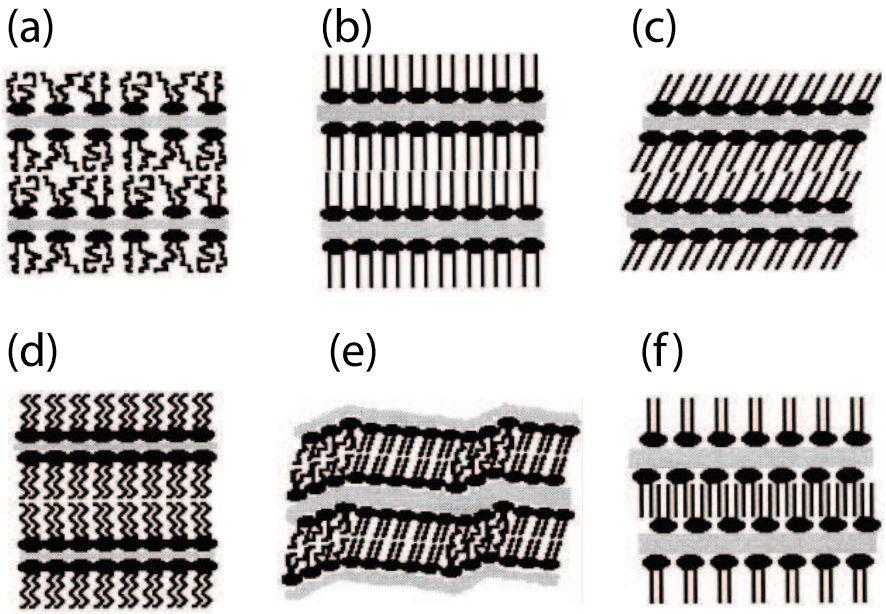

Figure 2.7 Lipid phases in bilayers. (a) Liquid-disordered, L_α phase with highly disordered hydrophobic chains. (b) Gel phase, L_β, with the acyl chains ordered parallelly to the bilayer normal; or (c) tilted with respect to it, in the tilted gel phase, $L_{\beta'}$. (d) Liquid-ordered phase, L_c, with intermediate ordination of the acyl chains. (e) Ripple-phase, P_β, gel-like phase with a periodic modulation deforming the lamellae. (f) Interdigitated gel phase, L_β^{int}, where the acyl chains are ordered and overlap the hydrophobic region occupied by the opposing leaflet of the bilayer.

diffusion coefficient being $D \sim 10^{-9}$ cm^2/s, in between L_α and L_β phases). This phase is usually represented as l_o, or L_c (c for crystalline).

There are other lamellar phases that can be found among lipid mixtures, as the gel ripple phase, P_β, where the lamellae are deformed by a periodic modulation (see Fig. 2.7e); or many kinds of interdigitated gel phases, L_β^{int}, where fatty acid chains interdigitate with respect to each other in several possible conformations (see Fig. 2.7f).

3
Some aspects on mechanics of membranes and vesicles

3.1
Elastic properties of lipid bilayers: historical perspective

The problem of understanding which forces maintain the biconcave shape of human red blood cells [20] (see Fig. 3.1) has been an enigma since their discovery in the seventeenth century. Quoting D'Arcy Thompson's inspiring book *On Growth and Form* [247]:

> The form of the [red blood-]corpuscle is symmetrical; it is a solid of revolution, but its surface is not a surface of constant mean curvature. From the surface-tension point of view, the blood-corpuscle is not a surface of equilibrium; in other words, it is not a fluid drop poised in another liquid.

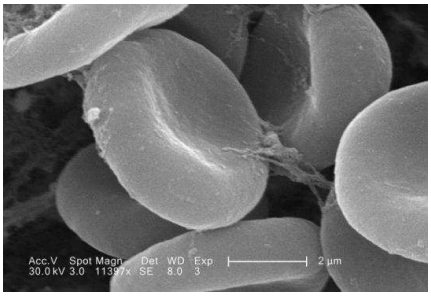

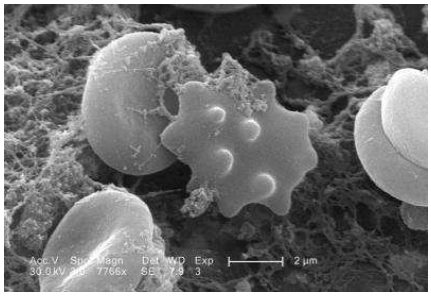

Figure 3.1 Highly enlarged scanning electron micrograph (SEM) depicting a closer look at the details exhibited by of number of red blood cells found enmeshed in a fibrinous matrix on the luminal surface of an indwelling vascular. (a) Healthy biconcave shaped red blood cells. (b) A crenated diseased red blood cell, or echinocyte, is shown in this micrograph. Both images are in the public domain. Content provider: Janice Carr, CDC (`http://www.cdc.gov`).

Observations made by R. P. Rand and others in the sixties (see [44] and references therein) showed that deformed red blood cells resumed to their equilibrium biconcave form within a fraction of a second. As P. B. Canham

pointed out [44], these observations show that biconcave shapes correspond to a configuration of minimum energy:

> We believe the energy minimization is the bending energy of the membrane, and that the membrane is solely responsible for the cell's shape.

In this paper [44], the first to our knowledge which characterizes the biconcave RBC's shape by its bending energy, Canham assumed the following main hypotheses:

- Bending energy minimization gives the red blood cell its characteristic biconcave shape.
- Bending energy vanishes for flat membranes, i.e., no possible asymmetry between the two leaflets of the bilayer is incorporated.
- The total cellular area remains fixed upon shape changes.
- The membrane is homogeneous over the entire surface.
- No shear stresses are taken into account.

These assumptions led him to write the following bending energy

$$U = \frac{D}{2} \int \left(\frac{1}{R_1^2} + \frac{1}{R_2^2} \right) \mathrm{d}A \quad : \quad D = \frac{Eh^3}{12\left(1-\nu^2\right)}, \tag{3.1}$$

where R_1 and R_2 are the two principal curvatures of the surface at a given point (see Appendix A), D is the bending rigidity, E is the Young's modulus of elasticity, h the thickness of the membrane, and ν the Poisson's ratio. This energy was minimized within a certain subfamily of curves, the modified ovals of Cassini, which account for both biconcave and non-biconcave shapes. It was found that, for fixed cell area and volume, the modified Cassini oval with the least bending energy corresponded to a biconcave one (see Fig. 3.2).

However, this approach has several limitations. First, the minimization procedure is only partial, since it is not performed over the whole function space, but only over a very restricted family of curves. Second, the derivation of the bending energy is not the most general possible given the hypotheses assumed in the paper. W. Helfrich, in his 1973 paper [109] formulated a theory of elasticity of lipid bilayers, which corrects some of these limitations. Considering the bilayer as a two-dimensional homogeneous fluid surface, he distinguished three kinds of strains affecting the bilayer elasticity: stretching, tilt, and curvature. He claimed that the only relevant mode of deformation for non-spherical vesicles is curvature. In that case, he assumed that the elastic

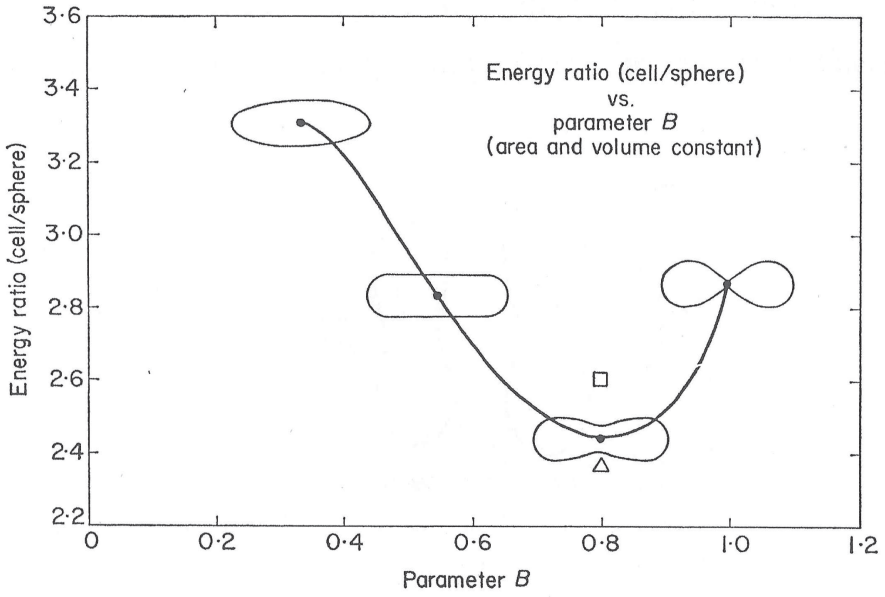

Figure 3.2 Bending energy ratio as a function of a parameter B parametrizing the modified Cassini ovals. The area and volume are constant in the graphic. Energy minimization show that a biconcave oval is the least energy shape. Figure taken from Canham's original paper, Ref. [44].

energy of curvature was a quadratic function of the derivatives of the vector normal to the bilayer, (n_x, n_y). The curvature elastic energy per unit area was written as

$$w_c = \frac{1}{2}\kappa\left(\frac{\partial n_x}{\partial x} + \frac{\partial n_y}{\partial y} - c_0\right)^2 + \bar{\kappa}\left(\frac{\partial n_x}{\partial x}\frac{\partial n_y}{\partial y} - \frac{\partial n_x}{\partial y}\frac{\partial n_y}{\partial x}\right), \tag{3.2}$$

where κ and $\bar{\kappa}$ are the curvature elastic moduli, analogous to the splay and saddle splay moduli of liquid crystal curvature elasticity [58,92]; and c_0 is the spontaneous curvature, allowing the two leaflets of the bilayer to be chemically different. Rewriting Eq. (3.2) as a function of the principal curvatures, c_m and c_p,

$$w_c = \frac{1}{2}\kappa\left(c_m + c_p - c_0\right)^2 + \bar{\kappa}\, c_m c_p, \tag{3.3}$$

or, defining the total and Gaussian curvatures (see Appendix A)

$$w_c = \frac{1}{2}\kappa\left(\mathsf{J} - c_0\right)^2 + \bar{\kappa}\,\mathsf{K}, \tag{3.4}$$

which is a usual notation used nowadays [224,263].

Comparing Canham energy Eq. (3.1) and Helfrich energy Eq. (3.3), we see that Canham equation can be written as

$$U = \frac{D}{2}\int\left(\frac{1}{R_1}+\frac{1}{R_2}\right)^2 \mathrm{d}A - D\int\frac{1}{R_1R_2}\mathrm{d}A, \tag{3.5}$$

which is a special case of Helfrich's, corresponding to the situation when $D = \kappa = -\bar{\kappa}$, and $c_0 = 0$. However, as Helfrich pointed out [109], the saddle splay term (the Gaussian curvature term) depends only on the boundary conditions, and can be omitted in many calculations, making both calculations analogous for the purpose of finding the shapes of least energy [1]. Furthermore, Helfrich derived the Euler-Lagrange equations for the bending energy for a given situation, in order to find the shape minimizing the bending energy without restricting to a given family of curves, as Canham did [44].

Besides, one has to note that these energies Eqs. (3.1), (3.3) are of second order in curvatures, meaning that the expressions are valid for small curvatures[2]. In addition, the internal structure of the bilayer is only effectively included in this model through the elastic parameters, since the bilayer is considered to be a two-dimensional surface.

One year later, Evans [77] studied the bending resistance of bilayers in order to understand a possible mechanism for red blood cell crenation [20]. He argued that the shape transformation from biconcave discs to crenated echinocytes might be due to chemically induced bending moments. He studied the bilayer as a composite of two *connected* or *unconnected* monolayers, depending on whether the layers slip relative to each other or not[3]. The effect of such a coupling can be considered as the initial seed for ulterior studies on more complex bending models, as the area difference elasticity model.

3.2 Gibbs' description of interfaces

The theory of interfaces was formulated in the late nineteenth century by J. W. Gibbs [100] in order to understand the elastic properties of layers of small but finite thickness. This is the case of amphiphile monolayers, but

1) This is by virtue of the Gauss-Bonnet theorem, which we comment in a while, in Sec. 3.5.2.

2) The units of curvature are inverse length, so we should compare them with another physical parameter with the same units, in this case, the thickness of the bilayer, δ. Meaning that the Canham-Helfrich approximation is valid for $c_i\,\delta \ll 1$, where c_i are the principal curvatures.

3) We use here the same words as in the original paper [77]. However, in the third Part of this thesis, we recall such a coupling between monolayers as laterally coupled and laterally uncoupled monolayers, respectively.

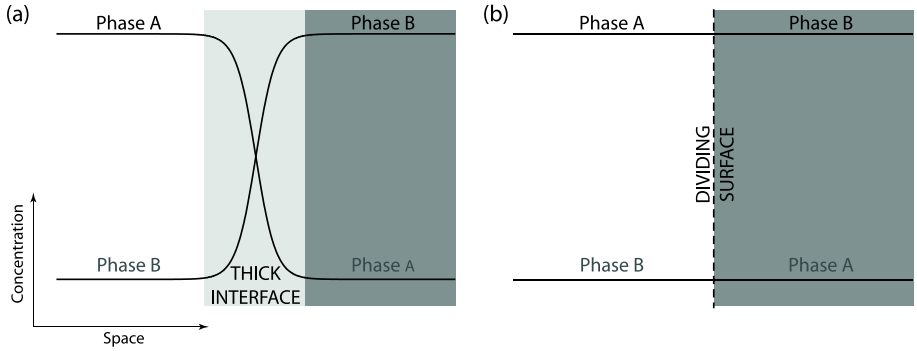

Figure 3.3 Surface excess approach. A thick interface between two different phases, A and B (a), is mapped into a dividing surface (b) which sharply separates both phases.

also of the transition region, of a few molecules width, between two immiscible liquid phases (as the water-oil interface, for instance). Here, we address one of the approaches to this problem, the so-called surface excess approach (see Ref. [141] for a broader description). Within this approach, the actual thick interface is mapped into a two-dimensional surface, located in the interfacial region, and characterizing the geometrical properties of the interface (position and orientation). Such a surface is called a dividing surface. The physical equivalence between both descriptions requires association of thermodynamic quantities to the dividing surface. These quantities correspond to the difference values between the actual system and the system we are taking into account, which extrapolates bulk properties up to the dividing surface (see Fig. 3.3). Note that the election of the dividing surface is arbitrary, and one can choose between multiple choices. In fact, as we will see in a while, choosing an appropriate dividing surface simplifies the whole mathematical description.

Let's see how the internal energy of an element of the dividing surface can be expressed. This element can be fully characterized, from a geometric point of view, by giving its area, A, and both invariants of curvature (see Appendix A): the total curvature, J, and the Gaussian curvature, K. One can thus express the changes of the internal energy of the dividing surface, $\mathrm{d}U^s$, as

$$\mathrm{d}U^s = T\,\mathrm{d}S^s + \sum_i \mu_i\,\mathrm{d}m_i^s + \gamma\,\mathrm{d}A + C_1 A\,\mathrm{dJ} + C_2 A\,\mathrm{dK}, \tag{3.6}$$

where variations of the entropy, S^s, and of the masses of the components, m_i^s, as well as of the geometric properties have been included. The stresses γ, C_1, and C_2 are called interfacial tension, and first and second bending moments, respectively. They are multiplied in Eq. (3.6) by the area of the surface element in order to be intensive quantities. They are defined by the partial derivatives

of the internal energy

$$\gamma = \left.\frac{\partial U^s}{\partial A}\right|_{S^s, m_i^s, \mathsf{J}, \mathsf{K}}, \tag{3.7}$$

$$C_1 = \left.\frac{1}{A}\,\frac{\partial U^s}{\partial \mathsf{J}}\right|_{S^s, m_i^s, S, \mathsf{K}}, \tag{3.8}$$

$$C_2 = \left.\frac{1}{A}\,\frac{\partial U^s}{\partial \mathsf{K}}\right|_{S^s, m_i^s, S, \mathsf{J}}. \tag{3.9}$$

It has to be noted that Gibbs' theory of interfaces is a linear theory for the changes of the energy, higher-order corrections being needed for large deformations of the dividing surface. Besides, it doesn't explicitly incorporate any information about the internal structure of the interface.

3.3 Curvature free energy

Let us now consider the free energy per unit area[4] of the membrane as being function of the geometric properties (we disregard the thermodynamic variables at this point). Up to second order in curvatures, it reads

$$f\,(A, \mathsf{J}, \mathsf{K}) = f_0(A) + f_1(A)\mathsf{J} + f_2(A)\mathsf{J}^2 + \bar{f}_2(A)\mathsf{K}. \tag{3.10}$$

The free energy in the flat state is $f(A, 0, 0) = f_0(A)$, and the equilibrium area of the surface element A_0, meaning that $f_0'(A_0) = 0$, and $f''(A_0) > 0$. Expanding the coefficients in the right-hand side of Eq. (3.10) around A_0 up to the same order, we get

$$\begin{aligned} f\,(A, \mathsf{J}, \mathsf{K}) \approx f_0(A_0) + \frac{1}{2} f_0''(A_0)\,(A - A_0)^2 + f_1(A_0)\mathsf{J} \\ + f_1'(A_0)\,(A - A_0)\,\mathsf{J} + f_2(A_0)\mathsf{J}^2 + \bar{f}_2(A_0)\mathsf{K}. \end{aligned} \tag{3.11}$$

If we minimize it with respect to the surface area A to find the equilibrium area of the curved surface, A^*, we get

$$A^* = A_0 - \frac{f_1'(A_0)}{f_0''(A_0)}\,\mathsf{J}, \tag{3.12}$$

4) We follow here a similar derivation to the one for the free energy per molecule, presented in Ref. [218].

And therefore, evaluating Eq. (3.11) for the equilibrium area of the surface element Eq. (3.12), we get the curvature free energy

$$f\left(A^*, \mathsf{J}, \mathsf{K}\right) = f_0(A_0) + f_1(A_0)\,\mathsf{J} + \left(f_2(A_0) - \frac{f_1'^2(A_0)}{2f_0''(A_0)}\right)\mathsf{J}^2 + \bar{f}_2(A_0)\mathsf{K}. \tag{3.13}$$

3.4 Neutral surface

In the previous Section, we calculated the free energy considering a general dividing surface. One can, however, choose a specific dividing surface which decouples the area stretching mode and the bending mode. This surface is called the neutral surface. Shifting the dividing surface a quantity λ to a new parallel surface, the new geometric quantities (see Appendix A), up to second order in deformations, are

$$A' = A\left(1 - \lambda\mathsf{J}\right), \tag{3.14}$$

$$\mathsf{J}' = \mathsf{J}\left(1 + \lambda\mathsf{J}\right) - 2\lambda\mathsf{K}, \tag{3.15}$$

$$\mathsf{K}' = \mathsf{K}. \tag{3.16}$$

Therefore, after some algebra, the free energy Eq. (3.11) becomes

$$\begin{aligned} f\left(A', \mathsf{J}', \mathsf{K}'\right) \approx\ & f_0 + \frac{1}{2}f_0''\left(A' - A_0\right)^2 + f_1\mathsf{J}' \\ & + \left(f_1' + 2A_0\lambda f_0''\right)\left(A' - A_0\right)\mathsf{J}' + \bar{f}_2\mathsf{K}' + f_1\lambda\mathsf{K}' \\ & + \left(2f_0''A_0^2\lambda^2 + 2f_1'A_0\lambda + f_2 - 2f_1\lambda\right)\mathsf{J}'^2. \end{aligned} \tag{3.17}$$

From the definition of the neutral surface as the surface on which the stretching and bending modes are decoupled, we have to ask the coefficient behind the coupling term in Eq. (3.17) to vanish

$$f_1' + 2A_0\lambda f_0'' = 0 \ \Rightarrow\ \lambda = -\frac{f_1'}{2A_0f_0''}, \tag{3.18}$$

giving the location of the neutral surface depending on the details of the model. The free energy, after minimizing with respect to the area of the neutral plane, reads

$$f\left(A'^*, \mathsf{J}', \mathsf{K}'\right) \approx f_0 + f_1\,\mathsf{J}' + \left(f_2 + \frac{f_1f_1'}{f_0A_0} - \frac{f_1'^2}{2f_0''}\right)\mathsf{J}'^2 + \left(\bar{f}_2 - \frac{f_1f_1'}{2A_0f_0''}\right)\mathsf{K}',$$

(3.19)

where $A'^{*} = A_0$. One can also compare this with the Helfrich model Eq. (3.4) to get the values of the elastic moduli as a function of the model parameters [218].

3.5 Curvature models and stationary shapes of fluid vesicles

Stationary shapes of fluid vesicles are found when the corresponding energy is minimized according to certain geometrical constraints, imposed by some physical properties of vesicles. Besides, for homogeneous fluid vesicles one can ignore the Gaussian curvature term of the Canham-Helfrich energy since it is a topological invariant. Shape diagrams can be traced telling which is the stationary shape given all the independent parameters of the specific model. In this Section we briefly discuss these facts in order to get a general perspective on the topic. We refer to [224] for an exhaustive review on curvature models and configurations of fluid membranes.

3.5.1 Geometric constraints

As we reported in Ch. 2 of this thesis, membrane lipids are amphiphilic molecules which in aqueous solution self-assemble due to the hydrophobic effect [244, 245, 257]. The concentration of lipid molecules in solution out of the formed bilayer structure is very small, typical values ranging from one to hundred molecules per μm^3 [165]. If there is no externally applied flux of lipids coming into or going away from the bilayer, the number of lipids within a vesicle membrane remains constant. Since the area per lipid is also fixed at constant temperature, due to the relatively high energy needed to stretch the membrane, the total area of the vesicle surface is also constant.

The energy for a water molecule to cross the hydrophobic core of a lipid bilayer is of the order of the thermal energy, so lipid bilayers are permeable to water. However, the same energy for ions or large molecules is of at least hundred-fold times the thermal energy, meaning that the bilayer is not permeable to these molecules, and that is also the reason why ion channels and pumps exist in biological membranes [116, 222]. The presence, deliberate or not, of some of these molecules osmotically control the volume enclosed by the vesicle, since the generation of osmotic pressure can't be counterbalanced by the bending forces of the membrane [109].

The shape of a fluid vesicle has to be found taking into account these constraints on fixed surface area and vesicle inner volume. A way to include them in the energy model is by defining two Lagrange multipliers, Σ and P, for

the conservation of total membrane surface area, $A[\Omega]$, and enclosed volume, $V[\Omega]$, respectively. Thus, one can write the following variational effective free energy

$$F_{\text{eff}} = F_{\text{curv}} + \Sigma A[\Omega] + PV[\Omega], \tag{3.20}$$

where F_{curv} stands for the bending energy of the desired curvature model (see below).

3.5.2 Gauss-Bonnet theorem

The Gauss-Bonnet theorem [68, 130] states that the integral of the Gaussian curvature, K, of a compact Riemannian manifold M; plus the integral of the geodesic curvature, k_g, along its boundary, ∂M; plus the sum of the jump angles of this boundary, α_i, is proportional to the Euler characteristic, $\chi(M)$, of the manifold. Mathematically,

$$\int_M \mathsf{K} \mathrm{d}A + \int_{\partial M} k_g \mathrm{d}s + \sum_i \alpha_i = 2\pi\chi(M). \tag{3.21}$$

This is the most general way to write the Gauss-Bonnet theorem. However, this expression simplifies when the manifold M is a closed regular surface. In this case there is no boundary, and the Gauss-Bonnet theorem reads

$$\int_M \mathsf{K} \mathrm{d}A = 2\pi\chi(M). \tag{3.22}$$

The Euler characteristic χ is a topological invariant, meaning that it only changes when the topology of the shape changes, but remains constant as long as continuous deformations (homotopies) [180] are performed. For a regular surface, it can be expressed as

$$\chi = 2\,(N - g), \tag{3.23}$$

where N is the number of objects, and g is the genus of the surface, i.e. the number of handles or holes it has. For example, a sphere has Euler characteristic $\chi(\text{sphere}) = 2$; and a one-handle torus has Euler characteristic $\chi(\text{1-torus}) = 0$ (see Fig. 3.4). This theorem implies that the Gaussian term of the Helfrich bending energy is a topological constant as long as (i) we are dealing with a closed regular surface, and (ii) the Gaussian rigidity, k_G, is homogeneous all over this surface. During the rest of this Chapter, we will restrict ourselves to discuss the physics arising from the bending terms without considering the Gaussian curvature term. However, we will see along the thesis that the Gaussian curvature term might be relevant in different physical situations while studying membrane morphology.

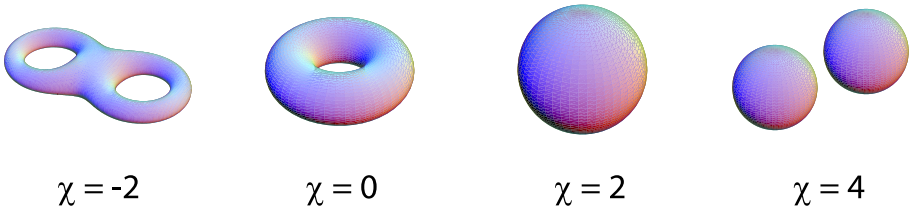

Figure 3.4 Euler characteristic, χ, for different topologies.

3.5.3 Shape equation

The problem of finding the stationary shapes of vesicles given an energy model and the needed constraints is the problem of finding the minimum of the energy in the subspace of shapes on which the above mentioned constraints hold. Lots of effort have been made in solving this problem, and different approaches appeared in the last decades. Here, we will just mention some of them, and give some references for further information.

The first approach, and probably the most used, goes back to Helfrich's seminal paper [109], and is due to variational calculus [99]. He set up an Euler-Lagrange equation for the shape of rotationally symmetric bilayers. Shape equations as Euler-Lagrange equations for the energy functional under consideration have been widely studied since then [64, 109, 126, 128, 140, 176, 225, 261, 262]. Although a general shape equation can be found without assuming any symmetry of the resulting shapes, it is usually of practical reason to get an axisymmetric parametrization of the vesicle shape. Such a simplification results in a non-linear ordinary differential equation whose solution under certain boundary conditions gives the stationary shapes of vesicles[5]. We will use this approach in the second part of this Thesis where we study the shape of periodic biphasic lipid tubes.

In addition to this method, numerical minimization on triangulated surfaces has been implemented to find non-axisymmetric shapes [259], and also in order to find red blood cell shape transformations coupling the curvature model with the cytoskeleton elasticity [159, 178]. Mesoscopic simulations using dissipative particle dynamics (DPD) have been performed by Noguchi and Gompper [187–189] to study hydrodynamic effects on lipid vesicles. Lattice Boltzmann methods [158,237] have also been used to study vesicle shapes.

Different phase-field models have also been implemented to study the stationary shapes of vesicles [15, 38, 72]. In the first Part of this thesis we will

5) Since the variational problem $\delta^{(1)} F = 0$, and therefore the shape equation, is only a necessary but not sufficient condition of energy minimality, further inspection has to be done in order to check the stability of the solution.

present our derivation of a bending phase-field model and apply it to study different dynamic instabilities on membranes.

3.5.4 Stationary shapes and shape diagram of the minimal model

The so-called minimal model, as discussed above, is nothing else than the initial Canham model [44], or the Helfrich model [109] with no preferred curvature for the bilayer, meaning that a free piece of membrane would relax to a flat state with zero curvature. Let us recall here this bending energy,

$$F_{\mathrm{M}} = \frac{\kappa}{2} \int_{\Omega} (2\mathsf{H})^2 \, \mathrm{d}s, \tag{3.24}$$

where κ is the bending rigidity, H is the mean curvature[6], and the integral is done over the whole membrane surface, Ω. It has to be pointed out that the only elastic parameter in this model is the bending rigidity, which defines the energy scale, but does not affect the minimization procedure. Besides, when the area and volume constraints are applied (see Eq. (3.20)), these two new parameters appear. However, due to the scale invariance of the bending energies, only the area to volume ratio is relevant for the shape diagram. The so-called reduced volume, v, is defined as the dimensionless volume to area ratio,

$$v \equiv \frac{V}{V_{\mathrm{sph}}(A)}, \tag{3.25}$$

where $V_{\mathrm{sph}}(A)$ is the volume of a sphere with area A, namely

$$V_{\mathrm{sph}}(A) = \frac{4\pi}{3} \left(\frac{A}{4\pi} \right)^2, \tag{3.26}$$

which implies that the reduced volume is bound between $0 < v \leq 1$, where $v = 1$ only holds for a sphere, and $v = 0$ is the limit case of vanishing volume or infinite area. Therefore, for a given reduced volume, and a given topology, it is theoretically possible to find the stationary shapes. Seifert and coauthors [225] used the Euler-Lagrange equation for axisymmetric shapes of spherical topology to find the stationary shapes of vesicles according to different curvature models. For the minimal model, they found three branches of local minima, corresponding to three qualitatively different shapes: prolates, oblates and stomatocytes (see Fig. 3.5 a). Some of these shapes can be found as metastable shapes (see Fig. 3.5 b).

6) In this thesis, we use indistinctly both the mean curvature H, and the total curvature $\mathsf{J} = 2\mathsf{H}$ (see Appendix A).

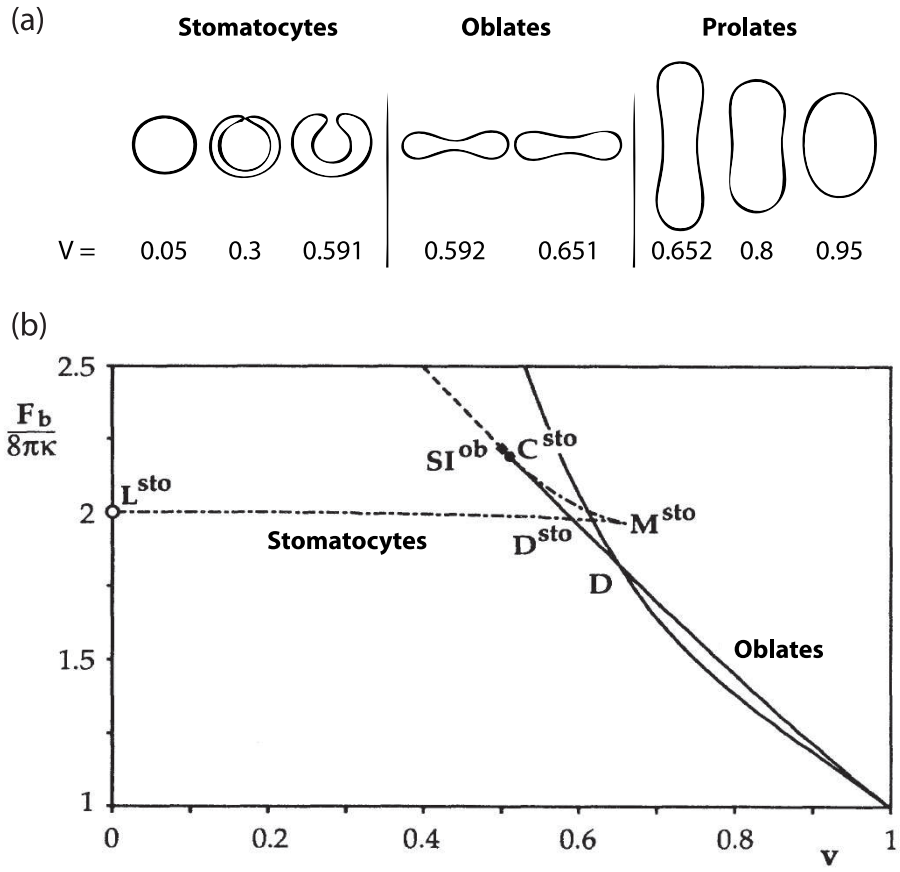

Figure 3.5 Stationary shapes for the minimal model. (a) Shapes of minimal curvature energy for different values of the reduced volume, v: stomatocytes, oblates, and prolates (from left to right), separated by two discontinuous transitions. (b) Shape diagram showing the bending energy Eq. (3.24) as a function of the reduced volume, v, for the three different stable shapes mentioned above. Figures adapted from Ref. ([225]).

For non-spherical topologies, lot of work has also been done (see Ref. [224] and references therein), and different branches of stable shapes have been found. In Fig. 3.6 we present some of the genus-1 toroidal shapes that minimize the energy of the minimal model.

3.5.5 Refined curvature models

Already in Helfrich's paper [109], an improvement of the minimal model is given, by letting the free membrane have a preferred curvature. This model is known as the spontaneous curvature (SC) model. Let us recall its correspond-

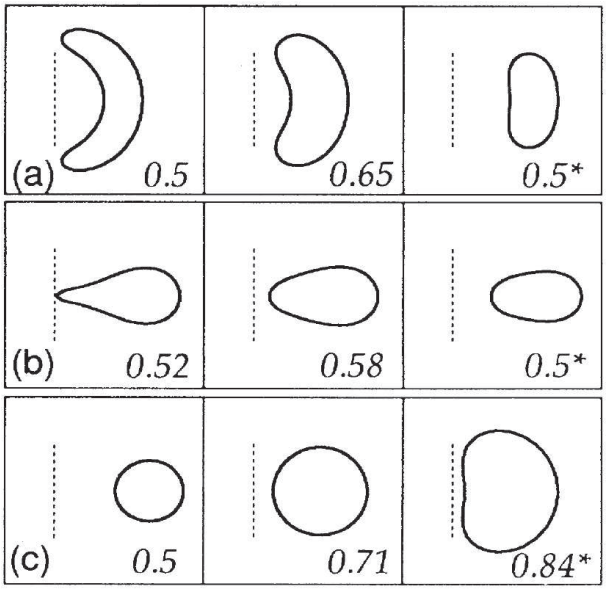

Figure 3.6 Shapes of genus 1 toroidal topology, from Ref. [223]. Sickle-shaped tori (a), discoids (b), and circular toroids (c) can be found for different values of the reduced volume v.

ing bending energy,

$$F_{SC} = \frac{\kappa}{2} \int_{\Omega} (2H - c_0)^2 \, ds, \tag{3.27}$$

where c_0 is the spontaneous curvature of the bilayer. The physical origin of this spontaneous curvature may stem from different origins. Depending on the shape of the lipids, they can have a positive or negative spontaneous curvature [263]. However, if the two monolayers are similar in composition, the resultant bilayer spontaneous curvature vanishes, since one monolayer curvature tendency opposes to the other's. Thus, an asymmetry between the two monolayers can be an origin of a bilayer spontaneous curvature. In the third Part of this thesis we will study mechanisms by which proteins induce spontaneous curvature to membranes.

We saw above that the minimal model grasps some of the experimentally observed vesicle shapes. However, it doesn't explain, for instance, pear-like shapes. The spontaneous curvature model explain such shapes, and a shape diagram has been constructed for a large region of the $v - c_0$ phase-space [225] (see Fig. 3.7).

In the eighties, Svetina and coauthors introduced another model, the bilayer couple (BC) model [239–241]. In this model, an extra constraint is required. Not only the whole area of the bilayer remains fixed, but also the areas of the two monolayers separately. Thus, the area difference between the outer and

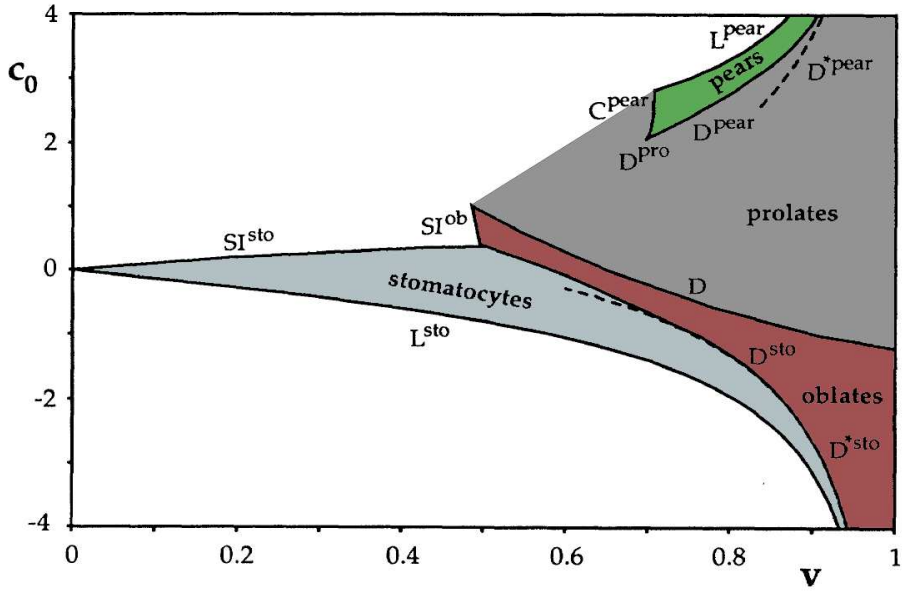

Figure 3.7 Stationary vesicle shapes corresponding to the spontaneous curvature model. Stomatocytes (blue region), oblates (red region), and prolates (gray region) are found similarly to the minimal model. In addition, pears (green region) are found for positive values of the spontaneous curvature, c_0. White regions correspond to unexplored regions of the parameter space. See [225] for further details on the distinct transitions. Figure modified from Ref. [225].

the inner monolayers is also fixed (provided that flip-flop of lipids from one monolayer to the other is slow, and thus not relevant in that situation). This extra constraint also predicts pear-like shapes [225].

Later on, based on the mechanism proposed in the mid seventies by Sheetz and Singer [229], and also by Evans [77], several groups proposed the area-difference-elasticity (ADE) model [28, 226, 258], where the hard constraint of the BC model was relaxed, and an elastic energy was added to take into account the energy penalty for deviations of a preferred area difference.

3.6 Thermal fluctuations

Membranes and vesicles are of course subject to thermal fluctuations. Actually, the typical energy scale of a piece of membrane, given by its bending rigidity, is of the order of a few tens of k_BT. Bending energy is thus comparable to thermal energy, and thermal undulations will be visible. However, it isn't still large enough to keep a well-defined shape. Shape fluctuations of giant vesicles can indeed be seen by light microscopy.

The main effect of these fluctuations is to absorb membrane area. Therefore, the real area of the vesicle is larger than the projected area, and the membrane becomes rough. Using Fourier representation of the Helfrich energy in a Monge representation (see Appendix A) for the height of an almost planar membrane, the energy of a bending mode can be defined as [111, 224]

$$E_0(\boldsymbol{q}) = \kappa \boldsymbol{q}^4, \tag{3.28}$$

where $\boldsymbol{q}$ is the Fourier wavevector. The mean square amplitudes are controlled by the equipartition theorem [121] which, in equilibrium, assigns to each mode a mean deformational energy of $1/2\, k_B T$ [111].

3.7 Microscopic realization of the bending energy

Let us go back for a moment to the basics of elastic theory of surfaces. The three classic deformation modes of a two-dimensional surface are (i) area stretching-compression, (ii) shear deformation, and (iii) curvature [78, 146]. Both area stretching and shear are in-plane deformations, while curvature generates out-of-plane strains.

For lipid membranes in a fluid state, shear deformations can be neglected, since lipid molecules can freely diffuse along the membrane plane[7].

The stretching mode accounts for the energy cost of changing the area of a surface element. Assume that, under no externally applied stresses, the surface preferred area is A_0. Considering the stretching energy being a function of the actual area, i.e. $E_{\mathrm{ST}} = E_{\mathrm{ST}}(A)$, we have that

$$\left.\frac{\partial E_{\mathrm{ST}}(A)}{\partial A}\right|_{A_0} = 0. \tag{3.29}$$

Therefore, the stretching energy, up to the lowest order, and defining the zero energy at the flat state, can be written as

$$E_{\mathrm{ST}}(A) = \frac{1}{2} E''_{\mathrm{ST}}(A_0)\ (A - A_0)^2, \tag{3.30}$$

where $E''_{\mathrm{ST}}(A_0) = \left.\frac{\partial^2 E_{\mathrm{ST}}}{\partial A^2}\right|_{A_0}$. By defining the overall stretching-compression modulus,

$$\Gamma \equiv A_0\, E''_{\mathrm{ST}}(A_0), \tag{3.31}$$

7) Note that, at this level of description, we are not taking into account the inner structure of a monolayer. In the third Part of this thesis, we will see that transverse shear is important when building a microscopic model of the monolayer matrix.

we can rewrite Eq. (3.30) as

$$E_{\mathrm{ST}}(A) = \frac{1}{2}\,\Gamma\frac{(A-A_0)^2}{A_0}. \tag{3.32}$$

The value of the overall stretching-compression modulus has been measured experimentally by micropipette aspiration techniques [75, 76, 206], and is of the order of $\Gamma \approx 0.1$ N/m, for typical monolayers.

The bending mode has been widely discussed above. We will see now how this mode can be recovered from the energy of stretching and compression of the different layers of a thick monolayer. Let us assume the monolayer to be a thick layer of a homogeneous and isotropic elastic material. Because of this homogeneity, the neutral surface, i.e. the surface which does not vary its area under bending (see Sec. 3.4), lies in the middle of this layer. Let us further assume that the monolayer adopts a cylindrical configuration of radius R, and therefore total curvature $\mathrm{J} = 1/R$. Because of the homogeneity of the layer, the overall stretching-compression modulus is given by

$$\Gamma = \int_{-h/2}^{h/2} \lambda(z)\mathrm{d}z = \lambda h, \tag{3.33}$$

where $\lambda = \lambda(z)$ is the local stretching-compression modulus which we assumed to be homogeneous, h is the monolayer thickness, and the integration is done with respect to the z-axis, normal to and centered at the neutral surface. Upon bending, the layers above the neutral plane are stretched, while the layers below are compressed. The area of a given layer changes as (see Appendix A)

$$A(z) = A_0\ (1 + \mathrm{J}z)\,. \tag{3.34}$$

Note that the area of the neutral plane (located at $z = 0$) does not change. Therefore the total elastic energy of such a monolayer is

$$E_{\mathrm{monolayer}} = \frac{1}{2}\int_{-h/2}^{h/2} \lambda(z)\ \frac{(A(z)-A_0)^2}{A_0}\mathrm{d}z, \tag{3.35}$$

which, using Eqs. (3.33), (3.34), gives

$$E_{\mathrm{monolayer}} = \frac{1}{2}\left(\frac{1}{12}\,\Gamma\,h^2\right)\mathrm{J}^2\,A_0. \tag{3.36}$$

which is nothing else than the Canham-Helfrich bending energy for a cylindrical monolayer. Comparing it with Eq. (3.4), the monolayer bending modulus can be expressed as function of the overall monolayer stretching-compression modulus [111, 146]

$$\kappa_m = \frac{1}{12}\,\Gamma\,h^2. \tag{3.37}$$

This relation, although being obtained considering homogeneity along the monolayer, gives a good prediction for the monolayer bending modulus. For the values of the overall stretching-compression modulus of $\Gamma \approx 0.1$ N/m, and taking the monolayer thickness to be $h = 2$ nm, it gives $\kappa_m \approx 10\ k_B T$, in qualitative accordance with experimental measurements (see Sec. 3.9 below).

3.8 Lateral stress profile

We mentioned that lipids in a flat monolayer at equilibrium and under not too heavy fluctuations acquire their preferred area per lipid. This area per lipid is the result of a compromise between attractive and repulsive lateral forces between lipids. Attraction comes from the hydrophobic effect, since the more distant are the lipids to each other, the more area of the membrane hydrophobic core is exposed to the polar environment [245]. Repulsion comes from excluded volume interaction between molecules [69]. Other effects are of course present, such as electrostatics of the polar head groups interaction, and lipid tails cohesive and repulsive terms [17,160]. In any case, the configuration of minimum energy dictates the area per lipid, and therefore creating lateral stresses along the membrane. This profile, $\sigma_L^0(z)$, is usually called lateral stress or lateral pressure profile [111,160,165,166] (see Fig. 3.8).

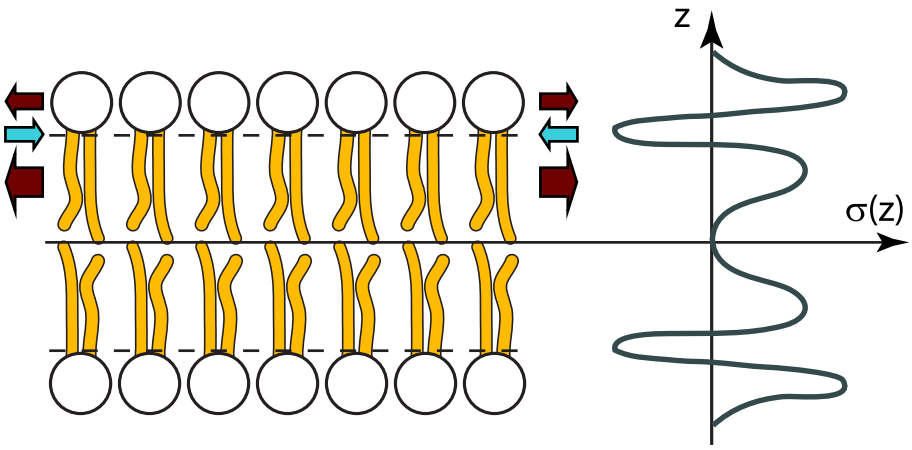

Figure 3.8 Qualitative behavior of the lateral stress profile, $\sigma(z)$, for a lipid bilayer. Headgroup and chain repulsion is represented by red arrows, while hydrophobic interface attraction is represented by blue arrows (all arrows shown only for the top monolayer, for the sake of clarity).

Some of the elastic parameters of the Canham-Helfrich model can be expressed as moments of this lateral stress profile [110]. The zeroth moment being the lateral tension, the first moment is related to the spontaneous cur-

vature and the second moment to the Gaussian modulus. Adding the lateral stress profile to the monolayer energy Eq. (3.35), and not assuming the neutral plane to be located at the middle of the monolayer,

$$E_{\text{monolayer}} = \int_0^h \left[\frac{1}{2}\lambda(z)\ \frac{(A(z)-A_0)^2}{A_0} + \sigma_L^0(z)\ (A(z)-A_0) \right] \mathrm{d}z. \tag{3.38}$$

Using $A(z) = A_0\,\mathsf{J}\,(z - z_n)$, z_n being the coordinate of the neutral plane measured from the bottom of the monolayer, Eq. (3.38) is simplified to

$$\frac{E_{\text{monolayer}}}{A_0} = \frac{1}{2}\,\mathsf{J}^2 \int_0^h \lambda(z)\ (z-z_n)^2\,\mathrm{d}z + \mathsf{J}\int_0^h \sigma_L^0(z)\ (z-z_n)\,\mathrm{d}z. \tag{3.39}$$

From direct comparison between Eq. (3.39) and Eq. (3.4), we get

$$\kappa_m = \int_0^h \lambda(z)\ (z-z_n)^2\,\mathrm{d}z, \tag{3.40}$$

and

$$\mathsf{c}_0^m = -\frac{\displaystyle\int_0^h \sigma_0^L(z)\ (z-z_n)\,\mathrm{d}z}{\displaystyle\int_0^h \lambda(z)\ (z-z_n)^2\,\mathrm{d}z}. \tag{3.41}$$

3.9 Elastic parameter: experimental measurements

In the spontaneous curvature model there are three different elastic parameters of the membrane: the bending rigidity, κ; the Gaussian rigidity, $\bar{\kappa}$; and the spontaneous curvature c_0. These parameters integrate out the local elastic moduli through the membrane thickness to obtain one modulus defined at the neutral plane. Lots of effort have been made for experimentally measure these parameters.

The bending modulus has been measured by different techniques [25, 184, 206]. For instance, it can be measured by micropipette pressurization of giant bilayer vesicles. In such experiments, apparent area expansion (see Sec. 3.6) under very low tensions, a regime dominated by smoothing of thermal bending modes, led to obtain bending rigidities for bilayers composed by different kinds of lipid molecules [206]. The values found for phosphatidylcholines in a fluid state are in the range of $\kappa = 5 - 12 \times 10^{-20}$ J (or, in units of thermal energy, $\kappa = 12 - 30\ k_B T$, where k_B is the Boltzmann's constant, and T is room temperature, 25°C), depending on the chainlength and the unsaturation level of the different lipids.

To the best of our knowledge, no direct measurement of the Gaussian curvature elastic modulus, $\bar{\kappa}$, has been able to be made yet. Thermodynamic stability of vesicles impose a range of suitable Gaussian curvature elastic modulus, $-2\kappa \leq \bar{\kappa} \leq 0$ [105]. Note that this modulus is negative, contrarely to the classic plate theory [146]. The study of the energetics of the transition from lamellar and inverted cubic phases for pure lipidic bilayers in the fluid state, has recently determined the Gaussian modulus to bending rigidity ratio in a pure phospholipid system [232]. The calculated ratio is $\bar{\kappa}/\kappa = -0.83 \pm 0.08$, for monolayers.

Depending on its structure, lipids have an effective spontaneous curvature [263]. Different experimental measurements have been reported on the literature [48, 95, 96, 136, 157, 242]. Typical values for dioleoylphosphatidylcholine (DOPC) are $c_0 \sim (-1/20) - (-1/8.7)\ \mathrm{nm}^{-1}$ [48, 242] (see Tab. 11.1).

Part I On dynamic instabilities in membranes

4
Introduction

The first Part of this thesis is concerned on the theoretical study of membrane morphology. In particular, the aim of this Part is to introduce a numerical model to study dynamic instabilities in vesicles. Thus, in Ch. 5, we derive a phase-field model to deal with membrane bending energies of the kind we reviewed in Ch. 3. In order to understand the reasons why we decided to use a phase-field model, in this introductory chapter we explain the pros and cons of phase-field models.

After deriving the phase-field model, in Ch. 6 we apply it to find the stationary shapes of fluid vesicles in the simplest of the bending models. Afterwards we proceeded to study a richer system, composed by lipid membranes with anchored polymers. Those studies, inspired by experimental findings by the group of J. Stavans [250, 251], are presented in Ch. 7, which talks about the pearling instability in membranes, and Ch. 8, which deals with a polymer-induced tubulation phenomenon in vesicles.

4.1
Method: phase-field model

Imagine we pour some oil drops in a glass full of water. We observe how these small oil drops floating on the water surface rapidly start to coalesce with each other. The physics involved in this process is quite complex. First, one have to take into account the hydrodynamic field on the water, which gets altered by the addition of the oil drops. Imagine we disregard these effects and assume that the water is still and that the addition of oil is made quasi-statically, so no disturbance is caused to the water. We could also take into account the properties of the glass material, which bounds the water surface. In addition, the oil drops are three-dimensional [1]. Imagine we disregard these three-dimensional effects, and stay with a two-dimensional surface. In this very simplified case, we have small circular oil drops in a circular water surface surrounded by

1) With a large enough free water surface, an oil drop will eventually spread completely and form a monomolecular film, as could be seen in the famous Lord Rayleigh experiment [208].

hard walls. The physics of this system is given by an interfacial energy, since oil molecules and water molecules want to minimize the two-phase boundary length. Therefore, small drops start to fuse with each other in order to form larger drops with less perimeter.

In this problem, we see an example of a physical system driven by interfacial effects between two phases, where the location of the interface changes with time, and even suffers from topological transitions. Although the physics is quite simple, the study of the dynamics of such a problem is very complex. This is an example of a free boundary problem. Traditional methods to deal with this kind of problems need to track the position of the interface at each time, and solve the coupled problem of the bulk dynamics and the dynamics of this moving boundary.

The fact that the sharp interface has to be tracked during all the system evolution is a huge technical limitation. The aim of so-called phase-field models is to write a dynamic equation for a bulk field (the phase-field) without any need to explicitly supply information on the interface position. Indeed, the sharp interface of free boundary problems is treated as a diffuse interface in phase-field models, in order to assimilate it to the bulk. Phase-field models convert free boundary problems into a set of partial differential equations, which in principle are simpler to integrate numerically (see [83, 106] for reviews).

So, which characteristics should one require to a phase-field? Being a two-dimensional [2] two-phase problem, the phase-field, ϕ, has to be a smooth well-behaved function which takes real values in the whole two-dimensional domain, Ω,

$$\begin{aligned} \phi &: \Omega \subset \mathbb{R}^2 \longrightarrow \mathbb{R} \\ & \boldsymbol{x} \in \mathbb{R}^2 \longmapsto \phi(\boldsymbol{x}) \in \mathbb{R}. \end{aligned} \tag{4.1}$$

Besides, we require the constituent dynamic equations to be such that the solution for the phase-field acquires two different plateaux, ϕ_A and ϕ_B, one for each phase (see Fig. 4.1). Therefore, it will be possible to know in which physical phase a point is by checking the value of the phase-field. The actual values of these two plateaux are arbitrary, but in the literature they are mainly chosen to be ± 1, or 0 and 1.

In the diffuse interface region, the phase-field can't have any of these two bulk values, but it has to change abruptly, albeit continuously, from one to the other (Fig. 4.1). The width of this region is characterized by a small parameter of the model, let us call it ϵ. The abrupt interface, as we said, can be recalled at any time by finding the level-set $\{\boldsymbol{x} \in \Omega \ : \ \phi(\boldsymbol{x}) = \phi_0\}$, where, again, ϕ_0 is an arbitrary position between the two bulk phases, but it is normally taken to be $\phi_0 = (\phi_A + \phi_B)/2$.

2) We define here the two-dimensional formalism, for simplicity, but it can be analogously done in any number of spatial dimensions.

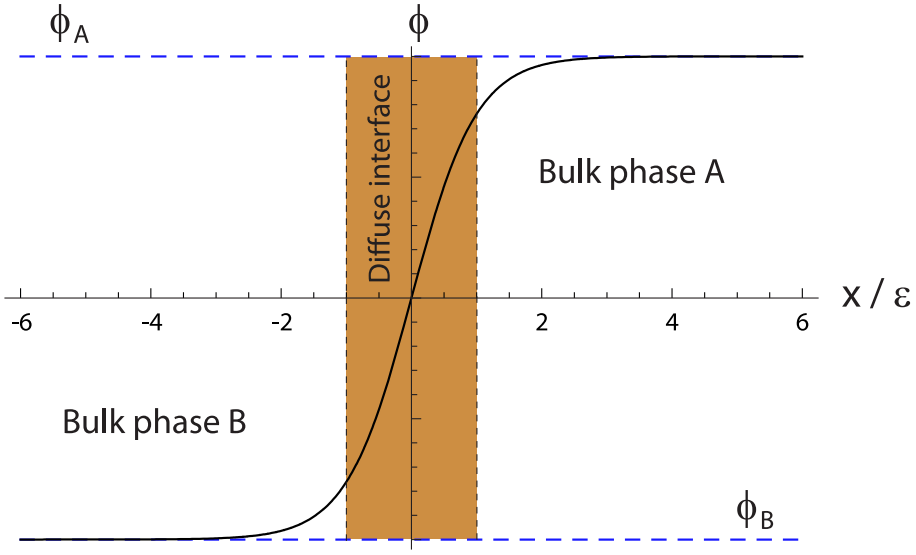

Figure 4.1 Qualitative profile for a phase-field, $\phi(x)$, in one dimension. Two plateaux ϕ_A and ϕ_B, correspond to each of the two stable phases, A and B; and the phase-field continuously goes from one to the other in a thin but finite region, the diffuse interface (dark region).

Using a phase-field method it is possible to substitute a moving boundary condition by a partial differential equation for this auxiliary field. This new equation has to be constructed in such a way that the interfacial dynamics was the most similar possible to the free boundary problem's. Therefore, one asks that in the so-called sharp interface limit [74], i.e. the limit when the width of the diffuse interface goes to zero, the resulting physics will be the same as in the original problem.

This makes to whole thing simpler, but usually more time-consuming from a computational point of view. In addition, phase-field models naturally allow for topological changes. On the contrary, a new length-scale, the width of the diffuse interface, is introduced on the model. Although the sharp-interface limit guarantees equivalence between the free boundary problem and the phase-field problem, in practice one has to choose a finite value for this small parameter, ϵ. This parameter has to be smaller than all the other length scales in the system, but it still needs to be resolved by the lattice, in case the partial differential equations were discretized.

Phase-field models were introduced for the first time in the eighties to study solidification phenomena [33, 52, 84, 148]. They were based in a Ginzburg-Landau model for the dynamics of phase transitions, the so-called model C in Hohenberg and Halperin taxonomy [117]. This model was shown to be a mesoscopic representation of the microscopic solidification free boundary

problem. Even simpler models of this kind, as model A or Allen-Cahn model [6], and conserved models as model B or Cahn-Hilliard model [34] can be seen as phase-field models. Besides the solidification problem, phase-field models have been used in studying different types of interfacial problems, like the viscous fingering instability in fluids [85–87, 113, 150] or imbibition processes [2, 149, 201, 202], among others.

4.1.1 Cahn-Hilliard equation

Here, as a matter of an example, we present a brief derivation of the so-called Cahn-Hilliard model [34], or model B. This model was born to study spinodal decomposition in binary alloys. In this case, the phase-field, ϕ, has a clear physical interpretation, it is the concentration of one of the two components of the alloy. Although in the literature it is common to find this field named by the variable C, we will keep the general variable ϕ in this Section.

Assume that the total free energy of the system, $\mathcal{F}$ can be represented by a free energy density, $f_{\text{tot}}(\boldsymbol{x})$, such as

$$\mathcal{F} = \int_{\Omega} f_{\text{tot}}(\boldsymbol{x}) \mathrm{d}\boldsymbol{x}, \tag{4.2}$$

where Ω is the integration domain. Then, consider that the free energy density is a function of the concentration and its gradients, $f_{\text{tot}} = f_{\text{tot}}(\phi, \boldsymbol{\nabla}\phi)$. By symmetry, if the system is isotropic and homogeneous, up to lowest order we can write

$$f_{\text{tot}}(\phi, \boldsymbol{\nabla}\phi) = f(\phi) + \frac{\epsilon^2}{2} |\boldsymbol{\nabla}\phi|^2 . \tag{4.3}$$

The first term is usually referred to as the homogeneous term, while the second is called the gradient penalty. The homogeneous term may be different depending on the physics of the system. In the case of a binary alloy, it is chosen to be a bistable potential, as in the Ginzburg-Landau approach. The parameter ϵ is the coupling parameter of the gradient term.

Assuming that the system is large enough, we can define the potential μ as

$$\mu = \frac{\partial \mathcal{F}}{\partial \phi} = -\epsilon^2 \nabla^2 \phi + f'(\phi). \tag{4.4}$$

In the Cahn-Hilliard model, the concentration is locally conserved. Then, the dynamics can be written like a Fick's law [59], as the divergence of a flux, $\boldsymbol{J}$,

$$\frac{\partial \phi}{\partial t} = -\boldsymbol{\nabla} \cdot \boldsymbol{J}, \tag{4.5}$$

where the flux, up to first order is

$$\boldsymbol{J} = -M_\phi \boldsymbol{\nabla} \mu, \tag{4.6}$$

with M_ϕ being the mobility coefficient, which can depend on the phase-field.

Considering a bistable homogeneous term as

$$f(\phi) = -\frac{\phi^2}{2} + \frac{\phi^4}{4}, \tag{4.7}$$

the final dynamic equation for the Cahn-Hilliard model with a homogeneous mobility is

$$\frac{\partial \phi}{\partial t} = M_\phi \boldsymbol{\nabla}^2 \left(-\phi + \phi^3 - \epsilon^2 \nabla^2 \phi \right). \tag{4.8}$$

In the case, the concentration was not a conserved variable, the dynamic equation is written as a model A dynamics,

$$\frac{\partial \phi}{\partial t} = -M_\phi \frac{\partial \mathcal{F}}{\partial \phi}, \tag{4.9}$$

which gives the Allen-Cahn equation [6],

$$\frac{\partial \phi}{\partial t} = M_\phi \left(\phi - \phi^3 + \epsilon^2 \nabla^2 \phi \right). \tag{4.10}$$

4.1.2 Level-set methods

Another similar kind of bulk models for dealing with interfaces are the so-called level-set methods [190, 191]. These methods are based in the definition of the surface, Γ, by implicit means [24] using the level-set function, ϕ,

$$\Gamma = \{(x, y, z) \in \mathbb{R}^3 \ : \ \phi(x, y, z) = 0\}. \tag{4.11}$$

The level-set function must be smooth and regular enough. Signed distance functions are a subset of these implicit functions. They are defined as

$$d(\boldsymbol{x}) = \min \left(|\boldsymbol{x} - \boldsymbol{x}_I| \right) \quad \forall \, \boldsymbol{x}_I \in \Gamma. \tag{4.12}$$

Then, level-set methods add dynamics to these implicit surfaces. They were first introduced by Osher and Sethian [191] using the idea of applying the Hamilton-Jacobi approach to numerical solutions of a time-dependent equation for a moving implicit surface. These methods have been applied in many disciplines, such as image processing, computer graphics, computational geometry, optimization, and computational fluid dynamics (see Ref. [190] for a review).

4.1.3 Phase-field models and lipid vesicles

A vesicle can be seen, from an abstract point of view, as a boundary separating two media, the inner volume and the outer volume. The shape of this surface changes dynamically according to the hydrodynamics of the aqueous solutions surrounding it, and also according to its own energetics, given by some of the models reviewed in Ch. 3. Besides, additional destabilizing effects can be included in the system, as for instance proteins or polymers changing the morphology and/or the properties of the membrane, and so on and so forth. This problem is again a free boundary problem. In this case the boundary is not a separation layer between two different phases as in the oil-water example, but a physically differentiated region, the membrane, separating two regions of the same phase[3]. In the simplest case where no destabilizing effects are added to the system, and hydrodynamics is not relevant, one might need a phase-field model for studying the morphology of vesicles given a bending energy model. This is the object of Ch. 6, where the phase-field model for the Canham-Helfrich free energy derived in Ch. 5 is solved to find the stationary shapes of fluid vesicles. Ch. 7 and Ch. 8 are concerned with the study of shape instabilities in membranes due to the anchoring of amphiphilic polymers.

3) In general, the inner and outer solutions can have different viscosities or densities, but we wanted to point out here the fact that the boundary between the phases is a real boundary and not a thin layer of two-phase mixture.

5
Dynamic model for the morphology of fluid vesicles

In this Chapter, we lay the mathematical bases of the curvature phase-field model we will be using through the first Part of this thesis. The derivations here shown, slightly differ from the ones published in our papers [38, 40, 43], in order to give a whole picture of the model. Thus, we proceed to calculate the curvature tensor as a function of the phase-field and, from that, the mean and the Gaussian curvatures, and therefore the bending energy as a function of the phase-field. This is not the way we initially derived the bending phase-field model, since our first publication on the topic [38] starts with an ansatz for the free energy functional, from which, after taking the sharp-interface limit, its equivalence to the curvature minimal model is shown. Later, while studying the way to implement the Gaussian curvature in our model [43], we found a more general way to derive the bending energy. We show here this last method, for the sake of clarity and generality.

5.1
Phase-field implementation of the Canham-Helfrich bending energy

As we explained in the preceding Chapter, we consider membranes, at this level of description, as mesoscopic objects with no internal structure. All the physical parameters describing these membranes are either mesoscopic/macroscopic, or effectively included in macroscopic averages of microscopic parameters. The membrane is thus considered to be a two-dimensional surface embedded in the Euclidean three-dimensional space.

In order to build a phase-field model that takes into account the bending energy of fluid vesicles (see Ch. 3), we should express the surface geometric properties (the ones involved in the bending energy) as a function of the phase-field. Also, as part of the physical constraints needed to be taken into account (see Sec. 3.5.1), the vesicle surface area and enclosed volume have to be included in the phase-field description.

Let us assume the existence of a field, $\phi : \mathbb{R}^3 \rightarrow \mathbb{R}$, in all the points of the Euclidean three-dimensional space $\mathbb{R}^3$. This field is the so-called phase-field (see Ch. (4)). Since phase-fields are regular functions, they can, in general, be

written in terms of any smooth function of the coordinates. In particular, the phase-field can be written as a function of the signed distance to the interface, $d(\boldsymbol{x})$,

$$\phi(\boldsymbol{x}) = f\left(\frac{d(\boldsymbol{x})}{\sqrt{2}\epsilon}\right) = \tanh\left(\frac{d(\boldsymbol{x})}{\sqrt{2}\epsilon}\right), \tag{5.1}$$

where we assumed a tanh-like profile for the phase-field, and ϵ is the mesoscopic parameter of the phase-field, related to the finite width of the diffuse interface. This parametrization is chosen because it involves the signed distance to the interface, whose first derivative is a unit normal vector to the interface

$$\boldsymbol{\nabla} d(\boldsymbol{x}) = \hat{n}, \tag{5.2}$$

and whose second derivative is the curvature tensor [68]

$$\boldsymbol{\nabla}\,\boldsymbol{\nabla}\, d(\boldsymbol{x}) = \mathsf{Q}_{ij}. \tag{5.3}$$

The derivatives of the phase-field with respect its argument are

$$f'\left(\frac{d(\boldsymbol{x})}{\sqrt{2}\epsilon}\right) = 1 - f^2\left(\frac{d(\boldsymbol{x})}{\sqrt{2}\epsilon}\right), \tag{5.4}$$

and

$$f''\left(\frac{d(\boldsymbol{x})}{\sqrt{2}\epsilon}\right) = -2f\left(\frac{d(\boldsymbol{x})}{\sqrt{2}\epsilon}\right)\left[1 - f^2\left(\frac{d(\boldsymbol{x})}{\sqrt{2}\epsilon}\right)\right], \tag{5.5}$$

where primes precisely denote the derivatives with respect to the argument, in this case, with respect to $\frac{d(\boldsymbol{x})}{\sqrt{2}\epsilon}$. Let us now consider the derivatives of the phase-field with respect to the x_i coordinates,

$$\partial_i \phi = \frac{1}{\sqrt{2}\epsilon} f' \partial_i d(\boldsymbol{x}), \tag{5.6}$$

$$\partial_{ij}{}^2 \phi = \frac{1}{2\epsilon^2} f'' \partial_i d \partial_j d + \frac{1}{\sqrt{2}\epsilon} f' \partial_{ij}{}^2 d, \tag{5.7}$$

where we used the notation $\partial_i \equiv \mathrm{d}/\mathrm{d}x^i$ for the partial derivatives with respect to the coordinates. From Eqs. (5.6) and (5.7), it is possible to express the second derivatives of the signed distance as a function of the phase-field and its derivatives, as

$$\partial_{ij}{}^2 d = \frac{\sqrt{2}\epsilon}{1-\phi^2}\left[\partial_{ij}{}^2 \phi + \frac{2\phi}{1-\phi^2}\partial_i\phi\partial_j\phi\right] = \mathsf{Q}_{ij}, \tag{5.8}$$

which is the three-dimensional tensor of curvature Q (see Appendix A).

This tensor has remarkable properties. First of all, it is a symmetric tensor, $\mathsf{Q}_{ij} = \mathsf{Q}_{ji}$. Second, since the gradient of the signed distance is a unitary vector (see Eq. (5.2)), the curvature tensor has a zero eigenvalue, with $\partial_i d$ being the corresponding eigenvector:

$$\partial_{ij}{}^2 d\, \partial_j d = \frac{1}{2}\partial_i \left[\left(\partial_j d\right)^2 \right] = 0. \tag{5.9}$$

Therefore, its determinant is zero.

An $n \times n$ tensor has at most n independent invariant quantities under changes of coordinates [147]. These invariants can be expressed by the coefficients of the characteristic polynomial. In the case of a 3×3 tensor, these coefficients correspond to the determinant, the trace, and the sum of the principal minors of the tensor matrix. Since the determinant of the curvature tensor Q is always zero, there are only two non-vanishing invariants. These two invariants are related to the mean and Gaussian curvatures of the surface [218]

$$\mathcal{H} = \frac{1}{2}\mathrm{tr}\left[\nabla_{ij}{}^2 d\right], \tag{5.10}$$

$$\mathcal{K} = \sum_{i,j}\left[\left(\mathsf{Q}_{ii}\mathsf{Q}_{jj} - \mathsf{Q}_{ij}^2\right)\,\frac{1-\delta_{ij}}{2}\right], \tag{5.11}$$

respectively. From the expression of the curvature tensor as a function of the phase-field, Eq. (5.8), we can thus write the curvature invariants also as a function of the phase-field and its derivatives. The mean curvature is

$$\begin{aligned}\mathcal{H}[\phi] &= \frac{\sqrt{2}\epsilon}{2\left(1-\phi^2\right)}\left[\nabla^2\phi + \frac{2\phi}{1-\phi^2}\left|\boldsymbol{\nabla}\phi\right|^2\right] \\ &= \frac{\sqrt{2}\epsilon}{2\left(1-\phi^2\right)}\left[\nabla^2\phi + \frac{1}{\epsilon^2}\phi\left(1-\phi^2\right)\right] \\ &= -\frac{\sqrt{2}}{2\epsilon\left(1-\phi^2\right)}\left(-\phi + \phi^3 - \epsilon^2\nabla^2\phi\right),\end{aligned} \tag{5.12}$$

where we used Eq. (5.4). We can express the Gaussian curvature, after some algebra, as

$$\mathcal{K}[\phi] = \frac{\epsilon^2}{\left(1-\phi^2\right)^2}\left(T_1 + \frac{2\phi}{1-\phi^2}T_2\right), \tag{5.13}$$

where

$$T_1 = \phi_{,11}\phi_{,22} + \phi_{,11}\phi_{,33} + \phi_{,22}\phi_{,33} - \left(\phi_{,12}\right)^2 - \left(\phi_{,13}\right)^2 - \left(\phi_{,23}\right)^2, \tag{5.14}$$

and

$$\begin{aligned}T_2 =& \phi_{,11}\left(\phi_{,2}\right)^2 + \phi_{,22}\left(\phi_{,1}\right)^2 + \phi_{,11}\left(\phi_{,3}\right)^2 + \phi_{,33}\left(\phi_{,1}\right)^2 + \phi_{,22}\left(\phi_{,3}\right)^2 \\ &+ \phi_{,22}\left(\phi_{,3}\right)^2 - 2\phi_{,1}\phi_{,2}\phi_{,12} - 2\phi_{,1}\phi_{,3}\phi_{,13} - 2\phi_{,2}\phi_{,3}\phi_{,23}.\end{aligned} \tag{5.15}$$

5.1.1 Minimal model

We are now in position to express the minimal model for the bending energy as a function of the phase-field. Just to bear in mind, we write here again the expression for the minimal model free energy (see Ch. 3),

$$F_{\mathrm{M}} = \frac{\kappa}{2} \int_{\Gamma} (2\mathsf{H})^2 \, \mathrm{d}\boldsymbol{s}, \tag{5.16}$$

where Γ is the membrane surface, H the mean curvature, and κ the bending modulus. There is a fundamental difference between this free energy and the one we seek in terms of the phase-field. This is that the former is a surface integral, and the latter should be a volume integral, since one of the aims of the phase-field method is that there is no need to track the interface (the membrane location in our case). Therefore, we seek for something of the form

$$\mathcal{F}[\phi] = \int_{\Omega} \rho_{\mathcal{F}}[\phi] \, \mathrm{d}\boldsymbol{x}, \tag{5.17}$$

where Ω is the three-dimensional domain of the phase-field, and $\mathrm{d}\boldsymbol{x}$ is the three-dimensional volume element.

One way to express a surface integral as a volume integral is by using distributions [209]. In our case, an obvious manner is by implementing a Dirac delta function on the interface, where the signed distance $d(\boldsymbol{x})$ vanishes,

$$\mathrm{d}\boldsymbol{s} = \delta\left(d(\boldsymbol{x})\right) \mathrm{d}\boldsymbol{x}. \tag{5.18}$$

We need then to find a representation of the Dirac delta in terms of the phase-field. Phase-field functions are continuous functions which only change substantially in a neighborhood of size $\sim \epsilon$ around the interface. In the sharp-interface limit, a phase-field function becomes a step function. For this reason, a first candidate for a delta function would be the derivative of the phase-field. Rewriting Eq. (5.4), using the tanh-like profile for the phase-field Eq. (5.1),

$$f'\left(\frac{d(\boldsymbol{x})}{\sqrt{2}\epsilon}\right) = \operatorname{sech}^2\left(\frac{d(\boldsymbol{x})}{\epsilon\sqrt{2}}\right). \tag{5.19}$$

Using the fact that

$$\lim_{\epsilon\to 0}\left\{\frac{3}{4\sqrt{2}\epsilon} \operatorname{sech}^4\left(\frac{d(\boldsymbol{x})}{\epsilon\sqrt{2}}\right)\right\} = \delta\left(d(\boldsymbol{x})\right), \tag{5.20}$$

we can write that

$$\mathrm{d}\boldsymbol{s} = \frac{3}{4\sqrt{2}\epsilon}\operatorname{sech}^4\left(\frac{d(\boldsymbol{x})}{\epsilon\sqrt{2}}\right) \mathrm{d}\boldsymbol{x} = \frac{3}{4\sqrt{2}\epsilon}\left(1-\phi^2\right)^2 \mathrm{d}\boldsymbol{x}. \tag{5.21}$$

Now, using Eqs. (5.12), (5.21), we are able to explicitly write the minimal model Eq. (5.16) as as a function of the phase-field

$$\mathcal{F}_{\mathrm{M}}[\phi] = \frac{3\sqrt{2}\kappa}{8\epsilon^3} \int_{\Omega} \left(-\phi + \phi^3 - \epsilon^2 \nabla^2 \phi\right)^2 \, \mathrm{d}\boldsymbol{x}, \tag{5.22}$$

or, in other words,

$$\mathcal{F}_{\mathrm{M}}[\phi] = \frac{\bar{\kappa}}{2} \int_{\Omega} (\Phi[\phi])^2 \, \mathrm{d}\boldsymbol{x}, \tag{5.23}$$

where

$$\Phi[\phi] = -\phi + \phi^3 - \epsilon^2 \nabla^2 \phi, \tag{5.24}$$

and

$$\bar{\kappa} = \frac{3\sqrt{2}}{4\epsilon^3} \, \kappa. \tag{5.25}$$

Note that the free energy density functional in Eq. (5.23), Φ^2, is nothing else other than the square of the chemical potential (the functional derivative of the free energy) associated with the Cahn-Hilliard problem [34] (see Ch. 4).

The minimum of the free energy Eq. (5.23) is ideally obtained by setting Eq. (5.24) equal to 0. In one dimension, this leads to the tanh-like solution $\phi(x) = \tanh\left(\frac{x}{\sqrt{2}\epsilon}\right)$, given the usual boundary conditions $\phi(\pm\infty) = \pm 1$. Therefore, we recover our original assumption on the profile of the phase-field Eq. (5.1).

5.1.2 Spontaneous curvature

With the phase-field expressions of the local geometric properties of the membrane found above, we can generalize the minimal model by letting the membrane adopt a non-vanishing preferred curvature. This model, first proposed by Helfrich [109] is normally referred in the literature as the spontaneous curvature model, as we explained in Ch. 3. Let us remind how it looks:

$$F_{\mathrm{SC}} = \frac{\kappa}{2} \int_{\Gamma} (2\mathsf{H} - \mathsf{c}_0)^2 \, \mathrm{d}\boldsymbol{s}, \tag{5.26}$$

where c_0 is the membrane spontaneous curvature. Proceeding similarly than before, we can write the spontaneous curvature free energy as a function of the phase-field [38]

$$\mathcal{F}_{\mathrm{SC}}[\phi] = \frac{\bar{\kappa}}{2} \int_{\Omega} (\Phi_{\mathrm{SC}}[\phi])^2 \, \mathrm{d}\boldsymbol{x}, \tag{5.27}$$

where

$$\Phi_{SC}[\phi] = \Phi[\phi] - \epsilon\, C_0 \left(1 - \phi^2\right), \tag{5.28}$$

where $C_0 \equiv c_0/\sqrt{2}$ may, in general, be position-dependent, or even ϕ-dependent. Indeed, we will use a non-homogeneous spontaneous curvature in Ch. 8 in order to study the elongation of membrane tubes by the anchoring of polymers inhomogeneously distributed in space.

5.1.3 Gaussian curvature

Up to this point we only used the mean curvature for the energy of a membrane. The Gaussian curvature did not play any role in our energetics due to the Gauss-Bonnet theorem (see Sec. 3.5.2), which basically states that the energy part coming from the Gaussian curvature only depends on the topology for monocomponent closed vesicles [1]. As we will see in Ch. 9, the Gaussian curvature term is relevant when phase separation occurs in the membrane, with the two phases having different elastic constants. In addition, when topological changes such as fusion and fission events happen in the dynamic evolution of membranes, one has to be aware of this energy term. Finally, it may even be relevant when none of these situations happen and the Gaussian curvature term might influence the dynamics to reach to a stationary state (which should be the same independently of this term).

We can calculate, with the knowledge form the previous parts, the part of the free energy due to the Gaussian curvature

$$F_G = \int_\Gamma \bar{\kappa}\, K \, ds, \tag{5.29}$$

where $\bar{\kappa}$ is the saddle-splay modulus, or Gaussian bending rigidity. Thus, using Eqs. (5.13), (5.21),

$$\mathcal{F}_G = \int_\Omega \bar{\kappa}' \left(T_1 + \frac{2\phi}{1-\phi^2} T_2\right) dx, \tag{5.30}$$

where

$$\bar{\kappa}' \equiv \frac{3\sqrt{2}\epsilon}{8}\, \bar{\kappa}. \tag{5.31}$$

5.1.3.1 Gaussian curvature in cylindrical coordinates

The general expression Eq. (5.11) for the Gaussian curvature in terms of the phase-field can be significantly simplified if we assume the existence of an

1) We should say, to be more precise, for monophasic monocomponent closed vesicles, since a phase-separation can even occur for monocomponent vesicles.

axis of symmetry. For this purpose, we use cylindrical coordinates $\{r, \varphi, z\}$, and assume that the phase-field does not depend on the angular coordinate φ, i.e. $\phi = \phi(r, z)$. The derivatives of the phase-field under such assumption can be written, in matrix notation, as

$$\partial_i \phi = \begin{pmatrix} \partial_r \phi \\ 0 \\ \partial_z \phi \end{pmatrix}, \tag{5.32}$$

$$\partial_i \phi \partial_j \phi = \begin{pmatrix} (\partial_r \phi)^2 & 0 & \partial_r \phi \partial_z \phi \\ 0 & 0 & 0 \\ \partial_r \phi \partial_z \phi & 0 & (\partial_z \phi)^2 \end{pmatrix}, \tag{5.33}$$

$$\partial_{ij} \phi = \begin{pmatrix} \partial^2_{rr} \phi & 0 & \partial^2_{rz} \phi \\ 0 & \frac{1}{r} \partial_r \phi & 0 \\ \partial^2_{rz} \phi & 0 & \partial^2_{zz} \phi \end{pmatrix}. \tag{5.34}$$

Then, we can rewrite the curvature tensor Q as

$$\mathrm{Q}_{ij} = \frac{\sqrt{2}\epsilon}{1-\phi^2} \begin{pmatrix} \partial^2_{rr} \phi + \frac{2\phi}{1-\phi^2} (\partial_r \phi)^2 & 0 & \partial^2_{rz} \phi + \frac{2\phi}{1-\phi^2} \partial_r \phi \partial_z \phi \\ 0 & \frac{1}{r} \partial_r \phi & 0 \\ \partial^2_{rz} \phi + \frac{2\phi}{1-\phi^2} \partial_r \phi \partial_z \phi & 0 & \partial^2_{zz} \phi + \frac{2\phi}{1-\phi^2} (\partial_z \phi)^2 \end{pmatrix}. \tag{5.35}$$

Since the curvature tensor has zero determinant, the expression for the Gaussian curvature as the sum of the principal minors simplifies as

$$\mathcal{K} = \frac{2\epsilon^2}{\left(1-\phi^2\right)^2} \frac{1}{r} \partial_r \phi \left(\nabla^2_{rz} \phi + \frac{2\phi}{1-\phi^2} \left| \boldsymbol{\nabla}_{rz} \phi \right|^2 \right), \tag{5.36}$$

where we defined the two-dimensional nabla operator, $\boldsymbol{\nabla}_{rz} \equiv \partial_r \hat{e}_r + \partial_z \hat{e}_z$.

Therefore, we can simplify expression Eq. (5.30) for axisymmetric vesicles as

$$\begin{aligned} \mathcal{F}_{\mathrm{G}}[\phi] &= 2 \int_\Omega \bar{\kappa_{\mathrm{G}}} \frac{1}{r} \partial_r \phi \left(\nabla^2_{rz} \phi + \frac{2\phi}{1-\phi^2} \left| \boldsymbol{\nabla}_{rz} \phi \right|^2 \right) \mathrm{d}\boldsymbol{x} \\ &= 4\pi \int_\Omega \bar{\kappa_{\mathrm{G}}}\, \partial_r \phi \left(\nabla^2_{rz} \phi + \frac{2\phi}{1-\phi^2} \left| \boldsymbol{\nabla}_{rz} \phi \right|^2 \right) \mathrm{d}r\mathrm{d}z, \end{aligned} \tag{5.37}$$

where we also expressed the volume element in cylindrical coordinates as $\mathrm{d}\boldsymbol{x} = 2\pi r \mathrm{d}r\mathrm{d}z$, where we integrated out the angular coordinate.

5.2 Geometrical constraints

Vesicle shapes are often subject to certain geometrical constraints. Their enclosed volume and surface area remain constant (see Sec. 3.5.1). Here, we implement these constraints in our phase-field model.

5.2.1 Local surface area

We have implemented this constraint in our phase-field model via a Lagrange multiplier function coupled with the surface area in the free energy functional. Thus, we define an effective free energy functional

$$\mathcal{F}_{\text{eff}}[\phi] = \mathcal{F}[\phi] + \int_{\Omega} \sigma(\boldsymbol{x}) a[\phi] \mathrm{d}\boldsymbol{x}, \tag{5.38}$$

where $\mathcal{F}[\phi]$ can be any bending free energy, e.g. Eqs. (5.23), (5.27), σ is a Lagrange multiplier (interpreted as a surface tension), and $a[\phi]$ is the local surface area functional,

$$a(\boldsymbol{x}) = \delta\left(d(\boldsymbol{x})\right), \tag{5.39}$$

which we rewrite in terms of the parameter ϵ using the representation of the delta, Eq. (5.20), as

$$a[\phi] = \frac{3}{4\sqrt{2}\epsilon}\left(1-\phi^2\right)^2 = \frac{3}{4\sqrt{2}\epsilon}\left|\boldsymbol{\nabla}\phi\right|^2. \tag{5.40}$$

Using Eq. (5.39), i.e. Eq. (5.40) in the sharp-interface limit, the last expression integrated over the whole domain Ω is equivalent to the surface area of the vesicle,

$$\lim_{\epsilon\to 0}\int_{\Omega} a[\phi]\mathrm{d}\boldsymbol{x} = \int_{\Gamma} \mathrm{d}\boldsymbol{s}. \tag{5.41}$$

5.2.2 Enclosed volume

An obvious way to implement the condition of fixed inner vesicle volume in the free energy would be, as done before with the surface area constraint, to introduce another Lagrange multiplier coupled with the volume term, ensuring its conservation. However, there is a straight-forward manner to implement this constraint without the need of a Lagrange multiplier. This is, to introduce it through the dynamic equation. Let us show that a Model-B-like dynamics (see Sec. 4.1.1) conserves the vesicle volume throughout the whole time evolution. The dynamic equation (see Sec. 5.3 below) is

$$\frac{\partial\phi}{\partial t} = \boldsymbol{\nabla}^2\left(\frac{\delta\mathcal{F}_{\text{eff}}}{\delta\phi}\right). \tag{5.42}$$

This dynamic equation ensures that $\int_\Omega \phi(\boldsymbol{x})\mathrm{d}\boldsymbol{x}$ is constant in time, since it is nothing else than the divergence of a flux (see Sec. 4.1.1). This integral is equal to the difference of the inner and outer volumes (ϕ takes its stable values $+1$ and -1 inside and outside the vesicle, respectively), as $\epsilon \to 0$. As the sum of the inner and outer volumes is the volume of the integration domain Ω (which is constant), then we can write the inner volume as

$$V_{\text{inn}} = \frac{1}{2}\left(V(\Omega) + \int_\Omega \phi(\boldsymbol{x})\mathrm{d}\boldsymbol{x}\right), \tag{5.43}$$

wherefrom it can be seen that model-B dynamics ensures conservation of the inner volume through the dynamic evolution.

5.3 Dynamic equation

The dynamic relaxation towards a free energy minimum is achieved in our model by conserved relaxation dynamics, Eq. (5.42). Relaxational dynamics [88] have been used before, for instance, to study phase-separation dynamics of two-component vesicles [246]. In our phase-field approach, we need to compute the functional derivative in Eq. (5.42). This calculation leads to the following dynamic equation for the phase-field $\phi(\mathbf{x})$ of the minimal model [2] Eq. (5.23)

$$\begin{aligned}\frac{\partial\phi}{\partial t} = \bar{\kappa}\boldsymbol{\nabla}^2\Big\{&(3\phi^2-1)\Phi[\phi] - \epsilon^2\boldsymbol{\nabla}^2\Phi[\phi] + \epsilon^2\bar{\sigma}(\boldsymbol{x})\boldsymbol{\nabla}^2\phi \\ &+ \epsilon^2\boldsymbol{\nabla}\bar{\sigma}(\boldsymbol{x})\cdot\boldsymbol{\nabla}\phi\Big\},\end{aligned} \tag{5.44}$$

where $\bar{\sigma}$ is defined as

$$\bar{\sigma}(\boldsymbol{x}) = \frac{\sqrt{2}}{6\epsilon^3\bar{\kappa}}\sigma(\boldsymbol{x}). \tag{5.45}$$

The term proportional to $\boldsymbol{\nabla}\bar{\sigma}(\boldsymbol{x})$ in the dynamic equation (the last term in Eq. (5.44)) is shown numerically to be small, and the Lagrange multiplier, $\bar{\sigma}$, can be considered homogeneous. To show this, we numerically computed these variations for an initial profile of $\bar{\sigma}(x)$, and see how they rapidly relax

2) Considering a functional such as

$$\mathcal{F}[\phi] = \int \mathrm{d}\boldsymbol{x} f\left(\phi(\boldsymbol{x}), \partial_\mu\phi(\boldsymbol{x}), \partial_\mu\partial_\nu\phi(\boldsymbol{x})\right),$$

its functional derivative with respect to $\phi(\boldsymbol{x})$ is (see e.g. [103])

$$\frac{\delta\mathcal{F}[\phi]}{\delta\phi(\boldsymbol{x})} = \frac{\partial f}{\partial\phi(\boldsymbol{x})} - \partial_\mu\frac{\partial f}{\partial\left(\partial_\mu\phi\right)} + \partial_\mu\partial_\nu\frac{\partial f}{\partial\left(\partial_\mu\partial_\nu\phi\right)}.$$

to a nearly constant function (i.e the time scale of the relaxation of the effective surface tension is smaller than the time scale related to the shape change). Moreover, $\sigma(\boldsymbol{x})$ appears as an effective surface tension which prevents the surface area from changing. In any case, its value in membranes is very small compared with other energy scales in the system (e.g. bending rigidity) [76]. Therefore, its variations are also small.

We can write down the dynamic equation for the spontaneous curvature model Eq. (5.27), as

$$\frac{\partial \phi}{\partial t} = \bar{\kappa}\boldsymbol{\nabla}^2\Big\{ \Big(3\phi^2 - 1 - 2\epsilon C_0(\boldsymbol{x})\,\phi\Big)\,\Phi_{\mathrm{sc}}[\phi] - \epsilon^2\boldsymbol{\nabla}^2\Phi_{\mathrm{sc}}[\phi] + \epsilon^2\bar{\sigma}(\boldsymbol{x})\boldsymbol{\nabla}^2\phi\Big\}. \tag{5.46}$$

6
Stationary shapes of fluid vesicles

In this Chapter we present the results for the stationary shapes of fluid vesicles we obtained by integrating the phase-field model for the bending energy of monocomponent vesicles we derived in Ch. 5 [38]. We use here the most simple model, the minimal model, and compare the found results with existing solutions for the stationary shapes found by other means. The good agreement between these methods verify the ability of our phase-field model to deal with such energy minimization problems. Besides, the fact that our method is inherently dynamic, allows for out of equilibrium investigations, as those we present in Chs. 7 and 8.

6.1
Phase-field integration: numerical method

Vesicles adopt stationary shapes which correspond to the minimum energy of curvature subject to the constraints of fixed surface area and inner volume. In the previous Chapter, we derived a way of expressing this energy as a function of a phase-field in all the points of the Euclidean three-dimensional space. The zero isosurface of this field locates the position of the vesicle membrane at each time. From this energy, we build a relaxational conserved dynamic equation, which tells us how a vesicle in a non-stationary configuration evolves in time into its corresponding stationary shape. Our aim in this Section is to explain in which manner one can solve this dynamic equation and find which are the characteristic parameters defining a vesicle shape.

First, we have to realize that the partial differential dynamic equations Eqs. (5.44), (5.46) are highly non-linear (notice, for instance, the coupling between the field ϕ^2 and the functional $\Phi[\phi]$). We thus need to solve these equations numerically in order to study dynamic relaxation towards stationary vesicle shapes. We choose to discretize the partial differential equation in a regular lattice, and express the differential operators through second-order finite differences for the spatial dependence, and an Euler scheme for the time dependence [238]. Up to this order, the discrete derivatives of a general three-

dimensional function $f(x,y,z)$ can be written as [1,238] (see Fig. 6.1),

$$\frac{\partial f_{i,j,k}}{\partial x} = \frac{1}{2h}\left(f_{i+1,j,k} - f_{i-1,j,k})\right) + \mathcal{O}(h^2), \tag{6.1}$$

and

$$\nabla^2 f_{i,j,k} = \frac{1}{h^2}\left(f_{i+1,j,k} + f_{i-1,j,k} + f_{i,j+1,k} + f_{i,j-1,k} + f_{i,j,k+1} + f_{i,j,k-1} - 6f_{i,j,k})\right) + \mathcal{O}(h^2), \tag{6.2}$$

where h is the mesh size, which is homogeneous in all the directions since the lattice is assumed to be regular. The Laplacian in two dimensions, can be expressed as

$$\nabla^2 f_{i,j} = \frac{1}{h^2}\left(f_{i+1,j} + f_{i-1,j} + f_{i,j+1} + f_{i,j-1k} - 4f_{i,j})\right) + \mathcal{O}(h^2). \tag{6.3}$$

The time derivative in the Euler scheme is

$$\partial f_{i,j,k}(t+\Delta t) = \partial f_{i,j,k}(t) + \Delta t \frac{\partial f_{i,j,k}(t)}{\partial t} + \mathcal{O}\left(\Delta t^2\right). \tag{6.4}$$

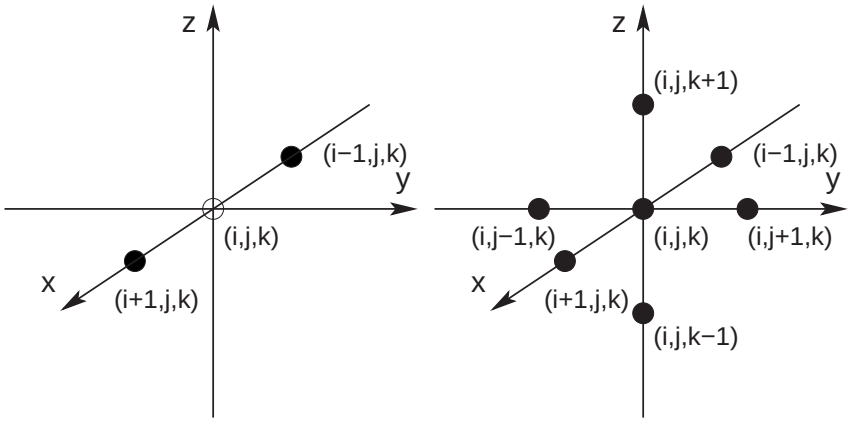

(a) Partial derivative (b) Laplacian

Figure 6.1 Finite differences scheme. Neighbors taken into account in the discretized version of (a) partial derivative with respect to the x coordinate, and (b) Laplacian.

This discretization of the differential equation (5.44) is a consistent finite difference method (standard second-order finite differences). We choose the time step following the Courant-Friedrichs-Lewy stability criterion, $\Delta t \leq |k|\ \Delta x$,

where k is some constant depending on the equation parameters. We can thus assume that the algorithms used are convergent [19, 204].

Second, the effective free energy functional Eq. (5.38) explicitly contains a Lagrange multiplier, $\sigma(\boldsymbol{x})$. Then, in order to assure the accomplishment of the associated constraint throughout the dynamic evolution, we need to know the time evolution of the Lagrange multiplier. To do this, we have used a first order Lagrangian method to study how the multiplier evolves to its stationary value [19]

$$\sigma^{k+1}(\boldsymbol{x}) = \sigma^{k}(\boldsymbol{x}) + \alpha \left(a[\phi^{k}(\boldsymbol{x})] - a_0(\boldsymbol{x}) \right), \tag{6.5}$$

where $\alpha > 0$ is the stepsize, k is the discretized time, and $a_0(\boldsymbol{x})$ is the fixed local surface area. Since we are not interested in the actual dynamics of the multiplier, our choice is justified because it does not change the dynamics of the phase-field, but it just keeps the surface area of the vesicle constant during the time evolution without altering the dynamics. We refer to Appendix B for more details on Lagrangian methods.

All we said is general in a three-dimensional space. However, most of the time we are only interested in axisymmetric shapes. In this case, the discretization of the dynamic equation is easier and we can perform it in a two-dimensional lattice.

Shape evolution is done starting from an arbitrary initial shape. Since the dynamic equation has no external noise (just numerical noise), we start from different initial shapes corresponding to each value of the reduced volume. The initial condition for the phase-field is a sharp distribution of $\phi = +1$ and $\phi = -1$. There is thus a transient period in the first steps of the evolution, where the diffuse interface is created and a tanh-like profile is obtained, which remains during the subsequent evolution. This transient is needed to calculate the surface area using Eq. (5.41), since a gradient in ϕ is required. The boundary conditions which we use here are reflexive, or non-flux, condition in the axis wall when axisymmetry is assumed, and periodic boundary conditions otherwise.

6.2 Results

In our model, there seem to be several free parameters (ϵ, A_0, V_0). However, ϵ is a small parameter of the phase-field model (the model is shown to be robust under variations of this parameter), which will be set, in what follows, to be equal to the mesh size.

In addition, scale invariance [224] causes that the ratio between the constrained total volume and the total surface area is the only relevant parameter in the model (for a fixed topology). Thus, we define a dimensionless volume

$v \in (0,1]$ as the ratio between the actual volume and the volume of a sphere with the same area,

$$v = \frac{V}{(4\pi/3)R_0^3}, \tag{6.6}$$

where

$$R_0 = \left(\frac{A}{4\pi}\right)^{1/2}, \tag{6.7}$$

analogously as in Sec. 3.5.4. We will thus look for stationary shapes for different fixed topologies: spherical (Euler characteristic equal to 2) and non-spherical (e.g. genus-1 toroidal topologies with Euler characteristic equal to 0). We will focus mainly on spherical topology, in order to discuss the model and the results obtained.

6.2.1 Spherical topology

For this topology, the three qualitatively different axisymmetric stationary shapes for the minimal model are found, in agreement with [225]. These are, in order of decreasing reduced volume, the prolate and oblate ellipsoids and the stomatocyte (see Fig. 6.2).

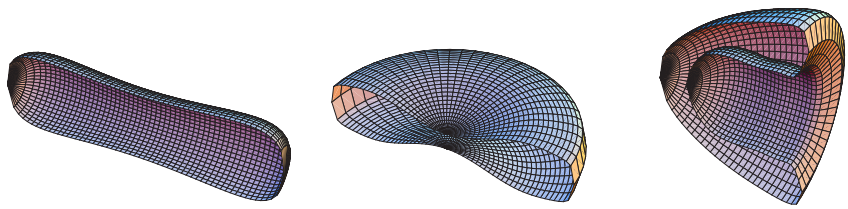

(a) $v = 0.69$ (b) $v = 0.60$ (c) $v = 0.43$

Figure 6.2 Stationary shapes for the minimal model, as stationary states of the dynamic evolution of certain initial conditions under Eq. (5.44). (a) Prolate, (b) oblate, and (c) stomatocyte are shown.

We have solved Eq. (5.44) numerically on a three-dimensional lattice. The possibility of finding non-axisymmetric shapes then arises. In Fig. 6.3, four snapshots of the shape evolution towards a prolate ellipsoid with $v = 0.69$ are shown. This is a stable shape, since the actual transition between prolates and oblates happens at a value of the reduced volume that is lower than this value

($v_D \simeq 0.65$) [225]. The dynamic evolution towards this axisymmetric prolate is done with general three-dimensional non-axisymmetric dynamics, and no axis of symmetry has been supposed at an rate. The initial shape (Fig. 6.3(a)) is a non-axisymmetric box, which dynamically evolves towards an axisymmetric shape.

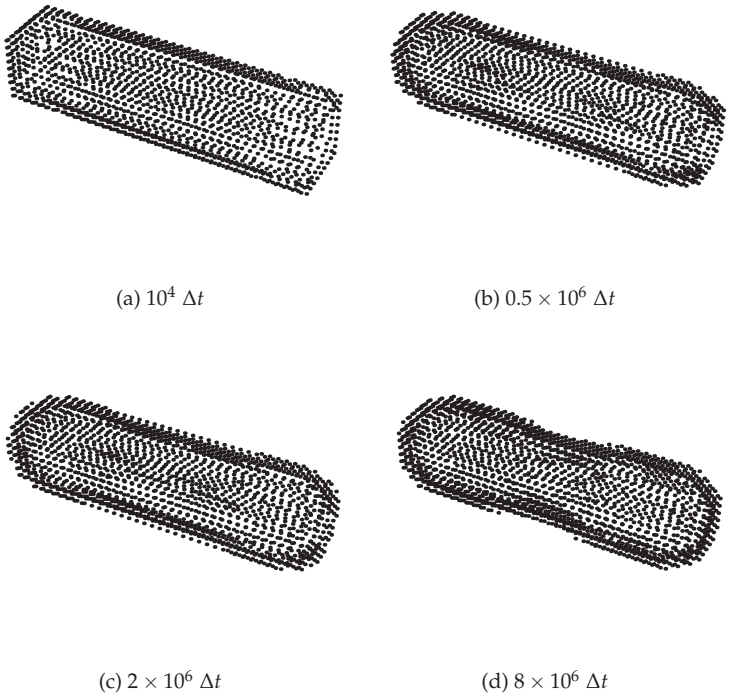

(a) $10^4\ \Delta t$ (b) $0.5 \times 10^6\ \Delta t$

(c) $2 \times 10^6\ \Delta t$ (d) $8 \times 10^6\ \Delta t$

Figure 6.3 Shape evolution for a vesicle with $v = 0.69$, which eventually reaches a prolate shape. the integration was performed on a 3-dimensional $50 \times 50 \times 50$ lattice with time step $\Delta t = 10^{-4}$. No axis of symmetry is supposed here, and the initial shape is a non-axisymmetric $40 \times 10 \times 10$ box.

We have also studied the behavior of the dynamic equation in the axisymmetric case, where we can discretize Eq. (5.44) on a two-dimensional lattice. Fig. 6.4 shows the time evolution to eventually reach a stomatocyte-like shape. Plots show the value of the phase-field on a gray-level scale, where black represents $\phi = +1$, or the inner volume of the vesicle; and white corresponds to $\phi = -1$, or the outer volume of the vesicle.

We have also found the level-set of these gray-level scale plots, to track the position of the vesicle membrane. In Fig. 6.5 a continuous fit of this contour is plotted and the evolution towards a discocyte-like shape is shown. We can see that the reduced volume corresponding to this figure is $v \simeq 0.5$, which

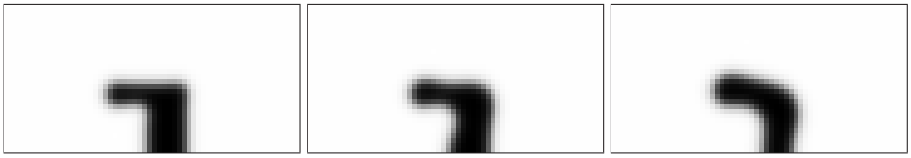

(a) $10^3\ \Delta t$ (b) $0.1 \times 10^7\ \Delta t$ (c) $0.5 \times 10^7\ \Delta t$

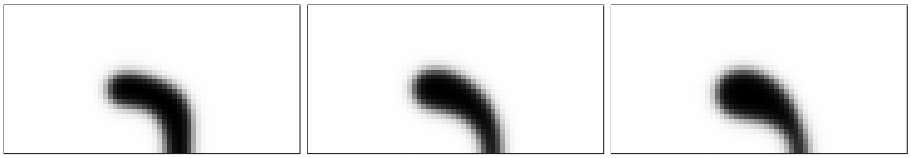

(d) $10^7\ \Delta t$ (e) $2 \times 10^7\ \Delta t$ (f) $8 \times 10^7\ \Delta t$

Figure 6.4 Shape evolution for a vesicle with $v = 0.43$, which eventually reaches a stomatocyte shape. A two-dimensional section is shown, where an axis of symmetry exists, located on the lower side of each snapshot. Integration was performed on an axisymmetric 60×30 lattice and the time step was $\Delta t = 10^{-4}$.

is conserved during evolution (so they are the surface area and the volume separately). This shape is known to be metastable. However, it is obtained here from the initial ellipsoid because the actual stable shape, corresponding to that value of the reduced volume, is far away in the shape landscape from our initial choice.

Note also that the dynamic equation (5.44) is such as the free energy (5.23) is a monotonically decreasing function[1], which reaches metastable or stable states where the value of the energy remains constant.

All these stationary shapes are collected in a shape diagram where the bending energy is plotted as a function of the reduced volume (see Fig. 6.6). The curvature energy of the shapes obtained as stationary states of the dynamic evolution under Eq. (5.44), is calculated in the following way. First, the inter-

1) This can be seen easily by calculating the derivative of the total free energy with respect to time [60]

$$\frac{\mathrm{d}F[\phi]}{\mathrm{d}t} = \frac{\mathrm{d}}{\mathrm{d}t}\int_\Omega f[\phi(\boldsymbol{x},t)]\mathrm{d}\boldsymbol{x} = \int_\Omega \frac{\delta f}{\delta \phi}\,\frac{\partial \phi}{\partial t}\mathrm{d}\boldsymbol{x},$$

which, using the general form of a relaxational conserved dynamics Eq. (5.42), and integrating by parts, can be written as

$$\frac{\mathrm{d}F[\phi]}{\mathrm{d}t} = \int_\Omega \frac{\delta f}{\delta \phi}\,\boldsymbol{\nabla}^2\left(\frac{\delta f}{\delta \phi}\right)\mathrm{d}\boldsymbol{x} = -\int_\Omega \left(\boldsymbol{\nabla}\frac{\delta f}{\delta \phi}\right)^2 \mathrm{d}\boldsymbol{x} \leq 0.$$

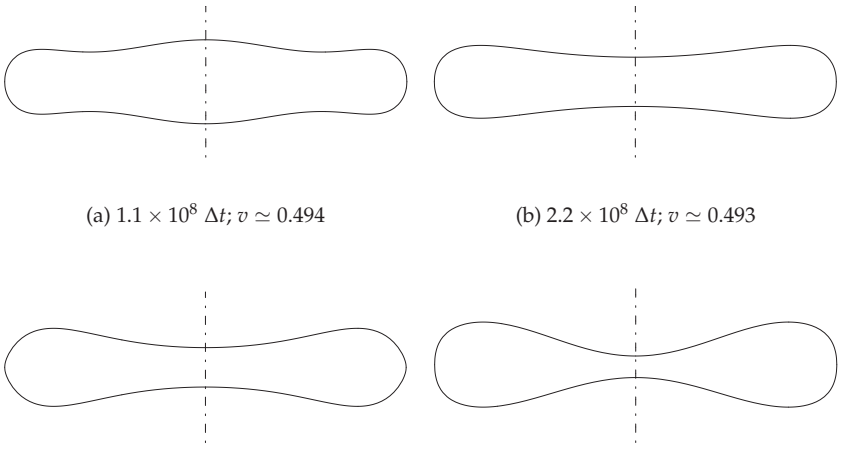

(a) $1.1 \times 10^8\ \Delta t$; $v \simeq 0.494$ (b) $2.2 \times 10^8\ \Delta t$; $v \simeq 0.493$

(c) $3.3 \times 10^8\ \Delta t$; $v \simeq 0.492$ (d) $7.8 \times 10^8\ \Delta t$; $v \simeq 0.496$

Figure 6.5 Snapshots of the time evolution towards a discocyte-like shape. Figures shown here are for the axisymmetric case. The dot-dashed line indicates the axis of symmetry. Curves are continuous fits of the level-set of the phase-field on a 80×40 lattice. The time step is set to $\Delta t = 10^{-4}$.

face is located as the level-set, $\phi = 0$, of the phase-field. An interpolation is then performed over the discrete data in order to obtain a continuous function describing the membrane. Using surface differential geometry [68, 218], the curvature tensor on the surface defined by the interpolating function rotated about the axis of symmetry is worked out. The trace of this tensor, related with the mean curvature, is then calculated. Integrating over the surface eventually gives the bending energy.

Once these pairs $\{v, F\}$ are obtained, a comparison with known results is presented. Thus, in Fig. 6.6, we plot the lines corresponding to the minimization of the Canham-Helfrich free energy, Eq. (5.16), with fixed volume and surface area [225]. There are three branches of different shapes (stomatocytes, oblates and prolates), which intersect at certain values of the reduced volume, v, where a change in the stability of the shape occurs. We see that the results obtained for stationary shapes with the phase-field Eq. (5.23) are in good agreement with this.

6.2.2 Non-spherical topologies

We have also studied non-spherical topologies, such as the genus-1 toroidal topology [129, 223] (see Figs. 6.7a and 6.7b). Circular tori are found for large

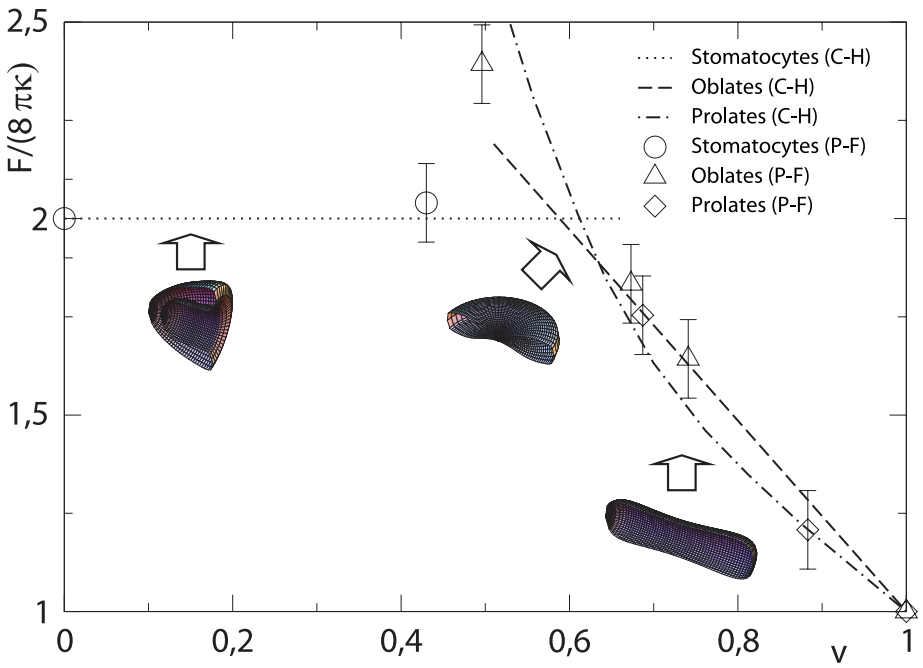

Figure 6.6 Shape diagram for the minimal model with spherical topology. Lines correspond to the minimization of the Canham-Helfrich energy (C-H) [225], and symbols to the results of the phase-field model (P-F). The three different kinds of shapes, stomatocytes, oblates and prolates, are also shown, respectively, from left to right.

values of the reduced volume v, and sickle-shaped tori for small values of v. Discoids can be found for intermediate values of v, although they are not stable shapes, and they will eventually fall to stable ones. In addition, spherical shells are also found (see Fig. 6.7c). They have a different topology with an Euler characteristic $\chi = 4$. These shapes can be thought of as a limit case of a sickle-shaped torus, when the outer radius vanishes thus changing the global topology of the shape (see Fig. 6.8).

The shapes shown in Fig. 6.7 may be found in different ways. First, it is possible to take an initial shape of a given topology, and let it relax to a stationary shape of that same topology. Within this relaxation process there is no topological change, and a non-spherical stationary shape can be found. Second, in some cases, dynamic evolution within a given topology leads to shapes close to a topological transition. Then, because of the natural way of dealing with topological transitions of phase-field models, topology may change. In Fig. 6.8, we show an example of how we get the shape in Fig. 6.7c in this way. In this Figure there is a topological transition between steps 6.8d and 6.8e. The poles of the torus get closer to the axis of symmetry and, eventually, fuse to

get spherical-shell-like topology. The actual dynamics of this transition is not explained by our model, neither by energetics of the Canham-Helfrich model, since the process of membrane fusion is beyond the scope of this model [49]. When membranes are fused or broken, the Helfrich approach is not valid, since the microscopic details of the bilayer become then relevant (namely, the radii of curvatures involved are of the order of the membrane width). In addition, when a topological change occurs, there is an energy change due to the Gaussian curvature term (see Sec. 3.5.2).

In any case, once the shape has changed its topology the evolution leads the shape to a stationary state given that new topology (we can think of the initial shape as being the shape after the topological change).

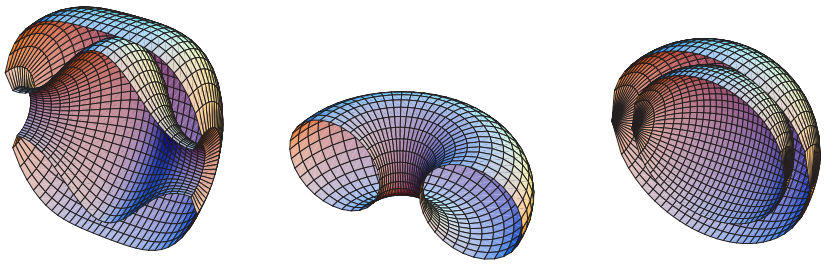

(a) $v = 0.44$ (b) $v = 0.71$ (c) $v = 0.27$

Figure 6.7 Stationary shapes for non-spherical topologies, as stationary states of the dynamic evolution of certain initial conditions under Eq. (5.44). (a) Sickle-shaped torus of genus-1 toroidal topology, (b) circular toroid (Clifford torus [223]) and genus-1 toroidal topology, and (c) spherical shell with an Euler characteristic $\chi = 4$ are shown.

6.3 Discussion and conclusions

To test the numerical robustness of our results, we performed simulations on lattices of different sizes and equivalent shapes and dynamic evolutions were obtained. In addition, during the time evolution, we checked the value of the free energy evolution in time to see how it relaxes to a stationary value in a monotonically decreasing way. The values of the inner volume and the surface area were also computed during the evolution and it can be seen that the volume remains constant (up to the numerical precision) during all the process, and similarly with the surface area (the value of the Lagrange multiplier converges rapidly to the stationary solution).

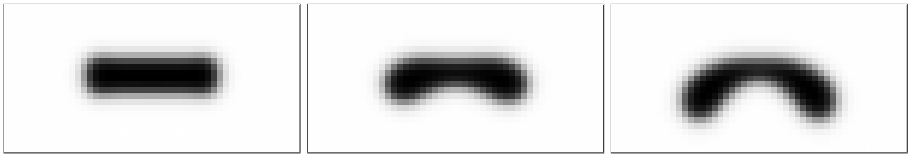

(a) $10^3\ \Delta t$ (b) $10^7\ \Delta t$ (c) $5 \times 10^7\ \Delta t$

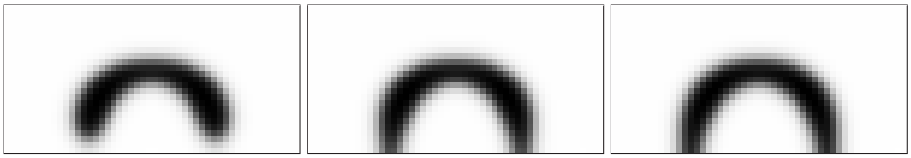

(d) $6.8 \times 10^7\ \Delta t$ (e) $7 \times 10^7\ \Delta t$ (f) $8 \times 10^7\ \Delta t$

Figure 6.8 Shape evolution for a vesicle with $v = 0.27$, which eventually reaches a spherical shell shape. A two-dimensional section is shown, where an axis of symmetry exists, located on the lower side of each snapshot. Integration was performed on an axisymmetric 50×25 lattice and the time step was $\Delta t = 10^{-4}$. The initial shape (a) has a genus-1 toroidal topology. It evolves dynamically until it changes its topology towards an spherical shell.

As a conclusion for this Chapter, we might say that the phase-field model for bending energy of fluid vesicles, and not surface tension as in usual phase-field models, derived in the previous Chapter has been studied. Within this framework, stationary shapes of vesicles with different topologies are found, in agreement with those obtained by minimization of the Canham-Helfrich free energy [224]. In addition, they are found dynamically, from arbitrary initial shapes. Moreover, a shape diagram for spherical topology vesicles is presented. These facts show that our phase-field model is a good description of the bending elasticity of membranes, and that it could be used within a generalized dynamic framework. This will be the subject of the next two Chapters of this thesis, where morphological changes in vesicles are induced by the anchorage of hydrophobic groups on the membrane.

Further generalization of the model could be done by including, for instance, hydrodynamic effects. In this case, a hydrodynamic equation for the velocity field (e.g. the Navier-Stokes equation) could be introduced, with a force acting on the membrane due to the bending elasticity [21, 254]. However, our future aim is to study the shape instabilities seen in [250, 251]. There, the relevant characteristic time scale that needs to be studied is that associated with the relaxation of the curvature, which turns out to be related to the diffusion coefficient of the polymer in the membrane, and not directly to the

membrane viscosity. Therefore, a dynamic model which couples the polymer concentration in the membrane with the local spontaneous curvature would be needed.

7
Pearling instability

In this Chapter, we study the curvature-driven pearling instability in vesicles induced by the anchorage of amphiphilic polymers on the membrane [39]. These polymers insert hydrophobic anchor groups on the outer part of the bilayer, generating membrane curvature. We use the phase-field model reported in Chap. 5 to understand the instability, in which the formation of a homogeneous pearled structure is achieved by consequent pearling of an initial cylindrical tube from the tip. Both homogeneous and inhomogeneous size distributions of pearls are found depending on the polymer concentration. These results are compared with experimental ones reported previously [251], which motivate our research on this topic. It is important to remark that this pearling instability is driven by curvature, and not by tension, as the classical Rayleigh-Plateau instability of liquid jets [46].

7.1
Experimental motivation

Experiments by Ringsdorf and collaborators [61, 210, 211], revealed a pearling instability in tubular vesicles incubated in a solution of amphiphilic polymers having a certain number of hydrophobic anchors in a polysaccharide hydrophilic backbone. This instability started when the polymer concentration was high enough. This critical concentration above which the instability was seen, decreased for increasing number of anchors per backbone. The instability was nonexistent when the polymers contained only the hydrophilic backbone, suggesting that the curvature generated by the anchorage of the hydrophobic anchors was a possible mechanism for the pearling of the vesicle.

Further experimental evidence for this claim was brought by the group of Joel Stavans at the Weizmann Institute of Science. They experimentally studied the morphological changes of lipid vesicles upon interaction with amphiphilic polymers [249]. In particular, they observed pearling of tubular vesicles [251]. The system they studied consisted of monocomponent membranes made of stearoyloleoylphosphatdylcholine (SOPC) with C_{18} alkyl chains in a liquid disordered state (see Ch. 2). Similarly to Ringsdorf and collabora-

tors, hydrophilic dextran was used as the polymer backbone. This polymer, consisting of multiple glucose units, was functionalized with dodecanoic nitrobenzoxadiazole (NBD) chains as fluorescent markers, and palmitoyl alkyl chains acting as hydrophobic anchor groups. For more details on these experiments, see Refs. ([249,251]).

By fluorescence imaging, they demonstrate first the association of polymer with the membrane (Fig. 7.1). Afterwards, they showed that there is a coupling between the polymer concentration on the membrane and the local curvature. The polymer hydrophobic backbones anchor to the outer leaflet of the bilayer in order to minimize its hydrophobic interaction [245], acting thus as a wedge changing locally the curvature of the bilayer (see Fig. 7.2).

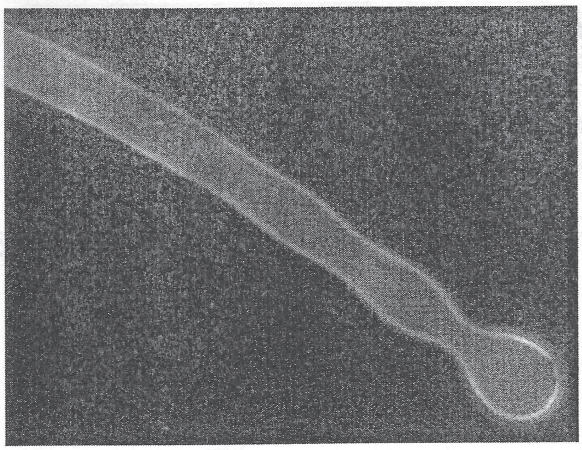

Figure 7.1 Polymer association with the membrane. Fluorescence image showing how polymer molecules attached to fluorescent probes are clearly associated with the membrane. Lighter colors represent fluorescent intensity. Figure taken from Ilan Tsafrir's Ph.D. thesis, Ref. [249].

7.2 Pearling instabilities in physics

The formation of pearled structure is ubiquitous in nature [247]. For instance, the classical Rayleigh-Plateau instability [198,207] which explains how a falling stream of fluid breaks up into smaller packets with the same volume but less surface area, is responsible for the pearling observed when water is dripping from a faucet. When the free surface of a liquid cylinder undulates with a wavelength λ, its area decreases [46], provided that λ is larger than the circumference of the cylinder (in the case of a liquid jet of radius R, larger than $2\pi R$) (see Fig. 7.3).

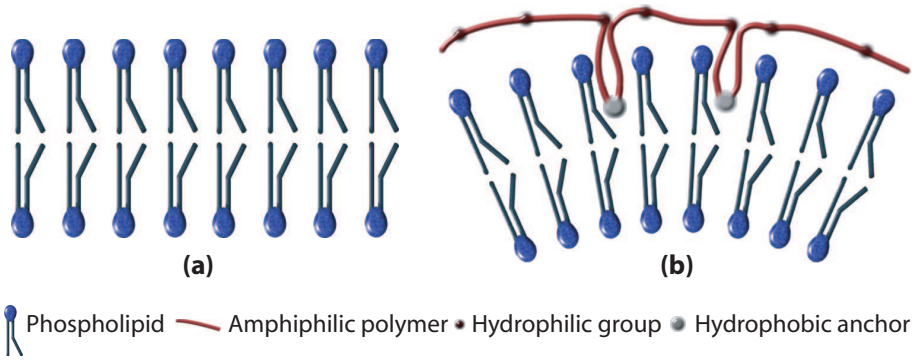

Figure 7.2 Polymer wedge effect inducing a spontaneous curvature in a bilayer. A bilayer formed by one kind of lipids with zero spontaneous curvature tends to be flat (a). When a certain amount of anchor groups of an amphiphilic polymer gets stuck in the outer leaflet of the bilayer, a spontaneous curvature is induced (b).

Figure 7.3 Rayleigh-Plateau instability. When water is dripping from a faucet, small drops form. When the initial jet starts to break apart due to the weight of the tip drop (a), a neck is formed and then stretched. If the diameter of the faucet is big enough, the neck doesn't get sucked back in, and it undergoes a Rayleigh-Plateau instability (b).

Besides, pearling instabilities in lipid vesicles have been reported due to different mechanisms. Pearling was induced when perturbing cylindrical vesi-

cles with optical tweezers. This produced tension in the membrane [12, 13]. Such an instability is understood also in the framework of the Rayleigh-Plateau instability [104, 181], in the sense that it is a capillary instability in which there exists a competition between creating droplets which minimize the surface energy, and the kinetic cost of moving such quantities of water over large distances. It has also been studied in charged membrane tubes [182].

In addition, the Rayleigh-Plateau instability has also been used as an analogy to study instabilities of black strings ([45]). It has to be noted that black hole event horizons have been studied in the so-called membrane paradigm, which considers them as a kind of fluid membrane [248].

Pearled geometries are also found in Golgi tubules [256]. This pearling and prefission neck narrowing are explained theoretically [230] by lateral partitioning of diacylglycerol (DAG), a membrane lipid with a large negative spontaneous curvature, using a fourth order elastic energy [177].

7.3 Curvature-driven pearling instability in membranes

A lipid vesicle subject to an effect which causes an asymmetry between the two monolayers can be elastically described, as we explained in Ch. 3, by the spontaneous curvature model Eq. (3.27), repeated here for convenience,

$$\mathcal{H}_{\mathrm{SC}} = \frac{\kappa}{2} \int_{\Gamma} (2\mathsf{H} - \mathsf{C}_0)^2 \, \mathrm{d}S, \tag{7.1}$$

where κ is the bending modulus, H is the mean curvature, and Γ is the vesicle surface. The asymmetry is enclosed in the spontaneous curvature, C_0.

To incorporate the effect of curvature generation by the anchored polymers, we assume a linear coupling between the spontaneous curvature and the polymer concentration [42, 156][1],

$$\mathsf{C}_0(\mathbf{x}, t) = \mathsf{C}_0^{(0)} + \mathsf{C}_0^{(1)} \, \rho(\mathbf{x}, t), \tag{7.2}$$

where $\mathsf{C}_0^{(0)}$ is the bare spontaneous curvature, i.e. due to the asymmetry between the two leaflets of the bilayer before the polymer anchorage, $\mathsf{C}_0^{(1)}$ is the polymer-induced spontaneous curvature, and $\rho(\mathbf{x}, t)$ is the local density of polymer. It has to be noted that here, the spontaneous curvature is, *a priori*, a dynamic non-homogeneous function.

1) In the third Part of this thesis, we quantify how the insertion of hydrophobic domains into the bilayer induces membrane curvature.

7.3.1 Delaunay shapes

Exact solutions to the spontaneous curvature model Eq. (7.1) for axisymmetric infinite tubelike vesicles were analytically found by H.J. Deuling and W. Helfrich [64]. For an axisymmetric geometry, as that sketched in Fig. 7.4a (see also Ch. 9), the two principal curvatures can be expressed as

$$\mathsf{c}_p = \frac{\sin\psi(x)}{x}, \tag{7.3}$$

$$\mathsf{c}_m = \cos\psi(x)\frac{\mathrm{d}\psi(x)}{\mathrm{d}x}, \tag{7.4}$$

which relate to the symmetry axis, z, as

$$\frac{\mathrm{d}z}{\mathrm{d}x} = -\tan\psi. \tag{7.5}$$

Since the spontaneous curvature energy Eq. 7.1 is positive defined, its minimum configuration might correspond, if possible, to the situation of vanishing energy. Namely,

$$\mathsf{c}_m(x) + \mathsf{c}_p(x) - \mathsf{c}_0 = 0. \tag{7.6}$$

From Eq. (7.4), we can rewrite it as

$$\frac{\mathrm{d}\mathsf{c}_p(x)}{\mathrm{d}x} = \frac{\mathsf{c}_0 - 2\mathsf{c}_p(x)}{x}. \tag{7.7}$$

We can solve this first order ordinary differential equation, up to an integration constant, as

$$\mathsf{c}_p(x) = \frac{\mathsf{c}_0}{2} + \frac{x_0}{x^2}, \tag{7.8}$$

where x_0 is this constant of integration. At the minimum and maximum values of the radial x-coordinate, R_m and R_M, respectively, the parallel curvature is $\mathsf{c}_p(x) = \frac{1}{x}$, which gives

$$\mathsf{c}_0 = \frac{2}{R_m + R_M}, \tag{7.9}$$

$$x_0 = \frac{1}{4}\left(R_m + R_M\right)\left[1 - \left(\frac{R_M - R_m}{R_M + R_m}\right)^2\right]. \tag{7.10}$$

The shape contour, $z(x)$, can be found by integration, leading to the following result,

$$z(x) = z(R_m) - \int_{R_m}^{x} \frac{x'\mathsf{c}_p(x')}{\sqrt{1 - x'^{\,2}\,\mathsf{c}_p^2(x')}}\mathrm{d}x', \tag{7.11}$$

which exist for spontaneous curvatures in the range $0 \leq c_0 R_M \leq 2$.

These shapes were already found in the mid nineteenth century by C. Delaunay [62], that is the reason why there usually known as Delaunay shapes. In C. Delaunay's own words [62], one can find such surfaces in the following manner:

> *Pour trouver la courbe méridienne de la surface de révolution dont la courbure moyenne est constante et égale à $\frac{1}{2a}$, il faut faire rouler sur l'axe de la surface une ellipse ou une hyperbole dont le grand axe ou l'axe transverse soit égal à $2a$, et le foyer décrira la courbe cherchée*[2].

In Fig. 7.4, we show some examples of Delaunay shapes, which are surfaces of constant mean curvature (see also the front and back covers of this thesis).

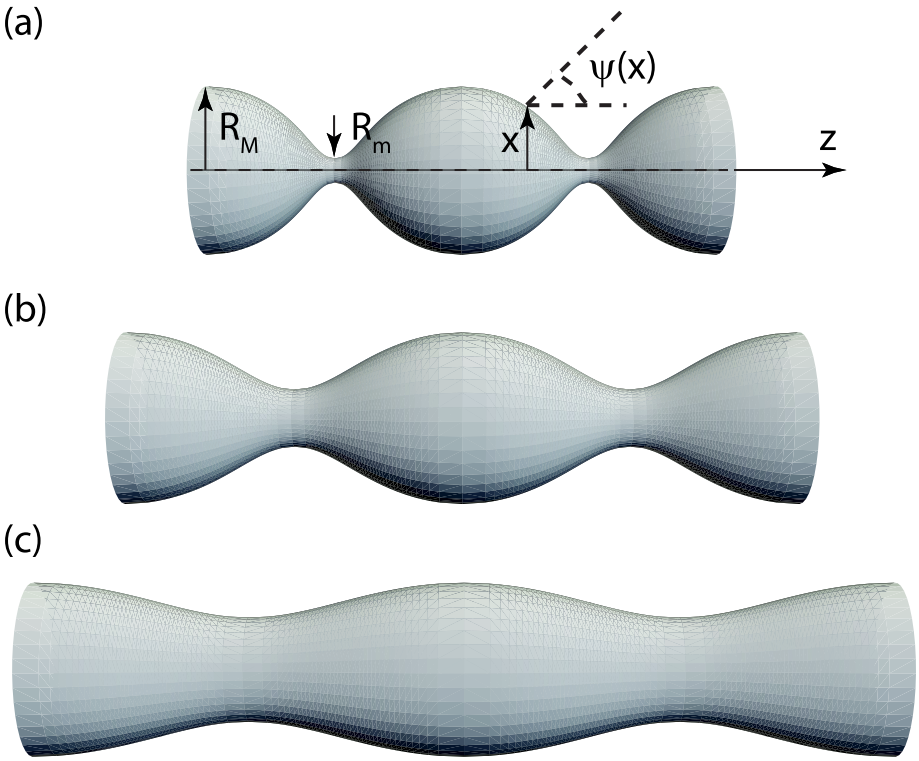

Figure 7.4 Delaunay shapes. Three example of Delaunay surfaces shown for (a) $c_0 R_M = 1.25$, (b) $c_0 R_M = 1.50$, and (c) $c_0 R_M = 1.75$. In (a) we sketch the axisymmetric coordinates used to describe Delaunay shapes.

2) To find the meridian curve of the surface of revolution whose mean curvature is constant and equal to $\frac{1}{2a}$, an ellipse or a hyperbole with one of both axes equals to $2a$ has to be rolled over the surface axis. The focus will follow the desired curve.

7.4 Results and discussion

In the experiments by Tsafrir *et al.* [251], amphiphilic polymers are introduced in the bulk outside the vesicle, both globally and locally close to the tip of the tube. These molecules diffuse in the bulk until they come across the membrane, where they get stuck in such a way that their hydrophobic part anchors in the bilayer (in order to satisfy the hydrophobic interaction). Once a polymer is anchored in the bilayer, it diffuses superficially within the membrane.

Here, we consider the situation of global application of the polymer. In this case, we assume that the polymer concentration almost immediately reaches a homogeneous profile along the membrane. The dynamic evolution is thus fully understood from the shape dynamics, so there is no need of a dynamic equation for the density field.

7.4.1 Onset of the instability

Tsafrir *et al.* [251] studied the pearling instability in tubes whose length is much larger than their diameter. Within our model, we can find the shape of the tube at the onset of the instability (see Fig. 7.5). The experimental and predicted shapes are in good qualitative and quantitative agreement with each other. For instance, we can measure the ratio between the radius of the first pearl and the radius of the neck connecting it with the tube, and see that it gives a value of about 3 in both the experiment and the simulation. We can thus assert that there is no need for an inhomogeneous polymer concentration on the membrane in order to start the instability, but it can just be triggered by the global change of the preferred curvature.

7.4.2 Low polymer concentration

Further addition of polymer solution increases the concentration of anchor chains in the membrane, therefore increasing the induced spontaneous curvature. Fig. 7.6 shows the time evolution of a long cylindrical tube with an endcap and the other end connected to a lipid reservoir. The homogeneous spontaneous curvature induced by the anchorage of the polymers made the initial cylindrical shape to be unstable and to create pearls.

We define the volume to area ratio, $\lambda = V/A$. For spontaneous curvatures between $C_0 = 1/(2\lambda)$ and $C_0 = 2/(3\lambda)$, Deuling and Helfrich [64] showed that there exist minimal surfaces, called Delaunay surfaces, which are global minima of the bending energy Eq. (7.1), for cylindrical shapes. The two limiting Delaunay shapes are a cylinder (for $C_0 = 1/(2\lambda)$) and a set of spheres ($C_0 = 2/(3\lambda)$). Unduloids, the one-parameter family of Delaunay shapes,

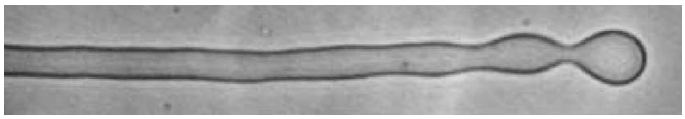

(a) Experimental result (from Ref. [251])

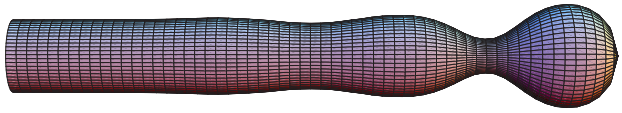

(b) Phase-field numerical result

Figure 7.5 Onset of the pearling instability. Comparison of the experimental result from Ref. [251] (a), and the phase-field numerical result (b). It is important to note that in the numerical integration there is no fitting parameter, but we just let the system evolve from an initial tubular shape, under a relatively low homogeneous induced spontaneous curvature, $C_0 = 0.48$, below the pearling instability limit.

interpolate smoothly between them. For higher spontaneous curvatures, the condition of vanishing bending energy cannot be fulfilled, and therefore the stationary shape corresponds to a non-vanishing minimum of the free energy. Our simulations show that, when the polymer solution is applied globally, i.e. when there is a simultaneous anchoring of polymer everywhere on the surface, the way of reaching a pearled structure from a cylindrical one is not by going through the family of equilibrium Delaunay shapes, but by a completely different dynamic evolution: creating pearls one by one from the tip of the tube (see Fig. 7.6b).

We checked how the free energy Eq. (5.27) varies in time seeing how each pearl formation is associated with an energy barrier which is crossed by thermal activation (due to numerical noise in our simulations). It is important to remark that there occurs no fission in the tube, but there is a narrow neck joining any pair of pearls, as seen in the experiments. The width of this neck is of the order of the mesh size. There is therefore no change in the topology of the tube. The tip of the semi-infinite tube is the point where pearls start when the polymer solution is applied both locally on the tip and globally [251]. The rate of formation of pearls with time is shown in Fig. 7.7.

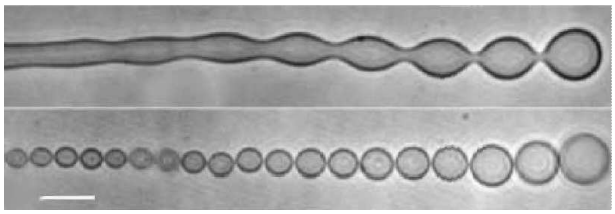

(a) Experimental result (from ref. [251])

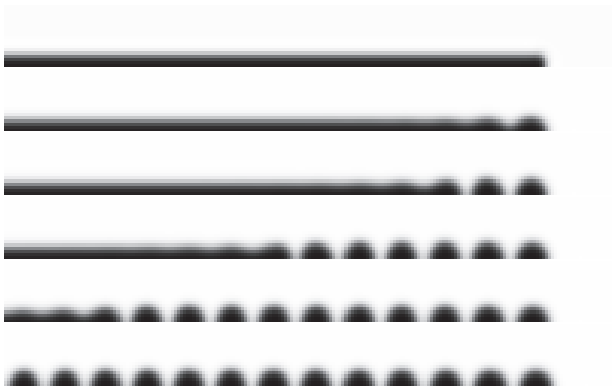

(b) Phase-field numerical result

Figure 7.6 Dynamic evolution (time goes by from upper images to down) of a tube with an polymer concentration on the membrane such that $C_0 = 0.68$. We show (a) the experimental results and (b) the phase-field numerical integration, for comparison. Pearls start at points where the tube loses its perfect cylindrical geometry, namely the cap. The simulation has been performed on a 200×40 axisymmetric lattice. No-flux boundary conditions at the lateral walls have been implemented.

7.4.3 High polymer concentration

It is seen in the experiments (see Fig. 7.8a) that when the concentration of anchored molecules on the membrane increases, there appears a gradient in the size of the pearls. The higher the concentration, the more pronounced the size gradient is. This is so because the higher the amount of anchored polymer on the membrane, the higher the induced spontaneous curvature. As we mentioned before, there are no energy-vanishing surfaces for $C_0 > 2/3$ (here, we define the lengthscale by setting $\lambda = 1$). Tsafrir *et al.* [251] suggested that a shape consisting of a chain of equally sized Helfrich spheres connected to a larger sphere is, in terms of free energy, favorable to a chain

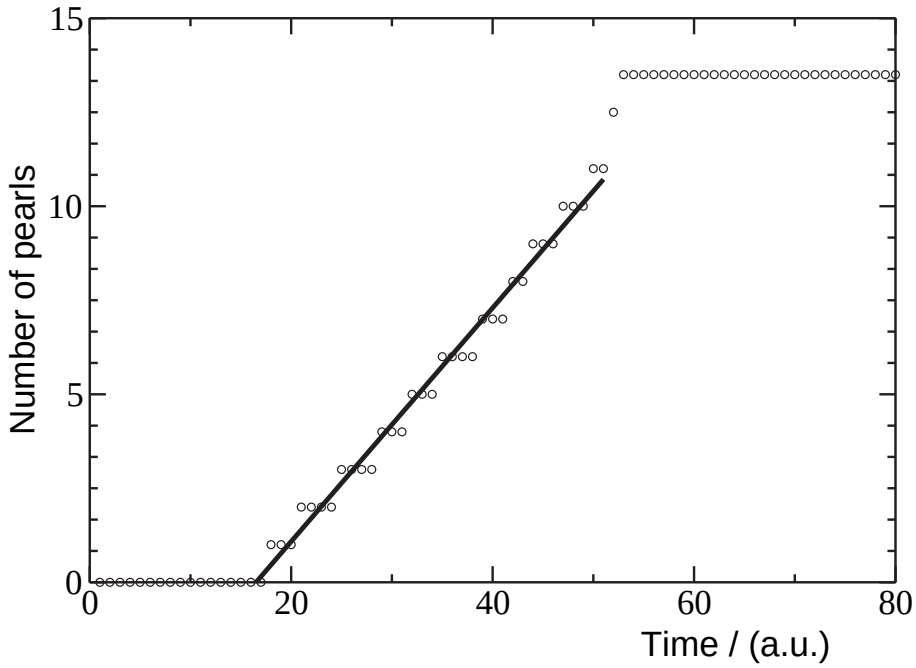

Figure 7.7 Number of pearls as a function of time (number of integration iterations) for a typical pearling numerical integration. Time scale is showed in arbitrary units. We see that the formation of pearls follow a linear behavior.

of equally-sized spheres. Some pearls having the mean curvature equal to the spontaneous curvature are formed, but not all of them can fulfill this condition, under the volume and area constraints. Then, a larger sphere should form in order to keep these constraints. They argued that an inhomogeneity in the polymer concentration on the membrane (and thus in the distribution of the induced spontaneous curvature), may reduce the Helmholtz free energy $F = \mathcal{H}_{\text{C-H}} - TS$, T being the temperature and S the entropy.

However, we found that for higher values of the spontaneous curvature, a situation with a pearl size gradient may be energetically favorable to that of a chain of equally-sized pearls, even with the same spontaneous curvature all along the vesicle (Fig. 7.8). It is interesting to note that for values of the spontaneous curvature just slightly higher than $2/3$, the homogeneous case keeps its stability against the inhomogeneous case. Once a critical value C_0^c is achieved, the homogeneous case destabilizes against the inhomogeneous one (see Fig. 7.8c). This critical value depends on the area of the vesicle or, in other words, on the length of the initial tube. This critical value decreases with

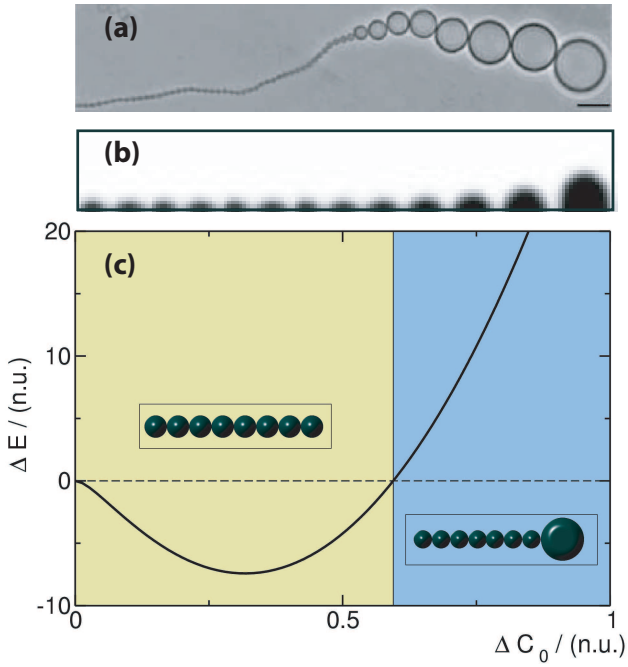

Figure 7.8 Inhomogeneous pearling. (a) Experimental result from Ref. [251], and (b) phase-field simulation using $C_0 = 1.1$. (c) Plot of the energy difference ΔE between the bending energy corresponding to a set of spheres, and the one associated with a set of small spheres added to a bigger one, with respect to the increment of spontaneous curvature from the value $C_0 = 2/3$, when equally-sized spheres have zero bending energy. For spontaneous curvatures bigger than a critical value, the homogeneous configuration is energetically less favorable than the inhomogeneous one. The area of the vesicle is finite, and chosen in such a way that the homogeneous pearled chain consists of 8 spheres. Magnitudes are measured in normalized units, given by $\kappa = 1$ and $\lambda = 1$.

increasing tube length, reaching $2/3$ in the case of infinite tubes. Therefore, we state that the inhomogeneous pearl size experimentally found by Tsafrir *et al.* [251], is not due to a inhomogeneous polymer distribution, but it is of a purely energetic nature.

7.5 Conclusions

In summary, a phase-field model for dealing with dynamic instabilities in vesicles has been studied in the case of curvature-driven pearling instability induced by the anchorage of amphiphilic polymers on the bilayer. We showed in this Chapter that the morphological changes reported in the experiments are explained by the generation of curvature by the anchors. We considered

the situation in which polymer is applied globally, accounting for the main experimental results. Calculations in the framework of the Canham-Helfrich model showed that for a high enough homogeneous concentration of anchors, the homogeneous pearled shape is energetically less favorable than an inhomogeneous one, with a large sphere connected to an array of smaller spheres.

8
Tubulation instability

In this Chapter, we present a mechanism of extraction of tubular membranes from a lipid vesicle due to the presence of amphiphilic polymers [41]. A concentration gradient of these anchoring polymers generates tubes from bud-like vesicle protrusions. We explain this mechanism in the framework of the Canham-Helfrich model reviewed in Ch. 3. The energy profile is analytically calculated and a tube with a fixed length, corresponding to an energy minimum, is obtained in a certain regime of parameters. Further, using the phase-field model derived in Ch. 5, we numerically corroborate these results. We obtain the growth of tubes when a polymer source is added, and the bud-like shape after removal of the polymer source, in accordance with experimental results [250].

8.1
Experimental motivation

As part of cellular dynamic processes, membranes adopt different shapes in order to exchange matter with their surroundings. Many possibilities appear here, from budding and eventual fission of small transport vesicles [79] to formation of large tethers connecting distant organelles, as in the Golgi apparatus and the endoplasmic reticulum (ER) [252, 255], or even between different cells [217]. Actually, the endoplasmic reticulum is a huge network of interconnected tubules, vesicles, and cisternae, which act as transport carriers for proteins and other functional entities to be transported to other parts of the cell [3].

The formation of these tethers can be driven by the application of a point-like force to the membrane [63, 200]. Understanding the nature of this force is of major importance, and we will review the main theoretical aspects of such a mechanism in Sec. 8.2.

There are different mechanisms leading to such a tubulation phenomenon in cells as, for instance, the growing of microtubules pushing the membrane from inside [97], and the extrusion from vesicles due to a hydrodynamic shear flow [26, 31, 213]. Other works have experimentally studied the force gener-

ated by molecular motors pulling membrane tubes *in vitro* [36, 151, 214] and by optical tweezers [55, 56, 138].

Besides, Tsafrir *et al.* studied the tubulation induced in highly oblate vesicles by the anchoring of amphiphilic polymers [249, 250] without any directed force. In those experiments, similar to the ones they did on pearling instability [251] (see Ch. 7), macromolecules containing hydrophobic groups were administered in the surroundings of a giant oblate vesicle. Those molecules diffused in the bulk and eventually anchored the membrane inducing a local spontaneous curvature by the mechanism of hydrophobic insertion [42, 263], leading to the formation of one or several buds. Even, under certain circumstances, those buds can grow into long tubular structures (see Fig. 8.1).

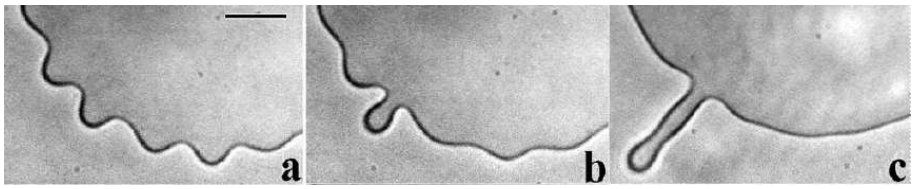

Figure 8.1 Tube formation in a highly oblate vesicle after local addition of multianchor polymer. Scale bar represents 10 μm. Experimental images from Ref. [250].

Motivated by these experimental results [250], we present a theoretical treatment of a novel mechanism of tube extraction, due to the generation of spontaneous curvature by anchoring macromolecules which are distributed along a gradient of concentration, maintained by a source. We show that the elongation of a bud into a tube may be, under certain circumstances, energetically favorable when a polymer concentration gradient is present. We obtain that these tubes do not grow indefinitely, but stop at a certain length. In Sec. 8.3, we analyze the problem in the framework of the Canham-Helfrich model [44,109] with a simple geometry and a stationary linear concentration profile, in order to solve analytically and to understand qualitatively the tube formation. Afterwards, we use the bending phase-field model derived in Ch. 5, coupled with a stationary polymer concentration profile, to numerically study the problem.

8.2 Theoretical background

When a force is applied on a small spot of a vesicle, deformation occurs. Depending on the conditions of this force a membrane tube can be extruded from the mother vesicle. There are lots of works, both experimental and theoretical, in the literature about the physics of membrane tube extraction by a directed

force. We will review here a theoretical explanation of tube extraction by a localized force, based on Refs. [63,200].

Given a fluid vesicle with fixed tension, σ, and pressure, p, on which a force, f, is locally applied normally outwards the vesicle, the energy can be written, according to the minimal model Eq. (3.24),

$$\mathcal{E} = \int_S \frac{\kappa}{2} (2\mathsf{H})^2 \, \mathrm{d}S + \sigma A - pV - fL, \tag{8.1}$$

where A and V are, respectively, the area and volume of the vesicle; L is the end-to-end distance in the direction defined by the force vector. For a cylindrical tube of length L, radius R, at vanishing osmotic pressure, since the pressure effects are misleading (see Ref. [200] for a discussion on this issue), the energy reads

$$\mathcal{E}_{\text{tube}} = \left(\frac{\kappa}{2R^2} + \sigma \right) 2\pi RL - fL, \tag{8.2}$$

where we see that the bending term favors the radial growth of the tube (since this decreases the bending energy), and the tension terms favors the tube shrinkage. Therefore, the competition between these two forces lead to an equilibrium intermediate solution that can be easily found by minimizing Eq. (8.2) with respect to the radius and length of the tube,

$$\frac{\partial \mathcal{E}_{\text{tube}}}{\partial R} = 0, \tag{8.3}$$

$$\frac{\partial \mathcal{E}_{\text{tube}}}{\partial L} = 0, \tag{8.4}$$

from where one obtains

$$R_0 = \sqrt{\frac{\kappa}{2\sigma}}, \tag{8.5}$$

$$f_0 = 2\pi\sqrt{2\kappa\sigma}. \tag{8.6}$$

This has been done for the minimal model Eq. 3.24. However, a membrane bare spontaneous curvature can also be straightforwardly introduced and proceed analogously (see Ref. [263]).

Typical values for this force and optimal radius, are of the order of $f_0 \sim 10$ pN, and $R_0 \sim 20$ nm. Actually, the value of the needed force to extract a membrane tube is of the order of the force generated by a few molecular motors [36,119], meaning that these motors are plausible candidates to extract and form intracellular carriers.

8.3
Polymer-induced tubulation in lipid vesicles

Let us assume that a hemispherical bud of radius R is already formed out from a giant vesicle. This bud has not to be necessarily stable, appearing for instance just as a vesicle rim fluctuation [250]. The mother vesicle is large enough to be considered as a lipid reservoir during the whole extraction process, so we can study the isolated tube on its own. In addition, there are amphiphilic macromolecules (e.g. polymers as in [250]) in the volume outside the vesicle. We assume here, in order to find analytical estimations for the extraction of membrane tubes due to an inhomogeneous polymer concentration in the bulk, that these macromolecules are applied in a line located at a distance z_p from the mother vesicle (see Fig. 8.2) and follow a linear stationary profile for this concentration,

$$\rho(\mathbf{r}, t) = \rho_0 \left(1 - |z/z_p - 1|\right), \tag{8.7}$$

where $\mathbf{r}_{\text{appl}} = (0, 0, z_p)$.

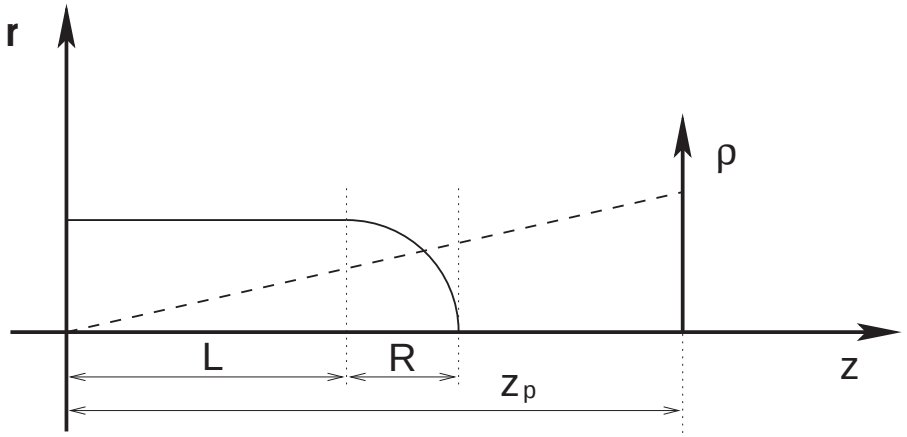

Figure 8.2 Geometrical sketch of the system: a cylindrical tube of radius R and length L, with a hemispherical cap of radius R. A linear polymer concentration gradient is $\rho(z)$ is also outlined in the figure (dashed line).

The bending energy of a membrane treated as an elastic sheet is given by the spontaneous curvature model Eq. (3.27),

$$E = \int_S \left(\frac{\kappa}{2} \left[2\mathsf{H}(\mathbf{r}) - \mathsf{c}_0(\mathbf{r}) \right]^2 + \sigma \right) \mathrm{d}A. \tag{8.8}$$

Since the tube is connected to a lipid reservoir, we have also included a surface tension term, where σ is the surface tension of the membrane. A pressure-like term could also be introduced, but its effects, as mentioned above, are subleading [200]. Using a cylindrical tube with a hemispherical cap, as sketched

in Fig. 8.2, Eq. (8.8) can be written as

$$E = \int_{S_L} \left(\frac{\kappa}{2} \left[\frac{1}{R} - c_0(\mathbf{r}) \right]^2 + \sigma \right) \mathrm{d}^2 A + \int_{S_R} \left(\frac{\kappa}{2} \left[\frac{2}{R} - c_0(\mathbf{r}) \right]^2 + \sigma \right) \mathrm{d}^2 A, \quad (8.9)$$

where R is the radius of the cylinder and the cap, and S_L and S_R denote the cylindrical and the hemispherical parts of the tube (Fig. 8.2) with areas A_L and A_R, respectively. The spontaneous curvature of the membrane is coupled with the local concentration since the hydrophobic anchor groups of the polymer tend to insert themselves into the bilayer, acting thus as a wedge[1]. A linear coupling [156], as stated previously while studying the pearling instability in Ch. 7, has shown to be justified, the spontaneous curvature field outside the vesicle being

$$c_0(z) = \bar{c}_0 \, \rho(z), \quad (8.10)$$

where $\bar{c}_0$ is the proportionality constant, depending on the nature of the polymer and of the membrane where it anchors.

Therefore, in the case where the polymer gradient in space is set to be linear (see Eq. (8.7), we get for the tube energy Eq. (8.9)

$$\frac{E}{\kappa\pi} = \frac{1}{3}\xi^2 L^3 + \xi\,(\xi - 1)\, L^2 + \left(\frac{\pi\xi^2}{2} - 4\xi + 2\bar{\sigma} + 1 \right) L + \left(\frac{2\xi^2}{3} - \pi\xi + 2\bar{\sigma} + 4 \right) \quad (8.11)$$

where $R = 1$ sets the length scale, $\bar{\sigma} = \sigma/\kappa$, and we defined $\xi = \bar{c}_0 \, \rho_0 / z_p$, as the slope of the linear spontaneous curvature profile.

In Fig. 8.3 (inset) we show how the tube energy Eq. (8.11) looks like as a function of the length L of the tube for different slopes of the spontaneous curvature profile, ξ, when the tension σ is negligible. Note that the energy Eq. (8.11) is cubic in the tube length. The energy extremes correspond to two equilibrium lengths: one stable length corresponding to an energy minimum,

$$L^* = 1/\xi - 1 + \sqrt{2/\xi - \pi/2 + 1}; \quad (8.12)$$

and another smaller length being unstable,

$$L_c = 1/\xi - 1 - \sqrt{2/\xi - \pi/2 + 1}. \quad (8.13)$$

The larger the slope of the linear concentration profile is, the smaller these lengths are. For

$$\xi > \xi^{\mathrm{crit}} = 4/\pi(1 - \sqrt{1 - \pi/8}) \simeq 0.28, \quad (8.14)$$

1) In the third Part of this thesis, we build a model to calculate the effective spontaneous curvature a shallow insertion, such as these hydrophobic anchor groups, induce depending on the elastic properties of the bilayer and the geometry of the insertion.

there is only a local minimum and no local maximum of the energy for positive lengths (see Figs. 8.4 and 8.3). This means that the initial bud becomes unstable against the formation of a tube. For smoother concentration gradients ($\xi < \xi^{\mathrm{crit}}$), the initial bud, in order to grow up to its preferred length L^*, needs to cross an energy barrier ΔE_0, or to start with a certain initial length larger than L_c (see Fig. 8.3). For very steep slopes of the concentration gradient

$$\xi > \xi^{\mathrm{max}} = 4/\pi(1+\sqrt{1-\pi/8}) \simeq 2.27, \tag{8.15}$$

the local energy minimum at L^* disappear, and no stable tubes can be found (see Fig. 8.4).

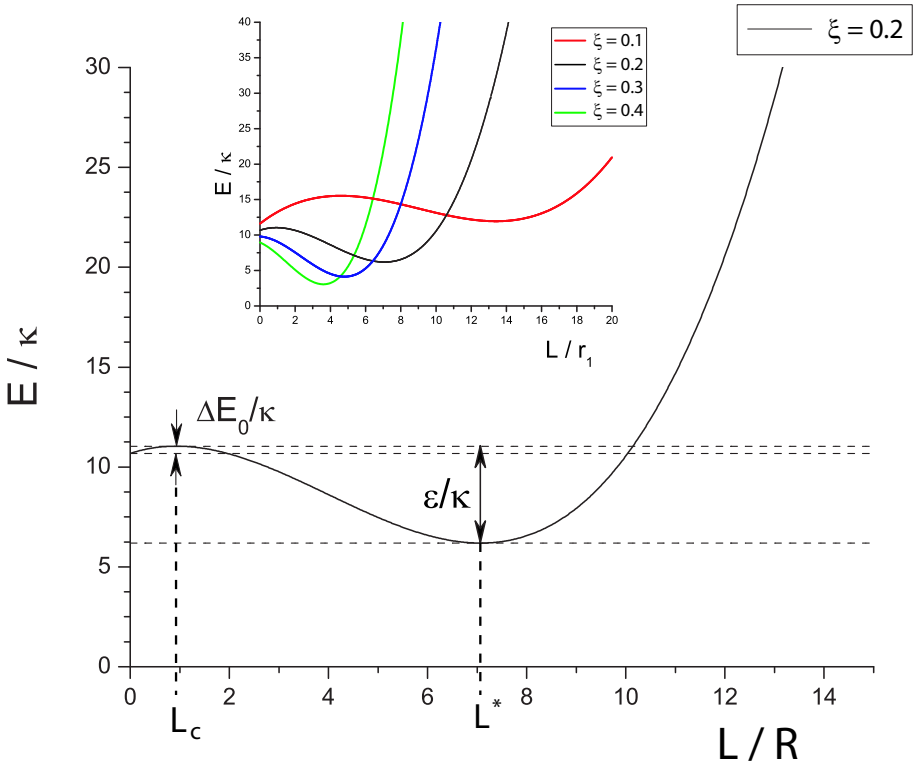

Figure 8.3 Energy vs. tube length for different values of the rate of polymer molecules added to the system, i.e. the slope of the linear polymer profile ξ (inset). Initial buds need to overcome an energy barrier ΔE_0 to elongate into tubes for a certain range of values of ξ. Then, the elongated tube needs to overcome another barrier ϵ in order to be reabsorbed by the mother vesicle. The surface tension here is negligible.

For an initially formed bud-like fluctuation ($L_{\mathrm{ini}} = 0$ in Fig. 8.4), when we increase the slope of the spontaneous curvature, ξ, the bud cannot grow unless the critical slope, ξ^{crit}, is reached, and then a finite-length tube is formed out (dashed line in Fig. 8.4). This transition is discontinuous in the value of

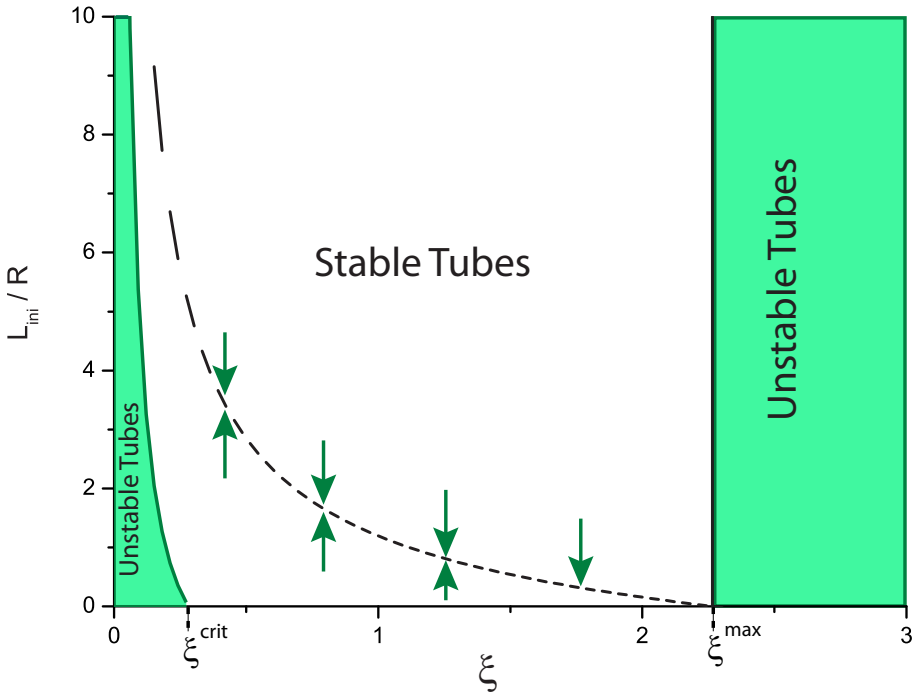

Figure 8.4 Stability diagram of tube formation as a function of the initial tube of length L_{ini} ($L_{\text{ini}} = 0$ corresponds to a bud), and the dimensionless slope of the spontaneous curvature gradient ξ. The dashed line correspond to the stable tube length, L^*, for a given concentration gradient.

the stable length of the tube. In addition, we see that the tube length is maximum for ξ^{crit}, decreasing for steeper profiles, $\xi > \xi^{\text{crit}}$. Eventually, at ξ^{max} the equilibrium tube length vanishes, and buds become again unstable. This transition is therefore continuous.

For non-vanishing but relatively small values of the surface tension, σ, the stable tube length decreases as

$$L^*(\bar{\sigma}) = L^*(0) - \bar{\sigma}/(\xi^2\sqrt{1-\pi/2+2/\xi}), \tag{8.16}$$

where $L^*(0)$ is the tube length for zero tension. For tensions larger than a critical tension $\bar{\sigma}_c = 4 - \pi/2$, bud to tube transition disappear, altough stable tubes may be formed out from a tube with a finite given length.

8.4 Numerical model

In the experiments by Tsafrir *et al.* [250], polymer molecules diffuse from a source and eventually anchor the membrane, inducing a local spontaneous curvature which modifies the vesicle shape. In order to study dynamically this process, we present here a numerical model dealing with a stationary polymer profile and the spontaneous curvature model without any assumption on the tube geometry.

In order to do so, we use the phase-field method developed in Ch. 5 to numerically deal with the bending energy of the membrane. Within this approach, the Helfrich Hamiltonian Eq. (8.8) is written as a dynamic function of a field, ϕ, whose level-set $\{\mathbf{x} : \phi(\mathbf{x}) = 0\}$ locates the membrane position at each time. The dynamic equation for the phase-field, and hence for the membrane shape, is given by Eq. (5.46) [39], which we rewrite here for convenience

$$\frac{\partial \phi}{\partial t} = \bar{\kappa}\boldsymbol{\nabla}^2\Big\{ \Big(3\phi^2 - 1 - 2\epsilon C_0(\boldsymbol{x})\,\phi\Big)\,\Phi_{\rm sc}[\phi] - \epsilon^2\boldsymbol{\nabla}^2\Phi_{\rm sc}[\phi] + \epsilon^2\bar{\sigma}(\boldsymbol{x})\boldsymbol{\nabla}^2\phi\Big\}. \tag{8.17}$$

where $\Phi[\phi(\boldsymbol{x}), \rho(\boldsymbol{x})] = (\phi^2 - 1)\,(\phi - \epsilon\, C_0(\rho(\boldsymbol{x}))) - \epsilon^2\boldsymbol{\nabla}^2\phi(\boldsymbol{x})$, $C_0(\rho(\boldsymbol{x})) = \bar{c}_0\,\rho(\mathbf{x})$ is the spontaneous curvature induced by the local concentration $\rho(\mathbf{x})$ of polymer molecules anchored on the membrane, and ϵ is a small parameter related to the width of the interface (see Ch. 4). This dynamic equation includes a tube surface tension $\tilde{\sigma}$, and conserves locally the inner volume, due to the use of a relaxational model-B-like conserved dynamics [117].

The assumption we did before of a linear stationary polymer profile is relaxed at this point. Since our aim is to show how an inhomogeneous stationary polymer concentration profile is a possible mechanism of tube formation, we are going to use in our numerical treatment a Gaussian stationary profile such as

$$\rho(\boldsymbol{x}) = \frac{\rho_0}{\Sigma\sqrt{2\pi}}\,\exp\left(-\frac{\left|\boldsymbol{x} - \boldsymbol{x}_{\rm appl}\right|^2}{2\Sigma^2}\right), \tag{8.18}$$

where Σ is the standard deviation, related with the width of the distribution, and ρ_0 is the total number of polymer molecules introduced in the system. This problem is then reduced to numerically solve Eq. (8.17) using this stationary polymer concentration for different sets of initial conditions and parameters. We used a standard finite-difference scheme for the spatial discretization and an Euler method for the time-derivatives (see Sec. 6.1).

The parameters which are relevant in these simulations in order to study the growth and the shrinkage of tubes are: the length of the initial tube, and

the characteristics of the polymer gradient profile. We fixed the position of the polymer source to be $z_p = 7.5\,R$, where R is the radius of the initial tube formed by a cylinder and a hemispherical cap. Due to the axisymmetry of the problem, the integration is performed in a two-dimensional lattice, whose size is 80×20 throughout this Chapter.

8.5 Results and discussion

In Fig. 8.1 we showed three snapshots of the experimental results from Ref. [250], where a fluctuating oblate vesicle undergoes a shape instability which forms an initial bud and eventually grows into a tube, due to the anchorage of amphiphilic polymer molecules. The presence of the polymer molecules enhance fluctuation of the vesicle rim (Fig. 8.1a). One can divide the dynamics of this process in four different regimes:

1. The formation of the initial bud and suppression of rim fluctuations (Fig. 8.1b).
2. When the tube starts to grow up to a certain length (Fig. 8.1c).
3. Then, the polymer source is shut down (Fig. 8.5a) and tubes shrink reaching a metastable bud-like shape (Fig. 8.5b).
4. In the last regime, they eventually disappear reabsorbed by the mother vesicle.

Within our model, we find, as shown in Fig. 8.5c, the shape of a large tube, which is qualitatively in good agreement with the experimental results. For a large range of values of the standard deviation, Σ, the tube length we get is essentially the same. In other words, when the source of polymer molecules is shut down, the concentration profile gets stretched as time goes by, but the length of the stable tube continues being the same.

Then, after some time, the polymer molecules are more homogeneously distributed, and a new configuration of short length is found (Fig. 8.5d). These buds are also in agreement with those found by Tsfarir *et al.* [250], and we can quantitatively compare them by measuring the ratio between their width and length to be ~ 0.3.

In other recent experiments, Roux *et al.* [216] generated dynamin-coated membrane tubes. They observed the growth of these tubes by the addition of this protein. Further addition of guanosine triphosphate (GTP) molecules to these tubes induces fission by a conformational change of dynamins. Although our model is capable of explaining the initial tubulation by the generation of membrane curvature by dynamin, it does not consider topological changes such as fission.

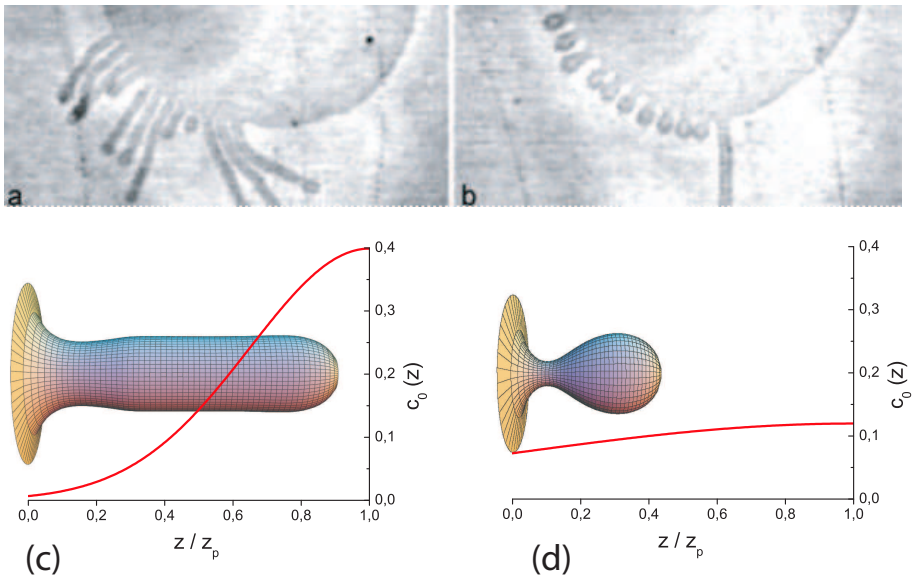

Figure 8.5 Tubes extruded from a vesicle by a non-homogeneous polymer profile. Comparison between the experimental results from Ref. [250] (a,b) and the phase-field integrations (c,d). For short times (small standard deviation Σ) long tubes are obtained (a,c), and for long time (wider distributions) buds appear (b,d). The resulting profile for the spontaneous curvature is shown for the phase-field integrations. We choose $\xi = 0.3$, $\Sigma = 3.5R$ (c), and $\xi = 0.3$, $\Sigma = 10R$ (d).

Part II On multicomponent membranes

9
Two-phase periodic membrane tubes

In this Chapter, we investigate the formation of two-phase lipidic tubes of membrane in the framework of the Canham-Helfrich model [37]. The two phases have different elastic moduli (bending and Gaussian rigidity), different tensions and a line tension prevents the mixing. For a set of parameters close to experimental values, periodic patterns with arbitrary wavelength can be found numerically. A wavelength selection is detected via the existence of an energy minimum. When the chemical composition induces an important enough size disequilibrium between both phases, a segregation into two half infinite tubes is preferred to a periodic structure.

9.1
Introduction

Inhomogeneous lipid membranes have received increasing attention recently [73, 168]. They are formed by multiple lipid components which laterally separate into coexisting liquid phases with specific composition. In cell biology, this separation is responsible for cholesterol-enriched micro-domain formation. These domains, called rafts, are believed to concentrate important biological functions such as polarized sorting of proteins [132, 234], cellular signaling [235], and viral entry and budding [233].

In this Chapter, we focus on inhomogeneous tubular membranes and we ask the question of the existence of periodic and steady patterns. Tubular membranes exist in the cell, allowing transport functions from an intracellular compartment to another. They also appear during cell development and motility [29]. Made of a ternary mixture of lipids (sphingomyelin (SM), dioleoylphosphatidylcholine (DOPC), and cholesterol) in varying composition (see Sec. 2.1.1), these vesicles exhibit various and complex shapes and domain organizations, as the temperature approaches the mixing/demixing composition temperature. For a composition which favors cholesterol enriched phases, periodic tubular vesicles have been experimentally observed [14]. Here, in the framework of the Canham-Helfrich model (see Ch. 3), we explain the existence of periodic membrane tubes and the selection of the wavelength in

terms of physical parameters such as the elastic coefficients, the surface and line tensions. Other non-periodic inhomogeneous tubes have been experimentally observed [5, 215] like quasi-semi infinite tubes where the complete separation seems to be energetically preferred: each half-infinite tube is made with a unique phase separated from the neighbor by a unique junction. Our goal is also to explain this duality between periodicity or homogeneity when the chemical composition between both phases is approximately balanced.

9.2 Variational treatment for biphasic tubes

The physics of membrane tube formation has been studied both theoretically and experimentally (see Sec. 8.2) [27, 63, 200]. We will use the variational free energy minimization that we adapt to an infinite periodic biphasic tube with a prescribed chemical ratio composition $S_{\mathrm{Lo}}/S_{\mathrm{Ld}}$, where S_{Lo} and S_{Ld} are the areas covered by the liquid ordered, Lo, and liquid disordered, Ld, phases, respectively (see Fig. 9.1). The free energy is obtained by extending the tubular energy with an effective force acting at some ends, giving

$$\mathcal{F} = \sum_{i=\mathrm{Ld,Lo}} \int_{\Omega_i} \left[\frac{\kappa_i}{2} (\mathsf{J} - \mathsf{c}_i)^2 + \bar{\kappa}_i \mathsf{K} + \sigma_i \right] \mathrm{d}S + \oint_{\partial\Omega} \tau \, \mathrm{d}\ell - \int f \, \mathrm{d}z. \tag{9.1}$$

We denote the two phases by Lo or Ld following the classical terminology which distinguishes a liquid-ordered and a liquid-disordered phase (see Sec. 2.3). Both phases will be treated in the same way but the Lo-phase is more rigid. For each phase, we integrate the free energy over its membrane area. The length of each phase i measured on the z-axis is λ_i and the total wavelength is thus $\lambda = \lambda_{\mathrm{Ld}} + \lambda_{\mathrm{Lo}}$. We choose as length unit the radius R_{Lo}, which is the value of the radius at its extremal value in the Lo-phase (see Fig. 9.1). Our study will fix all the lengths of the pattern as a function of R_{Lo}, which is fixed by the total available mass of lipids. The free energy Eq. (9.1) includes the spontaneous curvature model Eq. (3.4), where J is the total curvature, and K the Gaussian curvature. The characteristic elastic coefficients are κ_i and $\bar{\kappa}_i$, the bending and Gaussian rigidities, respectively. One can also include the spontaneous curvature of the phase i, c_i, if the two leaflets of the membrane are different. This occurs by anchoring amphiphilic molecules in vesicles for example, which may induce a tubular instability [41, 250] (see Ch. 8). In each phase, σ_i, the tension of the membrane in phase i, remains constant if the area per lipid does not vary, so the surface of each phase remains constant. Not included here, a small pressure effect may be incorporated [200]. The interface between the two phases is described by a jump in the values of the bending and Gaussian rigidities and in the values of the surface tension. Moreover, a line energy is associated to this interface, with a line tension τ.

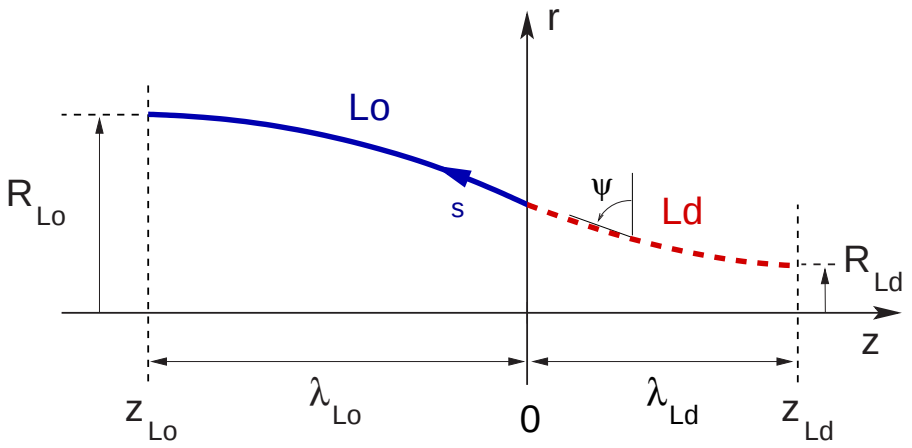

Figure 9.1 Geometry sketch of a periodic biphasic membrane tube. The z-axis is the axis of symmetry of the tubes. Half of the wavelength of both Ld and Lo phases is depicted. The $\{r, \psi\}$ parametrization used when deriving the Euler-Lagrange equations is shown. The interface is located at $s = z = 0$.

9.2.1 Axisymmetric parametrization

Since we consider here axisymmetric tubes, we parametrize the surface in cylindrical coordinates (see Fig. 9.1). We have therefore the following geometric relations

$$\dot{r} = \cos\psi, \tag{9.2}$$

$$\dot{z} = -\sin\psi, \tag{9.3}$$

where the dot represents the derivative with respect to the arclength, s, along the curve. The total and Gaussian curvatures can be written in these coordinates in the following way

$$\mathsf{J} = \dot{\psi} + \frac{\sin\psi}{r}, \tag{9.4}$$

$$\mathsf{K} = \frac{\sin\psi}{r}\dot{\psi}, \tag{9.5}$$

as well as

$$\mathrm{d}^2S = 2\pi r(s)\mathrm{d}s, \tag{9.6}$$

is the surface element. Therefore, we can rewrite the Canham-Helfrich part of the Hamiltonian (9.1) as

$$\mathcal{F}_{\mathrm{CH}}{}^{i} = \int_{\Omega_i} \left[\frac{\kappa_i}{2} \left(\dot{\psi} + \frac{\sin\psi}{r} - \mathsf{c}_0 \right)^2 + \bar{\kappa}_i \frac{\sin\psi}{r}\dot{\psi} + \sigma_i \right] 2\pi r \mathrm{d}s. \tag{9.7}$$

Since we describe the tube shape by the angle ψ and the local radius r as a function of the arclength s, one needs a Lagrange multiplier $\Gamma(s)$ to impose the relation Eq. (9.2). The total energy of the tube, in the axisymmetric variational form reads

$$\mathcal{F} = \sum_{i=\mathrm{Ld,Lo}} \left[{\mathcal{F}_{\mathrm{CH}}}^{i} + \int_{\Omega_i} f \sin\psi \mathrm{d}s + \int_{\Omega_i} \Gamma(s)\left(\dot{r} - \cos\psi\right) \mathrm{d}s \right]. \tag{9.8}$$

9.2.2 Euler-Lagrange equations and Hamiltonian of the system

In order to find an equation for the tube shape, we first need to derive the Euler-Lagrange equations of our variational problem. The free energy Eq. (9.1) is a Lagrangian, in classical mechanics vocabulary [103]. Since we are going to present some detailed calculations on how the shape equation is obtained, we will restrict ourselves here to the case of vanishing spontaneous curvatures, $c_i = 0$, for the sake of simplicity. The case for non-vanishing spontaneous curvatures can be done straightforwardly in an analogous way. Then, the Lagrangian of each phase, $\mathcal{L}_i$, reads

$$\begin{aligned}\frac{\mathcal{L}_i}{2\pi} = \frac{\kappa_i}{2}\left(r\dot{\psi}^2 + 2\dot{\psi}\sin\psi + \frac{\sin^2\psi}{r}\right) + \bar{\kappa}_i \sin\psi\dot{\psi} + r\sigma_i \\ + \bar{f}\sin\psi + \bar{\Gamma}(s)\left(\dot{r} - \cos\psi\right),\end{aligned} \tag{9.9}$$

where $\bar{f} = f/2\pi$ and $\bar{\Gamma}(s) = \Gamma(s)/2\pi$.

In order to find the two Euler-Lagrange equations, corresponding to the two coordinates, r and ψ, we need to find the partial derivatives with respect to these coordinates and their arclength-derivatives. Explicitly, for the ψ coordinate, we get

$$\begin{aligned}\frac{1}{2\pi}\frac{\partial\mathcal{L}_i}{\partial\psi} = \frac{\kappa_i}{2}\left(2\dot{\psi}\cos\psi + \frac{2\sin\psi\cos\psi}{r}\right) + \bar{\kappa}_i\cos\psi\dot{\psi} \\ + \bar{f}\cos\psi + \bar{\Gamma}(s)\sin\psi,\end{aligned} \tag{9.10}$$

$$\frac{1}{2\pi}\frac{\partial\mathcal{L}_i}{\partial\dot{\psi}} = \frac{\kappa_i}{2}\left(2r\dot{\psi} + 2\sin\psi\right) + \bar{\kappa}_i\sin\psi, \tag{9.11}$$

$$\frac{\mathrm{d}}{\mathrm{d}s}\left(\frac{1}{2\pi}\frac{\partial\mathcal{L}_i}{\partial\dot{\psi}}\right) = \kappa_i\left(2\cos\psi\dot{\psi} + r\ddot{\psi}\right) + \bar{\kappa}_i\cos\psi\dot{\psi}. \tag{9.12}$$

Wherefrom the Euler-Lagrange equation [103] associated to the variable ψ can be found. After some algebra,

$$r\ddot{\psi} + \cos\psi\dot{\psi} - \frac{1}{r}\sin\psi\cos\psi - \bar{f}\cos\psi - \bar{\Gamma}(s)\sin\psi = 0. \tag{9.13}$$

For the radial coordinate, r, the needed derivatives are

$$\frac{1}{2\pi}\frac{\partial \mathcal{L}_i}{\partial r} = \frac{\kappa_i}{2}\left(\dot{\psi}^2 - \frac{\sin^2\psi}{r^2}\right) + \sigma_i, \tag{9.14}$$

$$\frac{1}{2\pi}\frac{\partial \mathcal{L}_i}{\partial \dot{r}} = \bar{\Gamma}(s), \tag{9.15}$$

$$\frac{\mathrm{d}}{\mathrm{d}s}\left(\frac{1}{2\pi}\frac{\partial \mathcal{L}_i}{\partial \dot{r}}\right) = \dot{\bar{\Gamma}}(s). \tag{9.16}$$

And the corresponding associated Euler-Lagrange equation reads

$$\dot{\tilde{\Gamma}} = \frac{1}{2}\dot{\psi}^2 - \frac{\sin^2\psi}{2r^2} + \tilde{\sigma}_i, \tag{9.17}$$

where $\tilde{\Gamma} = \bar{\Gamma}/\kappa_i$ and $\tilde{\sigma}_i = \sigma_i/\kappa_i$.

Following the usual classical mechanical procedure [103], the Hamiltonian of the system is defined as

$$\mathcal{H} = \mathcal{L} - \dot{\psi}\mathcal{L}_{\dot{\psi}} - \dot{r}\mathcal{L}_{\dot{r}} \tag{9.18}$$

After some algebraic manipulation, we arrive to the following expression for the Hamiltonian,

$$\mathcal{H}_i = -2\pi\left[\frac{\kappa_i}{2}r\left(\dot{\psi}^2 - \frac{\sin^2\psi}{r^2}\right) - r\sigma_i - \frac{f}{2\pi}\sin\psi + \frac{\gamma}{2\pi}\cos\psi\right]. \tag{9.19}$$

Since the Lagrangian Eq. (9.9) does not depend explicitly on s, the Hamiltonian $\mathcal{H}_i$ is a constant in each phase. The mechanical equilibrium at the junction imposes that $\mathcal{H}_{\mathrm{Lo}} = \mathcal{H}_{\mathrm{Ld}}$. For a detailed discussion on the Hamiltonian, see Appendix A in Ref. [127]. Moreover, and as it is frequently done in standard experiments, we assume that at least one end of the tube is connected to a reservoir of lipids (a vesicle for example) at infinity so no force is required for an extension of the tube length. This imposes that

$$\mathcal{H}_{\mathrm{Lo}} = \mathcal{H}_{\mathrm{Ld}} = 0, \tag{9.20}$$

which gives an extra equation

$$\tilde{\Gamma}\cos\psi = -\frac{1}{2}r\dot{\psi}^2 + \frac{1}{2}\frac{\sin^2\psi}{r} + \tilde{\sigma}_i r + \tilde{f}\sin\psi. \tag{9.21}$$

9.2.3 Shape equation

Rewriting Eq. (9.13),

$$\tilde{\Gamma}(s)\sin\psi = r\ddot{\psi} + \cos\psi\dot{\psi} - \frac{1}{r}\sin\psi\cos\psi - \tilde{f}\cos\psi, \tag{9.22}$$

and if we perform the derivative with respect to the arclength to both sides of Eq. (9.22), we get that

$$\dot{\tilde{\Gamma}}(s)\sin\psi + \tilde{\Gamma}(s)\cos\psi\dot{\psi} = r\dddot{\psi} + 2\cos\psi\ddot{\psi} - \sin\psi\dot{\psi}^2 + \frac{1}{r^2}\sin\psi\cos^2\psi - \frac{1}{r}\left(\cos^2\psi - \sin^2\psi\right)\dot{\psi} + \tilde{f}\sin\psi\dot{\psi}. \tag{9.23}$$

Multiplying Eq. (9.17) by $\sin\psi$, we get

$$\dot{\tilde{\Gamma}}(s)\sin\psi = \frac{1}{2}\dot{\psi}^2\sin\psi - \frac{\sin^3\psi}{2r^2} + \tilde{\sigma}_i\sin\psi. \tag{9.24}$$

And multiplying Eq. (9.21) by $\dot{\psi}$,

$$\tilde{\Gamma}(s)\cos\psi\dot{\psi} = -\frac{1}{2}r\dot{\psi}^3 + \frac{1}{2}\frac{\sin^2\psi}{r}\dot{\psi} + \tilde{\sigma}_i r\dot{\psi} + \tilde{f}\sin\psi\dot{\psi}. \tag{9.25}$$

Plugging Eqs. (9.22), (9.21), and (9.25) together, we can write down, after some algebra, the shape equation

$$\dddot{\psi} = -\frac{\dot{\psi}^3}{2} - 2\frac{\cos\psi}{r}\ddot{\psi} + \frac{3}{2}\frac{\sin\psi}{r}\dot{\psi}^2 + \frac{3\cos^2\psi - 1}{2r^2}\dot{\psi} - \frac{\cos^2\psi + 1}{2r^3}\sin\psi + \frac{\sigma_i}{\kappa_i}\dot{\psi} + \frac{\sigma_i}{\kappa_i}\frac{\sin\psi}{r}, \tag{9.26}$$

which has to be solved together with the condition Eq. (9.2).

9.2.4 Boundary conditions at the junction

The continuity of the functions $r(s)$ and $\psi(s)$ across the junction, located at $s = 0$, by definition of the origin of the s-coordinate, can be expressed mathematically as

$$r(\epsilon) = r(-\epsilon),$$
$$\psi(\epsilon) = \psi(-\epsilon). \tag{9.27}$$

The boundary conditions at the junction, as coming from the variational minimization of the free energy [4, 103] are expressed as

$$\mathcal{L}_{\dot{\psi}}\,\delta\psi\Big|_{s=-\epsilon}^{s=\epsilon} + \left(\mathcal{L} - \mathcal{L}_{\dot{\psi}}\right)\delta s\Big|_{s=-\epsilon}^{s=\epsilon} = 0, \tag{9.28}$$

for the ψ coordinate. After some calculations it reads

$$\kappa_\alpha\dot{\psi}(\epsilon) - \kappa_\beta\dot{\psi}(-\epsilon) = \left(\kappa_\beta + \bar{\kappa}_\beta - \kappa_\alpha - \bar{\kappa}_\alpha\right)\frac{\sin\psi(0)}{r(0)}, \tag{9.29}$$

where we have assumed the continuity relations Eq. (9.27). Analogously, for the r coordinate, we have

$$\mathcal{L}_{\dot{r}}\delta r|_{s=-\epsilon}^{s=\epsilon} + 2\pi\tau\delta r(0) = 0, \tag{9.30}$$

which transforms into

$$\kappa_\alpha\ddot{\psi}(\epsilon) - \kappa_\beta\ddot{\psi}(-\epsilon) = \tau\frac{\sin\psi(0)}{r(0)} + \left(2\kappa_\alpha + \bar{\kappa}_\alpha - 2\kappa_\beta - \bar{\kappa}_\beta\right)\frac{\sin\psi(0)\cos\psi(0)}{r^2(0)}. \tag{9.31}$$

9.2.5 Effect of non-vanishing spontaneous curvatures

When non-vanishing spontaneous curvatures are considered in both phases, the previous results are modified. We present here the result, since the derivation can be easily done in the same way as we proceeded for the symmetric case. The condition of zero Hamiltonian in this case gives a first relation between the force f,the radius at the dip $r_{\min} = R_{\mathrm{Ld}}/R_{\mathrm{Lo}}$ and the tensions $\sigma_{\mathrm{Lo}} = \bar{\sigma}_{\mathrm{Lo}}R_{\mathrm{Lo}}^2$ and $\sigma_{\mathrm{Ld}} = \bar{\sigma}_{\mathrm{Ld}}R_{\mathrm{Lo}}^2$. As f is a constant, we get

$$\begin{aligned} R_{\mathrm{Lo}}f/\pi &= \frac{\kappa_{\mathrm{Ld}}}{r_{\min}}\left[(1-\mathsf{c}_{\mathrm{Ld}}\mathsf{r}_{\min})^2 + 2\sigma_{\mathrm{Ld}}r_{\min}^2/\kappa_{\mathrm{Ld}}\right] \\ &= \kappa_{\mathrm{Lo}}\left[(1-\mathsf{c}_{\mathrm{Lo}})^2 + 2\sigma_{\mathrm{Lo}}/\kappa_{\mathrm{Ld}}\right]. \end{aligned} \tag{9.32}$$

In addition, the shape equation in each phase [5,27,63,200] reads

$$\begin{aligned} \dddot{\psi} = &-\frac{\dot{\psi}^3}{2} - \frac{2\cos\psi}{r}\ddot{\psi} + \frac{3\sin\psi}{2r}\dot{\psi}^2 + \frac{3\cos^2\psi - 1}{2r^2}\dot{\psi} \\ &- \frac{\cos^2\psi + 1}{2r^3}\sin\psi + \frac{\sigma_i}{\kappa_i}\dot{\psi} + \frac{\sigma_i}{\kappa_i}\frac{\sin\psi}{r} + \frac{1}{4}\mathsf{c}_i^2\left[\dot{\psi} + \left(1 - 2\dot{\psi}\right)\frac{\sin\psi}{r}\right], \end{aligned} \tag{9.33}$$

with boundary conditions at the interface located at $s = 0$. From Eq. (9.33) we deduce two new relations,

$$\frac{\sigma_{\mathrm{Lo}}}{\kappa_{\mathrm{Lo}}} = \frac{1}{2} - \frac{1}{4}\mathsf{c}_{\mathrm{Lo}}^2, \tag{9.34}$$

and,

$$\frac{\sigma_{\mathrm{Ld}}}{\kappa_{\mathrm{Ld}}} = \frac{1}{2r_{\min}^2} - \frac{1}{4}\mathsf{c}_{\mathrm{Ld}}^2, \tag{9.35}$$

which finally give the value of both tensions σ_i as a function of $r_{\min}$, knowing the bending rigidities. The boundary conditions due to mechanical equilibrium (momentum and force balance [127]) at the junction give two of the

boundary conditions,

$$\kappa_{\mathrm{Ld}}\left(\dot{\psi}(\epsilon)-\frac{1}{2}\mathsf{c}_{\mathrm{Ld}}\right)-\kappa_{\mathrm{Lo}}\left(\dot{\psi}(-\epsilon)-\frac{1}{2}\mathsf{c}_{\mathrm{Lo}}\right)= \\ (\kappa_{\mathrm{Lo}}+\bar{\kappa}_{\mathrm{Lo}}-\kappa_{\mathrm{Ld}}-\bar{\kappa}_{\mathrm{Ld}})\,\frac{\sin\psi(0)}{r(0)}, \tag{9.36}$$

$$\kappa_{\mathrm{Ld}}\ddot{\psi}(\epsilon)-\kappa_{\mathrm{Lo}}\ddot{\psi}(-\epsilon)=\tau\frac{\sin\psi(0)}{r(0)} \\ +(2\kappa_{\mathrm{Ld}}+\bar{\kappa}_{\mathrm{Ld}}-2\kappa_{\mathrm{Lo}}-\bar{\kappa}_{\mathrm{Lo}})\,\frac{\sin\psi(0)\cos\psi(0)}{r(0)^2}, \tag{9.37}$$

with c_i the spontaneous curvature if the bilayer is asymmetric. It is possible to transform any of both Eqs. (9.26), (9.33) by integrating once to obtain a second order nonlinear equation for $\psi(r)$ with a free parameter [161,179]. That equation was useful to find explicit solutions and indicates that the space of possible solutions has three degrees of freedom for ψ and four for the profiles, which are necessary to solve the junction conditions.

9.3 Results and discussion

9.3.1 Exact results

It turns out that explicit solutions of Eq. (9.33) have been found but they require a lipid membrane model incorporating both a spontaneous curvature and pressure effect. A simplification arises for a periodic tube since we do not have to consider non divergent asymptotes at infinity and in principle we can truncate the solutions. As an example, the catenoid, which is a solution of Eq. (9.33), may be a good candidate to represent the concave phase of the tube. Exact known solutions have been discovered [161,179]; they include as special limits catenoids and unduloids. Taking into account our choice of length unit, they are represented by

$$\sin\psi=\frac{2}{\mathsf{c}_{\mathrm{Lo}}}\left[\left(r+\frac{1}{r}\right)\pm\sqrt{4-\frac{1}{2}\mathsf{c}_{\mathrm{Lo}}^2}\right], \tag{9.38}$$

for the Lo-phase while the concave Ld-phase may be represented by

$$\sin\psi=\frac{2}{\mathsf{c}_{\mathrm{Ld}}}\left[\left(\frac{r}{r_{\min}^2}+\frac{1}{r}\right)\pm\sqrt{\frac{4}{r_{\min}}-\frac{1}{2}\mathsf{c}_{\mathrm{Ld}}^2}\right]. \tag{9.39}$$

Since we have chosen as length unit R_{Lo} at its maximum, the spontaneous curvature c_{Lo}, which is indeed responsible for the length scale of the system, is equal to $8/3$ while $r_{min} = 2/3\, c_{\mathrm{Ld}}$. Except for the catenoid, these solutions exist only in the case where the two layers of the membrane are asymmetric, the tension and the pressure being Lagrange multipliers function of the spontaneous curvatures in both phases. Nevertheless, it turns out to be impossible to satisfy the boundary conditions Eqs. (9.36) and (9.37) simultaneously for arbitrary physical elastic coefficients since all the parameters of the solution are fixed by the spontaneous curvature of the bilayers. The only possibility remaining is the catenoid, $\sin\psi = r_{min}/r$, which may represent the concave phase when the spontaneous curvature c_{Ld} vanishes.

9.3.2 Linear analysis

From above, one notices that the known exact analytical solutions are too much constrained and one really need a family with three real degrees of freedom in ψ to solve the constraints at the interface. Moreover, we also neglect at this point the spontaneous curvature assuming the two leaflets of the membrane to be symmetric. Assuming a linear perturbation in the vicinity of the cylindrical exact solution for any of the two phases,

$$r(z) = R_i\,(1 + U_i(z))\,, \tag{9.40}$$

where R_i are the radii at the infinity, given by [63, 200] (see Sec. 8.2),

$$R_i = \sqrt{\frac{\kappa_i}{2\sigma_i}}, \tag{9.41}$$

and f is the force, which is unique for both phases, given by

$$f = 2\pi\sqrt{2\kappa_\alpha\sigma_\alpha} = 2\pi\sqrt{2\kappa_\beta\sigma_\beta}. \tag{9.42}$$

These two equations imply that

$$\frac{\kappa_\alpha}{\kappa_\beta} = \frac{\sigma_\beta}{\sigma_\alpha} = \frac{R_\alpha}{R_\beta}. \tag{9.43}$$

With this information, we can expand the useful quantities in terms of the perturbation function $U_i(z)$. Therefore, up to linear order in U_i,

$$z(s) = -s, \tag{9.44}$$

$$\sin\psi = -\dot{z} = 1, \tag{9.45}$$

$$\cos\psi = \dot{r} = R_i\frac{\mathrm{d}U_i(z(s))}{\mathrm{d}s} = -R_i U_i'(z), \tag{9.46}$$

$$\dot{\psi} = -R_i U_i''(z), \tag{9.47}$$

$$\ddot{\psi} = R_i U_i'''(z), \tag{9.48}$$

$$\dddot{\psi} = -R_i U_i^{(iv)}(z). \tag{9.49}$$

Linearizing the shape equation Eq. (9.26) gives a fourth-order linear differential equation

$$R_i^4 \frac{\partial^4 U_i}{\partial z^4} + U_i = 0. \tag{9.50}$$

Its solution, symmetric with respect to the middle of each domain $\varepsilon\lambda_i/2$ is

$$\begin{aligned} U_i(z) = A_i \Bigg[&\cosh\left(\frac{z+\varepsilon\lambda_i/2}{\sqrt{2}}\right)\cos\left(\frac{z+\varepsilon\lambda_i/2}{\sqrt{2}}\right) \\ &+ r_i \sinh\left(\frac{z+\varepsilon\lambda_i/2}{\sqrt{2}}\right)\sin\left(\frac{z+\varepsilon\lambda_i/2}{\sqrt{2}}\right)\Bigg], \end{aligned} \tag{9.51}$$

with $\varepsilon = +1$ for the Lo-phase, and $\varepsilon = -1$ for the Ld-phase. In a linear approach, A_i and r_i may be chosen arbitrarily, giving the four degrees of freedom needed to satisfy the junction conditions, which in the linear approximation read as

$$U_\alpha(0) = U_\beta(0) + \delta\tilde{\kappa}, \tag{9.52}$$

$$U_\alpha'(0) = U_\beta'(0), \tag{9.53}$$

$$U_\alpha''(0) - U_\beta''(0) = -\left(\delta\tilde{\kappa} + \Delta\tilde{\bar{\kappa}}\right), \tag{9.54}$$

$$U_\alpha'''(0) - U_\beta'''(0) = -\tilde{\tau}, \tag{9.55}$$

where we defined the following elastic dimensionless parameters,

$$\tilde{\kappa} = 1 + \delta\tilde{\kappa} = \kappa_\beta/\kappa_\alpha = R_\beta/R_\alpha, \tag{9.56}$$

$$\Delta\tilde{\bar{\kappa}} = \frac{\bar{\kappa}_\beta - \bar{\kappa}_\alpha}{\kappa_\alpha}, \tag{9.57}$$

$$\tilde{\tau} := \tau\frac{R_\alpha}{\kappa_\alpha}. \tag{9.58}$$

Note that the wavelength of the pattern $\lambda = \lambda_{\mathrm{Ld}} + \lambda_{\mathrm{Lo}} = \lambda_{\mathrm{Ld}}(1 + S_{\mathrm{Ld}}/S_{\mathrm{Lo}})$, is a real degree of freedom at fixed composition ratio between phases, $S_{\mathrm{Ld}}/S_{\mathrm{Lo}}$: in principle, the problem can be solved without fixing the wavelength.

9.3.3 Nonlinear numerical treatment

In order to check the validity of the former linear analysis and to show that solutions for periodic tubes exist, we have performed the numerical integration

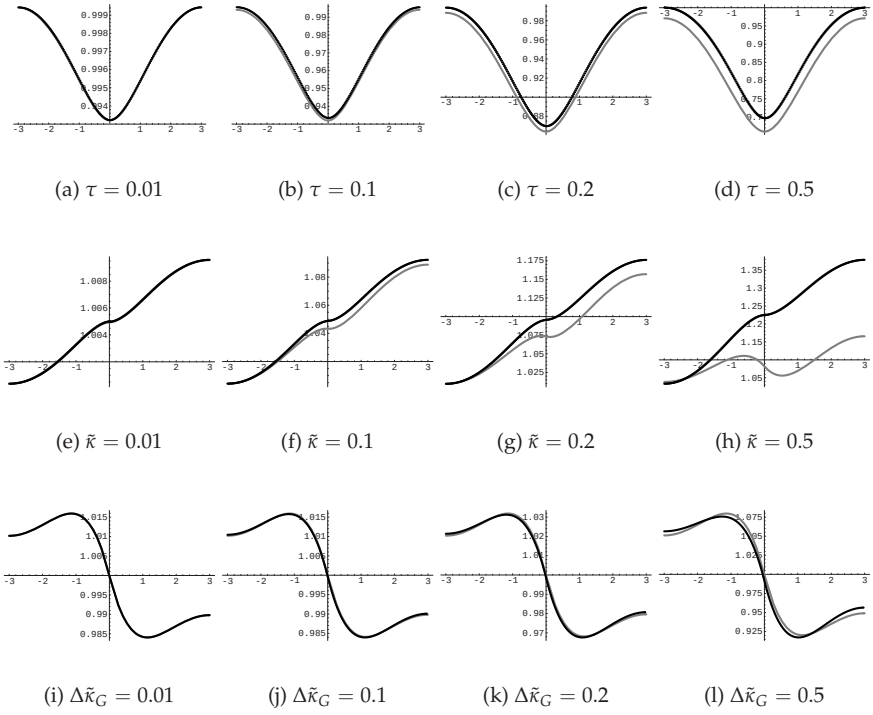

(a) $\tau = 0.01$ (b) $\tau = 0.1$ (c) $\tau = 0.2$ (d) $\tau = 0.5$

(e) $\tilde{\kappa} = 0.01$ (f) $\tilde{\kappa} = 0.1$ (g) $\tilde{\kappa} = 0.2$ (h) $\tilde{\kappa} = 0.5$

(i) $\Delta\tilde{\kappa}_G = 0.01$ (j) $\Delta\tilde{\kappa}_G = 0.1$ (k) $\Delta\tilde{\kappa}_G = 0.2$ (l) $\Delta\tilde{\kappa}_G = 0.5$

Figure 9.2 Tube profiles $r(z)$ for the periodic tube where $z_{Lo} = 3$, $z_{Ld} = -3$, and $R_{\text{Ld}} = 1$ (see Fig. 9.1). The elastic coefficients of both Lo and Ld phases are the same, except those mentioned. In each figure, we present the solution for the linearized problem (dark curves) and for the complete non-linear problem (light curves). We can see there that for small enough relative parameters, both curves are almost the same in each case.

of the non-linear differential equations Eq. (9.26), according to the matching relations Eqs. (9.27, 9.29, and 9.31), using the shooting to a fitting point numerical method [4, 204]. Integrations in the regime of validity of the linear analysis have been performed in order to check the consistency of both calculations. A systematic study of the tube profile $r(z)$ when changing uniquely one of the three elastic dimensionless parameters (see Fig. 9.2) allows to measure the effects of a mismatch between the physical constants of both phases. We systematically compare the non-linear solutions to the one found in the linear approximation, for double checking of our numerical procedure. As expected, we see that both solutions are almost equal when the differences between the elastic constants of the two phases are small, $\tilde{\kappa}$, $\Delta\tilde{\bar{\kappa}}$, $\tilde{\tau} \ll 1$. These figures illustrate the effects induced by the mismatch of elastic constants be-

tween the two phases and the line tension on the geometry of the periodic tube.

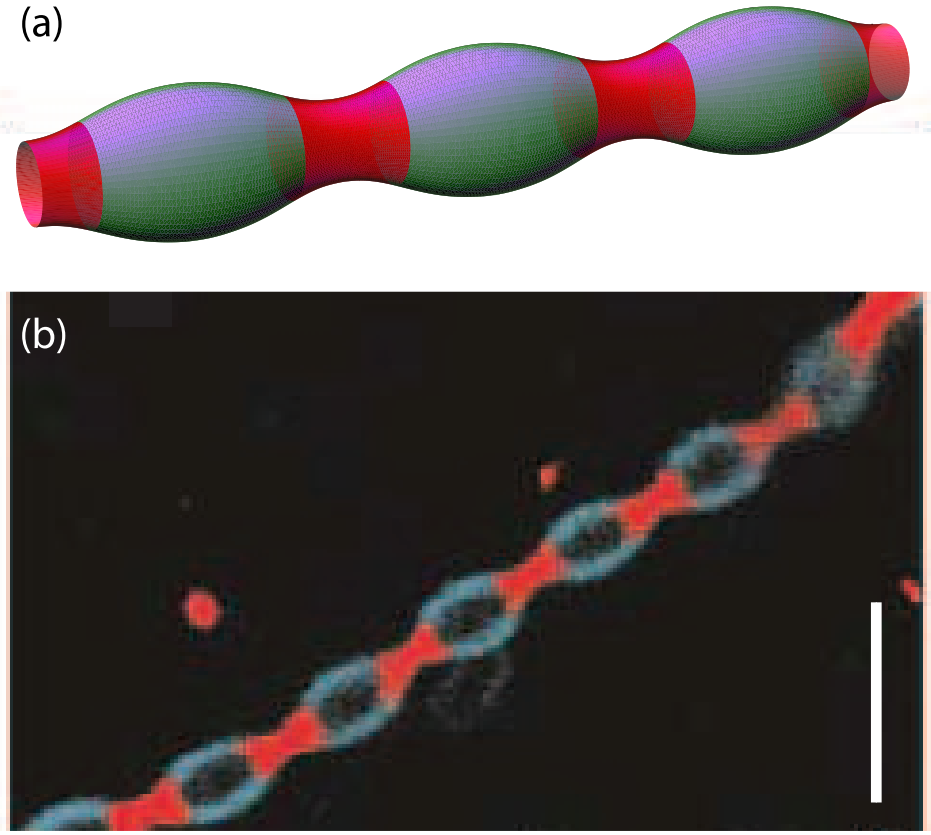

Figure 9.3 (a) Three-dimensional representation of the numerical tube, with the energetically selected wavelength. Blue (light) phase stands for the Lo-phase, and red (dark) phase for the Ld-phase. (b) the periodic multiphase tube, from Ref. [14]. Scale bar: 5 μm.

9.3.4 Comparison with experimental results

To treat a relevant example, we compare our analysis with the only experiment on periodic tubes we are aware of [14]. We choose the physical parameters given in Ref. [14] (see Fig. 9.3b). The ratio of the bending moduli is fixed to $\kappa_{\mathrm{Lo}}/\kappa_{\mathrm{Ld}} \simeq 1.25$, and the line tension $\tau \simeq 9 \times 10^{-13}$ N. The values of the Gaussian rigidities are hard to measure since the Gaussian elastic energy manifests itself only in topological changes for homogeneous membranes and as boundary contributions for inhomogeneous membranes (see Sec. 3.9). We use the values estimated in Ref. [232] of $\bar{\kappa}_i = -0.83\,\kappa_i$. The chemical composi-

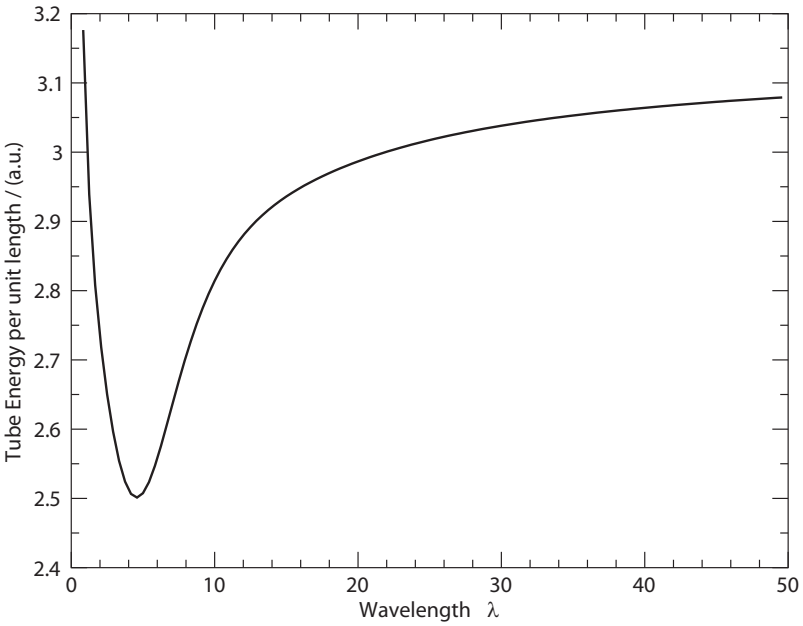

Figure 9.4 Tube energy per unit length as a function of the imposed wavelength in units of R_{Lo}

tion is set to keep the area ratio between both phases equal to $S_{\mathrm{Lo}}/S_{\mathrm{Ld}} = 1.5$. We perform different numerical integrations for different values of the wavelength of the periodic tube. In all these calculations, the wavelength value is an input, meaning that we can choose arbitrarily the domain size. In other words, solving the Euler-Lagrange Eq. (9.26) with the boundary conditions does not allow to find the wavelength, a situation which is commonly found in pattern formation such as rolls in Rayleigh-Bénard convection [46] or cells in directional solidification [16].

Since the wavelength can be chosen freely a priori, the wavelength selection for the periodic tube may result from energy minimization. Fixing the surface ratio of both phases to the chemical composition, we calculate the energy per unit length incorporating in Eq. (9.1) the numerical solutions given by the Euler-Lagrange equation (9.26). The plot of this energy density versus the domain size is presented in Fig. 9.4. The energy minimum corresponds to $\lambda = 4.4$ (in units of R_{Lo}), the experimental value [14] being $\lambda \sim 5$ in the same units. We can estimate that the results are in agreement since the determination of the experimental wavelength, not indicated by the experimentalists, is imprecise. Moreover, since tube formation occurs at a temperature close to the critical mixing temperature, one can expect some uncertainty on the value of the line tension, which vanishes at the critical temperature. Not surpris-

ingly, for a variational treatment, Fig. 9.4 shows that the competition between elastic and capillary energies occurs for a wavelength of the order of the tube radius, short and very large wavelength compared to this length scale being eliminated. Recall that long wavelengths correspond to a half-infinite tube, not selected for the parameters in Ref. [14].

9.3.5 Periodic tubes *vs*. two-phase separation

Imposing the bending rigidities and line tension as indicated previously, one can vary the composition value and calculate the selected wavelength. By changing the $S_{\mathrm{Lo}}/S_{\mathrm{Ld}}$ ratio, we can explore if a periodic tube is preferred to two half-infinite tubes. In Fig. 9.5 we plot the inverse of the size of the Ld-domain with respect to the area fraction. We can see there that for high enough composition difference, there is no finite wavelength selection, and the tube is completely phase-separated into two phases separated by a unique junction.

9.4 Conclusions

In this Chapter, periodic membrane tubes have been found numerically for arbitrary wavelength once the physical parameters like the chemical composition, the elastic rigidities and the line tension are fixed. We show that periodic tubes are preferred to a complete phase separation as soon as the chemical composition does not favor too much one phase, for a realistic set of physical constants. It means that the periodicity allows a decrease of the elastic energy which compensates the increase of capillary energy. The agreement between the only reported experiment and the numerics confirms the validity of the model for tubular structures and the accuracy of the physical constants.

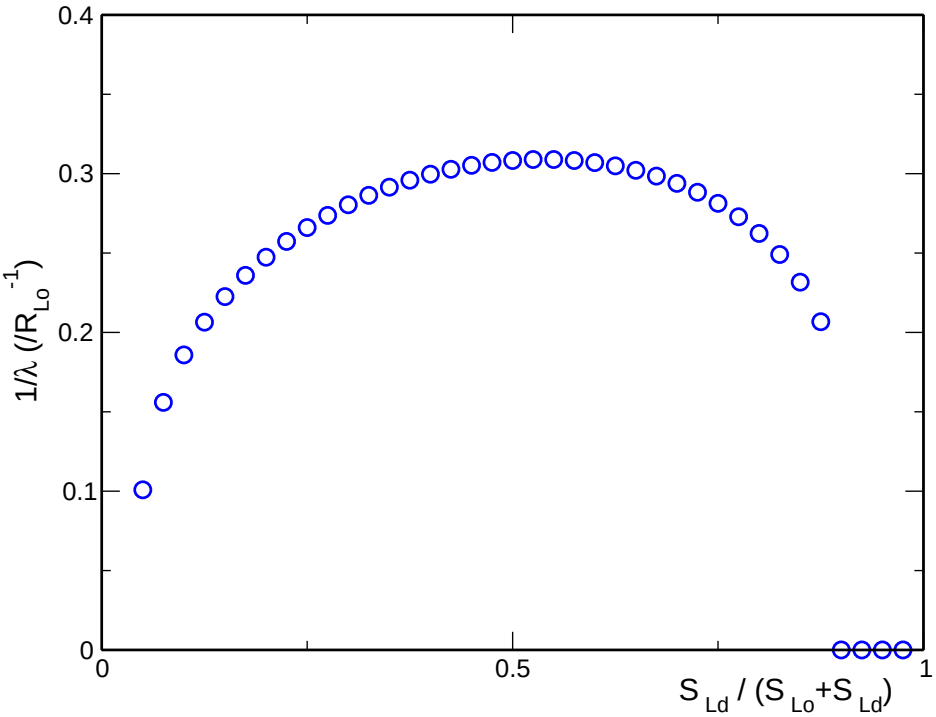

Figure 9.5 Plot of the inverse of the selected wavelength as a function of the normalized chemical ratio. For extreme chemical ratios, semi-infinite tubes are preferred.

10
Starfish shapes in monolayer lipid domains

10.1
Introduction

Monolayer lipid domains [160] are model systems for understanding the intermolecular interactions between lipids or proteins found in cell membranes. The competition between dipole-dipole interaction between lipid molecules and line tension leads to the formation of non-circular lipid domains, like starfish shapes. A deep comprehension of domain shapes in monolayers is a crucial step in order to seek for the stability and functionality of the so-called lipid rafts [234], cholesterol-enriched lipid domains found in *in vitro* experiments on multicomponent bilayer vesicles [67], and thought to be used as platforms for virus assembly in host cells [47].

Biological membranes are made of two opposed coupled lipid monolayers with proteins and other macromolecules anchored on them (see Ch. 2). Lipid monolayers can be studied at the air-water interface, behaving as an almost two-dimensional planar system. Hence, they become useful models for understanding not only the intermolecular interactions between different membrane components, but also the physics of two-dimensional systems [160].

As we explained in Sec. 2.3, the phase behavior of lipid monolayers depend on different factors. Lipid composition, surface pressure, and temperature are some of the most relevant among them. The addition of surfactant proteins, like the pulmonary surfactant protein B, has been shown to play a role in the micro- and nanostructure of phospholipid films [54]. In certain circumstances, both microdomains and nanodomains of ordered lipid phases bloom from the liquid expanded phase –the most common phase of actual biomembranes–, when the monolayer is compressed up to surface pressures in the plateau of the pressure–area isotherm [160].

These domains present a high diversity of forms, ranging from circular and elliptic domains, to starfish- and kidney-like shapes [54,131,152]. Understanding how these shapes are formed by the action of intermolecular interactions is of a conceptual importance for many different physico-chemical and biophys-

ical aspects. In addition, it is the comprehension of such fundamental issues which might lead to biomedical developments, as for instance the improvement of the treatment for neonatal respiratory distress syndrome, caused by a congenital lack of surfactant protein B [51, 186], which, as we mentioned above, alters the monolayer microstructure [54].

In order to understand the formation of such shapes, in this Chapter we study the monolayer domain model consisting of two opposing forces: a line tension between domains, and a long-range repulsive force due to dipole–dipole interaction [8, 131]. We use the approximation due to Iwamoto and Zhong-can [125] which maps the former model to a shape- and size-dependent line tension model with a bending term. This model can be dynamically studied within the framework of our bending phase-field model, derived in Ch. 5.

10.2 Theoretical treatment

The energy of monolayer lipid domains consists of, at least, two opposing forces. First, a line tension tends to minimize the interfacial length between the two phases. Second, as Andelman *et al.* proposed [8], long-range repulsive dipolar forces, either due to the presence of permanent dipoles in neutral monolayers, or being induced in charged monolayers, favor domain elongation. The total domain energy, F, can thus be split in an electrostatic term due to molecule polarization, F_{el}, and a line tension term, F_λ, as [131]

$$F = F_{\mathrm{el}} + F_\lambda = \frac{1}{2}\mu^2 \iint \left|\boldsymbol{r} - \boldsymbol{r}'\right|^{-3} \mathrm{d}A\mathrm{d}A' + \lambda \oint \mathrm{d}l, \tag{10.1}$$

where μ is the dipole density, $\boldsymbol{r}$ is the position vector within the domain, λ is the line tension, and $\mathrm{d}A$ and $\mathrm{d}A'$ are the area elements interior and exterior to the domains, respectively. The line tension term is shape independent, only depending on the domain length, while the electrostatic term is shape dependent. The total domain energy Eq. (10.1) is

$$F = -\frac{1}{2}\mu^2 \oint \oint \frac{\mathrm{d}\boldsymbol{l} \cdot \mathrm{d}\boldsymbol{l}'}{\left(|\boldsymbol{r}(l) - \boldsymbol{r}(l')|^2 + \delta^2\right)^{1/2}} + \lambda \oint \mathrm{d}l. \tag{10.2}$$

Iwamoto and Zhong-can [125] showed that –expanding the polarization energy term up to second order in a small parameter given approximately by the ratio between the dipole-dipole distance and the domain size– Eq. (10.2) has the approximate form

$$F = \alpha \oint \kappa^2 \mathrm{d}l + \tau \oint \mathrm{d}l, \tag{10.3}$$

where $\tau = \lambda - \frac{\mu^2}{2}\log(L/h)$ is an effective line tension, which can be either positive, negative, or zero; L is the boundary length; h is an effective cutoff of the order of the dipole-dipole separation distance [125,152]; and $\alpha = \frac{11}{96}\mu^2 L^2 \geq 0$ is an effective two-dimensional bending rigidity, since κ is the curvature. We have to note that although the actual line tension, λ, is always positive, the dipole-dipole interaction renormalizes it by introducing a μ-dependent term.

This last Eq. (10.3) is the two-dimensional analogous to the usual Canham-Helfrich bending energy for lipid vesicles [44,109], as it was already pointed out [125]. Here, we apply our phase-field model for bending energy [38,39,41] to study the morphology of two-dimensional lipid domains. We will thus be able to find the stationary domain shapes, as well as the dynamics of these processes. Expressing Eq. (10.3) as a function of a phase-field, $\phi(\boldsymbol{x})$ describing the phase within the monolayer [38],

$$\mathcal{F}[\phi] = \frac{3\sqrt{2}}{4\epsilon^3}\left[\alpha\int \Phi^2(\phi)\,\mathrm{d}A + \frac{\epsilon^2}{2}\tau\int\left(1-\phi^2\right)^2\mathrm{d}A\right], \tag{10.4}$$

where $\Phi(\phi) = -\phi + \phi^3 - \epsilon^2\nabla^2\phi$, and ϵ is a small parameter related to the interface width, whose limit $\epsilon \to 0$ corresponds to the macroscopic model Eq. (10.3) [38]. Besides, the length of the domain boundaries can be written, in terms of the phase-field, as $L = 3/(4\sqrt{2}\epsilon)\int(1-\phi^2)^2\mathrm{d}A$.

The time evolution of such a system is described by a conserved relaxational dynamic equation of the form $\frac{\partial\phi}{\partial t} = \nabla^2(\frac{\delta\mathcal{F}}{\delta\phi})$, which for the free energy functional Eq. (10.4) reads

$$\frac{\partial\phi}{\partial t} = \frac{3\sqrt{2}}{2\epsilon^3}\boldsymbol{\nabla}^2\Big\{\alpha\left[(3\phi^2-1)\Phi[\phi] - \epsilon^2\boldsymbol{\nabla}^2\Phi[\phi]\right] - \epsilon^2\tau\phi\left(1-\phi^2\right)\Big\}, \tag{10.5}$$

where, in turn, α and τ depend on a global shape property, its boundary length, L.

10.3 Results and discussion

Our problem is then reduced to numerically solve Eq. (10.5) with the appropriate initial and boundary conditions, taking into account that $\alpha = \alpha(t)$ and $\tau = \tau(t)$, since the domain boundary length, $L(t)$, changes in time. We used a standard finite-difference scheme for the spatial discretization and an Euler method for the time-derivatives [38]. In all the results here shown we used the value of the small parameter, ϵ, equal to the mesh size of the lattice. The results are robust under variations of this parameter. Both the time and space discretizations are chosen in order to satisfy the Courant-Friedrichs-Lewy stability criterion [19]. Besides, the cutoff length h is chosen to be equal to the mesh size, which in turn is of the order of the size of a lipid molecule.

The stationary domain shapes only depend on the dimensionless ratio of the lines tension to the squared dipole density, $\Lambda = \lambda/\mu^2 \geq 0$. For different values of this parameter, and starting with different initial shapes, it is possible to systematically explore this parameter space. In Figs. 10.1, 10.2 and 10.3, we present some of these shapes, and compare them with experimentally observed domain patterns.

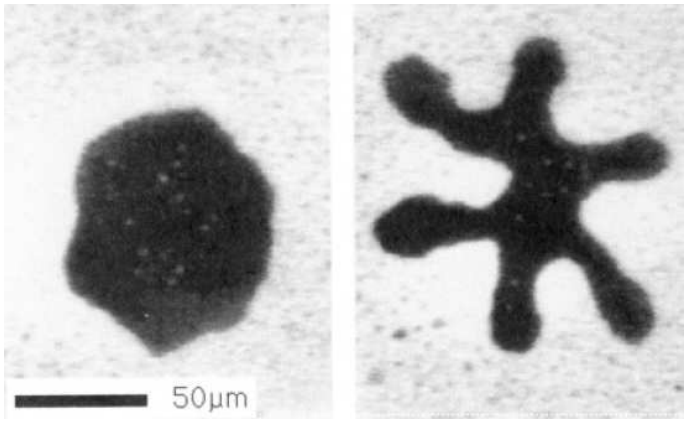

(a) Experimental figures from Ref. [152]

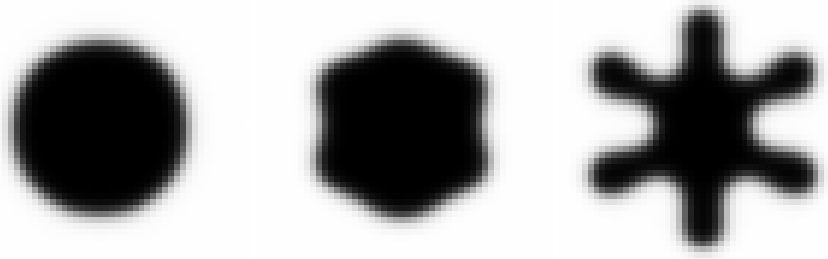

(b) initial condition (c) $3.6 \times 10^4 \Delta t$ (d) $7.2 \times 10^4 \Delta t$

Figure 10.1 Starfish domain shapes. (a) Experimental figures from Ref. [152], showing the shape transition from an initial circular domain (not shown) to a starfish shape (right), through a quasi-hexagon intermediate (left), in a lipid monolayer composed by a binary mixture of DMPC and dihydrocholesterol. (b-d) Three snapshots of the numerical integration of the phase-field dynamic equation Eq. (10.5), where an initially instable circular domain evolves into a starfish shape. This integration corresponds to a normalized negative effective line tension $\tau/\mu^2 = -50$. $\Delta t = 10^{-3}$.

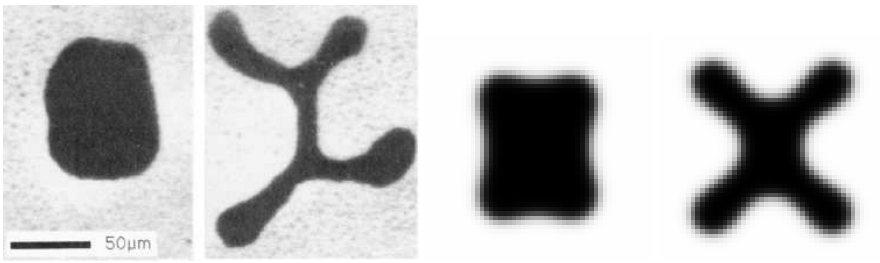

(a) Experimental figures from Ref. [152]

(b) $10^4 \Delta t$

(c) $2 \times 10^4 \Delta t$

Figure 10.2 Four-fold domain shapes. (a) Experimental figures from Ref. [152], showing the shape transition from an initial almost circular domain (left) to a shape with four branched arms (right), in a lipid monolayer composed by a binary mixture of DMPC and dihydrocholesterol. (b,c) Two snapshots of the numerical integration of the phase-field dynamic equation Eq. (10.5), where an initially instable elongated domain (not shown) evolves into a shape with a four-fold symmetry, through an intermediate shown in (b). This integration corresponds to a normalized negative effective line tension $\tau/\mu^2 = -20$. $\Delta t = 10^{-3}$.

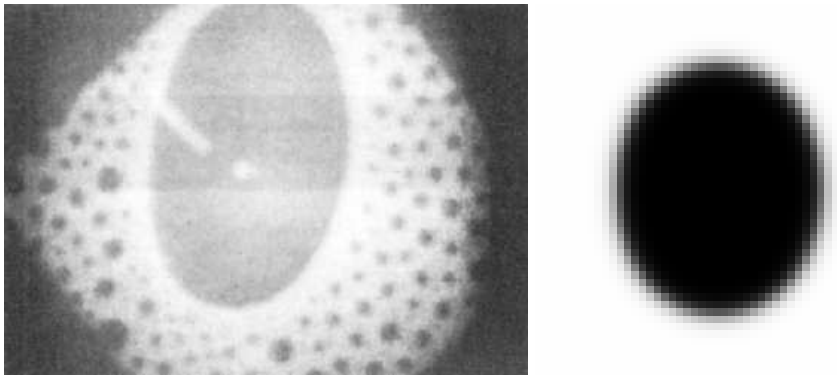

(a) Experimental figures from Ref. [131]

(b) Phase-field numerical integration

Figure 10.3 Elliptic domain shapes. Comparison between experimental observations (a) and a numerical integration of the phase-field model Eq. (10.5) (b). The normalized effective line tension vanishes in this integration, $\tau/\mu^2 = 0$.

10.4 Discussion and conclusions

Even when we did not performed a systematic exploration of the parameter space, the presented results clearly show that the competition between line

tension and polarization explains non-circular shapes found in lipid monolayer domains. Actually, our model is based on the Iwamoto approximation, which maps the line tension-polarization model into a two-dimensional curvature model with an effective line tension between domains. The fact that this effective line tension can either be positive or negative explains that during the dynamics the interface length may increase.

Again, it will be interesting to understand how chirality appears in domain shapes, as shown in, e.g., [170], and if, within this model, we can explain the effect of pulmonary surfactant protein B on the domain shape [54].

Part III On membrane curvature generation by proteins

11
Introduction

In the first Part of this thesis, we saw how to deal with membrane curvature models, in the framework of the Canham-Helfrich theory. The concept of spontaneous curvature was introduced, and afterwards, in Chs. 7 and 8, we applied it to study morphological instabilities and membrane shape dynamics in lipid vesicles with anchored polymers. We assumed that those polymers anchor some hydrophobic groups in the bilayer, mimicking integral monotopic proteins (see Sec. 2.1.2). However, we disregarded the way those anchor groups generate membrane curvature, and on which physical factors this curvature depends.

In this third Part of the thesis we address this question, that is, which are the mechanisms of membrane curvature generation in biological membranes, and how they work. In this introductory Chapter, we review the general mechanisms thought to date to be biologically relevant in such a process of both generation and stabilization of membrane curvature [79, 171, 263]. In particular, in Ch. 12, we quantitatively study one of these mechanisms, the hydrophobic insertion mechanism of membrane curvature by proteins. Then, in the last Chapter of this Part, the concept of curvature sensing by proteins is introduced and analyzed as opposed to curvature generation.

11.1
Mechanisms of membrane curvature generation

Most cellular membranes have regions of very high curvature yet lipid bilayers resist bending [109]. Therefore, active production of membrane curvature is one of the major challenges faced by a cell in the course of formation of its internal organelles and generation of membrane transport containers [3]. How proteins can produce and stabilize the enormous range of membrane curvatures that exist *in vivo* is beginning to be understood.

So far, we have seen that lipid bilayers composed by two equal monolayers, want to be locally flat, in order to minimize their energy. However, a flat bilayer would have some free edges which are energetically unfavorable. Then, lipid bilayers wrap themselves to form closed vesicles. In this process of vesi-

cle formation, curvature has been generated. The stationary vesicle shape will be according with the corresponding energy minimization together with the accomplishment of some geometric constraints (see Sec. 3.5.4).

Besides, in cells, different mechanisms of membrane curvature generation or stabilization have to exist, in order to create the broad range of trafficking intermediates, like membrane tubes and vesicles, to mention some. These mechanisms can be divided in five major groups [171]: due to lipid composition, transmembrane proteins, cytoskeleton activity, the scaffolding mechanism, or the hydrophobic insertion mechanism, as we will see in the following Sections.

11.1.1 By lipid composition

In actual biological membranes, the two leaflets of the bilayer are not symmetric at all, but differ in composition. For instance, phospholipids like phosphatidylserine (PS) are almost uniquely kept in the inner leaflet of cell membranes by a translocase enzyme. Flippase enzymes transfer phospholipid molecules from one leaflet of the bilayer to the other in a process called flip-flop or transverse diffusion. Although this diffusion is much slower than lateral diffusion, flippases may create membrane asymmetry [66,120,199].

Thus, the presence of lipids with large headgroups (thus with a positive spontaneous curvature) in one leaflet, but not in the other, induce curvature towards the former. Similarly, lipids with wide acyl chains, that is, with negative spontaneous curvature per lipid, also induce bilayer curvature when present mainly in one of the bilayer leaflets (see Fig. 11.1a). In Tab. 11.1, reproduced from Ref. [263], we present some experimentally measured effective spontaneous curvature for different lipids.

Table 11.1 Effective spontaneous curvature, J_s, for different membrane lipids. From Ref. [263] (see references therein).

Lipid	$J_s(\mathrm{nm}^{-1})$
Lysophosphatidic acid (LPA)	0.5
Lysophosphatidylcholine (LPC)	0.15 to 0.26
Dioleoylphosphatidylserine (DOPS)	0.07
Lysophosphatidylethanolamine (LPE)	< 0.025
Dioleoylphosphatidylcholine (DOPC)	-0.05 to -0.11
Phosphatidic acid (PA)	-0.22
Cholesterol	-0.34 to -0.43
Dioleoylphosphatidylethanolamine (DOPE)	-0.5
Dicaprylglycerol (DCG)	-0.77
Diacylglycerol (DAG)	-1

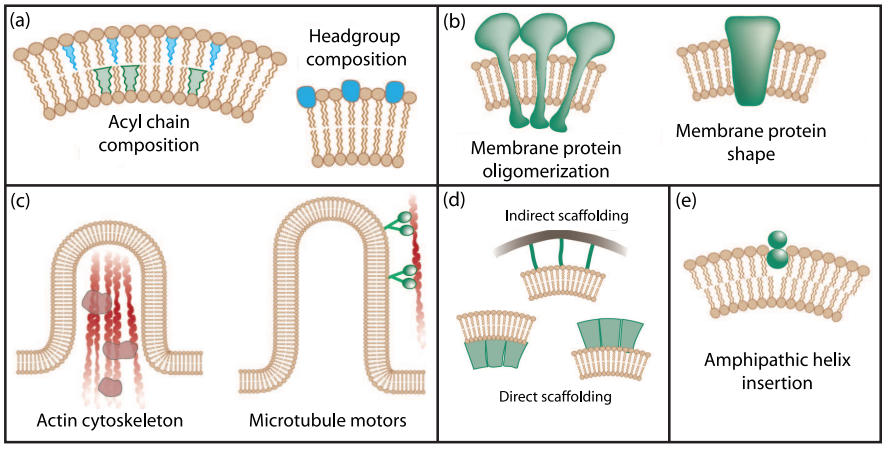

Figure 11.1 Mechanisms of membrane curvature generation. (a) By lipid composition, depending on the acyl chain or the headgroup compositions. (b) By transmembrane proteins, due to membrane protein oligomerization or shape. (c) By cytoskeleton activity, both due to the force done by actin polymerization and by microtubule-walking molecular motors. (d) By scaffolding mechanism, both direct or indirect. (e) By hydrophobic insertion mechanism, induced by the insertion of amphipathic helices. Figure modified from Ref. [171].

11.1.2 By transmembrane proteins

Transmembrane proteins spanning through the entire bilayer might induce membrane curvature in different ways. First, due to their shape, since some of these proteins have a net conical or funnel shape (see Fig. 11.1b, right). Even if the transmembrane domains of these proteins cannot induce curvature because of their geometry, it is possible that protein oligomerization still generates a bending deformation in the membrane if the protein domains which remain at each side out of the bilayer are asymmetric (see Fig. 11.1b, left). Some ion channels, for instance, seem to induce membrane curvature in such a way [162]. However, this field has not been yet extensively studied and it is poorly understood to date.

11.1.3 By cytoskeleton activity

The formation of cytoskeletal filaments affects the membrane shape because of its role in membrane remodelling and other trafficking events [119, 228]. Also, cell motility is in most cases due to the assembly and disassembly of cytoskeletal proteins [29]. Actin filaments, forming the cytoskeleton, are involved in such motility processes. They generate a force acting on the mem-

brane, which in turn reaccommodates its shape by bending itself if needed (Fig. 11.1c).

Besides, *in vitro* experiments showed that a small number of kinesins, molecular motor proteins, can pull tubular membranes out of a lipid vesicle [36, 151, 214, 215]. It is thus believed that such motor proteins are partly involved in the generation and maintenance of the shape of some tubulated and fenestrated cellular organelles, like Golgi or the endoplasmic reticulum.

11.1.4 By scaffolding mechanism

Different membrane proteins have curved domains which associate with the membrane by attaching to its surface like a scaffold. Protein coats that are known to cover the membrane surface in budding or endo- and exocytosis processes, like the COPI and COPII complexes, and the clathrin-adaptor-protein complex, are thought to provide membrane curvature using this scaffold mechanism. Scaffolding can either be direct or indirect (see Fig. 11.1d), depending on whether they bind directly to membrane lipids or this binding is mediated by other proteins.

BAR (Bin, amphiphysin, Rvs)-domain-containing proteins are involved in the formation of cylindrical membranes and vesicles. BAR domains are banana-shaped dimers which bind to lipid membranes through electrostatic interactions [264] between their concave shape and the membrane [195] (see Fig. 11.2).

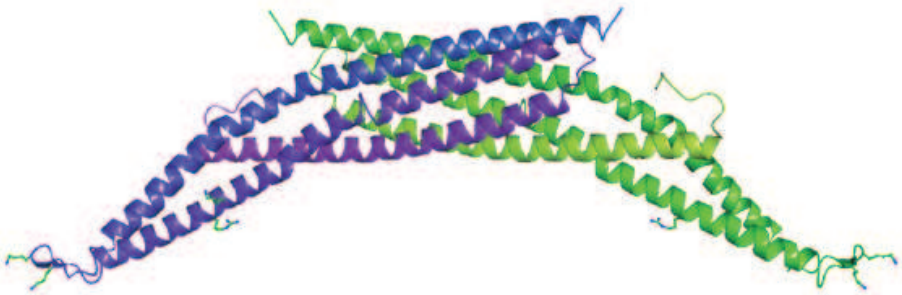

Figure 11.2 Amphiphisin BAR domain, formed by two dimers, and showing a crescent-like curved shape [195]. From H.T. McMahon's laboratory web page, `http://www.endocytosis.com`.

11.1.5 By hydrophobic insertion mechanism

We mentioned that lipid molecules might have an intrinsic non-zero spontaneous curvature. Then, if the bilayer is asymmetric, in the sense that the two

monolayers have different spontaneous curvatures, curvature is energetically favored. Proteins can also induce spontaneous curvature to the membrane by the insertion of amphipathic groups into the bilayer. Epsin is a protein involved in clathrin-mediated endocytosis [89]. It contains an ENTH (epsin N-terminal homology) domain, which in turn has an amphipathic helix that binds to membranes. These helices are generally small in size (of the order of half a lipid molecule), therefore upon membrane insertion, they might generate membrane curvature. In this Part of the thesis we quantitatively study this bending mechanism, and show that it is able to generate large membrane curvature as experimentally observed.

12
The hydrophobic insertion mechanism of membrane curvature generation by proteins

A wide spectrum of intracellular processes is dependent on the ability of cells to dynamically regulate membrane shape. Membrane bending by proteins is necessary for the generation of intracellular transport carriers and for the maintenance of otherwise intrinsically unstable regions of high membrane curvature in cell organelles. Understanding the mechanisms by which proteins curve membranes is therefore of primary importance. In this Chapter we suggest a quantitative mechanism of lipid membrane bending by hydrophobic or amphipathic rod-like inclusions which simulate amphipathic α-helices –structures shown to sculpt membranes. Considering the lipid monolayer matrix as an anisotropic elastic material, we compute the intra-membrane stresses and strains generated by the embedded inclusions, determine the resulting membrane shapes and the accumulated elastic energy. We characterize the ability of an inclusion to bend membranes by an effective spontaneous curvature, and show that shallow rod-like inclusions are more effective in membrane shaping than are lipids having a high propensity for curvature. Our computations provide experimentally testable predictions on the protein amounts needed to generate intracellular membrane shapes for various insertion depths and membrane thicknesses. We also predict that the ability of N-BAR domains to produce membrane tubules *in vivo* can be ascribed solely to insertion of their amphipathic helices.

12.1
Introduction

12.1.1
Biological motivation

Generation of high membrane curvature requires action of specialized membrane associated proteins [133, 171, 263]. These can either function as direct effectors by interactions with the membrane or as indirect scaffolds interacting with membranes via linking proteins [171]. The list of proteins and pro-

tein complexes shown to be crucial for strong bending of membranes is constantly expanding [9, 10, 30, 57, 79, 80, 89, 93, 94, 98, 102, 112, 154, 167, 195, 203, 231, 252]. Complexes of clathrin with accessory proteins [133, 219], and COPI and COPII coat-complexes [30,134,153] generate small vesicles. Narrow membrane tubules are produced by proteins of the dynamin family (see e.g. [115, 173, 203, 216, 227]), BAR domain-containing proteins [79, 80, 93, 94, 98, 112, 195], epsins [89], EHD-family proteins [57], C2 domain-containing proteins, such as synaptotagmins [167], and proteins of the reticulon and DP1/Yop1 families [231, 252].

Quantitative elaboration of the physical mechanisms by which proteins bend membranes is indispensable for classification of the rapidly accumulating phenomenology on the effects of proteins on membrane curvature and the understanding of the relationships between the structure of a protein and its efficiency in membrane shaping. It was suggested that proteins can generate the membrane curvature either by embedding small hydrophobic or amphipathic regions into the membrane matrix (see for reviews [171, 263]) or by attaching the membrane surface to the intrinsically curved protein scaffolds by virtue of cognate charge interactions [23, 171].

A common realization of the former mode of membrane bending referred to as the hydrophobic insertion mechanism is through a shallow embedding of amphipathic helices into the upper part of a lipid monolayer. Epsins were the first proteins shown to induce membrane curvature by amphipathic helix insertion [89]. On interaction with phosphatidylinositol-4,5-biphosphate polar groups amphipathic α-helices fold and embed into the lipid monolayer matrix, transforming the flat membrane into tubules of 20 nm diameter [89]. Small G-proteins Arf1 and Sar1 expose amphipathic α-helices upon exchange of GDP to GTP, which results in the anchoring of such proteins to lipid bilayers and the subsequent bilayer bending [10, 102, 154]. Amphipathic helices of N-BAR domains of amphiphysin and endophilin bind peripherally in the bilayer resulting in the midpoint of the helix insertion being aligned with the phosphate level of the lipid headgroups. This insertion is essential for generation of membrane tubules of $35 - 50$ nm diameter which get converted into vesicles of the same diameter at increased amounts of the protein [98, 195]. The C2A and C2B domains of synaptotagmin-1 interact in Ca^{2+}-dependent manner with the polar groups of negatively charged phospholipids and insert hydrophobic loops into the lipid monolayers at a depth of up to third of the monolayer thickness [114] resulting in the formation of narrow membrane tubes of ~ 17 nm diameter [167].

A number of proteins have the potential to scaffold membranes into curved shapes. These include dynamin family proteins [173, 236], BAR superfamily proteins [93,112,171], EHD2 [57], the clathrin coat [90] and COPI/IIcoats [153]. Notably, scaffolding proteins can contain hydrophobic and/or amphipathic

fragments able to penetrate the membrane to a certain depth, thus contributing to the membrane curvature generation. For example, while dynamin forms a helical oligomer capable of scaffolding high curvature, the variable loops of its PH domain are suggested to interact with the membrane and the VL1 loop is proposed to insert into the membrane [32, 174, 205, 260]. The efficiency of membrane bending by N-BAR domains depends crucially on the integrity of their amphipathic helices [98, 171]. COPI, COPII, and some clathrin adaptors, are recruited to the membrane by small G-proteins (Arf1p for AP1 and COPI, and Sar1p for COPII), which couple their respective scaffolding apparatuses to the potential to bend membranes by insertion of the amphipathic α-helices [172]. The reticulons and DP1/Yop1 family proteins possess two long hydrophobic hairpin segments which could induce membrane curvature changes by forming a wedge that occupies more space in the upper than the lower leaflet of a lipid bilayer [252].

Hence, it is becoming clear that the majority of membrane bending proteins may employ membrane insertion of hydrophobic or amphipathic regions with, in some cases, a coupling to scaffolding domains.

In this Chapter, we suggest and analyze quantitatively a mechanism by which the amphipathic and hydrophobic insertions bend membranes into tubular shapes with diameters of a few tens of nanometers [42]. The analysis is based on a physical model of lipid monolayers. Our computations show that membrane insertions like amphipathic α-helices are more powerful in membrane bending than use of non-bilayer lipids, and that biologically relevant numbers of such insertions are sufficient to create even the extreme membrane curvatures of intracellular organelles and transport intermediates. Our analysis also considers the role of lipid monolayer coupling in curvature generation and demonstrates that shallow insertions are best suited to the production of high membrane curvature. We draw the experimentally testable predictions on the dependence of the membrane curvature on the bilayer thickness and the membrane area fraction occupied by the amphipathic helices.

12.1.2 Qualitative essence of membrane bending by hydrophobic inclusions

We consider an initially flat lipid membrane with rod-like inclusions inserted into its interior (Fig. 12.1). To grasp the major features of the mechanism of membrane bending by inclusions, we address here a simple case of two-dimensional deformations, meaning that the membrane adopts a form of a tube with rod-like inclusions ordered in rows along the tubular axis. The membrane shape is then characterized by the form of the tube cross-section. The diameter of the inclusion rod is assumed to be 1 nm, which is typical

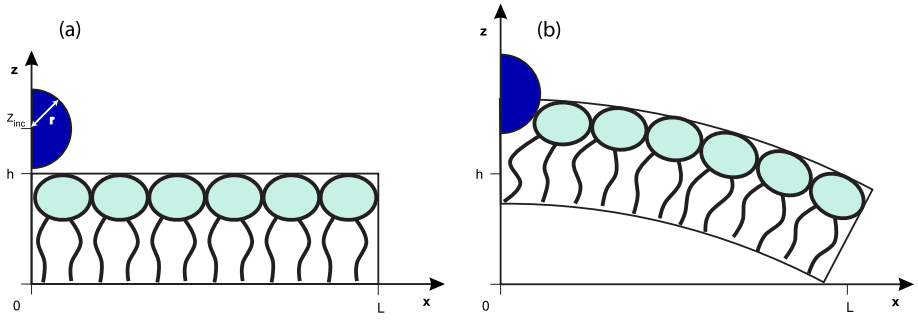

Figure 12.1 Schematic representation of lipid monolayer bending (lipid molecules shown in light blue) by insertion of a cylindrical inclusion (shown in dark blue), whereLis the half distance between the inclusions, h is the monolayer thickness, and is the inclusion radius. (a) The monolayer is flat before the inclusion insertion; (b) the monolayer bends as a result of inclusion insertion.

for an amphipathic α-helix with side chains; the lipid monolayer thickness is taken to be 2 nm.

The inclusion pushes aside the elements of the membrane matrix and produces, in this way, the intra-membrane strains and stresses leading to the accumulation of elastic energy. The curving of the membrane from the initial flat configuration results in the partial relaxation of these stresses and minimizes the elastic energy. While being a part of a peripheral membrane protein, an amphipathic-helix has a shallow membrane matrix penetration possibility. However, for generality and a broader understanding of the physics of membrane bending by small inclusions, we consider the effects of different modes of insertion including those where the inclusions reach the bilayer mid plane. The cases of deep insertions can account for membrane bending by isolated hydrophobic inclusions such as synthetic peptides mimicking fusion peptides. An inclusion inserted into one membrane monolayer results in curving of the whole bilayer. The extent of the bilayer bending depends on the way the monolayers are coupled to each other. There are two kinds of such coupling (Fig. 12.2). Due to their mutual attachment along the common hydrophobic interface the monolayers are always coupled in the transverse direction (perpendicular to the membrane plane). In addition, there may be monolayer coupling in the in-plane direction meaning that the areas of the two monolayers can not change independently [65].

In most of the biologically relevant circumstances the inclusions are inserted only into small fragments of a large membrane such as the membrane regions destined for conversion into intracellular membrane carriers (Fig. 12.2a). The two monolayers of such a fragment can, independently of each other, exchange their areas with the rest of the membrane, the latter providing a large reservoir of lipids (Fig. 12.2a). Due to the free and independent exchange

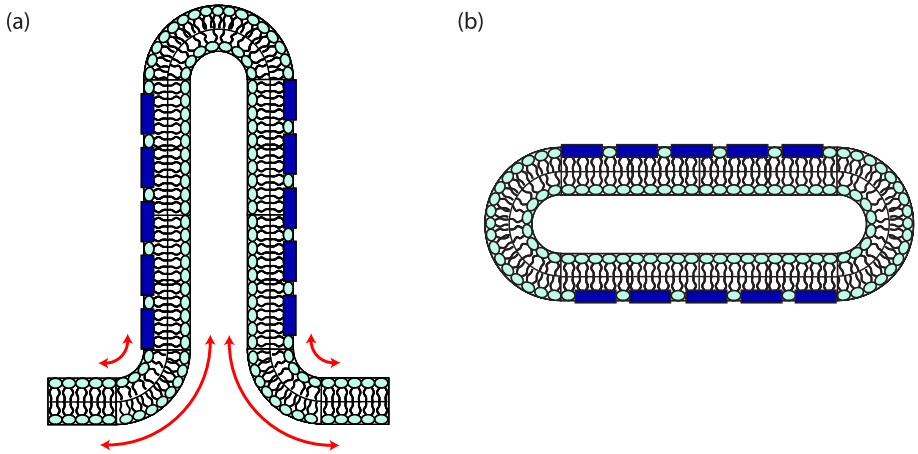

Figure 12.2 Different cases of monolayer coupling within a bilayer. (a) Laterally uncoupled monolayers. The inclusions (rectangles) are inserted only into a small fragment of a large membrane. The two monolayers of the fragment can independently exchange lipids with the monolayers of the surrounding membrane which plays a role of lipid reservoir (the exchange is indicated by the arrows). (b) Laterally coupled monolayers. The inclusions are inserted across the whole area of a closed membrane. The effects of slow trans-monolayer flip-flop of lipids are neglected.

of lipid between the reservoir and each of the monolayers of the membrane fragment in question, there is no in-plane coupling between the latter. The in-plane coupling comes into play if the inclusions are inserted across the whole area of a closed membrane. This happens, for example, in *in vitro* experiments where proteins are added to liposomes and embed without spatial restriction everywhere across the entire surfaces of the lipid membranes (Fig. 12.2b). In this case, there is no reservoir for the monolayer area exchange, and, provided that the effects of slow flip-flop of lipid molecules between the monolayers can be neglected, the expansion of one monolayer cannot proceed independently of deformation of the second monolayer.

Membrane monolayers subject to the transverse coupling only, will be referred to as the laterally uncoupled monolayers. In cases where there exists also in-plane coupling, the monolayers will be called laterally coupled. While *in vitro* experiments on liposome membrane curvature may not therefore closely mimic the *in vivo* situation, the potential for lateral monolayer coupling at the plasma membrane exists and may be provided by, for example, actin based corrals, which would limit lipid exchange with endocytic sites. For completeness we model both possibilities.

Consider first the case of laterally coupled monolayers. A shallow insertion of inclusions into the upper monolayer expands its upper part, while the rest of this monolayer underneath the inclusions and the lower monolayer resist this expansion. To minimize the generated stresses that are asym-

metrically distributed through the bilayer depth, the membrane must bulge towards the upper monolayer (Fig. 12.3a). According to a common convention, curvature resulting from bulging in this direction is defined as positive. A somewhat deeper insertion up to the middle of the upper monolayer expands this monolayer (Fig. 12.3b). Because of the lateral coupling between the monolayers, this expansion is opposed by the lower monolayer. According to the monolayer area asymmetry model [65], this leads to further generation of asymmetric stresses within the membrane and a positive membrane curvature (Fig. 12.3b). If the inclusion penetrates deeper into the membrane and reaches its mid plane, the strains and stresses are distributed symmetrically within the bilayer (Fig. 12.3c), so that bending in either direction will not relax the elastic energy. Such insertion does not induce membrane bending but results in the overall expansion of the membrane area (Fig. 12.3c). An even deeper inclusion insertion expands the lower membrane part with respect to its upper part, which results in bending towards the lower monolayer and, hence, generation of a negative curvature (Fig. 12.3d).

In the case of laterally uncoupled monolayers with inclusion inserted in the upper leaflet of the membrane, a qualitative consideration similar to the above one has to be applied to the upper monolayer only. Due to the transverse coupling between the monolayers, bending of the upper monolayer will result in bending also of the lower one, and, hence, of the whole membrane. Therefore, similarly to the above case of coupled monolayers, shallow insertions generating asymmetric strains in the upper monolayer produce a positive curvature of the latter and of the whole membrane (Fig. 12.4a). However, a bare expansion of the upper monolayer by an inclusion reaching its middle (Fig. 12.4b) will not result in the membrane bending since the upper monolayer can expand independently of the lower one due to the lipid exchange with the reservoir. As a result, for this depth of the inclusion insertion the membrane will be flat (Fig. 12.4b). This is different from the above case of coupled monolayers, in which insertion up to the middle of the upper monolayer resulted in the membrane curvature (Fig. 12.3b). Penetration of an inclusion into the lower part of the upper monolayer generates its negative curvature, and, hence, a negative curvature of the whole membrane (Fig. 12.4c).

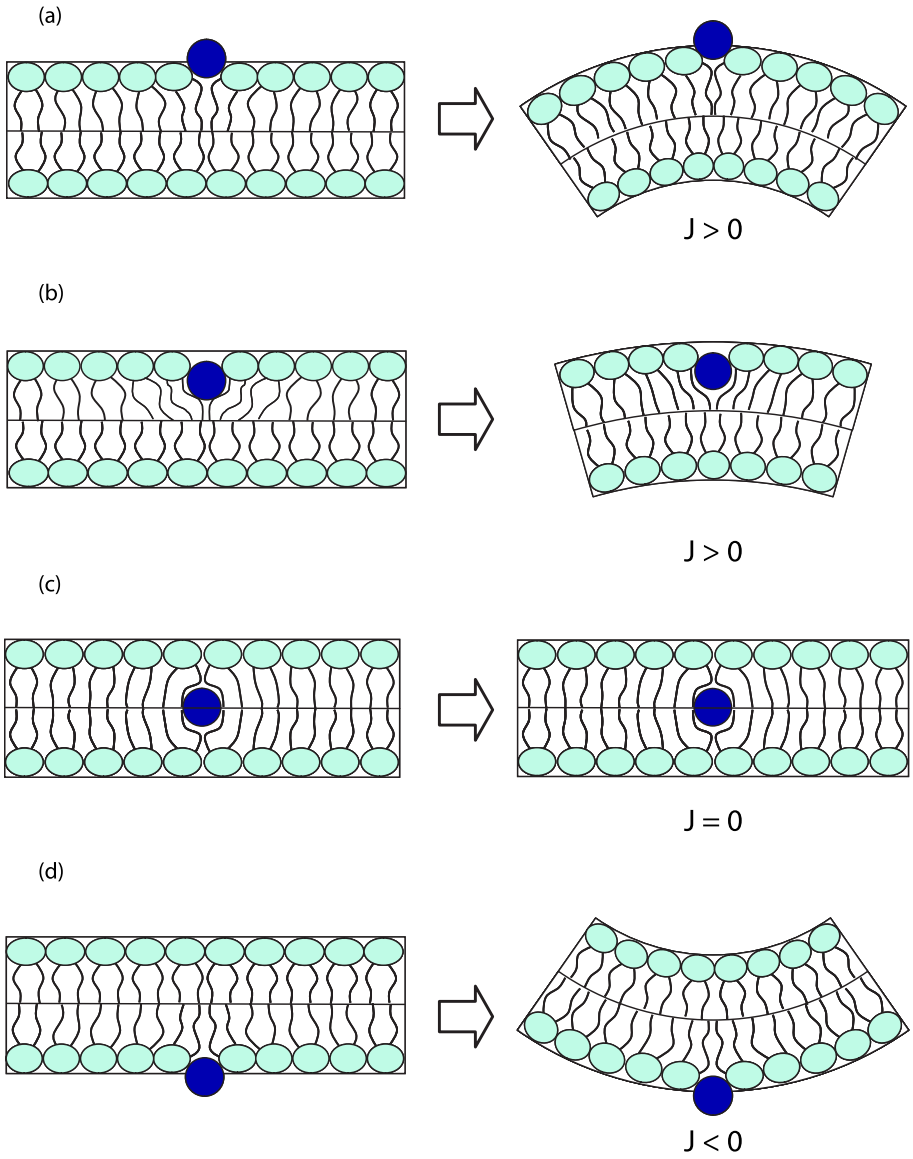

Figure 12.3 Qualitative essence of the mechanism of membrane bending by small cylindrical inclusions. The case of laterally coupled monolayers. (a) A shallow inclusion insertion expands the upper layer of the membrane (left). Partial relaxation of the generated stresses results in positive curvature ($J > 0$) (right). (b) Deeper insertion produces an expansion of the upper monolayer (left), which due to the lateral coupling generates stresses in the lower monolayer leading to positive membrane curvature (right). (c) Insertion in the bilayer mid plane generates symmetrically distributed stresses, causing an overall membrane expansion but no curvature. (d) Insertion into the lower monolayer expands the lower part of the membrane, hence generating negative curvature ($J < 0$).

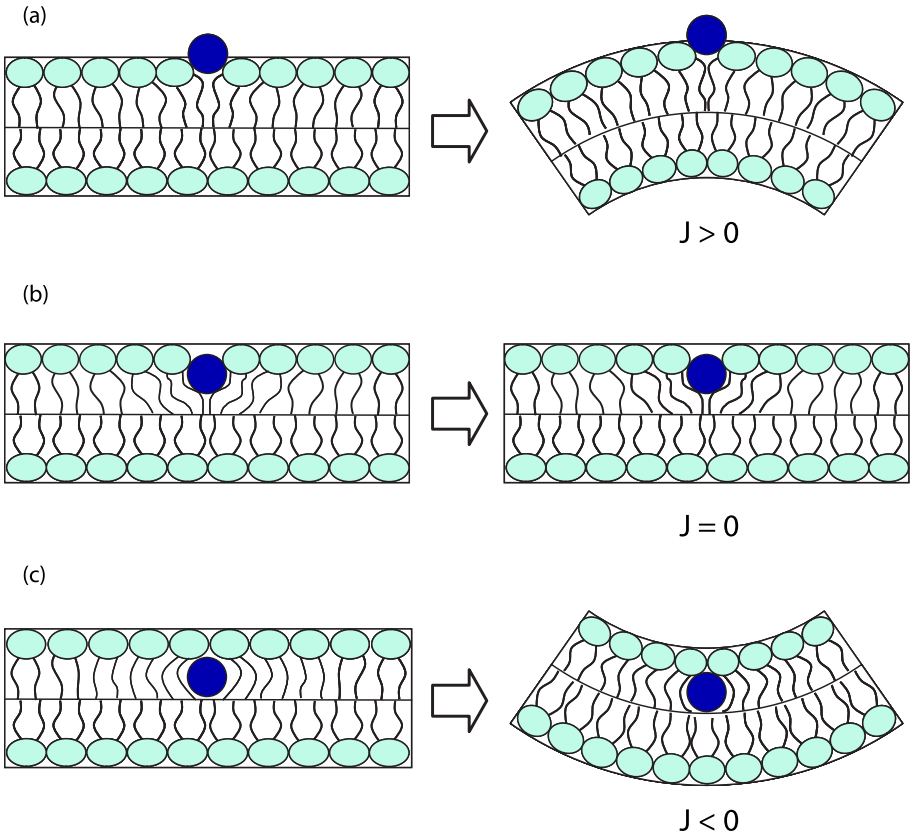

Figure 12.4 Qualitative essence of the mechanism of membrane bending by small cylindrical inclusions. The case of laterally uncoupled monolayers. (a) A shallow inclusion insertion expands the upper part of the upper monolayer (left), which generates a positive curvature of the upper monolayer leading to positive curvature of the whole membrane ($J > 0$) (right). (b) Deeper insertion produces a bare expansion of the upper monolayer, which, due to the monolayer uncoupling, does not generate curvature. (c) Insertions in the lower portion of the upper monolayer (left) induces negative membrane curvature ($J < 0$).

12.2 Model

12.2.1 Elastic model of a lipid monolayer

A large literature exists on modeling membrane deformations by proteins spanning the whole lipid bilayer and generating small membrane curvatures [11, 50, 81, 91, 144]. These studies employ the Helfrich model of bending elasticity considering a membrane as an elastic surface (see Ch. 3) [109]. Here we

can not use this common description since the cross-section of an inclusion in question is smaller than the lipid monolayer thickness and we are interested in the intra-membrane deformations for different depths of the inclusion insertion generating large curvatures. Therefore, we consider a lipid monolayer as a three-dimensional layer with finite thickness and bulk elastic properties. To describe the system, we use the standard theory of elasticity of an anisotropic three-dimensional medium (see Appendix C) [146]. The volume density of the elastic energy is determined by

$$f = \sigma^0_{ik} u_{ik} + \frac{1}{2} \lambda_{iklm} u_{ik} u_{lm}, \tag{12.1}$$

where σ^0_{ik} is the tensor of the initial intramonolayer stresses existing before the inclusion insertion; λ_{iklm} is the tensor of the elastic moduli of the monolayer interior; and u_{ik} is the strain tensor related to the displacement vector of the monolayer elements by

$$u_{ik} = \frac{1}{2} \left(\frac{\partial u_i}{\partial \xi^k} + \frac{\partial u_k}{\partial \xi^i} \right), \tag{12.2}$$

ξ^j, being the coordinates [146].

Since we consider only the tubulelike shapes of membranes, we choose the Cartesian system of coordinates, with the x, y axes lying in the initial membrane plane, the y axis directed along the tube axis, and x axis lying in the tube cross-section originating $(x = 0)$ in the middle of inclusion (Fig. 12.1). The z axis points towards the hydrophilic heads and originates $(z = 0)$ at the bottom surface of the monolayer. The position of the inclusion will be characterized by the coordinate of its center, z_{inc}.

The contribution to the elastic energy of an arbitrary anisotropic medium Eq. (12.1) depending on the elastic moduli can be simplified for the lipid monolayer, which has properties of an isotropic liquid in the lateral (x, y) direction. In this case, the energy Eq. (12.1) must be invariant with respect to rotations around the z direction perpendicular to the x, y plane, or, using cylindrical coordinates $\{r, \phi, z\}$, this condition is that there is no ϕ-dependence of the free energy. We define new variables, $\{\xi, \eta\}$, as

$$\begin{aligned} \xi &= x + i\, y, \\ \eta &= x - i\, y. \end{aligned} \tag{12.3}$$

Rotating the full system an angle ϕ around the z axis, these variable change according to

$$\begin{aligned} \xi &\to \xi^{(\phi)} \equiv \mathrm{e}^{i\,\phi}\, \xi, \\ \eta &\to \eta^{(\phi)} \equiv \mathrm{e}^{-i\,\phi}\, \eta, \end{aligned} \tag{12.4}$$

and, since the free energy should remain invariant under this rotation, we have that

$$f = \frac{1}{2}\,\lambda_{iklm}\,u_{ik}^{(\phi)}\,u_{lm}^{(\phi)}. \tag{12.5}$$

The only non vanishing components of the elastic modulus tensor are those which contain the same number of indexes ξ and η, in order to have no angular dependence. These components are $\lambda_{zzzz}, \lambda_{\xi\xi\eta\eta}, \lambda_{\xi\eta\xi\eta}, \lambda_{\xi\eta zz}, \lambda_{\xi z\eta z}$. Then, taking into account multiple counting in the summation in Eq. (12.1),

$$\begin{aligned} f = {} & \frac{1}{2}\,\lambda_{zzzz}u_{zz}^2 + \lambda_{\xi\xi\eta\eta}u_{\xi\xi}\,u_{\eta\eta} + 2\lambda_{\xi\eta\xi\eta}u_{\xi\eta}^2 \\ & + 2\lambda_{\xi\eta zz}u_{\xi\eta}\,u_{zz} + 4\lambda_{\xi z\eta z}u_{\xi z}\,u_{\eta z}. \end{aligned} \tag{12.6}$$

The tensor u^{ik} is a 2-contravariant tensor, therefore its components change according to the contravariant rules, that is, in the same way as the product of the coordinate changes (they are contravariant components as well) [221]. Thus,

$$\begin{aligned} u_{\xi\xi} &= u_{xx} - u_{yy} + 2iu_{xy}, \\ u_{\eta\eta} &= u_{xx} - u_{yy} - 2iu_{xy}, \\ u_{\xi\eta} &= u_{xx} + u_{yy}, \end{aligned} \tag{12.7}$$

and the free energy reads

$$\begin{aligned} f = {} & \frac{1}{2}\,\lambda_{zzzz}u_{zz}^2 + 2\lambda_{\xi\eta\xi\eta}(u_{xx}+u_{yy})^2 + \lambda_{\xi\xi\eta\eta}\left[\left(u_{xx}-u_{yy}\right)^2 + 4u_{xy}^2\right] \\ & + 2\lambda_{\xi\eta zz}\left(u_{xx}+u_{yy}\right)\,u_{zz} + 4\lambda_{\xi z\eta z}\left(u_{xz}^2+u_{yz}^2\right). \end{aligned} \tag{12.8}$$

On the other hand, the components of the elastic modulus tensor transform covariantly, therefore we have that,

$$\begin{aligned} \lambda_{xxxx} &= \lambda_{yyyy} = 4\lambda_{\xi\eta\xi\eta} + 2\lambda_{\xi\xi\eta\eta}, \\ \lambda_{xyxy} &= 2\lambda_{\xi\xi\eta\eta}, \\ \lambda_{xxyy} &= 4\lambda_{\xi\eta\xi\eta} - 2\lambda_{\xi\xi\eta\eta}, \\ \lambda_{xxzz} &= \lambda_{yyzz} = 2\lambda_{\xi\eta zz}, \\ \lambda_{xzxz} &= \lambda_{yzyz} = 2\lambda_{\xi z\eta z}, \end{aligned} \tag{12.9}$$

are the non-vanishing components of the tensor in the original cartesian coordinates. Therefore, there are only five independent components of the elastic modulus tensor, which are λ_{xxxx}, λ_{zzzz}, λ_{xxzz}, λ_{xzxz}, λ_{xxyy}.

The corresponding elastic energy per unit volume is given by

$$f = \frac{1}{4}(\lambda_{xxxx} + \lambda_{xxyy})\left(u_{xx} + u_{yy}\right)^2 + \frac{1}{2}\lambda_{zzzz}u_{zz}^2 + \lambda_{xxzz}(u_{xx} + u_{yy})u_{zz} + 2\lambda_{xzxz}\left(u_{xz}^2 + u_{yz}^2\right) + \frac{1}{4}(\lambda_{xxxx} - \lambda_{xxyy})\left[\left(u_{xx} - u_{yy}\right)^2 + 4u_{xy}^2\right], \tag{12.10}$$

with the last term of this expression corresponding to the lateral shear. Because of the lateral fluidity of the monolayer, the energy of the lateral shear must vanish meaning that $\lambda_{xxxx} = \lambda_{xxyy}$. The final form of the free energy is

$$f = \frac{1}{2}\lambda_{xxxx}\left(u_{xx} + u_{yy}\right)^2 + \frac{1}{2}\lambda_{zzzz}u_{zz}^2 + \lambda_{xxzz}(u_{xx} + u_{yy})u^{zz} + 2\lambda_{xzxz}\left(u_{xz}^2 + u_{yz}^2\right), \tag{12.11}$$

and the only four non-vanishing independent elastic moduli are λ_{xxxx}, λ_{zzzz}, λ_{xxzz}, and λ_{xzxz}.

For a quantitative analysis we need the values of all these bulk elastic moduli and their dependencies on the position within the lipid monolayer matrix.

To the best of our knowledge, only little experimental information has been obtained on the local elastic moduli of the lipid monolayer matrix. The orientational and positional average of the volume compressibility of lipid material was measured to constitute about $\sim 5 \times 10^{-11}$ cm^2/dyne [107], meaning that the corresponding averaged volume stretching-compression elastic modulus is 2×10^9 N^2/m^2. Yet separate measurements exist neither of anyone of the four bulk elastic moduli, nor of their dependence on the position within the monolayer. At the same time, the values have been determined for the overall elastic moduli characterizing a lipid monolayer as a surface, namely, the moduli of monolayer bending, $\kappa \approx 4 \times 10^{-20}$ J [184], area stretching-compression, $\Gamma \approx 0.1$ N/m [75], and tilt of the lipid hydrophobic chains with respect to the membrane plane, $\kappa_t \approx 0.03$ N/m [108, 169]. In addition, experimental studies revealed position within lipid monolayers of the so called neutral surface, an intra-monolayer plane for which the deformations of bending and stretching-compression are energetically decoupled [142, 143, 157]. For monolayers of different lipid compositions, the neutral surface was found to lie close to the interface between the lipid polar heads and the hydrocarbon tails at a depth of about one third of the monolayer thickness, meaning that the coordinate of neutral surface can be taken to be $z_N = \frac{2}{3}h$.

There are few relationships between the bulk elastic moduli of the monolayer material and the overall elastic moduli of lipid monolayer as a surface. The transverse shear modulus can be related to the monolayer tilt modulus by

$$\int_0^h \lambda_{xzxz}\mathrm{d}z = \kappa_t, \tag{12.12}$$

where the integration is performed over the monolayer thickness h. We will assume that the two volume stretching-compression moduli are equal at any position within the monolayer, $\lambda_{xxxx} = \lambda_{zzzz}$, and denote their values by λ_{ST}. The modulus and λ_{ST} the coupling modulus λ_{xxzz} are related to the overall monolayer stretching-compression modulus Γ by

$$\int_0^h \lambda_{\mathrm{ST}} \left(1 - \frac{\lambda_{xxzz}^2}{\lambda_{\mathrm{ST}}^2}\right) \mathrm{d}z = \Gamma. \tag{12.13}$$

Finally, the position of the monolayer neutral surface (51-53), z_{N} , corresponds to vanishing first moment of $\lambda_{\mathrm{ST}}(1 - (\lambda_{xxzz}^2/\lambda_{\mathrm{ST}}^2))$,

$$\int_0^h \lambda_{\mathrm{ST}} \left(1 - \frac{\lambda_{xxzz}^2}{\lambda_{\mathrm{ST}}^2}\right) (z - z_{\mathrm{N}}) \mathrm{d}z = 0. \tag{12.14}$$

The bulk elastic moduli must satisfy the relationships Eqs. (12.12, 12.13, 12.14).

To satisfy Eq. (12.14) for the position of the neutral surface z_{N}, we assume that the moduli λ_{ST} and λ_{xxzz} have different values in the regions of the lipid polar heads and the hydrocarbon tails. Taking the interface between these two regions to lie at $z_0 = 2/3\,h$, we present the two bulk moduli as step functions

$$\begin{aligned} \lambda_{\mathrm{ST}} &= \begin{cases} \lambda_{\mathrm{ST}}^{\mathrm{h}}, & z_0 < z < h \\ \lambda_{\mathrm{ST}}^{\mathrm{t}}, & 0 < z < z_0 \end{cases} \\ \lambda_{xxzz} &= \begin{cases} \lambda_{xxzz}^{\mathrm{h}}, & z_0 < z < h \\ \lambda_{xxzz}^{\mathrm{t}}, & 0 < z < z_0 \end{cases} . \end{aligned} \tag{12.15}$$

Inserting Eq. (12.15) into Eq. (12.14) and requiring that, in accord with the measurements, the coordinate of the neutral surface coincides with that of the interface between the polar groups and the hydrocarbon tails, $z_{\mathrm{N}} = z_0 = 2/3\,h$, we obtain

$$\lambda_{\mathrm{ST}}^{\mathrm{t}} \left[1 - \left(\frac{\lambda_{xxzz}^{\mathrm{t}}}{\lambda_{\mathrm{ST}}^{\mathrm{t}}}\right)^2\right] = \frac{1}{4} \lambda_{\mathrm{ST}}^{\mathrm{h}} \left[1 - \left(\frac{\lambda_{xxzz}^{\mathrm{h}}}{\lambda_{\mathrm{ST}}^{\mathrm{h}}}\right)^2\right]. \tag{12.16}$$

Taking into account this relationship together with Eq. (12.13) and a requirement that the positional average of the bulk stretching-compression modulus is $\frac{1}{h}\int_0^h \lambda_{\mathrm{ST}} \mathrm{d}z = 2 \times 10^9$ N/m^2 , we obtain $\lambda_{\mathrm{ST}}^{\mathrm{h}} = 4 \times 10^9$ N/m^2, $\lambda_{xxzz}^{\mathrm{h}} = 3.93 \times 10^9$ N/m^2, $\lambda_{\mathrm{ST}}^{\mathrm{t}} = 10^9$ N/m^2, $\lambda_{xxzz}^{\mathrm{t}} = 0.98 \times 10^9$ N/m^2.

The transverse shear modulus is assumed to be constant through the monolayer thickness and equal $\lambda_{xzxz} = 1.5 \times 10^7$ N/m^2. In the case of coupled monolayers, we take a vanishing shear modulus λ_{xzxz} at the interface between the two monolayers. We assume the inclusions to be much more rigid than the lipid material, and, therefore, neglect the potential for the inclusions themselves to be deformed.

12.2.2 Computations

The equilibrium membrane configurations can be found by solving a set of equations for the intramonolayer displacements u_l following from minimization of the elastic energy (Eq. (12.1)) [146]. We assume that the inclusions are evenly distributed along the circumference of the membrane tube cross-section, and using the related symmetry of the cross-section shape we perform calculations for a membrane element corresponding to half distance between the neighboring inclusions (Fig. 12.1). The total membrane shape is composed of such elements.

We derive the equilibrium equations based on the local force balance. The condition of local mechanical equilibrium, which is a vanishing total force acting on each infinitesimal element of the system, is expressed through the gradient of the stress tensor σ_{ik} by [146]

$$\frac{\partial \sigma_{ik}}{\partial x^k} = 0. \tag{12.17}$$

The stress tensor, $\sigma_{ik} = \lambda_{iklm}\, u_{lm} + \sigma^0_{ik}$, consists of a contribution of the deformation expressed by a product of the strain tensor u_{lm} and the elastic modulus tensor λ_{iklm}, and the initial stresses σ^0_{ik}. In the following we will consider only the former contribution to the stress tensor since σ^0_{ik} must satisfy Eq. (12.17) on its own -provided that the initial configuration is an equilibrium one.

Based on Eq. (12.17), we can write one equilibrium equation for each spatial direction. To this end, we first express explicitly the components of the stress tensor through the strains. Using the relationships between the nonvanishing components of the elastic modulus tensor ($\lambda_{xxxx} = \lambda_{yyyy} = \lambda_{xxyy}$, λ_{zzzz}, $\lambda_{xzxz} = \lambda_{yzyz}$, $\lambda_{xxzz} = \lambda_{yyzz}$) derived above, the components of the stress tensor can be presented as

$$\begin{aligned}
\sigma_{xx} &= \sigma_{yy} = \lambda_{xxxx}(u_{xx} + u_{yy}) + \lambda_{xxzz} u_{zz},\\
\sigma_{zz} &= \lambda_{zzzz} u_{zz} + \lambda_{xxzz}(u_{xx} + u_{yy}),\\
\sigma_{xz} &= 2\lambda_{xzxz} u_{xz},\\
\sigma_{yz} &= 2\lambda_{xzxz} u_{yz}.
\end{aligned} \tag{12.18}$$

Plugging these relations into Eq. (12.17) and after some algebra, we get the equilibrium equations for a monolayer with rotational invariance with respect to the z axis and lateral fluidity:

$$\begin{cases}
\lambda_{xxxx}\left(\frac{\partial^2 u_x}{\partial x^2} + \frac{\partial^2 u_y}{\partial x \partial y}\right) + \lambda_{xzxz}\frac{\partial^2 u_x}{\partial z^2} + (\lambda_{xxzz} + \lambda_{xzxz})\frac{\partial^2 u_z}{\partial x \partial z} = 0,\\
\lambda_{xxxx}\left(\frac{\partial^2 u_y}{\partial y^2} + \frac{\partial^2 u_x}{\partial x \partial y}\right) + \lambda_{xzxz}\frac{\partial^2 u_y}{\partial z^2} + (\lambda_{xxzz} + \lambda_{xzxz})\frac{\partial^2 u_z}{\partial y \partial z} = 0,\\
\lambda_{xzxz}\left(\frac{\partial^2 u_z}{\partial x^2} + \frac{\partial^2 u_z}{\partial y^2}\right) + \lambda_{zzzz}\frac{\partial^2 u_z}{\partial z^2} + (\lambda_{xxzz} + \lambda_{xzxz})\left(\frac{\partial^2 u_x}{\partial x \partial z} + \frac{\partial^2 u_y}{\partial y \partial z}\right) = 0.
\end{cases}$$

(12.19)

Now, considering the case of two-dimensional deformations, where the y axis represents the tubular axis, we can simplify the former set of equations as

$$\begin{cases} \lambda_{xxxx}\frac{\partial^2 u_x}{\partial x^2} + \lambda_{xzxz}\frac{\partial^2 u_x}{\partial z^2} + (\lambda_{xxzz} + \lambda_{xzxz})\frac{\partial^2 u_z}{\partial x \partial z} = 0, \\ \lambda_{xzxz}\frac{\partial^2 u_z}{\partial x^2} + \lambda_{zzzz}\frac{\partial^2 u_z}{\partial z^2} + (\lambda_{xxzz} + \lambda_{xzxz})\frac{\partial^2 u_x}{\partial x \partial z} + \frac{\partial^2 u_y}{\partial y \partial z} = 0. \end{cases} \tag{12.20}$$

The equilibrium equations above (Eq. (12.20)) have to be solved for a membrane element related to one inclusion as illustrated in Fig. 12.1. To derive the boundary conditions for this solution, we characterize the position of the inclusion by coordinates of its center: $x = 0$, and $z = z_{\text{inc}}$. Based on the circular shape of the inclusion cross section, the horizontal displacement u_x at the left boundary of the membrane element, $x = 0$, must be

$$u_x(x = 0, z) = \begin{cases} 0 \ : \ z < z_{\text{inc}} - r \\ \sqrt{r^2 - (z - z_{\text{inc}})^2} \ : \ z \geq z_{\text{inc}} - r \end{cases}, \tag{12.21}$$

where r is the inclusion radius.

The vertical displacement at the left boundary must be constant for the region of insertion,

$$u_z(x = 0, z) = z_0^{\text{left}} \quad \text{for} \quad z \geq z_{\text{inc}} - r. \tag{12.22}$$

The top and bottom surfaces of the monolayer elements are free, and, therefore, the stresses σ_{ik} must vanish on these boundaries.

Finally, the right boundary of the membrane element separated from the left one by a distance L, is a symmetry plane. Therefore, it must remain straight but can rotate with respect to the left boundary by certain angle θ and get shifted in the horizontal and vertical directions by x_0^{right} and z_0^{right}, respectively.

We solve, numerically, the equilibrium equations (Eq. (12.20)) with the above-mentioned boundary conditions. We then compute the elastic energy of the obtained conformation by integrating the energy density Eq. (12.1) over the volume of the membrane fragment, and seek for the parameter values z_0^{left}, z_0^{right}, x_0^{right}, and θ corresponding to minimum of this energy. The resulting parameters determine the final membrane shape.

Although the obtained membrane shape is not ideally circular (Fig. 12.5) we can define its effective curvature, J_S, by the relationship

$$\mathrm{J}_S = \frac{\sin\theta}{L + x_0^{\text{right}}}, \tag{12.23}$$

where the values of θ and x_0^{right} are found in the course of the energy minimization.

To analyze the case of the laterally uncoupled monolayers, we compute the deformations of an isolated monolayer and determine the effective monolayer curvature generated by the inclusions. The curvature of the bilayer mid plane, J_S^b, can then be expressed, with good accuracy, through the induced curvatures of the upper, $\mathrm{J}_S^{\text{out}}$, and lower, J_S^{in} , monolayers,

$$\mathrm{J}_S^b = \frac{1}{2}\left(\mathrm{J}_S^{\text{out}} - \mathrm{J}_S^{\text{in}}\right). \tag{12.24}$$

In the case of laterally coupled monolayers, we compute deformations of the bilayer as a whole, accounting for the ability of the monolayers to locally slide with respect to each other, in spite of the global coupling between their areas, by taking a vanishing shear modulus λ_{xzxz} at the interface between the two monolayers.

To analyze the results, it is convenient to relate the induced curvature to the area fraction occupied by the inclusions on the membrane surface,

$$\phi = \frac{r}{L}, \tag{12.25}$$

where r is the radius of the inclusion cross-section and L is the half-distance between the inclusions (Fig. 12.1).

In the case of an isolated monolayer, we present this relation in the form

$$\mathrm{J}_S^{\mathrm{m}} = \zeta_{\text{inc}}\phi, \tag{12.26}$$

where $\mathrm{J}_S^{\mathrm{m}}$ is the monolayer curvature and ζ_{inc} can be seen as a spontaneous curvature of an effective particle composed of the inclusion and the deformed portion of the lipid matrix. The value ζ_{inc} referred to as the inclusion spontaneous curvature can, in general, depend on the area fraction ϕ.

In the case of laterally coupled monolayers, where the computed value is the curvature of the bilayer, $\mathrm{J}_S^{\mathrm{b}}$, we will use the relationship

$$\mathrm{J}_S^{\mathrm{b}} = \frac{1}{2}\zeta_{\text{inc}}\phi, \tag{12.27}$$

taking into account that the tendency of one monolayer to bend due to the inclusion insertion is offset by the second monolayer and the resulting bilayer curvature is smaller than the favored monolayer curvature by a factor of two.

We perform here the calculations for a vanishing initial intra-monolayer stress profile, $\sigma_{\mathrm{L}}^0(x)$. Analysis presented below shows that $\sigma_{\mathrm{L}}^0(x)$ does not significantly change the induced membrane curvature. We perform the calculations by the designated COMSOL Multiphysics 3.3 software.

12.3 Results

12.3.1 Isolated monolayer (laterally uncoupled monolayers)

A typical conformation of a bilayer consisting of two laterally uncoupled monolayers with inclusions inserted at a relatively large distance from each other is presented in Fig. 12.5. The internal strains and stresses of the lipid matrix are maximal near the inclusion and decay along the monolayer with a characteristic length ξ of a few nanometers. Such an order of magnitude of the relaxation length could be expected based on the ratio between the overall shear, $\kappa_t = 30$ mN/m, and bending, $\kappa = 4 \times 10^{-20}$ J, moduli of a lipid monolayer $\sqrt{\frac{\kappa}{\kappa_t}} \approx 1$ nm [108].

The monolayer as a whole undergoes sharp bending within the strained areas around the inclusions and remains nearly flat in the regions between the inclusions where the strains vanish. The resulting monolayer shape is not smoothly circular but can be characterized by an effective curvature J_S^m (see Sec. 12.2.2). Dependence of J_S^m on the inclusion area fraction ϕ (Eq. (12.25)) is presented in Fig. 12.6 for a depth of insertion typical for amphipathic α-helices [98]. This dependence appears linear unless ϕ approaches the values for which the distance between the adjacent inclusions is comparable to the decay length of the intra-monolayer stresses, ξ. For even smaller interinclusion distances, the growth of J_S^m with increasing ϕ becomes stronger than linear (Fig. 12.6).

In the range of the linear dependence of J_S^m on ϕ, the effective spontaneous curvature of the inclusion, ζ_{inc} , defined according to Eq. (12.26), is constant and represents a convenient characteristic of the capability of the inclusion to curve the monolayer. The value of the inclusion spontaneous curvature is presented in Fig. 12.7a as a function of the insertion depth. In early stages of insertion, ζ_{inc} grows with the insertion depth and reaches its maximal value when more than half of the inclusion cross-section is embedded into the monolayer matrix. The maximal value of ζ_{inc} corresponds to the insertion depth of $\sim 40\%$ of the monolayer thickness ($0.4h$) typical for the amphipathic α-helices [98]. Further insertion of the inclusion results in the monolayer unbending and the inclusion spontaneous curvature vanishes when the center of the inclusion attains a position just above the monolayer mid plane. Continuation of the inclusion insertion results in generation of a negative monolayer curvature, which goes over a maximal negative value and then vanishes when the inclusion leaves the monolayer (Fig. 12.7a).

It is instructive to determine the dependence of the effective inclusion spontaneous curvature ζ_{inc} on the lipid monolayer thickness, h, which is variable for different cell membranes. This dependence is illustrated in Fig. 12.8. The

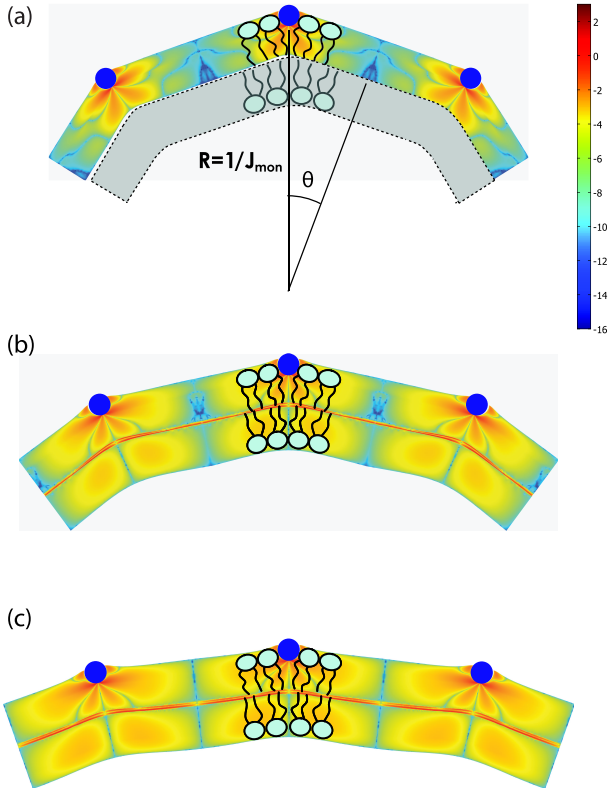

Figure 12.5 A typical conformation of a membrane with cylindrical inclusions (dark blue). (a) The case of laterally uncoupled monolayers (where the second monolayer is not considered to influence the ability to bend). The membrane shape corresponds to the preferred shape of the upper monolayer containing the inclusions as if the lower monolayer (depictured in gray) would not resist bending and just fit the upper one. (b) The case of laterally uncoupled monolayers. The membrane shape is determined by the interplay of the tendency of the upper monolayer to adopt the conformation presented in (a) and the resistance of the lower monolayer to bend. (c) The case of laterally coupled monolayers. The shear strain (dimensionless) in the monolayers is represented as a logarithmic color scale.

value of ζ_{inc} is weakly dependent on h (Fig. 12.8a). The slow decrease of ζ_{inc} with increasing h is illustrated in Fig. 12.8b for the insertion depth of ~ 0.8 nm characteristic for the amphipathic α-helices.

12.3.2
Laterally coupled monolayers

A representative conformation of a bilayer with laterally coupled monolayers containing inclusions is presented in Fig. 12.5c. The spontaneous curvature of the inclusion, ζ_{inc}, determined according to Eq. (12.27) from the computed

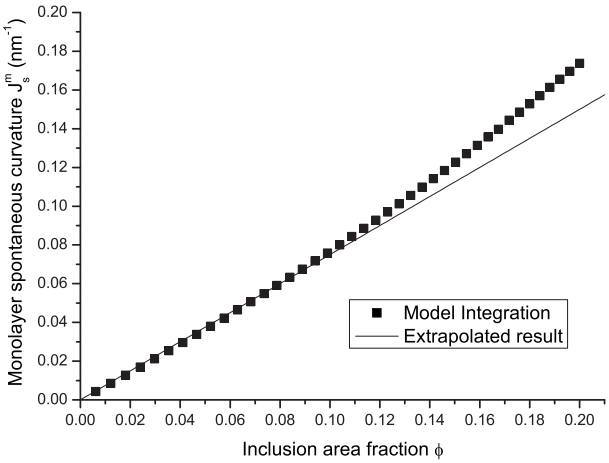

Figure 12.6 Monolayer spontaneous curvature plotted as a function of the inclusion area fraction for a 0.8 nm depth of insertion.

bilayer curvature J_S^b is presented in Fig. 12.7b. There is a qualitative difference between the behavior of ζ_{inc} in the cases of laterally uncoupled and coupled monolayers. In the latter case, ζ_{inc}, remains positive for all depths of the inclusion penetration into the upper membrane monolayer, while in the former case ζ_{inc} changes its sign as discussed above. The reason for this difference is stretching of the upper monolayer area induced by the inclusions, which has no effect on the curvature for the case of laterally uncoupled monolayers but generates a positive contribution to the bilayer curvature in the case of laterally coupled monolayers. At the same time, in the cases of both laterally uncoupled and coupled monolayers, the inclusion spontaneous curvature reaches its maximum for shallow insertions of the inclusion into the membrane matrix (Fig. 12.7).

We define the energetic penalty of the inclusion insertion as the elastic energy accumulated within the monolayer matrix in the course of embedding of the inclusion. The density of this energy per unit length of the cylindrical inclusion is presented in Fig. 12.9 as a function of the insertion depth. The nonmonotonous character of this function is related to the uneven profile of the intramonolayer elastic moduli (Eq. (12.13)) and a complex distribution of strains generated within the monolayer matrix by a cylindrical inclusion. For the typical depth of $0.4h$, the energy density is $1.2\ k_BT/\text{nm}$.

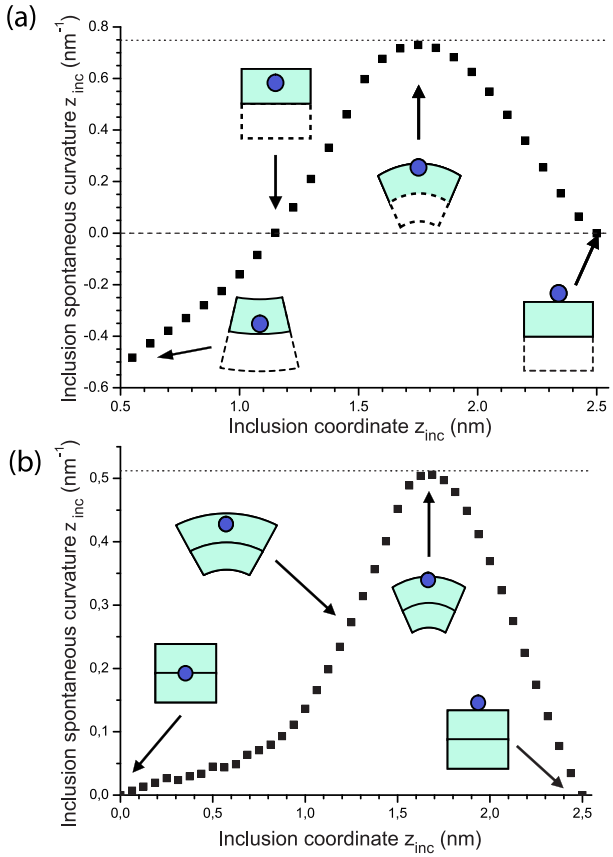

Figure 12.7 Spontaneous curvature for an inclusion plotted as a function of the position of the center of the inclusion for (a) uncoupled, and (b) coupled monolayers. Cartoons of the bilayer are shown for different insertion depths.

12.3.3 The hydrophobic insertion mechanism is sufficient for N-BAR domains to tubulate membranes

The N-BAR domains constitute one of best explored groups of protein modules capable of membrane bending *in vivo* and *in vitro* [79,80,98,195]. The N-BAR domain-containing proteins amphiphysin and endophilin are very important for membrane budding in endocytosis, and their N-BAR domains were shown to convert flat lipid bilayers into tubules of 35-50 nm diameter [98,195]. As mentioned in Sec. 12.1, the N-BAR domains have the potential to bend membranes according to two mechanisms: scaffolding the membrane by attaching its surface to the crescent-shaped BAR dimer, and by inserting amphipathic helices into the membrane matrix. Dimerization of N-BAR domains results in an effective local concentration of the amphipathic helices un-

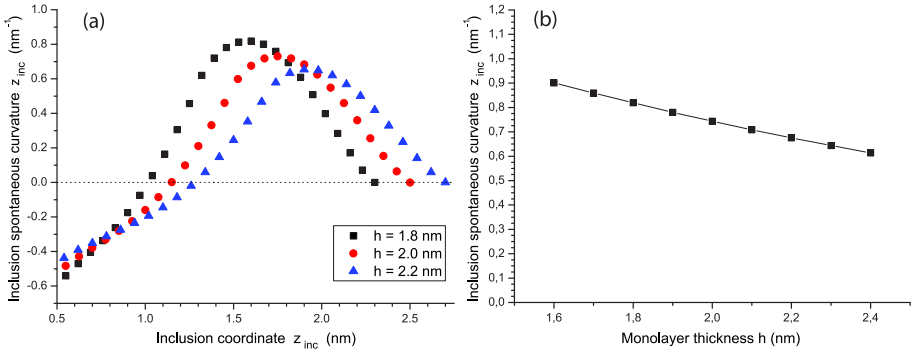

Figure 12.8 Sensitivity of the effective spontaneous curvature of the inclusion, ζ_{inc}, to the monolayer thickness h. (a) ζ_{inc} as a function of the position of the center of the inclusion for different values of the monolayer thicknesses h, where h can either be 1.8, 2.0 or 2.2 nm. (b) ζ_{inc} as a function of the monolayer thickness h for the insertion depth of 0.8 nm.

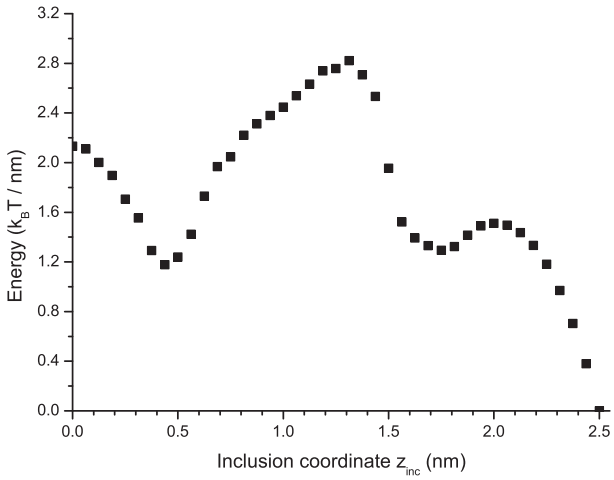

Figure 12.9 Energetic penalty per unit length of the inclusion plotted as a function of the depth of the insertion for coupled monolayers.

derneath the BAR scaffold, and, hence, enhances the ability of the protein to bend membranes. A question arises about the contribution of the hydrophobic insertion mechanism to the membrane tube formation by N-BAR domains and whether this mechanism may solely drive the entire membrane bending process.

To answer this question we computed the area fraction ϕ of the α-helices needed to produce membrane tubes of $35 - 50$ nm diameter. The results are illustrated in Fig. 12.10, which presents the range of the required values of ϕ for different depths of insertion of the α-helices. We found that for a broad range of insertion depths, the required inclusion area fractions ϕ are $< 15\%$.

For the most relevant depths of $\sim 0.4h$, to produce the experimentally observed curvature, only 7-10% of the tubule area has to be occupied by the inclusions in the case of laterally uncoupled monolayers and 9-15% for laterally coupled monolayers. The obtained values of are feasible. Indeed, according to crystallographic measurements the total area occupied in the membrane plane by one N-BAR dimer and one α-helix are 47 nm^2 and ~ 6 nm^2, respectively. Hence, for amphiphysin, which has two α-helices per N-BAR dimer, the maximal possible area fraction ϕ corresponding to a complete coverage of the membrane by the N-BAR domains is $\sim 25\%$. For endophilin having four α-helices per N-BAR dimer assuming that the second amphipathic helix on each N-BAR monomer has the same length and inserts to the same depth, the maximal can approach 50%. In both cases, the limit of the α-helix area fraction is considerably larger than the inclusion amount required to induce the $35-50$ nm tubes. This means that the hydrophobic insertion mechanism alone may drive the experimentally observed membrane bending by N-BAR domains. However, given that BAR domain alone can generate membrane curvature *in vitro*, one should not ignore the significance of this structure. Given the potency of curvature generation by amphipathic helix insertions it is likely that BAR domains function more as curvature stabilizers/limiters (or sensors) (see Ch. 13).

12.3.4 Effect of the initial lateral stress profile

To model the distribution of the initial stresses over the monolayer thickness, we follow the results of the extensive previous studies of this issue [166] and assume the initial stresses to be directed only along the monolayer plane and to be isotropic in this plane $\sigma^0_{xx} = \sigma^0_{yy} = \sigma^0_{\rm L}(z)$. We take the distribution of $\sigma^0_{\rm L}(z)$ through the monolayer thickness to be similar to the stress profile found by computer simulations [122]. The parameters of this distribution, have to be specified based on the relationship between $\sigma^0_{\rm L}(z)$ and the monolayer spontaneous curvature in the initial state J^0_S determined at the neutral surface,

$$\mathrm{J}^0_S = -\frac{\displaystyle\int_0^h \sigma^0_{\rm L}(z)\,(z-z_{\rm N})\mathrm{d}z}{\displaystyle\int_0^h 2\lambda_{\rm ST}\left(1-\frac{\lambda^2_{xxzz}}{\lambda^2_{\rm ST}}\right)(z-z_{\rm N})^2\mathrm{d}z}, \tag{12.28}$$

where the integration is performed over the monolayer thickness. The initial stress profile we use corresponds to the monolayer spontaneous curvature of $\mathrm{J}^0_S = -0.1$ nm^{-1} characterizing the most abundant lipid DOPC [48].

We took into account the initial inter-monolayer stress profile, $\sigma^0_{\rm L}(z)$, by computing deformation of the whole bilayer in the case of laterally coupled

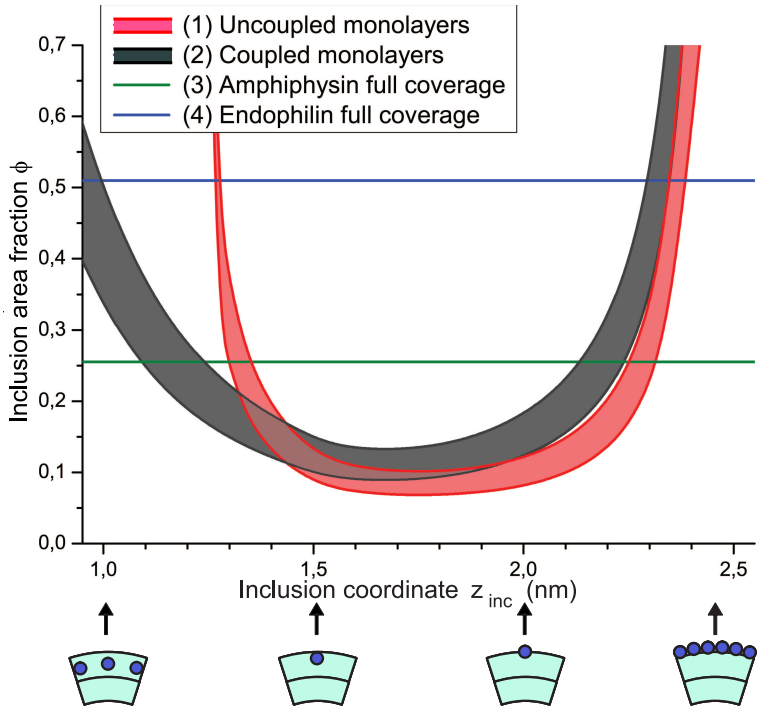

Figure 12.10 The range of α-helix area fractions required to form cylindrical membrane tubes of diameter 35-50 nm, plotted as a function of the position of the center of the inclusion, for uncoupled (red) and coupled (gray) monolayers. The maximal possible area fractions of α-helices for endophilin and amphiphysin are represented by straight lines.

monolayers. According to our results, $\sigma_{\mathrm{L}}^{0}(z)$, practically, does not change the bilayer conformation and, consequently, the inclusion spontaneous curvature (Fig. 12.11). This is expected since the effects of a non-vanishing on the shapes of the two monolayers mutually compensate and do not affect the bilayer shape. At the same time, the energetic penalty of the inclusion insertion is sensitive to $\sigma_{\mathrm{L}}^{0}(z)$. Fig. 12.12 represents the elastic energy density per unit length on the cylindrical inclusion for the case of laterally coupled monolayers with and without $\sigma_{\mathrm{L}}^{0}(z)$. According to these results, the initial stress profile noticeably alters the energetic penalty of the inclusion insertion.

12.3.5 Three-dimensional results

In all this Chapter, we addressed the case of two-dimensional membrane deformations, induced by two-dimensional inclusions. Here, we present some preliminar computations which demonstrate that three-dimensional membrane deformations generated by rodlike inclusions mimicking amphipathic

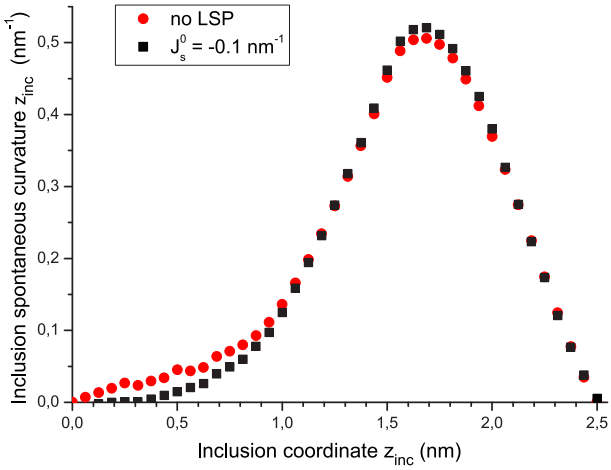

Figure 12.11 The effective spontaneous curvature of inclusion as a function of the position of the center of the inclusion in the case of coupled monolayers (a) without any lateral stress profile and (b) with a lateral stress profile accounting for a monolayer spontaneous curvature in the initial state $J_S^0 = -0.1$ nm^{-1}.

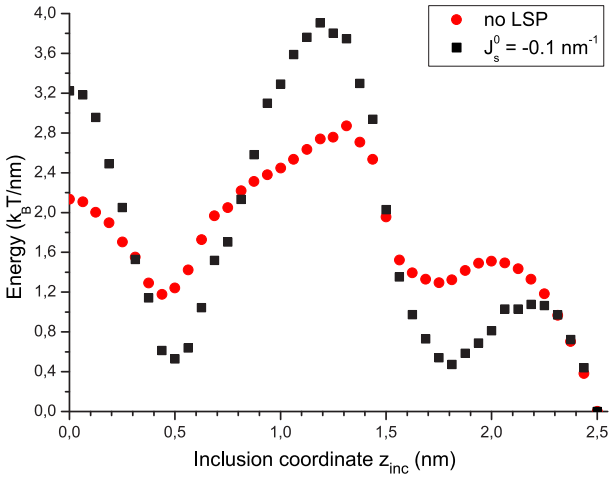

Figure 12.12 The energy penalty of the inclusion insertion per inclusion unit length as a function of the position of the center of the inclusion in the case of coupled monolayers (a) without any lateral stress profile and (b) with a lateral stress profile accounting for a monolayer spontaneous curvature in the initial state $J_S^0 = -0.1$ nm^{-1}.

α-helices are characterized by curvatures very similar to those obtained in the two-dimensional case. In Fig. 12.13, we present the qualitative geometric description of a finite rodlike particle inserting into a monolayer.

We computed the generated curvature upon insertion as a function of the angle. As we show in Fig. 12.14a, the monolayer spontaneous curvature is

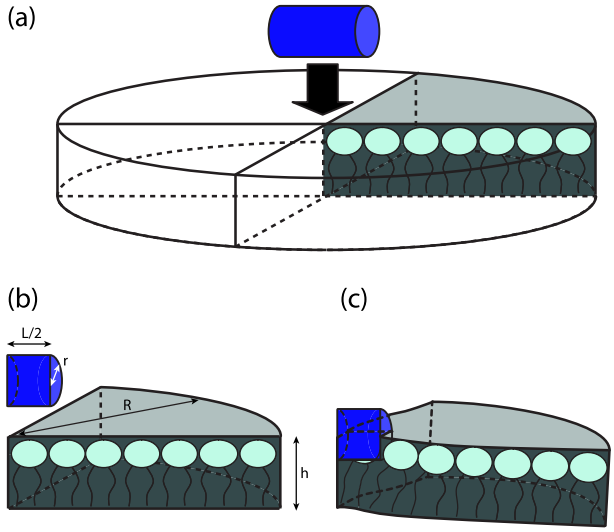

Figure 12.13 Geometric sketch of a three-dimensional rodlike inclusion inserting into a monolayer. (a) A circular piece of a monolayer divided in four equal-sized parts and the cylindrical inclusion (blue) outside the monolayer. (b) Geometry used for the computations, which do not need to include the whole domain in (a), for symmetry reasons. (c) Cartoon of the monolayer response to a particle insertion.

almost angle-independent (up to numerical precision). In Fig. 12.14a,b, we compare the calculated shape for the monolayer, with a catenoidal decay a symmetric inclusion would induce. We see that after a certain characteristic length in each direction, ξ_x, and ξ_y, the catenoidal fit is almost exact, meaning that the monolayer loses any knowledge about the actual shape of the insertion beginning from a certain distance. A spontaneous curvature per particle can thus be defined.

Since a spontaneous curvature can be defined, we calculate it as a function of the insertion depth for both laterally coupled and uncoupled monolayers. We present such results in Fig. 12.15, where we compare them with the two-dimensional results.

12.4 Discussion

We computed the membrane deformations generated by cylindrical inclusions which model the amphipathic α-helices inserted into the membrane matrix, and analyzed the dependence of the resulting membrane curvature on the depth of the inclusion insertion and the area fraction occupied by the inclusions on the membrane surface. We considered the effects of inclusions in two cases. In the first case, perhaps most relevant for the intracellular processes of

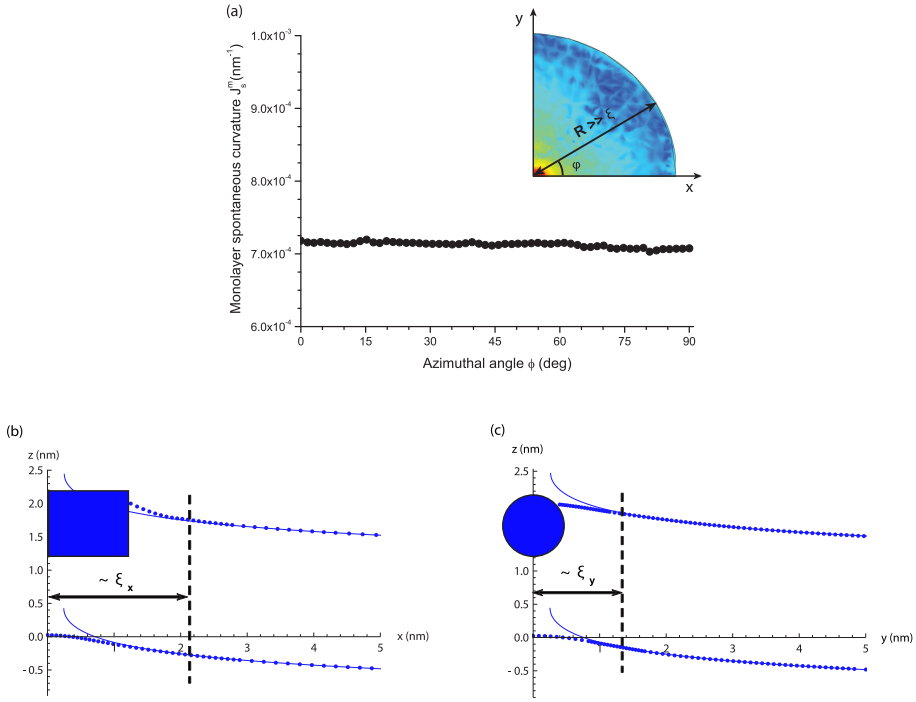

Figure 12.14 Monolayer spontaneous curvature as a function of the in-plane azimuthal angle, ϕ, as referenced in the inset of (a). Resulting shape after insertion in two perpendicular in-plane directions (b,c). Dots represent the actual calculated shape, while solid lines correspond to catenoidal fits.

membrane bending, the membrane monolayers are laterally uncoupled. This corresponds to a situation where the inclusions are inserted only into a small fragment of a large membrane for example representing the site of a forming endocytic vesicle on the plasma membrane. In the second case, which is likely most relevant for *in vitro* experiments with lipid vesicles (or areas of intracellular membranes where lateral translocation of lipids is limited), the inclusions are inserted along the whole membrane and the membrane monolayers are laterally coupled.

12.4.1 Amphipathic helices are potent membrane curvature generators

According to Fig. 12.6, the dependence of the induced monolayer curvature, J_S^m, on the inclusion surface fractions ϕ is practically linear as long as the inclusions do not occupy $> 10\%$ of the membrane surface ($\phi < 0.1$) which corresponds to interinclusion separations that are > 10 nm. Under these conditions, the effective spontaneous curvature of the inclusion, ζ_{inc}, determined

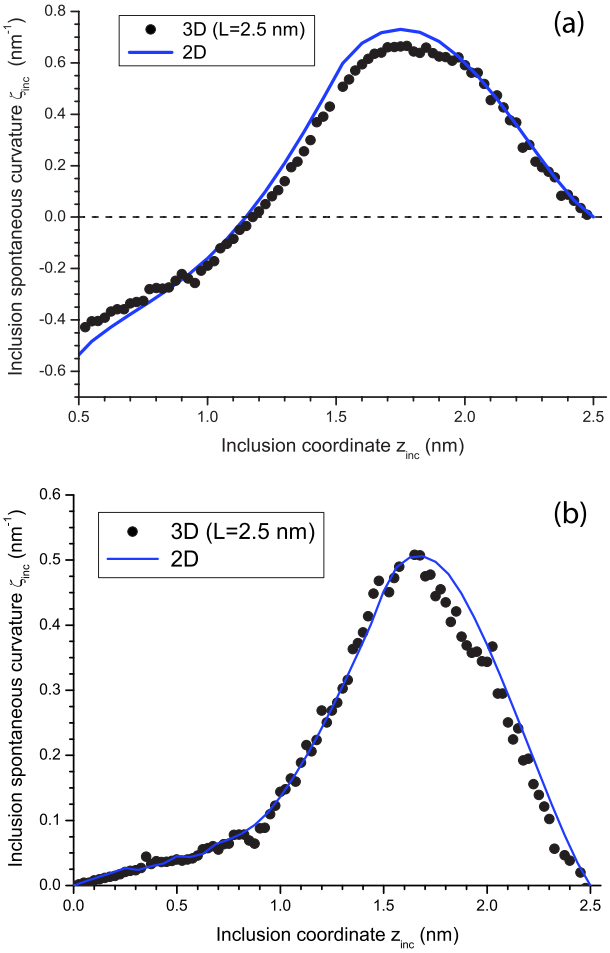

Figure 12.15 Effective spontaneous curvature per inclusion. The three-dimensional case is shown and compared with the two-dimensional case. The inclusion dimensions are $r = 0.5$ nm, and $L = 2.5$ nm. (a) The case of laterally uncoupled monolayers. (b) The case of laterally coupled monolayers.

according to Eq. (12.26), is a convenient characteristic of the ability of the inclusion to bend lipid monolayers. A representative value of $\zeta_{\rm inc}$ corresponds to a typical penetration depth of the amphipathic helices, which constitutes $\sim 40\%$ of the monolayer thickness (13) ($z_{\rm inc} = 1.7$ nm., in Fig. 12.7). According to Fig. 12.7, such a penetration depth provides the maximal possible value of the inclusion spontaneous curvature which, in the case of laterally uncoupled monolayers, equals $\zeta_{\rm inc} \approx 0.75$ nm^{-1}. It is instructive to compare this value with the spontaneous curvatures of phospholipids.

While the inclusion spontaneous curvature is positive i.e. produces membrane bulging towards the polar heads, most phospholipids have a negative spontaneous curvature [263]. The exceptions are lysolipids which lack one out of two hydrocarbon chains and phospholipids whose polar heads carry an electric charge such as phosphatidylserine and phosphatidic acid under neutral pH. The largest positive spontaneous curvature of physiologically relevant lipids measured to date is that of lysophosphatidylcholine (LPC) and equals $\zeta_{\mathrm{LPC}} \approx 0.26\ \mathrm{nm}^{-1}$ [96]. LPC belongs to the class of so-called nonbilayer lipids since they do not self-organize in bilayer structures in the absence of canonical lipids necessary for bilayer integrity. Hence, according to our computations, the inclusion spontaneous curvature ζ_{inc} is considerably larger than the spontaneous curvatures measured for any of the positively curved non-bilayer lipids. This means that amphipathic α-helices are more powerful than phospholipids in generating positive membrane curvature.

12.4.2 Repartitioning of nonbilayer lipids does not impede membrane bending by inclusions

It may be argued that bending of cell membranes containing lipids of different kinds by amphipathic inclusions will be much weaker than that predicted by the present study which assumes a homogeneous lipid composition. Indeed cell membranes include a small fraction of non-bilayer lipids such as diacylglycerol (DAG) which are characterized by strongly conical effective molecular shapes or a large negative spontaneous curvature [157]. Redistribution of such lipid molecules into the direct proximity of the inclusions may considerably reduce the stresses generated by the inclusions, and hence, weaken the membrane tendency to bend. Estimations based on our results show however, that this effect is unlikely to be significant. Indeed, a maximal elastic energy, which can be released by one conically shaped lipid molecule approaching the helical inclusion, can be estimated as $\mu_{\mathrm{relax}} = -l_{\mathrm{lip}}\, f_{\mathrm{el}}$, where l_{lip} is the lipid dimension in the membrane plane and f_{el} is the accumulated elastic energy per unit length of the inclusion. Based on Fig. 12.9, for the typical insertion depth of the amphipathic α-helices ($z_{\mathrm{inc}} \approx 1.7$ nm.) the value of f_{el} in the biologically relevant case of laterally uncoupled monolayers is $f_{\mathrm{el}} \approx 1.2\ k_B T\,\mathrm{nm}$, meaning that $\mu_{\mathrm{relax}} \approx -1\ k_B T$. At the same time, the entropic penalty for the lipid redistribution can be estimated as $\mu_{\mathrm{ent}} = -k_B T\, \ln c_{\mathrm{lip}}$ per lipid molecule, where c_{lip} is the molar fraction of the strongly conically shaped lipid in the membrane and $k_B T \approx 0.6$ kcal/mol is the product of the Boltzmann constant and the absolute temperature. Taking into account that the molar fraction of molecules such as diacylglycerol in cell membranes is small and can be estimated as $c_{\mathrm{lip}} \leq 0.001$, the entropic penalty is $\mu_{\mathrm{ent}} \geq 7\ k_B T$, which exceeds the

energy gain by an order of magnitude, $|\mu_{\text{ent}}| \gg |\mu_{\text{relax}}|$. Hence, the redistribution effects must be minor.

12.4.3 Sensitivity of results to the model's assumptions and parameters

The major assumption of our model is a steplike profile of distribution through the lipid monolayer matrix of the local elastic moduli (Eq. (12.15)). To test the sensitivity of the model predictions to this assumption, we repeated the calculations for a completely different transmonolayer distribution of the elastic moduli, which also satisfies the experimental data. We assumed a homogeneous distribution of the elastic moduli λ_{ST} and λ_{xxzz} throughout the whole monolayer thickness except for the plane $z = 2/3h$, where the elastic moduli were larger than elsewhere (a δ-functionlike profile). The results were similar to those presented above meaning that the predictions are insensitive to the details of the unknown distribution of the intramembrane elasticity.

Another issue concerns the specific parameter values we used and which are not known accurately. The major parameter is the transverse shear modulus λ_{xzxz}. We explored the sensitivity of the computed membrane curvature induced by the inclusions and the energy penalty of the inclusion insertion to the value of the monolayer transverse shear modulus which is not known with a good accuracy and of the lipid bilayer thickness which varies for different cell membranes.

Fig. 12.16 shows that the inclusion spontaneous curvature is practically independent of the specific value of as long as the latter remains within a reasonable range.

Figs. 12.17 and 12.18 illustrate the sensitivity of the results obtained for the case of coupled monolayers to the monolayer thickness h and the transverse shear modulus λ_{xzxz}. Dependence of ζ_{inc} of the parameters is similar to that obtained for the uncoupled monolayers. The energy penalty is weakly sensitive to the values of but varies considerably with λ_{xzxz}.

Fig. 12.19 shows the dependence of the effective spontaneous curvature of the inclusion on the inclusion radius for both laterally uncoupled (Fig. 12.19a) and coupled (Fig. 12.19b) monolayers. The sensitivity of these results to the inclusion radius is weak for a reasonable range of the inclusion size.

While the elastic energy of the inclusion insertion does exhibit a noticeable dependence on the parameter values, it remains of the same order of magnitude so that the qualitative conclusions based on this energy do not change.

We presented the results for inclusions having a shape of a cylindrical rod with a radius corresponding to the size of a typical α-helix with side chains. Probing computation for a squarelike cross section of the inclusions provided very similar values of the inclusion effective spontaneous curvature showing that the major predictions of the model are insensitive to the details of the

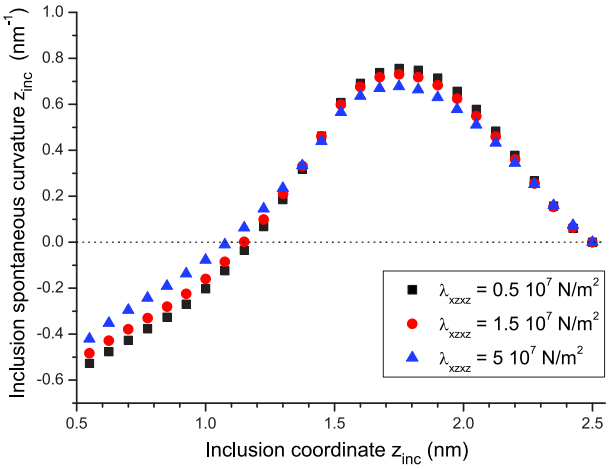

Figure 12.16 Sensitivity of the effective spontaneous curvature of the inclusion, ζ_{inc}, to the specific value of the transverse shear modulus λ_{xzxz}.

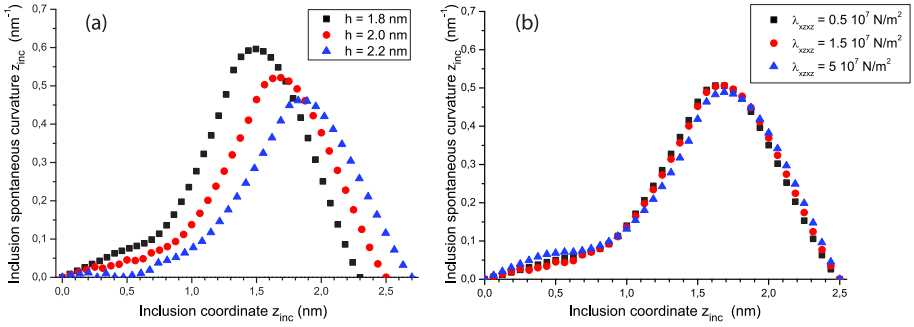

Figure 12.17 Sensitivity of the effective spontaneous curvature to (a) the monolayer thickness and (b) the transverse shear modulus for the case of coupled monolayers.

inclusion shapes. The dependence of the results on the size of the inclusion cross section is presented above (Fig. 12.19). While the effective spontaneous curvature of the inclusion does change with the radius of the inclusion cross section, qualitatively, these changes are not significant.

12.5 Conclusions

Insertion of small hydrophobic inclusions into the upper part of membrane monolayers is a potent method for proteins to induce membrane curvatures *in vivo*. Notably, there are differences in the physics of bending by inclusions for the cases of laterally coupled and uncoupled membrane monolayers. In

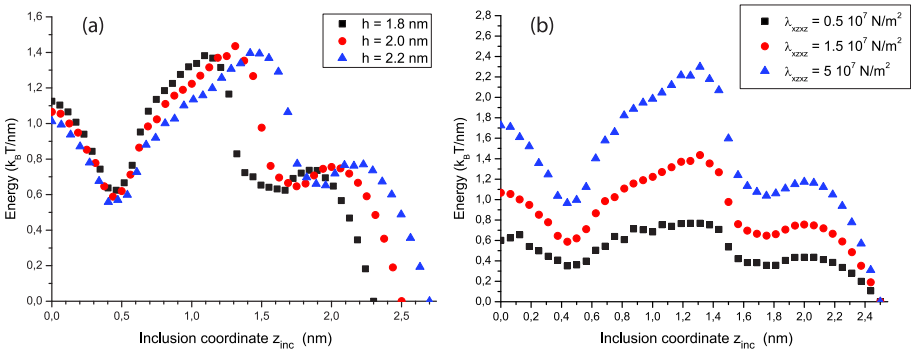

Figure 12.18 Sensitivity of the energy penalty of the inclusion insertion per inclusion unit length in the case of coupled monolayers to (a) the monolayer thickness $h$and (b) the transverse shear modulus λ_{xzxz}.

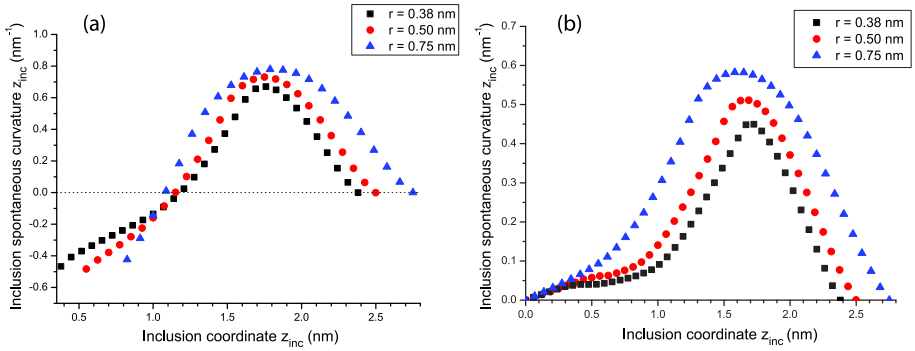

Figure 12.19 Sensitivity of the effective spontaneous curvature to the inclusion radius for the cases of (a) uncoupled monolayers, and (b) coupled monolayers.

the biologically relevant case of laterally uncoupled monolayers the shallowness of the inclusion insertion is crucial for the membrane bending. The shallow membrane inclusions penetrating $\sim 40\%$ of monolayer thickness [98] are predicted to be extremely effective in membrane shaping and their ability to produce positive curvatures considerably exceeds that of nonbilayer lipids.

13
Curvature sensing by amphipathic helices

13.1
Introduction

In this Chapter, we explain, from a quantitative point of view, the concept of curvature sensing that frequently appears in biological literature but is loosely defined. We base our analyses on the results found in Ch. 12. Generally speaking, we could define curvature sensing as the ability of some membrane proteins to bind liposomes preferentially depending on their curvature. Thus, incubating α-helical motifs with liposomes of different radii, it is experimentally observed that the amount of membrane-bound proteins strongly depends on the liposome radius [22,71,175].

We start by analyzing the thermodynamics of protein binding to membranes, and see how we can quantify experimentally accessible quantities in terms of the elastic bending energy. Next, we calculate this elastic energy for already curved membranes, and find a mathematic expression for the amount of protein bound to liposomes. We compare our results with experimental data, showing that we can fit our theory in a good agreement with that data.

13.2
Thermodynamic approach

We study the binding of bulk particles to surfaces. The chemical potentials in the bulk and in the surface are, respectively,

$$\begin{aligned} \mu_B &= \mu_B^0 + k_B T \log(c_B)\,, \\ \mu_S &= \mu_S^0 + k_B T \log(c_S)\,, \end{aligned} \tag{13.1}$$

where c_B, c_S are the molar fraction of particles in the bulk and on the surface, respectively; $k_B T \approx 0.6$ kcal/mol is the product of the Boltzmann constant and the absolute temperature; and μ_B^0, μ_S^0 are the bare chemical potentials in the bulk and on the surface, respectively. Thermodynamic equilibrium implies

equality of the chemical potentials,

$$\mu_B = \mu_S, \tag{13.2}$$

which leads to

$$c_S = c_B \exp\left(\frac{\mu_B^0 - \mu_S^0}{k_B T}\right). \tag{13.3}$$

The bare chemical potential on the surface can be separated as

$$\mu_S^0 = \tilde{\mu}_S^0 + E_{\mathrm{el}}(\mathrm{J}), \tag{13.4}$$

with this last term being the elastic energy penalty of the inclusion, which in our case depends on the membrane curvature, J. Therefore, Eq. (13.3) can be rewritten as

$$c_S(\mathrm{J}) = c_B(\mathrm{J})\, k \exp\left(-\frac{E_{\mathrm{el}}(\mathrm{J})}{k_B T}\right), \tag{13.5}$$

with

$$k = \exp\left(\frac{\mu_B^0}{k_B T}\right) \exp\left(-\frac{\tilde{\mu}_S^0}{k_B T}\right). \tag{13.6}$$

On the other hand, we shall relate the molar fraction in the bulk to the molar fraction on the surface. We consider that our system contains a fixed number of lipids (l), water molecules (w), and anchoring protein groups (p). The total number of these proteins is divided between the bulk and the surface as

$$p = p_B + p_S. \tag{13.7}$$

We define the amount of protein which is bound to the liposome surfaces, B, that is an experimentally accessible quantity, as

$$B = \frac{p_S}{p} = \frac{p_S}{p_B + p_S}. \tag{13.8}$$

The protein mole fractions in the bulk and on the surface are

$$c_S = \frac{p_S}{p_S + l}, \tag{13.9}$$

$$c_B = \frac{p_B}{p_B + w}, \tag{13.10}$$

assuming that the concentration of lipids in solution is small. Therefore, we can relate the protein molar fractions as

$$c_B(c_S) = \frac{1}{1 + \frac{w}{p - \frac{l c_S}{1 - c_S}}}. \tag{13.11}$$

The quotient between the molar fraction of proteins on the surface and in the bulk is defined as

$$F(c_S) = \frac{c_S}{c_B}, \tag{13.12}$$

and in terms of the amount of bound proteins can be written as

$$F(B) = \frac{B\left(1 - B + \frac{w}{p}\right)}{\left(B + \frac{l}{p}\right)(1 - B)} \simeq \frac{w}{l}\frac{B}{1 - B}, \tag{13.13}$$

where we assumed in the last step that $w/p, l/p \gg 1$. Therefore, we can compare the amount of binding for two different liposome curvatures J_1 and J_2,

$$\frac{\frac{B_1}{1-B_1}}{\frac{B_2}{1-B_2}} = \exp\left(-\frac{E_{\mathrm{el}}(\mathsf{J}_1) - E_{\mathrm{el}}(\mathsf{J}_2)}{k_B T}\right), \tag{13.14}$$

where $B_i = B(\mathsf{J}_i)$.

13.3 Elastic binding energy

The energy of the membrane when no insertion is anchored on it, as a function of its curvature is

$$E_{\mathrm{out}} = \frac{\kappa}{2}\mathsf{J}^2 A. \tag{13.15}$$

We computed numerically the energy penalty of an inclusion for a tubular vesicle of a given curvature J. The results are presented in Fig. 13.1.

It turns out that we can analytically explain the dependence of this energy as a function of the vesicle curvature. It is so because of the fact that the stresses induced by the inclusion insertion are localized in the surroundings of the insertion. We calculated this energy penalty for a flat membrane in our previous study on the curvature generation by amphipathic helices. We name this energy as E^0_{inc} which does not depend on the pre-existent membrane curvature, but only on the parameters such as the geometry of the inclusion or the depth of embedding. We used the parameters of typical amphipathic helices like those found in endophilin or amphiphysin. Therefore, we can assume that the energy of the curved membrane is

$$E_{\mathrm{el}}(\mathsf{J}) = E_{\mathrm{in}} - E_{\mathrm{out}} \tag{13.16}$$

Where the bilayer spontaneous curvature can be worked out from the already calculated effective spontaneous curvature for such an inclusion as

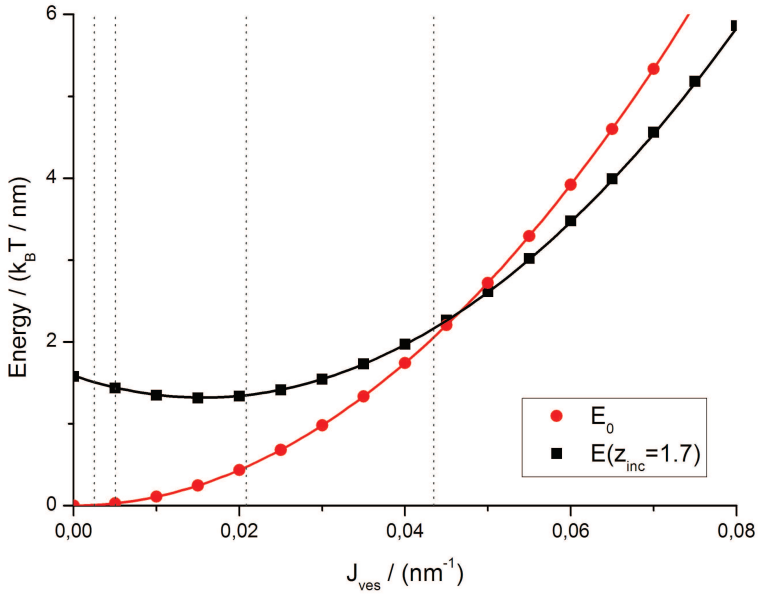

Figure 13.1 Energy penalty per inclusion length as a function of the curvature of the liposome, J_{ves}, to which they bind. We show the case where there is no inclusion (red circles), and where the inclusion is inserted at a certain depth corresponding with $z_{inc} = 1.7$ nm (black squares). Lines show the analytic estimation.

$J_s = \zeta_{inc}\phi$, $\phi = r/L$ being the area fraction occupied by the inclusions, and $A = \Delta y L$. We define the elastic binding energy as the energy difference between a bilayer with an embedded inclusion and a bare bilayer, both given a fixed curvature:

$$E_{el}(J) = E_{in} - E_{out}. \tag{13.17}$$

From Eq. (13.14) and Eq. (13.17), we can write

$$\frac{\frac{B_1}{1-B_1}}{\frac{B_2}{1-B_2}} = \exp\left[\frac{\kappa}{k_B T}\zeta_{inc} r \Delta y\,(J_1 - J_2)\right]. \tag{13.18}$$

Therefore, we can calculate the amount of binding as a function of the vesicle curvature provided that we know the amount of binding for one given curvature. In other words, defining a fitting parameter,

$$\alpha(B_2, J_2) = \frac{B_2}{1-B_2}\exp\left[-\frac{\kappa}{k_B T}\zeta_{inc} r \Delta y J_2\right], \tag{13.19}$$

and a length scale,

$$\xi = \frac{\kappa}{k_B T}\zeta_{inc} r \Delta y, \tag{13.20}$$

the amount of binding as a function of the curvature takes the form of a sigmoid-like function

$$B(\mathrm{J}) = \frac{\alpha}{\alpha + \mathrm{e}^{-\mathrm{J}\xi}}. \tag{13.21}$$

In order to understand the expression in Eq. (13.21) for the amount of protein bound to the membrane, we should ask how the parameter α depends on physical parameters as the non-elastic part of the chemical potential. For the pair J_2, B_2 we have that

$$\frac{1}{c_l}\frac{B_2}{1-B_2} = k \exp\left[-\frac{E_{\mathrm{el}}(\mathrm{J}_2)}{k_B T}\right], \tag{13.22}$$

Where $c_l = l/w$ is the lipid concentration. We can therefore write

$$\frac{B_2}{1-B_2} = k c_l \exp\left(\xi \mathrm{J}_2\right). \tag{13.23}$$

Using the definitions of α and k above, we reach to

$$\alpha = c_l \exp\left(-\frac{\tilde{\mu}_s^0 - \mu_B^0}{k_B T}\right). \tag{13.24}$$

13.4 Results and discussion

In order to proceed to compare our model for the amount of bound protein as a function of the liposome curvature, we can proceed in two easy. The expression gives the amount of bound protein given the elastic an geometric parameters (included in ξ), but requires the knowledge of a reference point (the pair B_2, J_2 contained in α). Therefore, we can either assume these pair from the experimental knowledge, and from there the function $B(\mathrm{J})$, or we can treat α as a fitting parameter.

In Ref. [71], curvature sensitivity for ALPS1, a membrane-binding amphipathic α-helix identified in the Golgi-associated protein ArfGAP1 was studied. In order to compare with those results, we choose the following geometric parameters:

$$\begin{aligned}
&r = 0.5\ \mathrm{nm},\\
&\Delta y = 6\ \mathrm{nm},\\
&z_{\mathrm{inc}} = 1.7\ \mathrm{nm},\\
&h = 2\ \mathrm{nm},\\
&\zeta_{\mathrm{inc}} = 0.45 - 0.5\ \mathrm{nm}^{-1},\\
&\kappa = 136\ k_B T.
\end{aligned} \tag{13.25}$$

The value for the effective spontaneous curvature of the inclusion corresponds to that found in Ch. 12. The bending rigidity for a bilayer consisting in two coupled monolayers is also found according to the profiles for the elastic moduli of the monolayers. The curvature in that case was found for tubular vesicles. Here, we assume that the induced curvature in the spherical liposomes by the insertions is the same, meaning that $J = 1/R$, R being the liposome radius. With all these considerations, we can assume a value for the length scale close to $\xi = 200$ nm. Besides, one can also perform a two-parameter fit of the data, and see that the outcoming length scale ξ is comparable to the experimental guess (see Fig. 13.2).

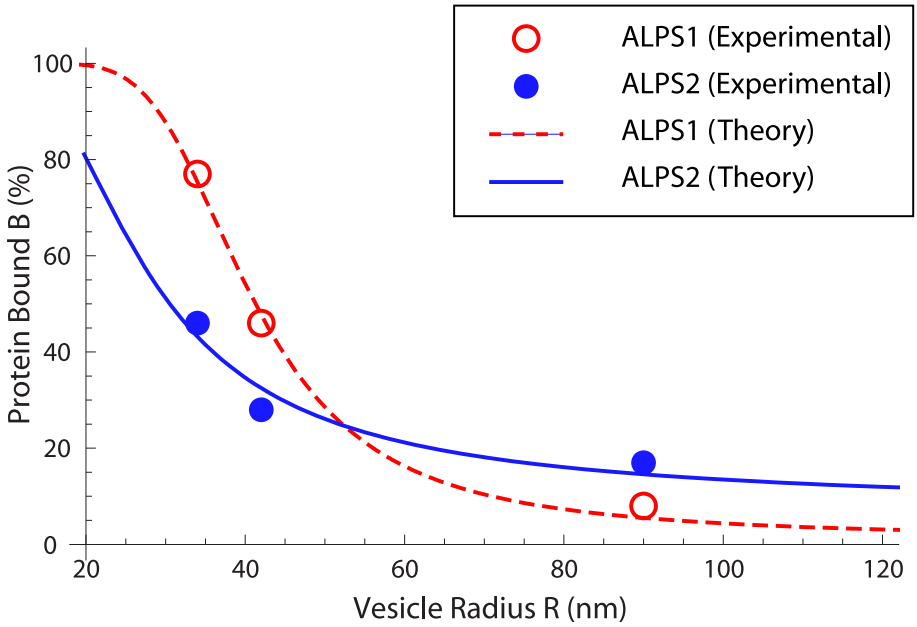

Figure 13.2 Binding amount, B, (normalized to 1) of ALPS1 (red) and ALPS2 (blue) as a function of the liposome radius. Circles correspond to experimental points from Ref. [71], and linesto the two-parameter fit of the data, according a sigmoid-like function as in Eq. (13.21).

Part IV Conclusions

14
General conclusions

Understanding how membrane-bound biological entities –like liposomes, cell organelles, or even cells– are shaped according to their surface elastic properties has been the common thread on which we conducted this thesis. We studied, from a theoretical point of view, various membrane shapes found in different situations, and we compared them with experimental data in order to better understand some biophysical phenomena appearing in biological membranes.

A biological membrane is a complex formed by several kinds of biochemical molecules. The basic structure is that of a lipid bilayer, which can, however, consist of dozens of different kinds of lipid molecules. In addition, such a purely lipidic membrane can have phase separated domains, some of them being fluid, some of them being in a more gelly phase, and some others being solidlike. Biological membranes are believed to present such a richness, albeit a fluidlike state is known to be the predominant phase. Moreover, biomembranes include, as we reviewed in Ch. 2, different kinds of associated proteins. These proteins are not only functional in order to communicate with other cells or cell organelles, but they are also involved in membrane shaping.

In the first Part of the thesis, we studied a simple model membrane, consisting of monocomponent fluid lipid bilayers, closed to form vesicles. These are, perhaps, the most simple models for biological membranes. Obviously, they can not include all the complexity of actual membranes, but they indeed grasp some essence of their behavior. Such lipid bilayers are mathematically described as two-dimensional surfaces embedded in a three-dimensional space. From a purely geometric description, they can be characterized by giving, at each point, the value of the radii of curvature in two perpendicular directions. From there, and using symmetry considerations, it is possible to describe the bilayer energy in terms of those curvatures, in the so-called Canham-Helfrich model [44, 109] (explained in Ch. 3).

The Canham-Helfrich theory states that the energy of a lipid bilayer can be described by means of its curvature. This energy is given by nothing else than the bending elasticity of a piece of surface. Among our aims in this thesis, we wanted to study the dynamics of membrane shapes in different circum-

stances. For that purpose we chose to work with a class of dynamic models for interfaces, the phase-field models, whose basics were presented in Ch. 4. The bending energy of a two-dimensional bilayer is mapped into a free energy functional which takes real values in the whole three-dimensional domain (i.e. in the membrane, but also in the outer and inner media). In this sense, in Ch. 5 we derived a mathematical model of the phase-field kind to deal with the Canham-Helfrich bending energy. A dynamic equation is worked out, dictating the time evolution of the phase-field, which, in turn, contains the information of the membrane location.

In Ch. 6 we numerically solved the dynamic equation in order to find the stationary shapes of fluid vesicles for different topologies, as well as the dynamic relaxation towards them. For the simplest bending model, the so-called minimal model, and for a given topology, there is only one free parameter on which the stationary vesicle shapes depend [224]. This is the so-called reduced volume, a dimensionless normalized area to volume ratio. For different values of the reduced volume, we found the three different shapes for axisymmetric vesicles of spherical topology: oblates, prolates, and stomatocytes. Thus, it is possible to build a shape diagram saying which shape a vesicle has as a function of its reduced volume. Such a shape diagram found by means of our phase-field model quantitatively agrees with previous results found by other techniques.

Afterwards, in Chs. 7 and 8, we applied our phase-field model to study systems with a further degree of complexity. In addition to considering a symmetric lipid bilayer, we also took into account the presence of anchor molecules on the membrane (such as amphiphilic polymers, mimicking small membrane proteins). The effect these polymer molecules have is of inducing a local curvature to the bilayer, thus breaking the symmetry between the two leaflets. This effect was introduced through a spontaneous curvature coupled to the presence of anchored molecules in the membrane.

We first analyzed, in Ch. 7, the dynamics of the curvature-induced pearling instability in tubular vesicles with anchored polymers, as experimentally reported in Ref. [251]. We found that the pearling instability can be explained by means of a homogeneous distribution of polymer molecules on the membrane. After a global application of polymer molecules on the membrane, the initial tubelike vesicle destabilizes beginning from its tip, by forming a pearl. Subsequent pearls are then formed one by one from that first one. In addition, when the polymer concentration on the membrane is high enough, equally sized pearls are not the minimum energy solution. Instead, pearls following a size gradient appear.

In Ch. 8, we studied a similar system, also consisting of monocomponent fluid lipid bilayers and amphiphilic molecules. In that case, we wanted to understand how membrane tubes can be extruded from oblate vesicles in such

a system, as experimentally observed in Ref. [250]. When a polymer source is present at a certain position in the space outside a lipid vesicle, the concentration of these molecules follows a non-homogeneous profile. Therefore, the concentration of anchoring molecules is higher close to the source than away from it. We studied how such a polymer gradient induces a tubulation phenomenon in vesicles. Depending on the characteristics of this gradient, different structures may be formed. Long tubes and short buds are among them. We analyzed this system both analytically and numerically (using our phase-field model). Our results are in agreement with the experimentally reported observations previously mentioned, and open the possibility for transport phenomena in cells not due to directed forces (like molecular motors pulling membrane tubes), but due to the presence of concentration gradients of curvature generating proteins in the intracellular medium.

Thus, in the first Part of the thesis we presented our results regarding dynamic shape instabilities in membranes due to the anchorage of molecules. We may conclude that the phase-field model we derived is valid for studying such instabilities. They can be understood in the framework of the Helfrich model where anchored polymers induce a local spontaneous curvature to the membrane. In addition, hydrodynamic effects are not important in what shaping membrane concerns, although it would be interesting in the future to couple our model with the proper hydrodynamics of both the membrane and the aqueous media surrounding it. Summing up the main conclusions to this first Part of the thesis, we should say that

- we derived a **dynamic model** of the phase-field kind to deal with **curvature energies**, and not with surface tension as usual phase-field models.
- The **stationary shapes** of fluid vesicles were recovered by means of numerically solving the bending phase-field model.
- **Three-dimensional** non-axisymmetric shapes are included in the model formalism.
- **Dynamic relaxation** towards these stationary shapes can be studied.
- The **pearling instability** which appears in membrane tubes when amphiphilic polymer molecules anchor the bilayer is **curvature-induced**.
- Phase-field integrations showed that the **dynamics** of the instability consists on a **subsequent pearl formation**, and not through a set of Delaunay shapes, even when the polymer molecules are **globally applied** to the membrane.
- **High homogeneous polymer concentrations** explain the **breaking of symmetry** in the **size of the pearls**.

- A **polymer concentration gradient** can explain the **tubulation** phenomenon observed in vesicles.
- The **size of the tubes** is finite, and depends on the characteristics of the polymer concentration profile.
- There is **no force acting directly** on the membrane in this polymer-induced tubulation mechanism.

Just as in the first Part we introduced anchoring molecules in our model membranes, in the second Part the complexity arose by studying multicomponent systems. As we explained in Ch. 2, membranes consisting of a mixture of lipid molecules can present phase separation. In Ch. 9 we studied a ternary membrane system composed by a sphingolipid, a phosphoglyceride, and cholesterol. For certain compositions, a cholesterol-enriched phase forms a separate liquid ordered phase, in contrast to the other liquid disordered phase. *In vitro* experiments [14] show that, at certain composition ratios, undulated tubular lipid vesicles are formed, displaying a periodic disposition of these two phases. Using a variational treatment for the Canham-Helfrich energy of biphasic axisymmetric vesicles, we found both analytically (in a linear approximation) and numerically the tube shapes, in a very good agreement with the experimental microscopy images. Further, wavelength selection for such periodic tubes is performed by energy minimization. In addition, a shape diagram is built showing at which area fractions between the two phases periodic tubes of a certain wavelength are favorable rather than a complete two domain separation.

Besides, in Ch. 10, we studied multicomponent lipid monolayers in a flat substrate. This system is very simple, but very inspiring as well, in the sense that it allows for the possibility of studying the shapes of two-dimensional domains. A competition between two opposing forces defines those shapes. First, a line tension avoiding separation between lipid phases tends to form circular domains. Second, a polarization term tends to elongate the domains. This model can be mapped, in a first approximation, to a two-dimensional beding model *à la* Canham-Helfrich, where the bending rigidity depends on the domain length, as well as the effective line tension, which can either be positive or negative [125]. We used our bending phase-field model derived in the first Part, to study such shapes, and how circular shapes become unstable against the formation of elliptic shapes or harmonically distorted shapes as starfish shapes. We compared our results with experimental images reported by H. M. McConnell's group [131, 152].

As a summing-up of this Part, we might assert that,

- **periodic** lipidic biphasic **membrane tubes** can be explained theoretically by means of a **competition** between **curvature** energy and **line tension**.

- **Different elastic moduli** between the two phases is the responsible for the **undulated form** of the periodic tubes.
- **Periodic tubes** are energetically **favorable to a complete two-phase separation** when the chemical composition does not favor too much one phase.
- The **Iwamoto approximation** to the domain energy composed by a line tension term and a polarization term is studied within the **bending phase-field model** framework.
- **Starfish shapes** can be found for **negative effective line tensions**.

In those two Parts of the thesis, we used the curvature Canham-Helfrich model to describe the membrane energy. This model is very powerful but has its limitations. Mainly, it loses its validity when relatively large membrane curvatures are involved, since it only takes into account small deformations. It does not consider either any internal structure of the bilayer, since it deals with it as a two-dimensional surface. In the third Part of the thesis, we derived an elastic model for the membrane as a thick elastic medium, where the internal strains and stresses are taken into account according to the system symmetries. We did so because our aim there was to study how the inclusion of small hydrophobic groups in the membrane, like α-helices, generates curvature (as it is presented in Ch. 12). Those groups are present in many different membrane proteins, like epsins, amphiphysins, or endophilins. There is experimental evidence that such domains insert up to more or less one third of the outer leaflet of the bilayer. This is the reason why we needed to use a description for the intramembrane deformations. Our findings showed that such small shallow inclusions are powerful curvature generators, more than nonbilayer lipids. In addition, reasonable concentrations of N-BAR domain containing proteins on the membrane can explain, by solely the hydrophobic insertion mechanism, the formation of narrow membrane tubes [98, 195] (different mechanisms of membrane curvature generation are briefly discussed in Ch. 11). Also, we analyzed a three-dimensional system, showing that the main conclusions for two-dimensional deformations also hold for the three-dimensional case.

Next, in Ch. 13, we analyzed the mechanism by which some proteins preferentially bind to strongly curved vesicles. Such a curvature dependent binding can be explained in terms of the elastic energies, and the concept of curvature sensing is discussed.

This third Part can be recapitulated by the following assertions:

- We developed an **elastic model of a lipid monolayer** by considering it as a **three-dimensional layer** with a finite thickness and **bulk elastic properties**.

- We calculated the only four non-vanishing independent **transmonolayer elastic profiles** according to the experimentally known overall moduli.
- The **equations of equilibrium** for the internal monolayer **strains** are obtained from our elastic model.
- A small inclusion inserted into a bilayer generates an **effective spontaneous curvature** to the membrane, which in turn is concentration-independent for small concentration of insertions.
- We calculated the **spontaneous curvature** of an inclusion as a function of different parameters for both **laterally coupled** and **laterally uncoupled** monolayers.
- The **hydrophobic insertion mechanism** is sufficient for **N-BAR domains** to **tubulate membranes**, as experimentally reported.
- **Three-dimensional** inclusions (finite rods) generate **similar isotropic curvatures** to two-dimensional ones (infinite rods).
- **Amphipathic helices** are more **powerful positive curvature generators** than lipids.
- **Repartitioning** of nonbilayer lipids does **not impede membrane bending** by inclusions.
- Our elastic model can explain by **energetic considerations** the fact that some proteins **bind preferentially to highly curved vesicles**.

In this thesis, we presented results on how membranes are shaped, according to different shaping elements, like hydrophobic domain inclusions or lipid composition. Although the biological solution to curve membranes differ from case to case, there is a common underlying physical mechanism, for the generation and stabilization of membrane curvature which is intimately related to the elasticity of the lipid bilayer.

15
Future perspectives

The great mathematician Évariste Galois wrote, a few hours before his premature death, the following sentence:

> La science est l'œuvre de l'esprit humain, qui est plutôt destiné à étudier qu'à connaître, à chercher qu'à trouver la vérité[1].

Thus, when a scientist starts to study a problem, and to search for an answer, he comes across new questions, new problems to study. It's like the ancient explorers going upriver and finding other rivers flowing into the first one, and more rivers flowing into those tributaries, and so on and so forth. This is how science grows: answer one question to get at most one answer and at least ten new questions. This thesis is not an exception to this rule. In this Chapter we briefly discuss some of the open questions for further research we have encountered, and give some ideas on how to start studying them.

15.1
Coupled dynamic model

In Chs. 7 and 8 we used the dynamic equation for the phase-field model assuming a certain given polymer concentration. There, we considered situations where the polymer concentration was fixed, either to be homogeneous along the membrane, or to follow a given profile. One possibility to extend that analysis is to soften the condition for the polymer concentration profile and let the polymer molecules diffuse according to their own dynamics.

15.1.1
Fokker-Planck equation

We first assume that polymer molecules in the bulk, far from the membrane, freely diffuse. Then, the concentration, $\rho(\mathbf{x}, t)$, at position $\mathbf{x}$ and time t de-

1) Science is the work of the human spirit, which is rather intended to study than to know, to search than to find the truth. Cited at the speech made by M. Émile Picard for the fifty anniversary of the *Société mathématique de France* [197]

scribes the distribution of these Brownian moving polymers. This concentration can be formally written as

$$\rho(\mathbf{x}, t) = \langle \delta(\mathbf{x} - \mathbf{x}(t) \rangle \,. \tag{15.1}$$

Under no other forces than the stochastic thermal forces, the evolution equation for the polymer concentration profile is governed by a diffusion equation,

$$\frac{\partial}{\partial t}\rho(\mathbf{x}, t) = \nabla \cdot (D \nabla \rho(\mathbf{x}, t)) \,, \tag{15.2}$$

where D is the diffusion coefficient, which in turn satisfies Einstein's relation $D = k_B T/\eta$, $k_B T$ being the thermal energy, and η the viscosity.

On the other hand, the deterministic dynamics of the Newton's second law with an external potential, $V(\mathbf{x}(t))$, in the overdamped regime, is given by

$$\eta \dot{\mathbf{x}}(t) = -\nabla V(\mathbf{x}(t)). \tag{15.3}$$

According to a Liouville equation [145], the probability density (in our case, the concentration field) evolves as

$$\frac{\partial}{\partial t}\rho(\mathbf{x}, t) = \nabla \cdot \left(\frac{\nabla V(\mathbf{x})}{\eta} \rho(\mathbf{x}, t) \right) . \tag{15.4}$$

Since the concentration field appears linearly in both Eqs. (15.2) and (15.4), a Fokker-Planck equation [212] can be written down as a linear combination of these two effects

$$\frac{\partial}{\partial t}\rho(\mathbf{x}, t) = \nabla \cdot \left(D \frac{\nabla V(\mathbf{x})}{k_B T} \rho(\mathbf{x}, t) \right) + \nabla \cdot (D \nabla \rho(\mathbf{x}, t)) \,, \tag{15.5}$$

where we used again Einstein's relation. The first term on the right-hand side of the equation is a *drift term*, and the second one is a purely diffusive term. This dynamic equation gives the evolution of random particles subject to an energy potential.

15.1.2 Anchorage Potential on the Membrane

In order to model the anchorage of amphiphilic polymers on the membrane after bulk diffusion [251], and its eventual diffusion along the membrane, we choose to assign a phenomenological elastic potential for this anchoring process. It is chosen in such a way that it ensures free diffusion in the bulk outside the vesicle, and free diffusion on the membrane once a certain amount of polymer concentration has reached it. Such a potential can be written as

$$V(\mathbf{x}) = \alpha \left(\phi^2(\mathbf{x}) - 1 \right) , \tag{15.6}$$

where $\alpha > 0$ is the strength of the attractive potential, and $\phi(\mathbf{x})$ is the phase-field, which equals to 0 in the membrane, $+1$ inside the vesicle, and -1 outside. Therefore, this potential vanishes far enough from the membrane, and it is attractive in the membrane, letting the polymer diffuse within the membrane (see Fig. 15.1).

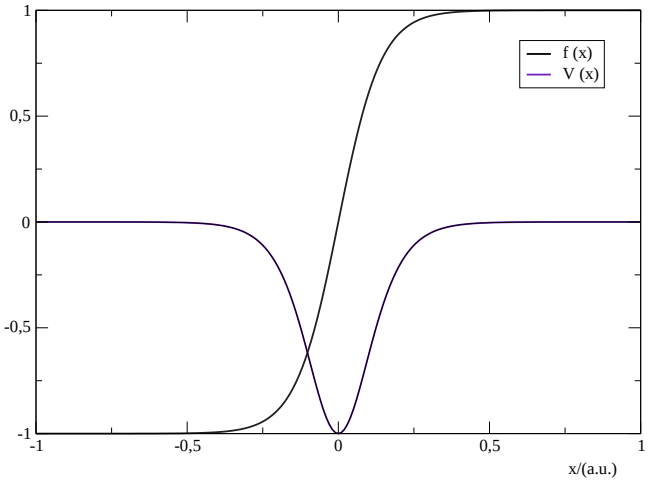

Figure 15.1 Plot of a one-dimensional tanh-like profile for the phase-field, and its related confining potential $V(x)$. The model parameters have been arbitrarily chosen to show the confinement in the area of radius ϵ around to the level-set $\phi = 0$.

This equation assumes equal polymer diffusion coefficients in the bulk and in the membrane. Due to the nature of phase-field models, it is also possible to use different diffusion coefficients for the aqueous media and for the membrane, by changing the diffusion coefficient into a function of the phase-field, as

$$D(\mathbf{x}) = D_b\phi^2(\mathbf{x}) + D_m\left(1 - \phi^2(\mathbf{x})\right), \tag{15.7}$$

where now D_b is the bulk diffusion coefficient, and D_m is the membrane diffusion coefficient. Thus, we might write the evolution equation for the polymer concentration for our problem as

$$\frac{\partial}{\partial t}\rho(\mathbf{x},t) = \frac{2\alpha}{k_BT}\nabla\cdot\left(\frac{1}{D(\mathbf{x})}\phi(\mathbf{x})\nabla\phi(\mathbf{x})\rho(\mathbf{x},t)\right) + \nabla\cdot\left(D(\mathbf{x})\nabla\rho(\mathbf{x},t)\right). \tag{15.8}$$

15.1.3 Preliminary results

To get a preliminary feeling, we have numerically solved Eq. (15.8) in the case where the diffusion coefficient is homogeneous. Then, the diffusion coefficient has no dependence on the position, and Eq. (15.8) reads as

$$\frac{\partial}{\partial t}\rho(\mathbf{x},t) = \bar{\alpha}\,\nabla\cdot(\phi(\mathbf{x})\nabla\phi(\mathbf{x})\rho(\mathbf{x},t)) + D\,\nabla^2\rho(\mathbf{x},t), \tag{15.9}$$

where we defined $\bar{\alpha} = \frac{2\alpha}{D k_B T}$. Also, in this very preliminary study, we have chosen to fix the phase-field, only to see how the polymer gets concentrated in the membrane. These results are shown in Fig. 15.2.

Another possibility would be to analyze the effects of taking into account two different diffusion coefficients in the bulk and in the membrane (D_b and D_m, respectively).

15.1.4 Further work

Once this dynamic model for the polymer concentration is assumed, we can couple it with the dynamic equation for the phase-field (e.g. Eq. (5.46). Then, we could study the dynamic effects polymer diffusion has on pearling and tubulation phenomena studied in Chs. 7 and 8.

In addition, we could also not assume a dynamic equation for the polymer, but find the stationary profile which optimizes a total free energy for the whole membrane-polymer system.

15.2 Gaussian curvature

In Ch. 5, we presented the expression for the Gaussian curvature as a function of the phase-field. However, we didn't use this curvature in the treatment of the subsequent Chapters of the first Part of the thesis, since no topological changes were taken into account in the dynamics.

Two questions arise here. First, which is the role of a Gaussian curvature term in the dynamics of monocomponent lipid vesicles when no topological change occurs? And second, can we say something about fusion/fission events if we are able to include a Gaussian curvature term in our dynamic model?

To answer the first question, we should derive the dynamic equation for a bending energy including the Gaussian curvature term. Such a dynamic equation can be straightforwardly worked out, although it is mathematical expression is quite complex, even in the case of axisymmetric geometries. Therefore,

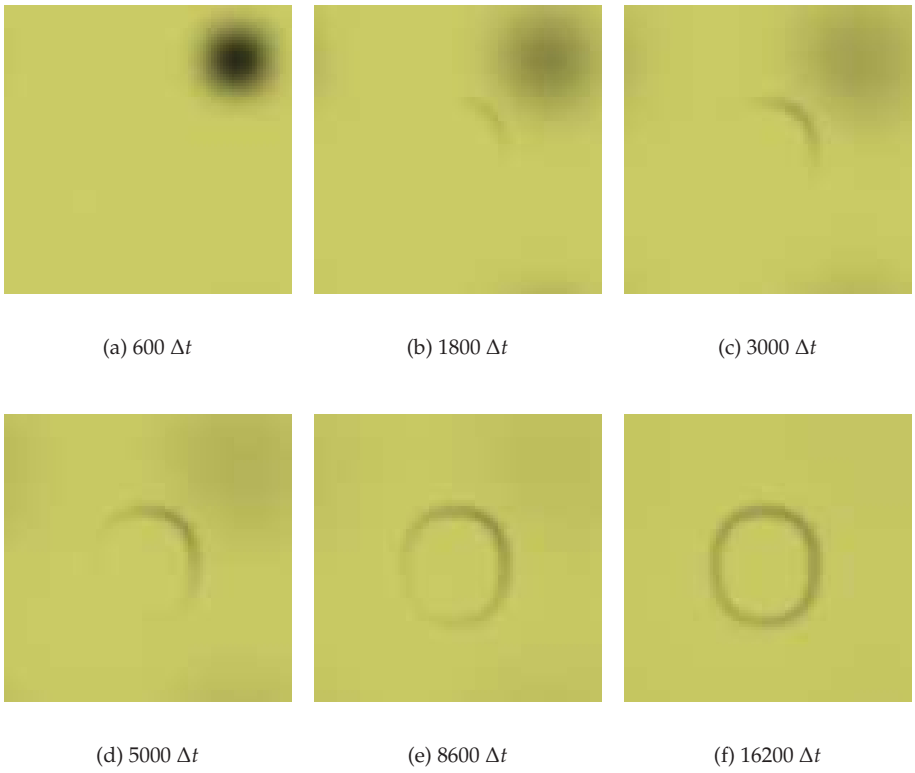

(a) 600 Δt (b) 1800 Δt (c) 3000 Δt

(d) 5000 Δt (e) 8600 Δt (f) 16200 Δt

Figure 15.2 Polymer diffusion from a localized small region outside the vesicle (a), anchorage of some amount of polymer to the membrane (b-c), and diffusion along the membrane (d-e). Stationary state with all the concentration of polymer anchored in the membrane (f). Periodic boundary conditions are assumed. The following arbitrary set of parameters is used in this integration: $\Delta t = 0.01$, $D = 1$, $\bar{\alpha} = 0.05$. Colour-scale represents the polymer density (blackish means high concentration, and greenish means low concentration, scale not shown). Integration performed in a 50×50 square lattice.

to numerically deal with that expression increases significantly the computational cost of the integrations. However, since we discretize the dynamic equations using a second-order finite differences scheme, the expression for the Gaussian curvature part of the discretized dynamic equation should be tractable [43].

About the second question, one has to be very cautious. Topological changes in membranes correspond to very large curvatures, a limit on which the classical Canham-Helfrich model is not valid, and microscopic models for the membrane have to be used (see Ch. 12). However, fission proteins localize in membrane necks (narrow catenoidal or tube-like membrane patches con-

necting two vesicles before an eventual fission), and in turn might generate spontaneous curvature to the membrane. The existence of a protein-coated neck domain is associated with a change in certain elastic parameters, as the Gaussian curvature modulus. Thus, this situation is analogous as the system studied in Ch. 9, where different phases were characterized by different elastic moduli. In this sense, within our phase-field model, we could be able to describe such a system with a inhomogeneous Gaussian curvature modulus.

15.3
Shape of lipid domains in monolayers and bilayers

In Ch. 10 we studied two-dimensional monolayer domain shapes. Such a model can be studied in a more systematic way, in order to get the full shape diagram corresponding to the competition between line tension and dipole-dipole interaction. In addition, the effect of adding surfactant proteins to the lipid mixture of the monolayers is a matter of further research both theoretically and experimentally [54]. Raising the constraint of two-dimensionality, and moving into the study of bilayer vesicles in the space is a key point in understanding the role curvature has on shaping membrane domains.

15.4
Curvature sensing by proteins

The results presented in Ch. 13 are only preliminary results, and more insight is needed for a deep understanding of this problem. In this direction, further computations on the three-dimensional results on curvature generation presented in Sec. 12.3.5 are needed.

15.5
Prokaryotic cell division

When a cell divides, a cascade of biochemical reactions help in finding the cell's midplane. Also, the genetic information has to be duplicated and separated in the two parts of the cell. By some means, the cell membrane has to squeeze the cell midplane in order to finish the division process. This fission process involves the action of a force. Protein ring-like filaments, like FtsZ, are believed to generate such a force in bacterial divisions [164], since they wrap on the bacterial membrane midplane. Studying the competition between the protein generated force [118] and the membrane elastic restoring force can lead to get some insights on prokaryotic cell division mechanisms.

Part V Resum en Català

16
Introducció

Les formes a les cèl·lules. Aquest és el títol d'aquesta tesi doctoral. Després el segueix un subtítol més específic sobre la recerca feta, però, ja que som en una introducció, deixeu-nos explicar què volem dir quan parlem de les formes a les cèl·lules. Per una banda, la forma és, segons el Diccionari de l'Institut d'Estudis Catalans, *"[l']aparença externa d'una cosa, conjunt de línies i superfícies que en determinen el contorn"*. Per l'altra, tenim les cèl·lules, les entitats fonamentals de la vida. Així doncs, en aquesta tesi estudiem quines són les aparences, les propietats geomètriques i morfològiques, que trobem en les unitats essencials de què estan formats els éssers vius. És important remarcar el fet que estudiem no només les formes *de* les cèl·lules, sinó també les dels diversos orgànuls i regions que es troben al seu interior.

Fets aquests aclariments preliminars, ja podem enunciar la segona part del títol d'aquesta tesi: inestabilitats dinàmiques, morfologia i curvatura en membranes biològiques. Al llarg d'aquest resum, anirem desgranant un per un aquests temes i veurem quina ha estat la nostra contribució a cadascun d'ells.

16.1
Motivació

La forma que tenen els objectes de la natura, formats per purs processos naturals sense la intervenció de l'ésser humà, no és pas arbitrària. De fet, són el resultat de processos ja sigui evolutius, com pot ser sovint el cas en organismes vius, o deguts a mecanismes físics, com els que expliquen la morfologia dels cossos celestes. Aquests dos exemples són també il·lustratius perquè donen dues escales de complexitat completament oposades. La primera, la d'un organisme pluricel·lular com pot ser qualsevol animal superior, amb els coneixements científics actuals no es pot tractar amb el mateix nivell de detall que la segona, un cos celeste com pot ser una estrella de neutrons. Aquesta és una de les característiques que poden diferenciar els mètodes emprats en biologia i en física.

Ara bé, com en qualsevol classificació creada artificialment, hi ha fronteres difuses. Així, és en aquestes regions de, diguem-ne, complexitat mitjana, on

la metodologia de la física pot ser útil per entendre certs processos i sistemes biològics. I quin millor que el que es refereix a la unitat mínima de la vida?

En aquesta tesi, doncs, estudiem, amb un enfocament teòric i utilitzant la metodologia i la maquinària de la física, quins són els mecanismes que porten a la formació de certes estructures cel·lulars.

16.2 Membranes biològiques

Les cèl·lules, així com la major part dels seus orgànuls, estan definides i separades de les seves veïnes mitjançant una mena de paret que les embolcalla. Aquesta paret s'anomena membrana. Les membranes biològiques estan bàsicament formades per lípids i proteïnes. Els lípids (vegeu Fig. 16.1a,b) són molècules que tenen un cap hidrofílic –és a dir, que té afinitat amb els medis polars, com l'aigua– i, generalment, dues cues hidrofòbiques –amb afinitat pels medis apolars, com l'oli. Aquesta naturalesa amfífila fa que en solució aquosa els lípids s'autoassemblin de forma que l'energia d'interacció amb el medi sigui mínima. Els lípids que formen les membranes cel·lulars tenen una geometria aproximadament cilíndrica (vegeu Fig. 16.1b). En aquestes condicions, els lípids s'associen geomètricament en forma de bicapa, de manera que les cues hidrofòbiques resten en contacte mutu, evitant el medi polar per la presència dels caps hidrofílics [123] (vegeu Fig. 16.1c).

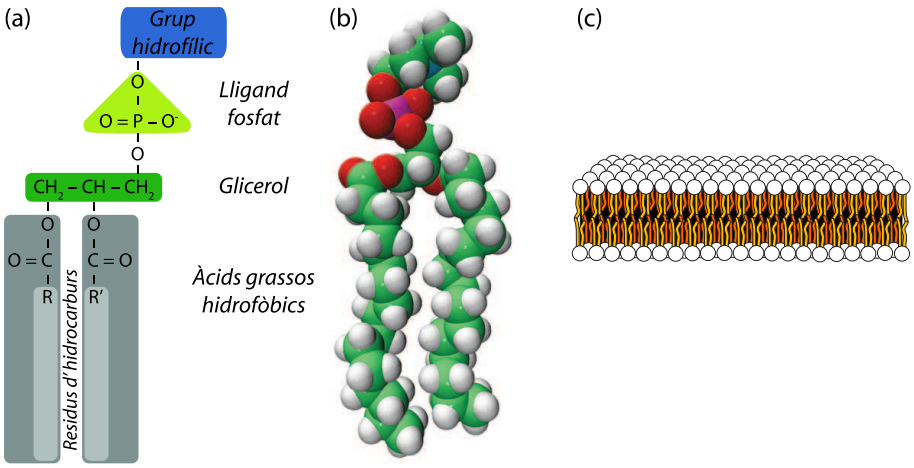

Figura 16.1 Lípids de membrana. (a) Esquema d'un lípid de membrana, un fosfoglicèrid, concretament, amb les parts hidrofíliques i hidrofòbiques detallades. (b) Model molecular de boles del mateix lípid que a (a). (c) En presència d'un medi polar, aquests lípids s'autoassemblen en forma de bicapa.

Les membranes biològiques són extremadament fines en comparació amb la mida cel·lular mitjana. Així, el gruix d'una bicapa lipídica és de l'ordre dels quatre o cinc nanòmetres, mentre que el diàmetre cel·lular està en l'ordre de les micres, és a dir, tres ordres de magnitud més. Cal dir, però, que en el cas d'orgànuls intracel·lulars, com les vesícules de transport, aquestes mides poden arribar a ser del mateix ordre i, per tant, el gruix de la membrana és comparable a la mida de la vesícula que forma. Aquesta última situació la tractarem més endavant, quan parlarem de mecanismes de generació de curvatura per proteïnes. Així doncs, en el cas més comú, les membranes poden ser considerades com superfícies bidimensionals en un espai tridimensional.

Per altra banda, hem de tenir en compte certes propietats de les membranes. Per la funció d'encapsulació del medi intracel·lular, la membrana ha de ser suficientment rígida per no trencar-se fàcilment per la dinàmica cel·lular, però prou flonja per respondre ràpidament i elàstica a canvis sobtats de la seva geometria (com pot ser el cas dels glòbuls vermells en passar per capil·lars fins). A més, la membrana és permeable a l'aigua, però no a ions grans, que creuen d'una banda a l'altra de la membrana per mitjà de canals i bombes iòniques.

Els lípids dins la bicapa tenen generalment una difusió ràpida i no estan ordenats de manera cristal·lina. Diem, doncs, que la bicapa es troba en un estat fluid o, més precisament, en un estat fluid desordenat. Depenent de certs factors, com ara la temperatura o la composició, les membranes poden presentar dominis de diverses fases, no només de la fase líquida desordenada [160].

Ja hem avançat que les membranes no són només la bicapa lipídica, sinó que hi ha altres molècules que les doten de certes funcionalitats específiques. Són les proteïnes de membrana, com poden ser els canals i bombes iòniques entre moltes d'altres [3].

Podem, per tant, definir com és una membrana model dient que és una bicapa fluïda de lípids amb proteïnes ancorades en el seu si que la doten de certa funcionalitat.

16.3
Models elàstics per a bicapes lipídiques

Considerem la membrana com una superfície bidimensional elàstica. Podem descriure geomètricament aquesta superfície, suposant que és suficientment ben comportada, donant les dues curvatures a cada punt. Cada una d'aquestes dues curvatures és l'invers d'un dels dos radis de curvatura que es poden definir localment en una superfície (vegeu Fig. 16.2).

A aquesta superfície li associarem una certa energia deguda a la curvatura. Per tal de construir una teoria invariant sota canvis de coordenades, em-

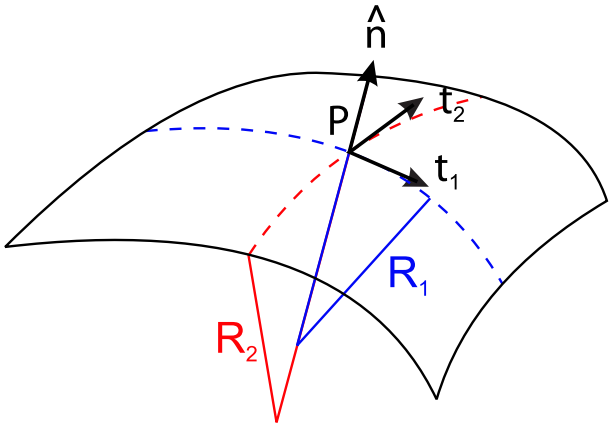

Figura 16.2 Radis de curvatura d'una superfície bidimensional. Localment, a un punt P d'una superfície podem definir-hi dos vectors tangents, $\boldsymbol{t}_1$ i $\boldsymbol{t}_2$, i un vector normal, $\hat{\boldsymbol{n}}$. Els dos radis de curvatura (els inversos de les dues curvatures principals) venen descrits geomètricament com mostra la figura.

prarem, en lloc de les curvatures principals de la superfície, els dos invariants de curvatura. Un és la curvatura total, J, que no és més que la suma de les dues curvatures principals; l'altre, la curvatura Gaussiana, K, que n'és el producte. Fent una expansió fins a segon ordre en curvatures, i utilitzant criteris de simetria, podem escriure l'anomenada energia elàstica de Canham-Helfrich [44, 109] com,

$$F = \int_S \left[\frac{\kappa}{2} \left(\mathsf{J} - \mathsf{c}_0 \right)^2 + \bar{\kappa} \mathsf{K} \right] \mathrm{d}\boldsymbol{s}, \tag{16.1}$$

on κ i $\bar{\kappa}$ són respectivament els mòduls de rigidesa flectora i Gaussiana; S és la superfície de membrana que estem considerant; i c_0 és l'anomenada curvatura espontània, que s'esdevé a causa de possibles asimetries entre les dues capes de la bicapa o a la pròpia geometria dels lípids en si. Si la curvatura espontània és zero, la membrana és simètrica i, per tant, l'estat de mínima energia és el que correspon a una membrana plana.

De totes maneres, l'existència de membranes obertes no és sovint factible, a causa del cost energètic que això tindria ja que el nucli hidrofòbic dels lípids als extrems estaria en contacte amb el medi aquós. Per tant, si considerem membranes tancades, és a dir, vesícules o liposomes, encara que la solució local de mínima energia fóra la d'una membrana plana, aquesta no és abastable globalment. A part d'això, cal afegir dos lligams sobre les condicions geomètriques de les vesícules. El primer és que el volum intern es manté constant pel control osmòtic que efectua la membrana. El segon, que l'àrea també es manté constant, pel fet que la membrana és un fluid incompressible, en molt bona aproximació, i que el nombre de lípids no varia.

La minimització de l'energia de curvatura Eq. (16.1) subjecta a aquests dos lligams dóna lloc a la cerca de formes estacionàries. De fet, en aquest cas el terme de curvatura Gaussiana es pot menystenir, perquè l'anomenat teorema de Gauss-Bonnet diu que la integral sobre una superfície tancada de la curvatura Gaussiana és un invariant topològic. Per a una topologia esfèrica i en el cas que no hi hagi curvatura espontània, les formes estacionàries depenen d'un sol paràmetre, el volum reduït, que és una mesura de la raó entre el volum i l'àrea de la vesícula.

17
Resultats

17.1
Model dinàmic i formes estacionàries de vesícules lipídiques

En la primera Part de la tesi, hem formulat un model de camp de fase per tractar de manera dinàmica l'energia de curvatura de Canham-Helfrich, Eq. (16.1). Els models de camp de fase són un tipus de models matemàtics que s'han utilitzat en múltiples camps per tractar problemes d'interfícies físiques. Es basen en l'existència d'un camp matemàtic, $\phi(\boldsymbol{x})$, en cada punt de l'espai, que descriu en quina fase es troba el sistema en aquell punt. Així, en un sistema bifàsic, el camp de fase tindrà dos replans, corresponents a cadascuna de les dues fases (en general es prenen els valors $\phi = \pm 1$ per a aquests replans). La interfície no és bidimensional, sinó que té un cert gruix, proporcional a un cert paràmetre ϵ. El valor del camp de fase interpola contínuament però abrupta entre els valors al volum de cada fase. Podem localitzar la interfície mitjançant la corba de nivell $\{\boldsymbol{x} \ : \ \phi(\boldsymbol{x}) = 0\}$. A més a més, aquests models són dinàmics, en el sentit que a partir d'aquest camp de fase és possible construir una energia lliure que descrigui el sistema, i a partir de la qual se'n pugui derivar una equació dinàmica. En el límit d'interfície abrupta, quan $\epsilon \to 0$, el model macroscòpic i el model de camp de fase han de ser equivalents.

El model de camp de fase que derivem en el Cap. 5 de la tesi ve descrit per la següent energia lliure,

$$\mathcal{F}_{\mathrm{SC}}[\phi] = \frac{\bar{\kappa}}{2} \int_{\Omega} \left(\Phi_{\mathrm{SC}}[\phi]\right)^2 \, \mathrm{d}\boldsymbol{x}, \tag{17.1}$$

on $\bar{\kappa} = \frac{3\sqrt{2}}{4\epsilon^3}\,\kappa$,

$$\Phi_{\mathrm{SC}}[\phi] = -\phi + \phi^3 - \epsilon^2 \nabla^2 \phi - \epsilon\, C_0 \left(1 - \phi^2\right), \tag{17.2}$$

i $C_0 \equiv \mathrm{c}_0/\sqrt{2}$.

D'aquesta energia lliure, Eq. (17.1), n'hem calculat una equació dinàmica que mantingui els lligams geomètrics durant tota l'evolució temporal. Aques-

ta equació dinàmica és,

$$\frac{\partial \phi}{\partial t} = \bar{\kappa}\nabla^2\Big\{ \Big(3\phi^2 - 1 - 2\epsilon C_0(\boldsymbol{x})\,\phi\Big)\,\Phi_{\rm sc}[\phi] - \epsilon^2\nabla^2\Phi_{\rm sc}[\phi] + \epsilon^2\bar{\sigma}(\boldsymbol{x})\nabla^2\phi\Big\}, \tag{17.3}$$

on $\bar{\sigma}$ és un multiplicador de Lagrange que ens assegura la conservació de l'àrea.

En el Cap. 6 de la tesi, hem resolt numèricament l'equació dinàmica Eq. (17.3), quan la curvatura espontània és zero per diverses topologies. En el cas de topologia esfèrica, trobem les formes estacionàries de les vesícules, d'acord amb els resultats trobats anteriorment per mitjà d'altres tècniques. En la Fig. 17.1, presentem el diagrama de formes per a aquest cas, on es mostren els tres tipus de vesícules que tenen lloc: l'estomatòcit (*stomatocyte*, en anglès), el discòcit (*oblate* o *discocyte*) i els esferoides prolats (*prolate*).

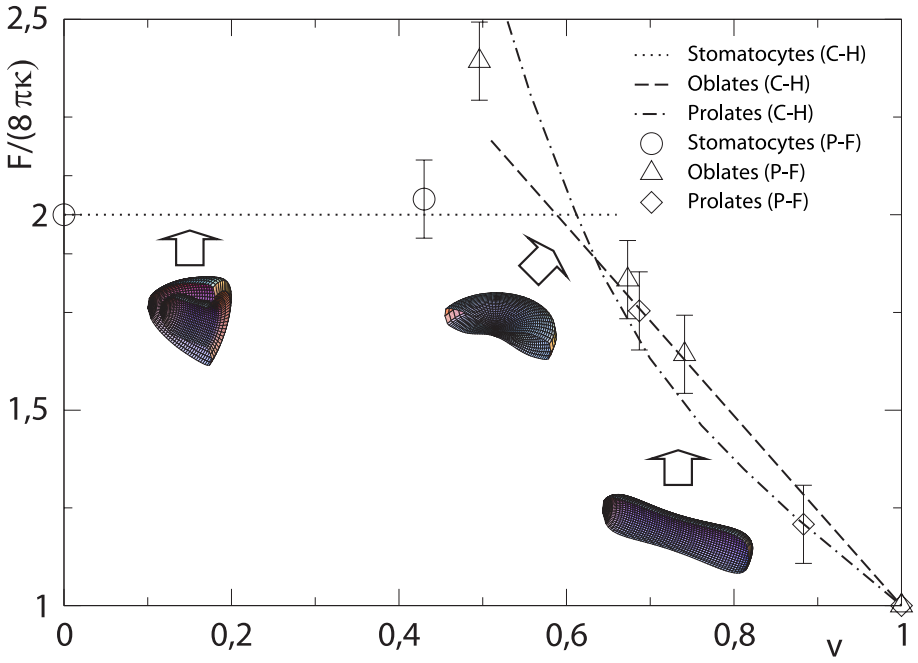

Figura 17.1 Diagrama de formes pel model de Canham-Helfrich sense curvatura espontània i amb topologia esfèrica. Les línies corresponen a la minimització de l'energia de Canham-Helfrich Eq. (16.1) (C-H) [224], i els símbols als nostres resultats amb el model de camp de fase Eq. (17.1) (P-F). Mostrem també els tres tipus de formes obtinguts, els estomatòcits, discòcits i esferoides prolats, respectivament d'esquerra a dreta.

A diferència dels mètodes anteriors per trobar formes estacionàries [224], el nostre model ens permet fer una minimització dinàmica i tractar de manera natural diferents topologies i formes no axisimètriques.

17.2
Inestabilitats dinàmiques: perlatge i tubulació

Tenir un model dinàmic de camp de fase per tractar l'energia de curvatura que caracteritza les membranes és el primer pas per poder entendre problemes més complexos. En l'apartat anterior hem explicat com el nostre model dinàmic és capaç de recuperar les formes d'equilibri per a vesícules formades per una única classe de lípids. En aquest apartat veurem com el model es pot fer extensible per estudiar inestabilitats dinàmiques o morfològiques en membranes.

La nostra anàlisi teòrica ha estat motivada pels resultats experimentals del grup de Joel Stavans a l'Institut Weizmann [250, 251]. En aquests s'estudiava la dinàmica de membranes monocomponents quan una certa concentració de polímers amfífils eren introduïts al sistema. Aquests polímers consten de parts hidrofòbiques que s'ancoren dins la bicapa per reduir-ne l'energia d'interacció amb el medi polar. Tal ancoratge produeix un efecte purament geomètric a la membrana, ja que els grups hidrofòbics actuen com una falca induint una certa curvatura de forma local a la membrana. Nosaltres hem modelitzat aquest efecte dient que tal ancoratge crea localment una curvatura espontània efectiva. Així doncs, cal acoblar la concentració de polímers en la membrana amb la curvatura espontània de la mateixa.

En el Cap. 7 estudiem la situació on aquests polímers són aplicats als voltants de membranes tubulars, i una inestabilitat de perlatge –on la geometria cilíndrica es transforma a una geometria formada per un conjunt d'esferes unides entre si– té lloc. Així, resolent numèricament el nostre model de camp de fase Eq. (17.3), per diferents concentracions homogènies de polímer en membranes tubulars, obtenim la mateixa dinàmica per a la inestabilitat de perlatge deguda a curvatura que s'observa experimentalment [39, 251]. L'aparició de la inestabilitat es mostra a la Fig. 17.2.

La inestabilitat de perlatge que hem estudiat és deguda a curvatura, és a dir, a la creació de curvatura espontània per part dels polímers. Aquest mecanisme és completament diferent a altres inestabilitats amb la mateixa morfologia, com pot ser la inestabilitat de Rayleigh-Plateau [46], que és deguda a tensió superficial, i és la responsable de la formació de gotes d'aigua en un raig fluint d'una aixeta.

Per a concentracions més grans de polímer, s'observa que posteriorment a la formació d'una primera esfera o perla, se'n van formant més subsegüentment, una a una, a partir del cap del tub. Cal esmentar que aquesta dinàmica de formació de perles no passa per l'ondulació global del tub i el pas continu d'un cilindre a un conjunt d'esferes mitjançant formes de Delaunay.

Aquestes perles que es formen són totes de la mateixa mida i estan connectades les unes a les altres per uns colls estrets. Si incrementem encara més la concentració de polímers, veiem com aquesta homogeneïtat en el radi de les

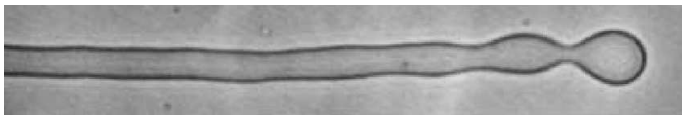

(a) Resultat experimental (de la Ref. [251])

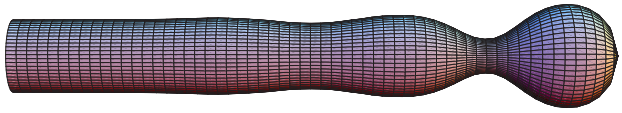

(b) Resultat numèric del camp de fase

Figura 17.2 Aparició de la inestabilitat de perlatge. Comparativa entre el resultat experimental de la Ref. [251] (a), i el resultat numèric de la integració del model de camp de fase (b). Cal dir que en la integració numèrica no s'ha emprat cap paràmetre d'ajust, sinó que tan sols hem deixat evolucionar dinàmicament el sistema des d'una configuració tubular inicial, amb una curvatura espontània induïda relativament petita, $C_0 = 0.48$, per sota del límit d'inestabilitat de perlatge.

perles es trenca i afavoreix una situació on la perla de la punta és la més gran i les subsegüents van disminuint progressivament el seu radi. En el marc del model analític de Canham-Helfrich, Eq. (16.1), hem comparat l'energia d'una configuració homogènia de perles amb la d'una composada per una esfera gran i la resta de més petites. Veiem que a partir d'una certa concentració crítica de polímer, la segona configuració és energèticament favorable envers la primera.

A més de la inestabilitat de perlatge, en el Cap. 8 hem estudiat un fenomen físic que apareix en un sistema molt semblant al primer. En aquest cas, quan s'incuben vesícules oblongues i el mateix tipus de polímers amfífils són afegits mitjançant una micropipeta al medi extravesicular, s'observa la formació de tubs de membrana de la vesícula mare [250]. Aquest canvi morfològic, anomenat digitació o tubulació, apareix per mitjà de diversos mecanismes físics. En general es requereix una força externa que, aplicada sobre un zona de la membrana, ajuda a extreure tubs de membrana. Pinces òptiques, motors moleculars o purs efectes hidrodinàmics són alguns dels agents que l'apliquen, ja sigui en experiments *in vitro* com *in vivo*.

Tanmateix, nosaltres proposem un mecanisme d'extracció de tubs de membrana que no s'efectua mitjançant una força dirigida. La nostra hipòtesi és que un gradient de concentració de polímers amfífils en el medi extravesicular pot

crear un perfil d'energia lliure que afavoreixi la tubulació. Així doncs, estudiem aquesta hipòtesi en el marc del model de curvatura de Canham-Helfrich, Eq. (16.1), i, primerament, per a una geometria simplificada que ens permeti un tractament analític. En aquestes condicions trobem que, depenent de la longitud inicial del pretub i d'un cert paràmetre que depèn de la concentració de polímer (assumida lineal, en aquesta aproximació) i de la posició de la font, es poden formar tubs estables de longitud finita.

Esperonats pels resultats analítics, estudiem el cas més complet on no fem cap suposició sobre la geometria dels tubs durant la dinàmica, i assumim una forma més general per la concentració de polímer (un decaïment Gaussià, concretament). En aquest cas, el tractament analític és impossible a causa de les no linealitats de les equacions, així que emprem el nostre model de camp de fase per assolir tals objectius. Depenent d'aquestes condicions, trobem dos tipus de tubs, uns de més llargs i uns altres més curts, amb forma de gemma (vegeu Fig. 17.3). Aquests resultats es poden comparar molt bé de manera qualitativa amb els experiments, per mostrar que el mecanisme de generació de tubs de membrana degut a l'existència de gradients de concentració de molècules amfífiles és plausible.

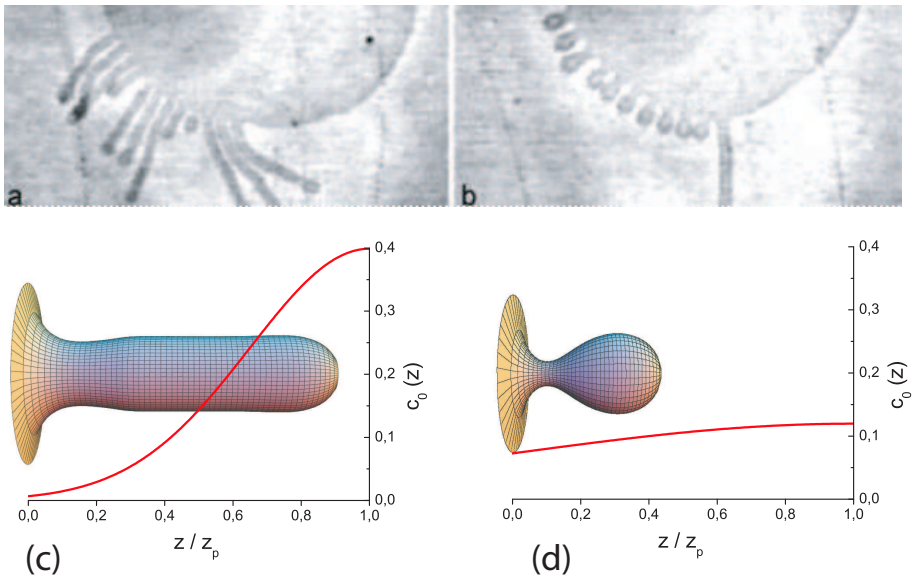

Figura 17.3 Tubs extrets d'una vesícula mitjançant una concentració no homogènia de polímers en el medi extravesicular. Comparativa entre els resultats experimentals de la Ref. [250] (a,b) i els resultats numèrics del model de camp de fase (c,d). A temps curts, obtenim tubs llargs (a,c), mentre que a temps llargs apareixen formes gemmades (b,d). També mostrem el perfil de curvatura espontània emprat en les integracions del camp de fase.

Aquests sistemes on s'estudien transicions morfològiques degudes a la inserció de polímers en membranes monocomponents són models simples per poder copsar els mecanismes físics subjacents en certs processos més complexos que succeeixen a la cèl·lula. Així, mecanismes de transport intracel·lular en el reticle endoplasmàtic i en l'aparell de Golgi són deguts a la generació de curvatura per part de proteïnes ancorades en les seves membranes. Amb el nostre estudi hem pretès entendre una mica millor aquests mecanismes, des d'un punt de vista físic i agafant els elements mínims essencials.

17.3 Tubs de membrana bifàsics periòdics

Anteriorment hem explicat com un sistema integrat per vesícules lípidiques fluïdes monocomponents i per polímers amfífils presenta una dinàmica morfològica molt rica. El fet d'introduir a les bicapes lípidiques un nou grau de complexitat, en aquell cas els polímers ancorats a la membrana, ha permès anar un grau més enllà en la direcció de la complexitat cel·lular.

En el Cap. 9, no tenim en compte la presència de possibles molècules generadores de curvatura, però enriquim la membrana fent-la pluricomponent. La presència de diversos tipus de lípids (recordem que en les membranes cel·lulars es compten per desenes) fa que el tractament físic de la membrana s'hagi de generalitzar. Per exemple, en mescles lipídiques composades per un fosfolípid insaturat (és a dir, amb algun doble enllaç entre els àtoms de carboni de les cues hidrofòbiques), un esfingolípid (un cert tipus de lípid de membrana) i colesterol, podem apreciar que es formen dominis de fases diferents. Concretament, s'observen dominis en la fase líquida desordenada (la fase fluïda que hem tractat anteriorment), però també en la fase líquida ordenada, en la qual la mobilitat dels lípids es redueix sense que aquests arribin a gelificar. En aquest sentit, s'ha discutit àmpliament en la literatura biològica l'existència dels anomenats rais lipídics, dominis funcionals que podrien existir *in vivo*. L'existència de dominis està clarament acceptada en mescles *in vitro*, una de les quals hem estudiat en aquesta tesi.

En concret ens hem basat en els estudis experimentals del grup de W. W. Webb [14], on observen per microscòpia confocal com es formen vesícules amb geometries diverses degudes a la separació de fases en el pla de la membrana. Més en concret encara, ens centrarem en l'existència de tubs periòdics bifàsics, en els quals s'alternen les dues fases amb una certa periodicitat, donada per una longitud d'ona (vegeu Fig. 17.4).

Físicament podem descriure les dues fases mitjançant diferents constants elàstiques. De fet, usant el formalisme de Canham-Helfrich, en aquesta situació tant el mòdul de rigidesa flectora, com el de rigidesa Gaussiana són

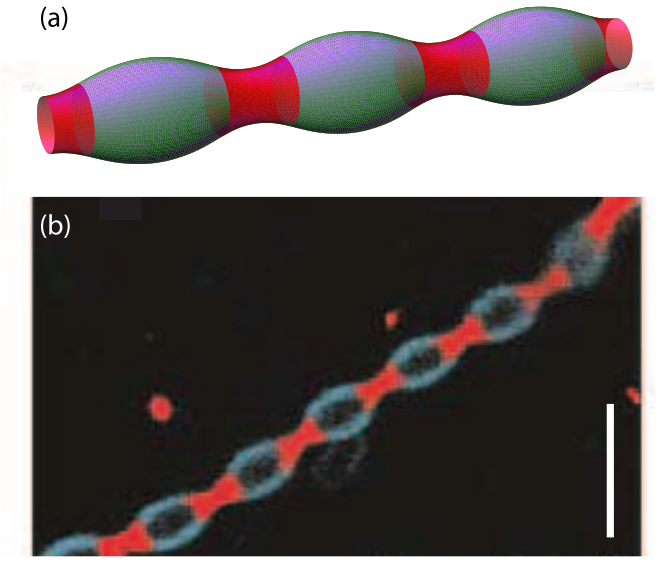

Figura 17.4 Tubs periòdics bifàsics. (a) Representació tridimensional del tub calculat numèricament, amb la longitud d'ona seleccionada energèticament. La fase blava (clara) correspon a la fase líquida ordenada, mentre que la vermella (fosca) ho fa a la líquida desordenada. (b) Imatge experimental d'un tub periòdic, extreta de la Ref. [14]. Escala: $5\ \mu$m.

diferents en una fase que en l'altra. Per tant, no podrem menystenir el terme de curvatura Gaussiana. L'energia del tub consisteix en l'energia de curvatura, Eq. (16.1), de cada fase i, a més, d'un terme de tensió de línia. La tensió de línia, anàloga bidimensional a la tensió superficial, existeix a causa del cost energètic que té la creació d'interfícies entre ambdues fases. A partir d'aquesta energia total, derivem les equacions d'Euler-Lagrange assumint simetria axial en la geometria del tub de membrana. A més, assumim que els tubs creats són prou llargs com per poder considerar-los infinits.

Tenint en compte certes consideracions tècniques sobre la derivació de les equacions d'Euler-Lagrange, obtenim l'anomenada equació de forma. Aquesta és una equació diferencial ordinària no-lineal de tercer ordre. Resolent aquesta equació, conjuntament amb unes certes condicions de contorn a la interfície, obtenim la forma d'energia mínima.

En aquesta tesi, hem resolt inicialment la versió lineal de l'equació de forma. Això ho podem fer analíticament. Després, per comparar els resultats, hem solucionat numèricament el problema, utilitzant el mètode de tir a un punt de fita [204]. Cal destacar el fet que, tant en una solució com en l'altra, en el règim de validesa de l'aproximació lineal, obtenim formes anàlogues pels tubs.

Sobre la longitud d'ona de la periodicitat cal dir que és, *a priori*, un paràmetre d'entrada a l'hora de resoldre les equacions. De totes maneres, veiem com la selecció d'aquesta longitud d'ona es fa energèticament *a posteriori*, ja que el

perfil d'energia en funció de la longitud d'ona té en certs casos un mínim per a una periodicitat finita. En la Fig. 17.4a mostrem la solució de longitud d'ona seleccionada emprant els paràmetres elàstics citats en els experiments de [14], i veiem com la coincidència amb aquests experiments és tant qualitativament com quantitativa remarcable.

Variant la composició de la membrana, és a dir, variant la fracció d'àrea entre la fase líquida ordenada i líquida desordenada, podem estudiar si existeix alguna longitud d'ona finita que sigui energèticament afavorida. Els nostres resultats mostren que en un gran rang de composicions, i per uns certs paràmetres elàstics, els tubs periòdics són favorables a una solució amb separació completa de fases.

17.4
Formes no circulars en dominis lipídics en monocapes

L'estudi de monocapes de lípids és una vessant molt important de la biofísica de membranes, ja que permet comprendre amb més profunditat les interaccions intermoleculars entre lípids i proteïnes. Les interaccions dipolars entre els lípids de membrana i la tensió de línia entre diferents dominis es troben entre aquestes interaccions, la competició de les quals crea dominis amb formes ben diverses, com les de les estrelles de mar, formes amb quatre braços o el·lipses, per citar-ne algunes.

Així, en el Cap. 10 estudiem aquestes formes que es creen en monocapes purament lipídiques a causa d'aquestes dues interaccions. Per tractar el problema de la forma, assumim que aquesta es pot descriure per mitjà de la interacció dipolar –repulsiva i de llarg abast– i per un terme que penalitza la separació de fases.

L'energia lliure de la monocapa que d'això en resulta pot ser desenvolupada en sèrie, de manera que una aproximació a segon ordre, deguda a Iwamoto i Zhong-can [125], pot escriure's com un anàleg bidimensional a l'energia de curvatura de Canham-Helfrich, Eq. (16.1), amb un terme de tensió de línia. Aquest desenvolupament renormalitza les constants elàstiques, de manera que la tensió de línia ara té un terme que depèn de la polarització i de la longitud de la interfície. Això implica que aquesta tensió efectiva pot tant ser positiva com ser negativa, donant lloc a estructures no circulars i ramificades.

El nostre model dinàmic de camp de fase que ens havia servit, en la primera Part de la tesi, per estudiar les formes de les vesícules, ens és útil en aquest punt per a estudiar les formes dels dominis. Així doncs, depenent dels valors de la polarització i de la tensió de línia, trobem diverses formes, i les comparem amb resultats experimentals, com mostrem en un exemple a la Fig. 17.5.

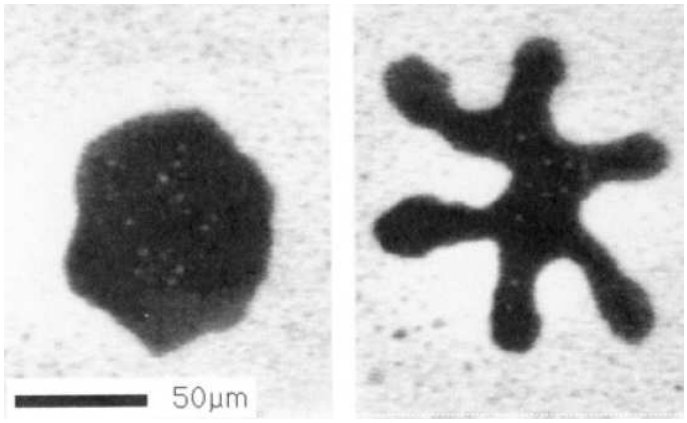

(a) Figures experimentals, de la Ref. [152]

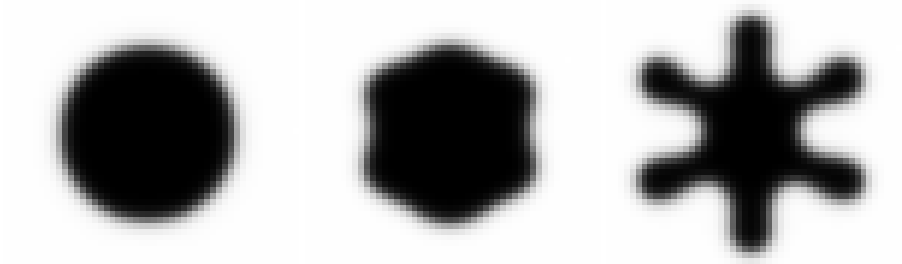

(b) condició inicial (c) $3.6 \times 10^4 \Delta t$ (d) $7.2 \times 10^4 \Delta t$

Figura 17.5 Dominis en forma d'estrella de mar. (a) Figures experimentals de la Ref. [152], que mostren la transició morfològica entre un domini circular inicial (no es mostra) a una forma d'estrella de mar (dreta), mitjançant una forma intermèdia quasi-hexagonal (esquerre), en una monocapa composada per una mescla binària de DMPC i dihydrocolesterol. (b-d) Tres imatges de la integració numèrica de l'equació dinàmica pel camp de fase, on un domini circular inicialment inestable evoluciona cap a una forma d'estrella de mar. $\Delta t = 10^{-3}$.

17.5 Mecanismes de generació de curvatura per proteïnes

Abans, quan hem parlat d'inestabilitats dinàmiques com ara el perlatge o la tubulació, hem assumit que la inserció de grups hidrofòbics en el si de la bicapa generava curvatura espontània. Ara ens fixem per mitjà de quins mecanismes microscòpic certes proteïnes poden generar aquesta curvatura.

Moltes de les membranes que troben a les cèl·lules contenen regions molt corbades, en les quals l'aproximació de Canham-Helfrich –vàlida per a radis de curvatura relativament petits en comparació amb el gruix de la bicapa– no es pot aplicar. El fet que les membranes es resisteixin en general a la curvatura fa que aquesta s'hi hagi de produir activament. Hi ha diversos mecanismes pels quals es pot generar curvatura [171, 263], ja sigui mitjançant la pròpia composició lipídica de la bicapa, per l'activitat del citoesquelet o per proteïnes de forma cònica que travessen d'una banda a l'altra la membrana. A més, algunes proteïnes tenen dominis amb una certa curvatura intrínseca, que s'associen amb la membrana adjuntant-s'hi com una bastida. Els anomenats dominis BAR, tenen una forma de mitja lluna i estan involucrats en fenòmens de vesiculació i tubulació intracel·lulars. Es creu que generen curvatura per mitjà del mecanisme de bastida.

Un altre mecanisme de generació de curvatura per part de proteïnes és el d'inserció hidrofòbica. Aquest mecanisme és el que hem assumit en la primera Part de la tesi que utilitzen certs polímers amb grups hidrofòbics per induir curvatura a la membrana. La inserció poc profunda de dominis amfífils, com ara les hèlices-α, creen una asimetria dins la monocapa exterior de la membrana. L'efecte falca que fan separa lleugerament els caps polars dels lípids, mentre que les cues romanen més o menys properes i es genera així una certa curvatura.

Moltes proteïnes generen curvatura gràcies a més d'un d'aquests mecanismes. Per exemple, les proteïnes que contenen els anomenats dominis N-BAR, com l'endofilina o l'amfifisina. Aquests dominis consten d'un domini BAR amb un cert nombre d'hèlices-α, així que *a priori* poden generar curvatura mitjançant tant el mecanisme de bastida com el d'inserció hidrofòbica. Aquestes hèlices, segons se'n desprèn dels resultats experimentals, s'insereixen a la bicapa de manera que el seu centre queda alineat amb el grup fosfat dels lípids de la monocapa externa. Aquesta inserció és essencial per a la formació de tubs de membrana d'uns $35 - 50$ nm. de diàmetre, que es transformen en vesícules del mateix diàmetre quan s'incrementa la concentració de proteïna a la membrana [98, 195].

En el Cap. 12 estudiem de manera quantitativa el mecanisme d'inserció hidrofòbica. Per tal d'assolir aquest objectiu, necessitem anar més enllà del model elàstic de Canham-Helfrich Eq. (16.1). A més, hem de tenir en compte l'estructura interna de la bicapa, ja que la inserció del grup hidrofòbic a la membrana és tant sols parcial.

De totes maneres, podem intuir com han d'anar els trets de manera qualitativa. Primer de tot, però, hem de diferenciar dos tipus de membranes segons com s'acoblen lateralment. En la major part de les situacions biològicament rellevants, la inserció d'aquests dominis es fa únicament de forma local en algun fragment petit d'una membrana més àmplia. Les dues mono-

capes d'aquest fragment de membrana on s'han ancorat les proteïnes poden intercanviar independentment lípids amb la resta de la membrana, que actua com un reservori de lípids. Això fa que no hi hagi cap acoblament en el pla entre les dues monocapes. Direm, doncs, que les monocapes estan *lateralment desacoblades*. Aquest acoblament juga un paper quan les proteïnes s'insereixen al llarg de tota l'àrea d'una membrana tancada, com en els experiments *in vitro* que hem esmentat abans [98, 195]. Com que no hi ha cap reservori de lípids, en aquest cas l'expansió d'una monocapa no es pot dur a terme independentment de l'altra. Direm que les monocapes estan *lateralment acoblades*. En la Fig. 17.6 mostrem diagrames qualitatius de com es corba la membrana depenent de la profunditat d'inserció de la partícula.

Com dèiem abans, per tal d'estudiar de manera quantitativa aquest fenomen, necessitem un model elàstic per descriure la monocapa. Nosaltres hem considerat la monocapa com una capa tridimensional amb gruix finit i propietats elàstics de volum. Fent servir la teoria clàssica d'elasticitat [146], utilitzant criteris de simetria i el fet que la membrana no resisteix l'esforç de cisallament lateral, podem escriure la densitat d'energia elàstica com

$$f = \frac{1}{2}\lambda_{xxxx}\left(u_{xx}+u_{yy}\right)^2 + \frac{1}{2}\lambda_{zzzz}u_{zz}^2 + \lambda_{xxzz}(u_{xx}+u_{yy})u^{zz} + 2\lambda_{xzxz}\left(u_{xz}^2+u_{yz}^2\right), \tag{17.4}$$

on u_{ik} són les components del tensor de deformacions [146], i els quatre únics mòduls elàstics independents són λ_{xxxx}, λ_{zzzz}, λ_{xxzz} i λ_{xzxz}. A més, hem fet estimacions d'aquests mòduls elàstics basant-nos en les mesures experimentals que hi ha a la literatura. La solució de mínima energia, de nou, ens dóna la configuració de les deformacions a la membrana.

Utilitzant COMSOL Multiphysics, un programari de resolució de problemes fisicomatemàtics mitjançant el mètode dels elements finits, hem resolt el problema en diverses situacions i consideracions. En la Fig. 17.7 mostrem la solució de mínima energia de bicapes tant acoblades com desacoblades lateralment, quan una certa concentració de partícules s'hi insereix.

D'aquests resultats veiem que els esforços i deformacions interns de les monocapes són màxims prop de les inclusions i que decauen amb una escala de longitud característica. Podem doncs definir una curvatura espontània induïda per aquestes inclusions. Fent càlculs per a diverses profunditats d'inserció podem traçar una gràfica de la curvatura espontània efectiva per partícula en funció de la profunditat d'inserció. Tant en el cas de monocapes lateralment acoblades con en el de desacoblades, la màxima curvatura generada correspon aproximadament a la profunditat d'inserció de les hèlices-α, del voltant del 40 % del gruix de la monocapa. En el primer cas aquesta val $0.50\ \mathrm{nm}^{-1}$, mentre que en el segon és de $0.75\ \mathrm{nm}^{-1}$. A part, també podem calcular el

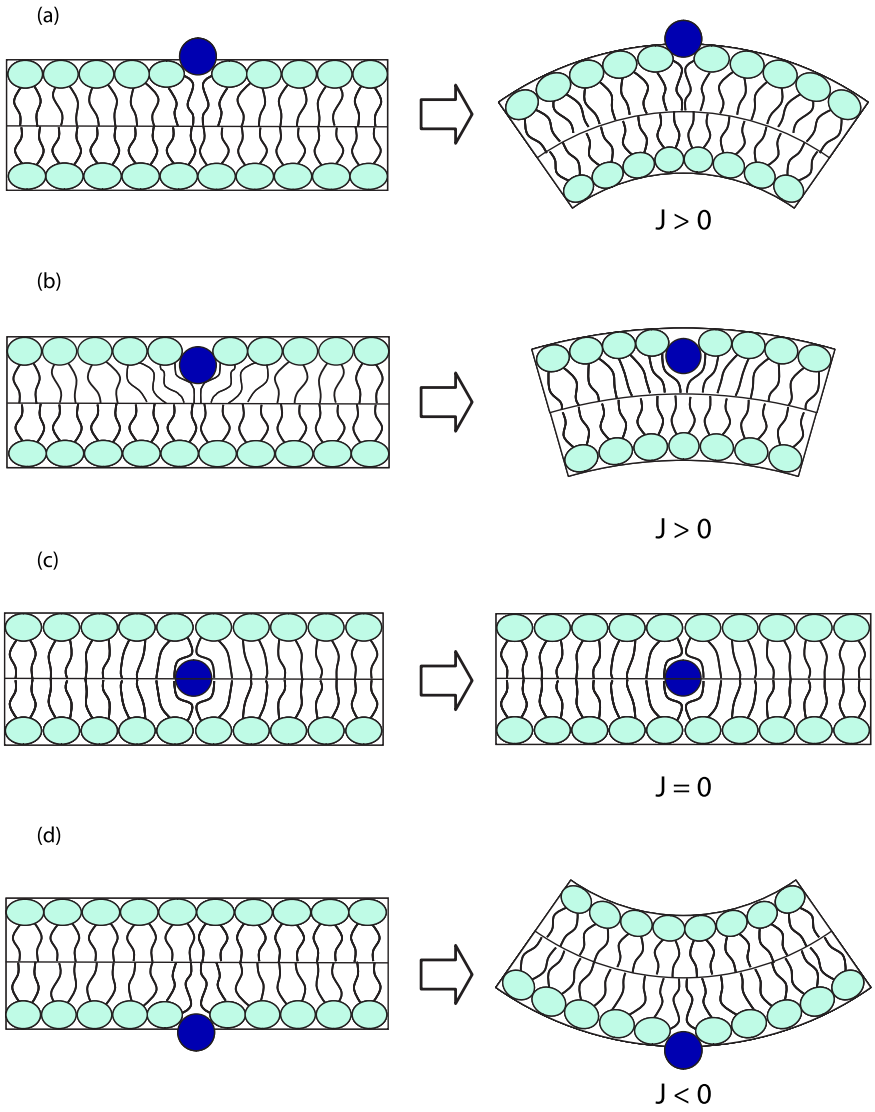

Figura 17.6 Essència qualitativa del mecanisme de generació de curvatura per petites partícules cilíndriques. El cas de monocapes lateralment acoblades. (a) Una inserció poc profunda expandeix la monocapa superior de la membrana (esquerra). La relaxació parcial dels esforços generats dóna com a resultat una curvatura positiva ($J > 0$) (dreta). (b) Insercions més profundes produeixen una expansió de la monocapa superior (esquerra), que degut a l'acoblament lateral genera esforços a la monocapa inferior, conduint a curvatura positiva (dreta). (c) Quan la inserció s'alinea amb el pla mig de la membrana, els esforços generats estan distribuïts simètricament, causant una expansió global de la membrana, però sense generar curvatura ($J = 0$). (d) Si la inserció es troba en la monocapa inferior, aquesta expandeix la part inferior de la membrana, generant-se així curvatura negativa ($J < 0$).

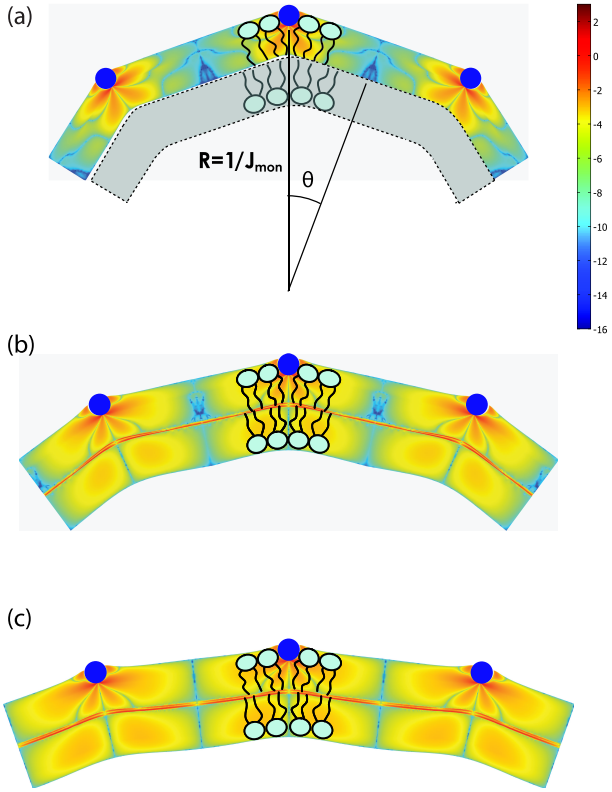

Figura 17.7 Conformació típica d'una membrana amb inclusions cilíndriques (blau marí). (a) El cas de monocapes lateralment desacoblades (on no es considera que la segona monocapa influenciï la capacitat de corbar-se de la primera). La forma de la membrana es correspon amb la forma preferida de la monocapa superior que conté les inclusions, com si la monocapa inferior (en gris) no resistís curvatura i senzillament encaixés amb l'altra. (b) El cas de monocapes lateralment desacoblades. La forma de la membrana ve determinada per la interacció entre la tendència de la monocapa superior a adoptar la conformació presentada a (a) i la resistència de la monocapa inferior a corbar-se. (c) El cas de monocapes lateralment acoblades. L'esforç de cisallament (adimensional) en les monocapes està representat per una escala de colors logarítmica.

cost energètic que té la inserció d'aquestes partícules, sent aquest de l'ordre de $1-2\,k_BT/\mathrm{nm}$.

Aquests resultats mostren que pel que fa als possibles mecanismes de generació de curvatura de proteïnes amb dominis N-BAR, el d'inserció hidrofòbica és capaç ell sol de crear els intermediaris de transport observats experimentalment [98, 195], tant en el cas de l'endofilina com en el de l'amfifisina. A més, veiem que aquest mecanisme és més potent que els lípids en si a l'hora de generar curvatura a la membrana.

Posteriorment, en el Cap. 13, presentem nous resultats per sistemes tridimensionals, veient que també es pot definir una curvatura espontània per partícula. A més, encara que la geometria de la partícula no tingui simetria axial, a partir d'una certa longitud característica, la curvatura generada passa a tenir aquesta simetria. També estudiem els efectes energètics que té el fet d'inserir partícules en membranes amb una certa curvatura. Amb això pretenem entendre el concepte de *determinació* de curvatura. Experimentalment es veu que certes proteïnes tenen una afinitat més gran en associar-se en vesícules molt corbades que en vesícules poc corbades [71]. En el marc del nostre model microscòpic per la membrana, i amb la comprensió quantitativa del mecanisme d'inserció hidrofòbica, podem entendre aquest fet. Comparant amb els experiments veiem un bon acord d'aquests amb les nostres previsions teòriques.

18
Conclusions

El fil conductor d'aquesta tesi ha estat el fet d'intentar comprendre quins mecanismes físics donen forma a les entitats biològiques recobertes per una membrana, com poden ser els orgànuls cel·lulars o els liposomes. Així doncs, hem estudiat teòricament diverses formes que adquireixen les membranes en situacions variades.

Una membrana biològica és un complex format per molts tipus diferents de molècules bioquímiques. L'estructura bàsica de les membranes és una bicapa lipídica, que pot estar formada per desenes de lípids diferents. A més, les bicapes lipídiques poden contenir dominis de fases diferents, ja siguin líquids, tipus gel, o fins i tot, sòlids. A més a més, les membranes biològiques també contenen un gran nombre de proteïnes. Aquestes proteïnes no només doten d'una certa funcionalitat les membranes, també poden veure's involucrades a mantenir, generar o estabilitzar la pròpia geometria de la membrana.

Per aquests motius, en aquesta tesi hem estudiat sistemes senzills però amb afegitons diferents que enriqueixen la complexitat del sistema en qüestió. Ja sigui l'efecte dinàmic en la forma de vesícules oblongues o tubulars, a causa de l'ancoratge de polímers amfífils; ja sigui la forma de tubs bifàsics periòdics formats a causa de la competició entre l'energia interficial entre dominis i l'energia de curvatura; o ja sigui l'estudi microscòpic dels mecanismes de generació i determinació de curvatura per part de la inserció de petites hèlices en el si de la membrana, tots aquests sistemes ens han permès entendre una mica més certs fenomens de morfologia intracel·lular, sense deixar-nos de meravellar per la gran riquesa de les formes a les cèl·lules.

A
Differential geometry of surfaces

A two-dimensional well-behaved surface embedded in Euclidean three-dimensional space, $\mathbb{R}^3$, is mathematically defined univocally by a vector field $\boldsymbol{R}$

$$\begin{aligned} \boldsymbol{R} : \Sigma \subset \mathbb{R}^2 &\longrightarrow \mathbb{R}^3 \\ \boldsymbol{\sigma} = (\sigma^1, \sigma^2) \in \mathbb{R}^2 &\longmapsto \boldsymbol{R}(\boldsymbol{\sigma}) \in \mathbb{R}^3, \end{aligned} \tag{A.1}$$

which maps a two-dimensional coordinate system, $\boldsymbol{\sigma} = (\sigma^1, \sigma^2) \in \Sigma$, onto a surface embedded in the three-dimensional space. This way of defining a surface is called the parametric form, since one needs a two-dimensional coordinate system to parametrize the surface. A surface can also be described by the so-called implicit form, i.e., by all the points in $\mathbb{R}^3$ that satisfy the surface equation $F(x, y, z) = 0$ [24].

A.1
Parametric form

Assume a surface defined in the parametric form. At each point P of this surface, a tangent plane is defined by two tangent vectors (see Fig. A.1) as

$$\boldsymbol{t}_i = \partial_i \boldsymbol{R}(\boldsymbol{\sigma}) = \frac{\partial \boldsymbol{R}}{\partial \sigma^i}, \quad i = 1, 2. \tag{A.2}$$

The scalar product of these tangent vectors defines the covariant metric tensor,

$$g_{ik}(\boldsymbol{\sigma}) = \boldsymbol{t}_i \cdot \boldsymbol{t}_k = \partial_i \boldsymbol{R} \cdot \partial_k \boldsymbol{R}. \tag{A.3}$$

The contravariant metric tensor is defined as

$$g^{ik} = (g^{-1})_{ik}, \tag{A.4}$$

which implies that

$$g^{ik} g_{kl} = \delta^i_{\ l}, \tag{A.5}$$

where δ is the Kronecker delta, and the Einstein summation convention, $c_i x^i \equiv \sum_i c_i x^i$, is used. From the metric tensor, the Euclidean distance between two infinitesimally close points on the surface, ds, can be calculated as

$$\mathrm{d}s^2 = [\boldsymbol{R}(\boldsymbol{\sigma} + \mathrm{d}\boldsymbol{\sigma}) - \boldsymbol{R}(\boldsymbol{\sigma})]^2 = g_{ik}(\boldsymbol{\sigma})\mathrm{d}\sigma^i \mathrm{d}\sigma^k. \tag{A.6}$$

Also, the infinitesimal area element can be found

$$\mathrm{d}S = \left| \boldsymbol{t}_1 \mathrm{d}\sigma^1 \times \boldsymbol{t}_2 \mathrm{d}\sigma^2 \right| = \sqrt{\det(g_{ik})}\mathrm{d}\sigma^1 \mathrm{d}\sigma^2. \tag{A.7}$$

At any point P on the surface, a unit normal vector perpendicular to the tangent plane can be defined (Fig. A.1). Due to the properties of the cross product, it is given by

$$\hat{\boldsymbol{n}} = \frac{\boldsymbol{t}_1 \times \boldsymbol{t}_2}{|\boldsymbol{t}_1 \times \boldsymbol{t}_2|}, \tag{A.8}$$

where the sign is arbitrarily chosen, so is the election of which coordinate is named σ^1 and which σ^2. The unit normal vector has remarkable properties in our context, since its changes along the surface define the so-called curvature tensor, K,

$$\partial_i \hat{\boldsymbol{n}} = K_{ik}\boldsymbol{t}^k = K_{ik} g^{kl} \boldsymbol{t}_l = K_i^k \boldsymbol{t}_k. \tag{A.9}$$

The sign of the curvature tensor is, again, arbitrary. In this thesis, we choose it in such a way that sphere-like curvatures are positive, as it is a normal convention in physics. In mathematical literature the sign is most often taken in the opposite way.

The curvature tensor is symmetric and diagonalizable. The two eigenvalues are the so-called principal curvatures, $c_1 = 1/R_1$, and $c_2 = 1/R_2$ (see Fig. A.1). These curvatures correspond to the inverse of the two principal radii of curvature of the surface at the given point. The two invariants of the curvature tensor, K, are its trace, J, and its determinant, K. The trace is called total curvature of the surface, J, and is represented by

$$\mathsf{J} \equiv \operatorname{tr} K_i^k = c_1 + c_2 = \frac{1}{R_1} + \frac{1}{R_2}. \tag{A.10}$$

Usually, the so-called mean curvature, H is also used to refer to this invariant, and is defined as the arithmetic mean of the principal curvatures, corresponding to half the total curvature,

$$\mathsf{H} = \frac{1}{2}(c_1 + c_2) = \frac{1}{2}\left(\frac{1}{R_1} + \frac{1}{R_2}\right). \tag{A.11}$$

The other invariant, the determinant, is called Gaussian curvature of the surface, K, and is given by the product of the principal curvatures,

$$\mathsf{K} = \det K_i^k = c_1\, c_2 = \frac{1}{R_1\, R_2}. \tag{A.12}$$

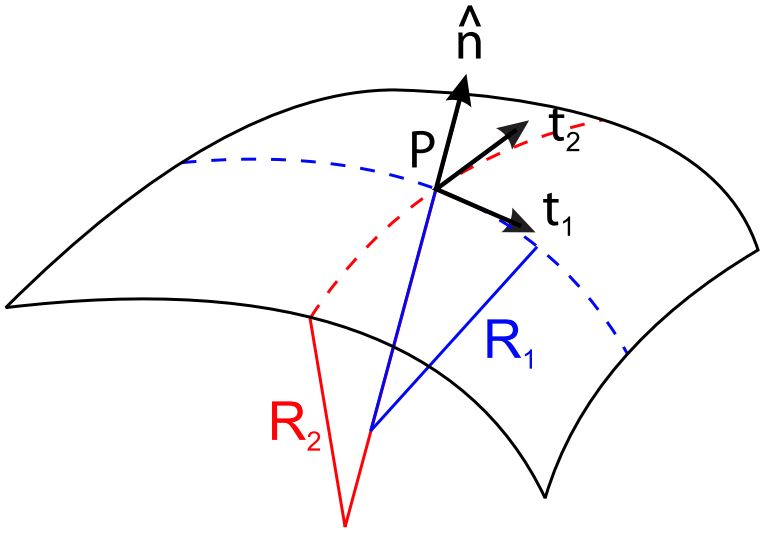

Figure A.1 Differential geometry of a surface. In the point P, two tangent vectors, $\boldsymbol{t}_1$ and $\boldsymbol{t}_2$, are defined. From them, a unit normal vector $\hat{\boldsymbol{n}}$ is constructed, pointing outwards. Also, two radii of curvature, R_1 and R_2, are geometrically traced at each point.

For a discussion on the signs of the curvatures depending on the different kinds of shapes, see Fig. A.2.

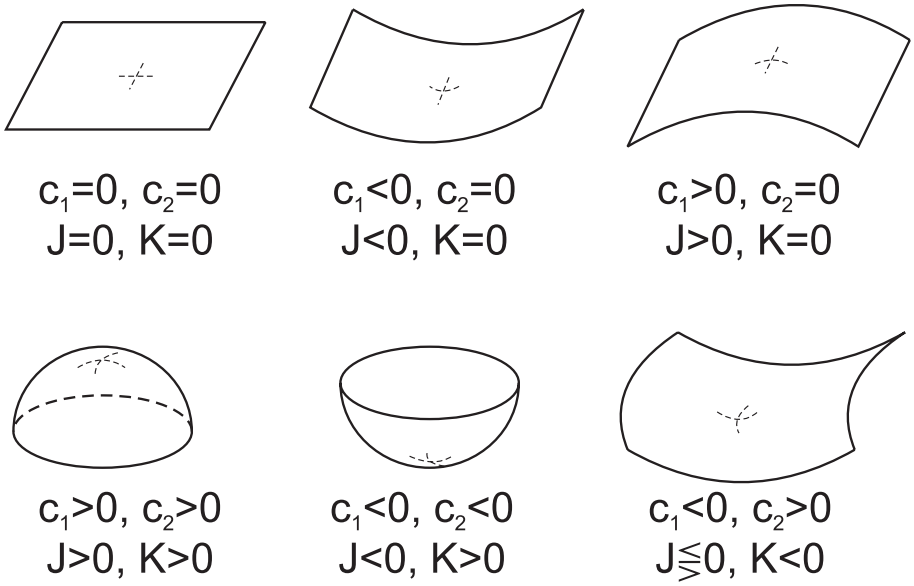

Figure A.2 Different kinds of surfaces classified by their curvatures. Depending on the sign of the two principal curvatures, different kinds of surface have positive/zero/negative combinations of the total and Gaussian curvatures, as written in the Figure.

A.1.1 Monge parametrization

All the definitions in the previous Section are general for any surface defined by a parametric form. A simple but useful example of a parametrization is one where the σ coordinates are nothing else than the x, y Cartesian coordinates, and the vector field describing the surface is

$$\boldsymbol{R}(x,y) = (x, y, h(x,y))\,, \tag{A.13}$$

where the third Cartesian coordinate, the *height*, is $z = h(x,y)$. This is called the Monge parametrization, named after the French mathematician Gaspard Monge. Under this parametrization, which is definitely valid for almost planar surfaces (the height function $h(x,y)$ has to be univaluated), the tangent vectors Eq. (A.2) are

$$\begin{aligned} \boldsymbol{t}_1(x,y) &= \partial_x \boldsymbol{R}(x,y) = \left(1, 0, \frac{\partial h(x,y)}{\partial x}\right), \\ \boldsymbol{t}_2(x,y) &= \partial_y \boldsymbol{R}(x,y) = \left(0, 1, \frac{\partial h(x,y)}{\partial y}\right), \end{aligned} \tag{A.14}$$

and the covariant metric tensor

$$g_{ik} = \begin{pmatrix} 1 + \left(\frac{\partial h(x,y)}{\partial x}\right)^2 & \frac{\partial h(x,y)}{\partial x}\frac{\partial h(x,y)}{\partial y} \\ \frac{\partial h(x,y)}{\partial x}\frac{\partial h(x,y)}{\partial y} & 1 + \left(\frac{\partial h(x,y)}{\partial y}\right)^2 \end{pmatrix}, \tag{A.15}$$

with determinant

$$\det(g_{ik}) = 1 + [\boldsymbol{\nabla} h(x,y)]^2\,. \tag{A.16}$$

The normal vector Eq. (A.8) is

$$\hat{\boldsymbol{n}} = \frac{\left(-\frac{\partial h(x,y)}{\partial x}, -\frac{\partial h(x,y)}{\partial y}, 1\right)}{\sqrt{1 + (\boldsymbol{\nabla} h)^2}}. \tag{A.17}$$

Wherefrom the total and Gaussian curvatures can be calculated:

$$\mathsf{J} = -\frac{\left(1 + h_x^2\right)\, h_{yy} + \left(1 + h_y^2\right)\, h_{xx} - 2 h_x h_y h_{xy}}{\left(1 + h_x^2 + h_y^2\right)^{3/2}}, \tag{A.18}$$

$$\mathsf{K} = \frac{h_{xx}\, h_{yy} - h_{xy}^2}{\left(1 + h_x^2 + h_y^2\right)^2}. \tag{A.19}$$

In the limit of nearly flat surface, where $h_x \ll 1$, and $h_y \ll 1$, the curvature invariants read

$$\mathsf{J} \approx -\left(h_{xx} + h_{yy}\right) = -\boldsymbol{\nabla}^2 h(x,y), \tag{A.20}$$

and

$$\mathsf{K} \approx h_{xx}h_{yy} - h_{xy}^2. \tag{A.21}$$

A.1.2 Axisymmetric surfaces

Consider another kind of parametrization given by the polar cylindrical coordinates of an axisymmetric surface, $\{\sigma^1 = r, \sigma^2 = \theta\}$. Such surface is described by a function $f(r)$ along the axis of revolution ($r = 0$). The position vector for such a surface is

$$\boldsymbol{R}(r,\theta) = \left(r, f(r)\cos\theta, f(r)\sin\theta\right). \tag{A.22}$$

The tangent vectors in this case are found by applying Eq. (A.2),

$$\begin{aligned} \boldsymbol{t}_1 &= \partial_r \boldsymbol{R} = \left(1, f'(r)\cos\theta, f'(r)\sin\theta\right), \\ \boldsymbol{t}_2 &= \partial_\theta \boldsymbol{R} = \left(0, -f(r)\sin\theta, f(r)\cos\theta\right). \end{aligned} \tag{A.23}$$

The covariant metric tensor is given by the dot product of the tangent vectors Eq. (A.3),

$$g_{ik} = \begin{pmatrix} 1 + [f'(r)]^2 & 0 \\ 0 & f^2(r) \end{pmatrix}, \tag{A.24}$$

whose determinant is

$$\det g_{ik} = f^2(r)\left(1 + \left[f'(r)\right]^2\right), \tag{A.25}$$

from where the infinitesimal area element Eq. (A.7) can be calculated, as

$$\mathrm{d}S = f(r)\sqrt{1 + [f'(r)]^2}\,\mathrm{d}r\mathrm{d}\theta. \tag{A.26}$$

The contravariant metric tensor is the inverse of the covariant one, Eq. (A.24):

$$g^{ik} = \begin{pmatrix} \frac{1}{1+[f'(r)]^2} & 0 \\ 0 & \frac{1}{f^2(r)} \end{pmatrix}. \tag{A.27}$$

On the other hand, the normal vector is given by the normalized cross product of the tangent vectors, Eq. (A.8),

$$\hat{\boldsymbol{n}} = \frac{(f'(r), -\cos\theta, -\sin\theta)}{\sqrt{1 + [f'(r)]^2}}. \tag{A.28}$$

The metric tensor can therefore be calculated, and, in its covariant form, reads

$$K_{ik} = \frac{1}{\sqrt{1+[f'(r)]^2}} \begin{pmatrix} -f''(r) & 0 \\ 0 & f(r) \end{pmatrix}. \tag{A.29}$$

Rising one of the indexes by means of the metric tensor, the mixed curvature tensor results from Eqs. (A.29), (A.4), in

$$K_i^k = K_{il}\, g^{lk} = \begin{pmatrix} -\frac{f''(r)}{\left[1+[f'(r)]^2\right]^{3/2}} & 0 \\ 0 & \frac{1}{f(r)\sqrt{1+[f'(r)]^2}} \end{pmatrix}. \tag{A.30}$$

The total and Gaussian curvatures are then easily found as

$$\mathsf{J} = \frac{1 - f(r)\, f''(r) + [f'(r)]^2}{f(r)\left(1+[f'(r)]^2\right)^{3/2}}, \tag{A.31}$$

and

$$\mathsf{K} = -\frac{f''(r)}{f(r)\left(1+[f'(r)]^2\right)^2}. \tag{A.32}$$

A.2 Implicit form

In the case where a two-dimensional surface is implicitly defined by a function F such as

$$F(x,y,z) = 0, \tag{A.33}$$

we can also find the curvature tensor and all the geometric properties of such a surface. First, we have to note that, since the surface is defined by the level-set of a function, this function is constant on the surface, therefore

$$\mathrm{d}F(x,y,x) = \mathrm{d}\boldsymbol{r} \cdot \boldsymbol{\nabla} F = 0, \tag{A.34}$$

where $\mathrm{d}\boldsymbol{r}$ is a vector which connects any two points in this surface, being tangent to a certain direction in the surface. Because of this fact, from Eq. (A.34) we infer that the vector $\boldsymbol{\nabla} F$ is normal to the surface at the point (x,y,z). The unit normal vector is found by normalizing it,

$$\hat{\boldsymbol{n}} = \frac{\boldsymbol{\nabla} F}{|\boldsymbol{\nabla} F|}. \tag{A.35}$$

Once the normal vector is known, the curvature tensor, Q, can be defined by the changes of this vector along the tangent directions, namely

$$\mathrm{d}\hat{\boldsymbol{n}} = \mathrm{d}\boldsymbol{r} : \mathsf{Q} \tag{A.36}$$

where the colon symbolizes tensor contraction. By differentiating Eq. (A.35), we can write the curvature tensor as a function of the derivatives of the implicit function as

$$\mathsf{Q}_{ik} = \frac{1}{\mathrm{Y}}\left[F_{ik} - \frac{F_i\,\mathrm{Y}_k}{\mathrm{Y}}\right], \tag{A.37}$$

where $\mathrm{Y} = |\boldsymbol{\nabla} F|$, and $F_i = \boldsymbol{\nabla} F|_i$. Note that this curvature tensor Q differs from the curvature tensor K_{ik} (Eq. (A.9)) we used in the previous Section. The former being represented by a 3×3 matrix, and the latter by a 2×2 matrix. Here, the tensor has three invariants, although one of them is a trivial one (the determinant of the tensor is zero [218]). The other two, the trace and the sum of the principal minors, define the total and Gaussian curvatures, respectively. They read as

$$\mathsf{J} = \frac{1}{\mathrm{Y}^3}\left[F_{ii}\left(F_k^2 + F_l^2\right) - 2F_iF_kF_{ik}\right]\tilde{\varepsilon}^{ikl}, \tag{A.38}$$

where $\tilde{\varepsilon}^{ikl}$ is a modified Levi-Civita symbol, such as $\tilde{\varepsilon}^{ikl} = 1$ for all even permutations of the indices, and zero otherwise. The Gaussian curvature is, similarly, given by

$$\mathsf{K} = \frac{1}{\mathrm{Y}^4}\left[F_{ii}F_{kk}F_l^2 - F_{ik}^2F_l^2 + 2F_{il}F_i\left(F_kF_{kl} - F_lF_{kk}\right)\right]\tilde{\varepsilon}^{ikl}. \tag{A.39}$$

The Monge representation can also be implemented by using an implicit form of the surface, by defining the function

$$F(x, y, z) = z - h(x, y). \tag{A.40}$$

A.3 Parallel surfaces

Consider a surface created by translating each point of an initial surface a certain distance δ along the normal direction, i.e.

$$\boldsymbol{R}'(\sigma^1, \sigma^2) = \boldsymbol{R}(\sigma^1, \sigma^2) + \delta\,\hat{\boldsymbol{n}}(\sigma^1, \sigma^2), \tag{A.41}$$

where primes denote the translated surface. These two surfaces are called parallel surfaces. It is useful in some cases to relate the geometric properties, such as the area element or the curvatures, of these surface to each other. Let

us work out the infinitesimal area element, $\mathrm{d}A'$, of the parallel surface. We will use here the Monge gauge. In this gauge, the position vector of the new surface, $\boldsymbol{R}'(x,y)$, given by Eq. (A.41), is

$$\boldsymbol{R}'(x,y) = \left(x - \delta\frac{h_x}{\sqrt{N}}, y - \delta\frac{h_y}{\sqrt{N}}, h + \frac{\delta}{\sqrt{N}}\right), \tag{A.42}$$

where we defined $N \equiv 1 + (\boldsymbol{\nabla} h)^2$, and the normal vector of the original surface is given in the Monge parametrization by Eq. (A.17). The new tangent vectors are

$$\boldsymbol{t}_1' = \left(1 - \delta\left(\frac{h_{xx}N - h_x^2 h_{xx}}{N^{3/2}}\right), -\delta\frac{h_{xy}\sqrt{N} - h_x h_y}{N}, h_x - \delta\frac{h_x h_{xx}}{N^{3/2}}\right), \tag{A.43}$$

which, for small curvatures, $h_x,\ h_y \ll 1$, simplify to

$$\boldsymbol{t}_1' = \left(1 - \delta\frac{h_{xx}}{\sqrt{N}}, -\delta\frac{h_{xy}}{\sqrt{N}}, 0\right). \tag{A.44}$$

Similarly, for the other tangent vector:

$$\boldsymbol{t}_2' = \left(-\delta\frac{h_{xy}}{\sqrt{N}}, 1 - \delta\frac{h_{yy}}{\sqrt{N}}, 0\right). \tag{A.45}$$

The infinitesimal area element of the parallel surface can be calculated according to Eq. (A.7), is

$$\mathrm{d}S' = \left|\boldsymbol{t}_1' \times \boldsymbol{t}_2'\right| \mathrm{d}x\mathrm{d}y, \tag{A.46}$$

which, for small displacements, using that $N \sim 1$, we get

$$\mathrm{d}S' = \left(1 + \mathsf{J}\,\delta + \mathsf{K}\,\delta^2\right) \mathrm{d}x\mathrm{d}y, \tag{A.47}$$

and, since in this limit, $\mathrm{d}S = \mathrm{d}x\mathrm{d}y$, we find the expected result,

$$\mathrm{d}S' = \mathrm{d}S\left(1 + \mathsf{J}\,\delta + \mathsf{K}\,\delta^2\right). \tag{A.48}$$

Similar derivations [101] can be made for the total and Gaussian curvatures, leading to the following results:

$$\mathsf{J}' = \frac{\mathsf{J} + 2\mathsf{K}\,\delta}{1 + \mathsf{J}\,\delta + \mathsf{K}\,\delta^2}, \tag{A.49}$$

$$\mathsf{K}' = \frac{\mathsf{K}}{1 + \mathsf{J}\,\delta + \mathsf{K}\,\delta^2}. \tag{A.50}$$

B
Lagrange multipliers theory

In this Appendix, we briefly review Lagrange multipliers theory, including some basics and fundamental definitions, as well as presenting algorithms and numerical schemes. Further information and broader explanations, as well as proofs of some of the theorem here presented, can be found in Ref. [19].

B.1
Introduction

We want to find a local minimum of a certain function, f,

$$\begin{aligned} &f : \mathbb{R}^n \longrightarrow \mathbb{R} \\ &x \longmapsto f(x), \end{aligned} \tag{B.1}$$

subject to some constraints $h_i(x) = 0$, such that

$$\begin{aligned} &h_i : \mathbb{R}^n \longrightarrow \mathbb{R} \\ &x \longmapsto h_i(x), \end{aligned} \tag{B.2}$$

for $i = 1, \ldots, m$. Here, we only enunciate a part of a theorem on necessary conditions of global minima of the above problem. To see a rigorous formulation and a proof of this theorem, see Ref. [19].

Theorem B.1 (Lagrange multiplier theorem – necessary conditions) *Let x^* be a local minimum of f subject to $h_i(x) = 0$, and assume $\{\nabla h_i(x^*)\}$ is a linearly independent set. Then $\exists!\quad \lambda^* = (\lambda_1^*, \ldots, \lambda_m^*)$ such that*

$$\nabla f(x^*) + \sum_{i=1}^{m} \lambda_i^* \nabla h_i(x^*) = 0. \tag{B.3}$$

B.1.1
The penalty approach

This approach consists in approximating the constrained problem by an unconstrained one. In order to do so, we introduce the so-called cost functions,

F^k, for $k = 1, 2, \ldots$, as

$$F^k(x) := f(x) + \frac{k}{2}\|h(x)\|^2 + \frac{\alpha}{2}\|x - x^*\|^2, \tag{B.4}$$

where the second term is a penalty temr which takes into account possible violations of the constraints; and the last term is just included for technical proof-related reasons [19].

The minimization of this function, F, is strictly equivalent to the constrained problem in the limit $k \to \infty$, where

$$\begin{aligned} &x^k \to x^* \\ &kh(x^k) \to \lambda^* = -\left(\nabla h(x^*) \cdot \nabla h(x^*)\right)^{-1} \nabla h(x^*) \cdot \nabla f(x^*). \end{aligned} \tag{B.5}$$

B.1.2 Lagrangian function

We define a function, L, as

$$\begin{aligned} &L : \mathbb{R}^n \times \mathbb{R}^m \longrightarrow \mathbb{R} \\ &(x, \lambda) \longmapsto L(x, \lambda), \end{aligned} \tag{B.6}$$

as

$$L(x, \lambda) := f(x) + \sum_{i=1}^{m} \lambda_i h_i(x), \tag{B.7}$$

which is called Lagrangian function. Then, the necessary conditions in Theorem B.1 can be written as,

$$\begin{aligned} &\nabla_x L(x^*, \lambda^*) = 0, \\ &\nabla_\lambda L(x^*, \lambda^*) = 0. \end{aligned} \tag{B.8}$$

B.2 Lagrange multiplier algorithms

B.2.1 Penalty and augmented Lagrangian methods

The augmented Lagrangian function, L_c,

$$\begin{aligned} &L_c : \mathbb{R}^n \times \mathbb{R}^m \longrightarrow \mathbb{R} \\ &(x, \lambda) \longmapsto L_c(x, \lambda), \end{aligned} \tag{B.9}$$

is defined in the following way,

$$L_c(x,\lambda) := f(x) + \lambda \cdot h(x) + \frac{c}{2}\|h(x)\|^2 \quad : \quad c > 0. \tag{B.10}$$

For feasible x, we have that $L_c(x,\lambda) \equiv f(x)$. Then, we expect that for nearly feasible x, we can approximate $L_c(x,\lambda) \simeq f(x)$.

B.2.1.1 The quadratic penalty method

This method consists in solving a sequence of problems:

1. Minimize $L_c(x,\lambda)$,
2. Do it subject to $x \in X$.

In the original version of this method, from the 1960s, they used

$$\lambda^k = 0 \quad \forall k = 0,1,\ldots \tag{B.11}$$

Another idea is to take a set, λ^k, which are *good* approximations to the actual set, λ, and let them vary in the course of the algorithm.

Theorem B.2 *For $k = 0,1,\ldots$ let x^k be a global minimum of the problem:*

- *minimize $L_{c^k}(x,\lambda)$: $\{\lambda^k\}$ is bounded,*
- *subject to $x \in X$.*

such that $0 < c^k < c^{k+1}$, $\forall k$; $c^k \to \infty$. Then every limit point of the sequence $\{x^k\}$ is a global minimum of the original problem.

Obviously, this algorithms do not reach the exact solution. The solution precisionis given by

$$\|\nabla_x L_{c^k}(x^k,\lambda^k)\| \leq \epsilon^k \quad : \quad 0 \leq \epsilon^k,\ \forall k;\ \epsilon^k \to 0. \tag{B.12}$$

Some limitation that might happen when using this algorithm are,

1. The method breaks down because none x^k can be found.
2. $\{x^k\}$ has no limit points, or $\exists x^*$: $\nabla h(x^*)$ has linearly independent columns.

B.2.1.2 Multiplier methods-main ideas

Let us consider now some ways to update λ^k in order to reach the actual Lagrange multiplier for large k.

A first update formula for λ^k in the quadratic penalty method, given by,

$$\lambda^{k+1} = \lambda^k + c^k h(x^k), \tag{B.13}$$

since,

$$\{\lambda^k + c^k h(x^k)\} \to \lambda^* \qquad \text{if} \qquad \{x^k\} \to x^*. \tag{B.14}$$

The quadratic penalty method together with this updating procedure is known as the method of multipliers.

Let us focus now on the choice of parameters, λ^0, and $\{c^k\}$. A useful scheme is the following,

1. Choose a moderate c^0 (if necessary, by preliminary inspection).
2. $c^{k+1} = \beta c^k \quad : \quad \beta > 1$ (for Newton–like methods, it is recommended to take a value $\beta \in [5, 10]$).

Another scheme is,

$$c^{k+1} = \begin{cases} \beta c^k & \text{if} \|h(x^k)\| > \gamma \|h(x^{k-1})\|, \\ c^k & \text{otherwise,} \end{cases} \tag{B.15}$$

where $\gamma < 1$ ($\gamma \simeq 0.25$ being recommended).

Different penalty parameters, c_i, for each constraint can also be used.

B.2.2 Exact penalties

They are exact in the sense that they require only one unconstrained minimization to obtain an optimal solution.

We define an exact penalty function, P, as

$$P(x, \lambda) := \|\nabla_x L(x, \lambda)\|^2 + \|h(x)\|^2. \tag{B.16}$$

Minimizing $P(x, \lambda)$ over $(x, \lambda) \in \mathbb{R}^{n+m} \to (x^*, \lambda^*)$ such that,

$$\begin{aligned} &\nabla_x L(x\lambda) = 0, \\ &h(x) = 0. \end{aligned} \tag{B.17}$$

B.2.3 Lagrangian methods

Here, we consider the minimization problem as a system of $(n + m)$ nonlinear equations with $(n + m)$ unknowns, (x, λ). Such a system is called a Lagrangian system, and can be written down as,

$$\left.\begin{array}{l} \nabla f(x) + \nabla h(x)\lambda = 0 \\ h(x) = 0 \end{array}\right\}, \tag{B.18}$$

or, similarly, as,

$$\nabla L(x, \lambda) = 0. \tag{B.19}$$

B.2.3.1 First order methods

The algorithms to solve Lagrangian systems, i.e. Lagrangian methods, can be formally written as:

$$\left.\begin{array}{l} x^{k+1} = G(x^k, \lambda^k) \\ \lambda^{k+1} = H(x^k, \lambda^k) \end{array}\right\}, \tag{B.20}$$

such that,

$$\begin{array}{l} x^* = G(x^*, \lambda^*), \\ \lambda^* = H(x^*, \lambda^*). \end{array} \tag{B.21}$$

The simplest of these methods is the following,

$$\left.\begin{array}{l} x^{k+1} = x^k - \alpha \nabla_x L(x^k, \lambda^k) \\ \lambda^{k+1} = \lambda^k + \alpha h(x^k) \end{array}\right\}, \tag{B.22}$$

where $\alpha > 0$ is the stepsize.

The direction $\left(-\nabla_x L(x^k, \lambda^k), h(x^k)\right)$ is a not ascent direction if the Hessian of the Lagrangian, $\nabla^2_{xx} L(x^k, \lambda^k)$, is positive definite. This condition is quite strong, actually stronger than the sufficient conditions for the existence of a solution to the Lagrangian system.

B.2.3.2 Newton-like methods

Being a Lagrangian system given by,

$$\nabla L(x, \lambda) = 0, \tag{B.23}$$

the Newton-like methods consist in iterating the system

$$\begin{array}{l} x^{k+1} = x^k + \Delta x^k, \\ \lambda^{k+1} = \lambda^k + \Delta \lambda^k, \end{array} \tag{B.24}$$

where,

$$\nabla^2 L(x^k, \lambda^k) \begin{pmatrix} \Delta x^k \\ \Delta \lambda^k \end{pmatrix} = -\nabla L(x^k, \lambda^k)\,. \tag{B.25}$$

A manner to implement this method is the following. First, let us write the Hessian matrix of the Lagrangian as

$$\nabla^2 L(x^k, \lambda^k) = \begin{pmatrix} H^k & N^k \\ N^{k'} & 0 \end{pmatrix} \quad : \quad \left\{\begin{array}{l} H^k = \nabla^2_{xx} L \\ N^k = \nabla h(x^k)\,, \end{array}\right. \tag{B.26}$$

$$\nabla L(x^k, \lambda^k) = \begin{pmatrix} \nabla_x L(x^k, \lambda^k) \\ h(x^k) \end{pmatrix} \tag{B.27}$$

Then, Eq. (B.24) leads to,

$$\begin{pmatrix} H^k & N^k \\ N^{k'} & 0 \end{pmatrix} \begin{pmatrix} \Delta x^k \\ \Delta \lambda^k \end{pmatrix} = - \begin{pmatrix} \nabla_x L(X^k, \lambda^k) \\ h(x^k) \end{pmatrix}, \tag{B.28}$$

or, in other words,

$$\begin{aligned} &H^k \Delta x^k + N^k \Delta \lambda^k = -\nabla_x L \\ &N^{k'} \Delta x^k = -h(x^k). \end{aligned} \tag{B.29}$$

Multiplying the first of these equations by $N^{k'}(H^k)^{-1}$, and using the information in the second one, we arrive to,

$$N^{k'} \left(H^k\right)^{-1} N^k \Delta \lambda^k = h(x^k) - N^{k'} \left(H\right)^{-1} \nabla_x L, \tag{B.30}$$

and being $N^{k'}(H^k)^{-1}N^k$ a non-singular matrix, we reach the solution for $\Delta\lambda^k$,

$$\Delta \lambda^k = \left[N^{k'} \left(H^k\right)^{-1} N^k\right]^{-1} \left(h(x^k) - N^{k'} \left(H^k\right)^{-1} \nabla_x L\right). \tag{B.31}$$

Since,

$$\nabla_x L = \nabla f(x^k) + N^k \lambda^k = \nabla_x L \left(x^k, \lambda^{k+1}\right) - N^k \Delta \lambda^k, \tag{B.32}$$

with iterations evolving under the following rule,

$$\begin{cases} \lambda^{k+1} = \left[N^{k'} \left(H^k\right)^{-1} N^k\right]^{-1} \left(h(x^k) - N^{k'} \left(H^k\right)^{-1} \nabla f(x^k)\right) \\ x^{k+1} = x^k - \left(H^k\right)^{-1} \nabla_x L \left(x^k, \lambda^{k+1}\right). \end{cases} \tag{B.33}$$

C
Theory of elasticity

In this Appendix, we present the fundamental equations of linear theory of elasticity. First, we introduce the basic concepts of strain and stress, in order to be able, later, to write elastic free energies based on the symmetries of the system under consideration. Then, equilibrium equations can be derived.

This Appendix is mainly based on the classic textbook on elasticity by Landau and Lifshitz [146]. A good and extensive introduction applied to the elasticity of biomembranes can be found in Ref. [78].

C.1
The strain tensor

Let us consider a solid-like body which, by some external means, is deformed. This deformation is described by the new position of all the points in the body,

$$x_i' = x_i + u_i(x_j), \tag{C.1}$$

where x_i are the components of the position vector of a given point in the body before being deformed; x_i' being the components of the position vector of the same point after the deformation; and $u_i(x_j)$ are the components of the displacement vector, which in principle depends on all the coordinates of the point before deformation, and accounts for the deformation itself. Thus, known the displacement vector at each point of the body, the deformation is completely determined.

Let us now calculate how the distance between two infinitesimally close points in the body changes after deformation

$$\mathrm{d}l'^{\,2} = \mathrm{d}x_i'\,\mathrm{d}x_i'. \tag{C.2}$$

From Eq. (C.1) we can write

$$\mathrm{d}l'^{\,2} = \mathrm{d}l^2 + 2\frac{\partial u_i}{\partial x_k}\,\mathrm{d}x_i\,\mathrm{d}x_k, \tag{C.3}$$

using the fact that $\frac{\partial u_i}{\partial x_k} << 1$, i.e. the relative displacements are small, and that $\mathrm{d}l^2 = \mathrm{d}x_i\,\mathrm{d}x_i$ is the infinitesimal distance between two points before the

deformation. We rewrite this expression as

$$\mathrm{d}l'^{\,2} = \mathrm{d}l^2 + 2u_{ik}\mathrm{d}x_i\,\mathrm{d}x_k, \tag{C.4}$$

where u_{ik} is a second-rank tensor. Now, we see that we can define this tensor in different ways, for instance:

$$u_{ik}^{\mathrm{NS}} = \frac{\partial u_i}{\partial x_k}, \tag{C.5}$$

or

$$u_{ik}^{\mathrm{S}} = \frac{1}{2}\left(\frac{\partial u_i}{\partial x_k} + \frac{\partial u_k}{\partial x_i}\right). \tag{C.6}$$

Both of these definitions for the tensor give the correct expression for Eq. (C.3). However, the first one is a non-symmetric tensor, while the second definition is that of a symmetric tensor. We shall adopt the second definition for this tensor, which will be called from here on the *strain tensor*, and denoted simply by u_{ik}. Since it is symmetric, $u_{ik} = u_{ki}$, we have that only $d(d+1)/2$ out of its d^2 components are independent *a priori*. Actually, the difference between Eqs. (C.5) and (C.6), is an antisymmetric tensor, which accounts for rotations of the solid body, which cause no deformations. Summarizing, the strain tensor is defined as

$$u_{ik} = \frac{1}{2}\left(\frac{\partial u_i}{\partial x_k} + \frac{\partial u_k}{\partial x_i}\right). \tag{C.7}$$

C.1.1 Geometrical meaning of the strain tensor

In order to see the geometrical meaning of the different components of the strain tensor, we are going to distinguish between the diagonal and non-diagonal terms.

- **Diagonal terms**

  Given a stretching deformation as that shown in Fig. C.1a, the diagonal terms of the strain tensor clearly show the relative stretching (or compression) in their direction. Namely,

  $$u_{ii} = \frac{\mathrm{d}x_i' - \mathrm{d}x_i}{\mathrm{d}x_i}. \tag{C.8}$$

- **Non-diagonal terms**

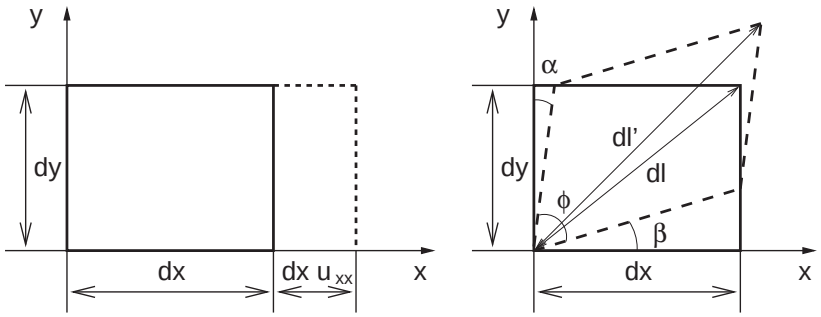

(a) Stretching deformation (b) Shear deformation

Figure C.1 Geometrical meaning of the components of the strain tensor. (a) Diagonal terms account for stretching deformations while (b) non-diagonal terms account for shear-like deformations.

The displacement vector in the deformation of an infinitesimal piece of surface due to a shear deformation is[1] (see Fig. C.1b),

$$\mathbf{u} = (\alpha y, \beta x), \tag{C.9}$$

then, the diagonal components of the strain tensor vanish, and the non-diagonal component are

$$u_{xy} = u_{yx} = \frac{1}{2}(\alpha + \beta). \tag{C.10}$$

The diagonal of the parallelogram after the shear deformation is

$$\mathrm{d}l'^{\,2} = \left(\frac{\mathrm{d}x}{\cos\beta}\right)^2 + \left(\frac{\mathrm{d}y}{\cos\alpha}\right)^2 + 2\frac{\mathrm{d}x\,\mathrm{d}y}{\cos\alpha\cos\beta}\cos\phi, \tag{C.11}$$

which, up to first order in deformations, is

$$\mathrm{d}l'^{\,2} = \mathrm{d}l^2 + 2\cos\phi\,\mathrm{d}x\,\mathrm{d}y. \tag{C.12}$$

From the definition of the strain tensor Eq. C.7, we get that

$$u_{xy} = \frac{1}{2}\cos\phi \simeq \frac{1}{2}\left(\frac{\pi}{2} - \phi\right) = \frac{1}{2}(\alpha + \beta), \tag{C.13}$$

as we expected. Thus, the geometrical meaning of non-diagonal terms of the strain tensor is related to the internal angle of the parallelogram resulting after the deformation.

1) We restrict ourselves to a two-dimensional case, for the sake of simplicity and clearness of the figures.

Besides, we see that the non-diagonal components of the strain tensor are responsible for shear deformations which do not change the volume. We can see which is the volume change caused by a general deformation using the fact that any symmetric tensor can be diagonalized. Thus, choosing the appropriate axes (the so-called principal axes of the deformation), the strain tensor can be written as

$$u_{ik} = u^{(i)}\,\delta_{ik}, \tag{C.14}$$

where $u^{(i)}$ are the tensor eigenvalues. In this case, $\mathrm{d}x_i' = (1 + u^{(i)})\,x_i$, and thus the infinitesimal volume element after deformation is

$$\mathrm{d}V' = \mathrm{d}V(1 + u^{(1)} + u^{(2)} + u^{(3)}) = \mathrm{d}V\,(1 + \mathrm{tr}\,(u_{ik}))\,, \tag{C.15}$$

where $\mathrm{tr}\,(u_{ik}) = u_{ii}$ is the trace of the tensor, which is a tensor invariant. Thus, the trace of the strain tensor gives the relative volume change caused by the deformation,

$$u_{ii} = \frac{\mathrm{d}V' - \mathrm{d}V}{\mathrm{d}V}. \tag{C.16}$$

C.2 The stress tensor

When a body is undeformed and in equilibrium there is a force field inside it which accomplishes the equilibrium conditions of a solid body. Once the body is deformed, in order to restore an equilibrium configuration of the molecules in the body, some extra forces appear inside the body. These are called the internal stresses.

Let us consider a box of volume V inside the body. The total force inside this piece of volume can be written as a surface integral, meaning that the force field can be expressed as the divergence of a tensor, namely

$$\int_V \mathbf{F}\,\mathrm{d}V = \oint_{\partial V} \mathrm{div}\sigma : \mathrm{d}\mathbf{S}, \tag{C.17}$$

or, in component notation,

$$F_i = \frac{\partial \sigma_{ik}}{\partial x_k}, \tag{C.18}$$

where σ_{ik} is a rank-2 tensor called the *stress tensor*. Actually, this tensor can be shown to be symmetric if we require mechanical equilibrium for the momenta [146], namely, $\sigma_{ik} = \sigma_{ki}$.

C.2.1
Geometrical meaning of the stress tensor

Consider a small volume $\mathrm{d}V = \mathrm{d}x\,\mathrm{d}y\,\mathrm{d}z$ inside the body. The component $\sigma_{ik}\,\mathbf{n}_k$ of the stress tensor is the component i of the force per unit area perpendicular to the k-direction, where $\mathbf{n}$ is the outwards-direction unit vector normal to the surface (see Fig. C.2).

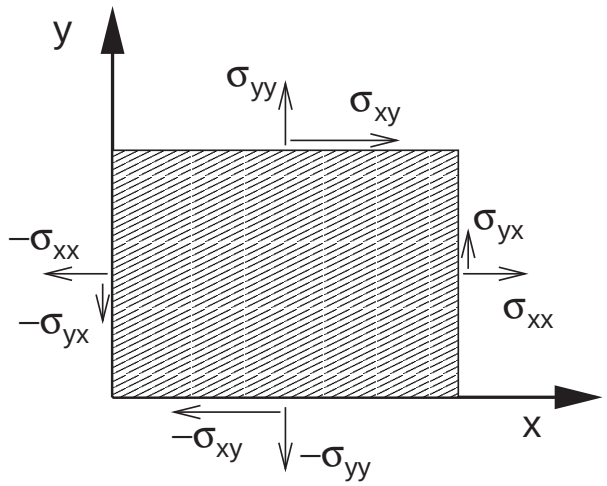

Figure C.2 Representation of the internal stresses in a two-dimensional system.

C.3
Thermodynamics of deformation

C.3.1
Work of deformation

From the definition of the stress tensor, we can calculate the work done by a deformation characterized by a given strain tensor. We detail here two simplified calculations, when the deformation is just a stretching in one direction, and when it is a simple in-plane shear.

C.3.1.1 One-dimensional stretching

In this case, we consider a uniform stretching in the y-direction, given by a non-vanishing u_{yy} component of the strain tensor. As we learned in Sec. C.1.1,

the relative displacement in that direction is given by

$$\delta y = u_{yy} \mathrm{d}y,$$

which is the only non-vanishing component of the relative displacement vector. In order to work out the work done in such a deformation we need to know which is the net force in the y-direction on the xz surface. By definition, this force is (see Eq. (C.18))

$$F_y = \sigma_{yy} \mathrm{d}x \mathrm{d}z.$$

Therefore, the work of deformation is

$$W = \mathbf{F} \cdot \mathbf{r} = F_y \, \delta y = \sigma_{yy} \, u_{yy} \mathrm{d}V. \tag{C.19}$$

One can generalize this result in the case of a homogeneous stretching in all the dimensions of the space, given by a diagonal strain tensor

$$W_{\text{stretching}} = F_i \, \delta x^i = \sigma_{ii} \, u^{ii} \mathrm{d}V. \tag{C.20}$$

C.3.1.2 **Simple shear**

Consider a simple shear in the yz plane, given by a non-vanishing u_{yz} component of the strain tensor. We know that the shear angle is related to this component as $u_{yz} = (\alpha + \beta)/2$, where α and β are the angles related to the yz-shear and to the zy-shear, respectively. Thus, the force on the y-direction on the xz face is given by

$$F_y = \sigma_{yz} \, \mathrm{d}x \, \mathrm{d}y,$$

and the moment of this pair of forces is

$$M_x = F_y \, \mathrm{d}z.$$

Since the relative angular displacement is given by the total shear angle $\alpha + \beta$, the work done in this deformation is

$$W = \mathbf{M} \cdot \delta\Theta = M_x \, (\alpha + \beta) = 2\sigma_{yz} \, u^{yz} \mathrm{d}V. \tag{C.21}$$

This work accounts for both yz and zy shears, then one can generalize the work done in a general shear deformation as

$$W_{\text{shear}} = \sigma_{ik} \, u^{ik} \mathrm{d}V \quad : \quad i \neq j, \tag{C.22}$$

where double counting has been taken into account.

C.3.1.3 Total work of deformation

Assembling these results, we can write the total work done in an arbitrary deformation characterized by a strain tensor u^{ik}, as

$$W = \sigma_{ik}\, u^{ik}. \tag{C.23}$$

C.3.2
Free energy of deformation

If we consider an adiabatic process, the free energy of deformation is given by

$$\delta E = \delta Q + \delta W = \delta W = \sigma_{ik} u^{ik} = F. \tag{C.24}$$

We have then the following thermodynamical relations

$$\frac{\partial F}{\partial u^{ik}} = \sigma_{ik}, \tag{C.25}$$

$$\frac{\partial F}{\partial \sigma_{ik}} = u^{ik}. \tag{C.26}$$

Note that these relations have only sense as a way to express the differential relation $\mathrm{d}F = \sigma_{ik}\mathrm{d}u^{ik}$.

C.4
Hooke's law of elasticity

In order to proceed in our understanding of the elasticity of solid bodies, and also to apply the general thermodynamic relations found in the previous Section, we need to specify which is the free energy, F, as a function of the strain tensor. The way of doing that is by making a series expansion,

$$F(u^{ik}) = \sum_k \text{scalars of order } k. \tag{C.27}$$

From Eq. (C.25), we see that there should be no linear term in strains in the free energy, because of the fact that when there is no deformation, there are no internal stresses in the body. Therefore, the first non trivial order in the expansion is the second order (the zeroth order is just a constant added to the energy). Truncating the series to this first non-trivial order gives what is called the Hooke's law of elasticity,

$$F = \frac{1}{2}\lambda_{iklm}\, u^{ik}\, u^{lm}, \tag{C.28}$$

where the fourth-rank tensor λ_{iklm} is the so-called elastic modulus tensor. Note that this is the most general scalar quantity of second order in deformations.

Therefore, the general formulation of the elastic free energy of a three-dimensional anisotropic body, according the the Hooke's law, is given by Eq. (C.28). The symmetry of the strain tensor impose some symmetries in the λ-tensor. Then, the number of independent components of this tensor is 21.

C.5 Equilibrium equations of an isotropic elastic body

There are (at least) two approaches for finding the equilibrium equations for an elastic body, via the minimization of the elastic free energy and via the condition of local force balance.

C.5.1 Minimization of the free energy

The free energy in Eq. (12.11) is a functional of the components of the strain tensor, namely, of the spatial derivatives of the components of the displacement field. The displacement field in the deformed body corresponds to a extreme of this functional given the boundary conditions. To minimize this functional, we work out its associated Euler-Lagrange equations, reading as

$$\delta_{u^i} F = 0 \quad \Rightarrow \quad \frac{\partial}{\partial x^k}\left(\frac{\partial F}{\partial \frac{\partial u^i}{\partial x^k}}\right) = 0 \quad \forall i. \tag{C.29}$$

C.5.2 Local force balance

From the condition of local equilibrium (vanishing total force)

$$\frac{\partial \sigma_{ik}}{\partial x^k} = 0 \quad \forall\, i, \tag{C.30}$$

and knowing that $\sigma_{ik} = \lambda_{iklm}\, u^{lm}$, we can, in principle, write one equation for each spatial dimension.

D
List of publications

- CAMPELO, F., AND HERNÁNDEZ-MACHADO, A. Dynamic model and stationary shapes of fluid vesicles. *Eur. Phys. J. E 20*, 1 (2006), 37–45.
- CAMPELO, F., ALLAIN, J.-M., AND BEN AMAR, M. Periodic lipidic membrane tubes. *Europhys. Lett. 77*, 3 (2007), 38006.
- CAMPELO, F., AND HERNÁNDEZ-MACHADO, A. Model for curvature-driven pearling instability in membranes. *Phys. Rev. Lett. 99*, 8 (2007), 088101.
- CAMPELO, F., AND HERNÁNDEZ-MACHADO, A. Shape instabilities in vesicles: a phase-field model. *Eur. Phys. J. Special Topics 143* (2007), 101–108.
- CAMPELO, F., AND HERNÁNDEZ-MACHADO, A. Polymer-induced tubulation in lipid vesicles. *Phys. Rev. Lett. 100*, 15 (2008), 158103.
- CAMPELO, F., MCMAHON, H. T., AND KOZLOV, M. M. The hydrophobic insertion mechanism of membrane curvature generation by proteins. *Biophys. J. 95* (2008), 2325–2339.
- CAMPELO, F., RIVERO, M., AND HERNÁNDEZ-MACHADO, A. Starfish shapes in monolayer lipid domains. *Preprint*.

Bibliography

1 ABRAMOWITZ, M., AND STEGUN, I. A. *Handbook of mathematical functions with formulas, graphs, and mathematical tables*, 9th ed. ed. Dover, New York, 1964.

2 ALAVA, M., DUBÉ, M., AND ROST, M. Imbibition in disordered media. *Adv. Phys. 53*, 2 (2004), 83–175.

3 ALBERTS, B., ET AL. *Molecular Biology of the Cell*, 4th ed. Garland Science, New York, 2002.

4 ALLAIN, J.-M. *Fission de tubes membranaires à deux phases*. PhD thesis, École Normale Supérieure, 2005.

5 ALLAIN, J.-M., STORM, C., ROUX, A., BEN AMAR, M., AND JOANNY, J.-F. Fission of a multiphase membrane tube. *Phys. Rev. Lett. 93*, 15 (2004), 158104.

6 ALLEN, S. M., AND CAHN, J. W. A microscope theory for antiphase boundary motion and its application to antiphase domain coarsening. *Acta Metall. 27* (1979), 1085.

7 ALLPORT, S. *The Queen of fats: why omega-3s were removed from the western diet and what we can do to replace them*. Univ. California Press, 2006.

8 ANDELMAN, D., BROCHARD, F., AND JOANNY, J.-F. Phase transitions in Langmuir monolayers of polar molecules. *J. Chem. Phys. 86* (1987), 3673.

9 ANTONNY, B. Membrane deformation by protein coats. *Curr. Opin. Cell Biol. 18*, 4 (2006), 386–394.

10 ANTONNY, B., BERAUD-DUFOUR, S., CHARDIN, P., AND CHABRE, M. N-terminal hydrophobic residues of the G-protein ADP-ribosylation factor-1 insert into membrane phospholipids upon GDP to GTP exchange. *Biochemistry 36*, 15 (1997), 4675–4684.

11 ARANDA-ESPINOZA, H., BERMAN, A., DAN, N., PINCUS, P., AND SAFRAN, S. Interaction between inclusions embedded in membranes. *Biophys. J. 71*, 2 (1996), 648–656.

12 BAR-ZIV, R., AND MOSES, E. Instability and pearling states produced in tubular membranes by competition of curvature and tension. *Phys. Rev. Lett. 73* (1994), 1392–1395.

13 BAR-ZIV, R., TLUSTY, T., MOSES, E., SAFRAN, S., AND BERSHADSKY, A. Pearling in cells: A clue to understanding cell shape. *Proc. Natl. Acad. Sci. USA 96*, 18 (1999), 10140–10145.

14 BAUMGART, T., HESS, S. T., AND WEBB, W. W. Imaging coexisting fluid domains in biomembrane models coupling curvature and line tension. *Nature 425* (2003), 821–824.

15 BEAUCOURT, J., RIOUAL, F., SÉON, T., BIBEN, T., AND MISBAH, C. Steady to unsteady dynamics of a vesicle in a flow. *Phys. Rev. E 69*, 1 (2004), 11906.

16 BEN AMAR, M., AND MOUSSALLAM, B. Absence of selection in directional solidification. *Phys. Rev. Lett. 60*, 4 (1988), 317–320.

17 BEN-SHAUL, A., AND GELBART, W. M. Statistical thermodynamics of amphiphile self-assembly: structure and phase transitions in micellar solutions. In *Micelles, Membranes, Microemulsions, and Monolayers*, W. Gelbart, A. Ben-Shaul, and D. Roux, Eds. Springer-Verlag, 1994, pp. 1–104.

18 BERG, J. M., TYMOCZKO, J. L., AND STRYER, L. *Biochemistry*. WH Freeman, New York, 1988.

19 BERTSEKAS, D. P. *Nonlinear programming*, 2nd ed. Athena Scientific, Belmont, MA, 1999.

20 BESSIS, M. *Living blood cells and their ultrastructure*. Springer-Verlag Berlin, 1973.

21 BIBEN, T., AND MISBAH, C. Tumbling of vesicles under shear flow within an advected-field approach. *Phys. Rev. E 67* (2003), 031908.

22 BIGAY, J., CASELLA, J. F., DRIN, G., MESMIN, B., AND ANTONNY, B. ArfGAP1 responds to membrane curvature through the folding of a lipid packing sensor motif. *EMBO J. 24* (2005), 2244–2253.

23 BLOOD, P. D., AND VOTH, G. A. Direct observation of Bin/amphiphysin/Rvs (BAR) domain-induced membrane curvature by means of molecular dynamics

simulations. *Proc. Nat. Acad. Sci. U.S.A. 103*, 41 (2006), 15068.

24 BLOOMENTHAL, J., BAJAJ, C., BLINN, J., CANI-GASCUEL, M.-P., ROCKWOOD, A., WYVILL, B., AND WYVILL, G. *Introduction to implicit surfaces*. Morgan Kaufmann Publishers, Inc. San Francisco, CA, 1997.

25 BO, L., AND WAUGH, R. E. Determination of bilayer membrane bending stiffness by tether formation from giant, thin-walled vesicles. *Biophys. J. 55*, 3 (1989), 509.

26 BORGHI, N., ROSSIER, O., AND BROCHARD-WYART, F. Hydrodynamic extrusion of tubes from giant vesicles. *Europhys. Lett. 64*, 6 (2003), 837–843.

27 BOZIC, B., SVETINA, S., AND ZEKS, B. Theoretical analysis of the formation of membrane microtubes on axially strained vesicles. *Phys. Rev. E 55*, 5 (1997), 5834–5842.

28 BOZIC, B., SVETINA, S., ZEKS, B., AND WAUGH, R. E. Role of lamellar membrane structure in tether formation from bilayer vesicles. *Biophys. J. 61* (1992), 963–973.

29 BRAY, D. *Cell movements*. Garland Pub., New York, 1992.

30 BREMSER, M., NICKEL, W., SCHWEIKERT, M., RAVAZZOLA, M., AMHERDT, M., HUGHES, C. A., SOELLNER, T. H., ROTHMAN, J. E., AND WIELAND, F. T. Coupling of coat assembly and vesicle budding to packaging of putative cargo receptors. *Cell 96* (1999), 495–506.

31 BROCHARD-WYART, F., BORGHI, N., CUVELIER, D., AND NASSOY, P. Hydrodynamic narrowing of tubes extruded from cells. *Proc. Natl. Acad. Sci. U.S.A. 103*, 20 (2006), 7660–7663.

32 BURGER, K. N., DEMEL, R. A., SCHMID, S. L., AND DE KRUIJFF, B. Dynamin is membrane-active: lipid insertion is induced by phosphoinositides and phosphatidic acid. *Biochemistry 39*, 40 (2000), 12485–12493.

33 CAGINALP, G. Surface tension and supercooling in solidification theory. In *Applications of Field Theory to Statistical Mechanics*, L. Garrido, Ed., vol. 216 of *Lecture Notes in Physics*. Springer, Berlin, 1984, p. 216.

34 CAHN, J. W., AND HILLIARD, J. E. Free energy of a nonuniform system. i. interfacial energy. *J. Chem. Phys. 28* (1958), 258.

35 CAMAZINE, S., DENEUBOURG, J.-L., FRANKS, N. R., J., S., THERAULAZ, G., AND E., B. *Self-organization in biological systems*. Princeton University Press, 2001.

36 CAMPÀS, O. *From molecular force generation to large scale cellular movements*. PhD thesis, Universitat de Barcelona, 2006.

37 CAMPELO, F., ALLAIN, J.-M., AND BEN AMAR, M. Periodic lipidic membrane tubes. *Europhys. Lett. 77*, 3 (2007), 38006.

38 CAMPELO, F., AND HERNÁNDEZ-MACHADO, A. Dynamic model and stationary shapes of fluid vesicles. *Eur. Phys. J. E 20*, 1 (2006), 37–45.

39 CAMPELO, F., AND HERNÁNDEZ-MACHADO, A. Model for curvature-driven pearling instability in membranes. *Phys. Rev. Lett. 99*, 8 (2007), 088101.

40 CAMPELO, F., AND HERNÁNDEZ-MACHADO, A. Shape instabilities in vesicles: a phase-field model. *Eur. Phys. J. Special Topics 143* (2007), 101–108.

41 CAMPELO, F., AND HERNÁNDEZ-MACHADO, A. Polymer-induced tubulation in lipid vesicles. *Phys. Rev. Lett. 100*, 15 (2008), 158103.

42 CAMPELO, F., MCMAHON, H. T., AND KOZLOV, M. M. The hydrophobic insertion mechanism of membrane curvature generation by proteins. *Biophys. J. 95* (2008), 2325–2339.

43 CAMPELO, F., TRAVASSO, R., AND HERNÁNDEZ-MACHADO, A. in preparation.

44 CANHAM, P. B. The minimum energy of bending as a possible explanation of the biconcave shape of the human red blood cell. *J. Theor. Biol. 26* (1970), 61–81.

45 CARDOSO, V., AND DIAS, Ó. J. C. Rayleigh-Plateau and Gregory-Laflamme instabilities of black strings. *Phys. Rev. Lett. 96*, 18 (2006), 181601.

46 CHANDRASEKHAR, S. *Hydrodynamic and hydromagnetic stability*. Courier Dover Publications, 1981.

47 CHAZAL, N., AND GERLIER, D. Virus entry, assembly, budding, and membrane rafts. *Microbiol. Mol. Biol. R.*, 226-237 (June 2003).

48 CHEN, Z., AND RAND, R. P. The influence of cholesterol on phospholipid membrane curvature and bending elasticity. *Biophys. J. 73*, 1 (1997), 267–276.

49 CHERNOMORDIK, L. V., AND KOZLOV, M. M. Mechanics of membrane fusion. *Nat. Struct. Mol. Biol. 15*, 7 (2008), 675.

50 CHOU, T., KIM, K. S., AND OSTER, G. Statistical thermodynamics of membrane bending-mediated protein-protein attractions. *Biophys. J. 80*, 3 (2001), 1075–1087.

51 CLARK, J. C., WERT, S. E., BACHURSKI, C. J., STAHLMAN, M. T., STRIPP, B. R., WEAVER, T. E., AND WHITSETT, J. A. Targeted disruption of the surfactant protein B gene disrupts surfactant homeostasis, causing respiratory failure in newborn mice. *Proc. Natl. Acad. Sci. USA 92*, 17 (1995), 7794–7798.

52 COLLINS, J. B., AND LEVINE, H. Diffuse interface model of diffusion-limited crystal growth. *Phys. Rev. B 31*, 9 (1985), 6119–6122.

53 COUDER, Y., CHOMAZ, J. M., AND RABAUD, M. On the hydrodynamics of soap films. *Physica D 37*, 1-3 (1989), 384–405.

54 CRUZ, A., VAZQUEZ, L., VELEZ, M., AND PEREZ-GIL, J. Effect of pulmonary surfactant protein SP-B on the micro- and nanostructure of phospholipid films. *Biophys. J. 86*, 1 (2004), 308–320.

55 CUVELIER, D., CHIARUTTINI, N., BASSEREAU, P., AND NASSOY, P. Pulling long tubes from firmly adhered vesicles. *Europhys. Lett. 71* (2005), 1015–1021.

56 CUVELIER, D., DERENYI, I., BASSEREAU, P., AND NASSOY, P. Coalescence of membrane tethers: experiments, theory, and applications. *Biophys. J. 88*, 4 (2005), 2714–2726.

57 DAUMKE, O., LUNDMARK, R., VALLIS, Y., MARTENS, S., BUTLER, P. J. G., AND MCMAHON, H. T. Architectural and mechanistic insights into an EHD ATPase involved in membrane remodelling. *Nature 449*, 7164 (2007), 923–927.

58 DE GENNES, P. G., AND PROST, J. *The physics of liquid crystals*, 2nd ed. Oxford U.P., 1993.

59 DE GROOT, S. R., AND MAZUR, P. *Non-equilibrium thermodynamics*. Dover Publications, 1984.

60 DE MELLO, E. V. L., AND TEIXEIRA DA SILVEIRA FILHO, O. Numerical study of the Cahn–Hilliard equation in one, two and three dimensions. *Physica A 347* (2005), 429–443.

61 DECHER, G., KUCHINKA, E., RINGSDORF, H., VENZMER, J., BITTER-SUERMANN, D., AND WEISGERBER, C. Interaction of amphiphilic polymers with model membranes. *Angew. Makromol. Chem. 166* (1989), 71–80.

62 DELAUNAY, C. Sur la surface de revolution dont la courbure moyenne est constante. *J. Math. Pures Appl. 6*, 1 (1841), 309–320.

63 DERÉNYI, I., JÜLICHER, F., AND PROST, J. Formation and interaction of membrane tubes. *Phys. Rev. Lett. 88*, 2 (2002), 238101.

64 DEULING, H. J., AND HELFRICH, W. Theoretical explanation for myelin shapes of red blood cells. *Blood Cells 3*, 3 (1977), 713–720.

65 DEVAUX, P. F. Is lipid translocation involved during endo-and exocytosis? *Biochimie 82*, 5 (2000), 497–509.

66 DEVAUX, P. F., HERRMANN, A., OHLWEIN, N., AND KOZLOV, M. M. How lipid flippases can modulate membrane structure. *Biochim. Biophys. Acta, Biomembr.* (2008).

67 DIETRICH, C., BAGATOLLI, L. A., VOLOVYK, Z. N., THOMPSON, N. L., LEVI, M., JACOBSON, K., AND GRATTON, E. Lipid rafts reconstituted in model membranes. *Biophysical Journal 80*, 3 (2001), 1417–1428.

68 DO CARMO, M. P. *Differential geometry of curves and surfaces*. Prentince–Hall, 1976.

69 DOI, M., AND EDWARDS, S. F. *The theory of polymer dynamics*. Oxford Science, 1986.

70 DOWHAN, W. Molecular basis fot membrane phospholipid diversity: why are there so many lipids? *Annu. Rev. Biochem. 66*, 1 (1997), 199–232.

71 DRIN, G., CASELLA, J. F., GAUTIER, R., BOEHMER, T., SCHWARTZ, T. U., AND ANTONNY, B. A general amphipathic alpha-helical motif for sensing membrane curvature. *Nat. Struct. Mol. Biol. 14* (2007), 138–146.

72 DU, Q., LIU, C., AND WANG, X. A phase field approach in the numerical study of the elastic bending energy for vesicle membranes. *J. Comput. Phys. 198* (2004), 450–468.

73 EDIDIN, M. The state of lipid rafts: from model membranes to cells. *Annu. Rev. Biophys. Biomol. Struct. 32* (2003), 257–83.

74 ELDER, K. R., GRANT, M., PROVATAS, N., AND KOSTERLITZ, J. Sharp interface limits of phase-field models. *Phys. Rev. E 64* (2001), 021604.

75 EVANS, E., AND NEEDHAM, D. Physical properties of surfactant bilayer membranes: thermal transitions, elasticity, rigidity, cohesion and colloidal interactions. *J. Phys. Chem. 91*, 16 (1987), 4219–4228.

76 EVANS, E., AND RAWICZ, W. Entropy-driven tension and bending elasticity in condensed-fluid membranes. *Phys. Rev. Lett. 64* (1990), 2094–2097.

77 EVANS, E. A. Bending resistance and chemically induced moments in membrane bilayers. *Biophys. J. 14*, 12 (1974), 923.

78 EVANS, E. E., AND SKALAK, R. *Mechanics and thermodynamics of biomembranes*. CRC Press, Inc., 1980.

79 FARSAD, K., AND DE CAMILLI, P. Mechanisms of membrane deformation. *Curr. Opin. Cell Biol. 15* (2003), 372–381.

80 FARSAD, K., RINGSTAD, N., TAKEI, K., FLOYD, S., ROSE, K., AND DE CAMILLI, P. Generation of high curvature membranes mediated by direct endophilin bilayer interactions. *J. Cell Biol. 155*, 2 (2001), 193.

81 FATTAL, D. R., AND BEN-SHAUL, A. A molecular model for lipid-protein interaction in membranes: the role of hydrophobic mismatch. *Biophys. J. 65*, 5 (1993), 1795–1809.

82 FEDER, J. *Fractals*. New York and London, 1988.

83 FIFE, P. C. Models for phase separation and their mathematics. *Electron, J. Differ. Equ. 2000*, 48 (2000), 1–26.

84 FIX, G. J. Phase field models for free boundary problems. In *Free Boundary Problems, Theory and Applications*, A. Fasans and M. Primicerio, Eds., vol. II. Pitman, Boston, MA, 1983, p. 580.

85 FOLCH, R. *Models de camp de fase per a fenòmens de digitació viscosa*. PhD thesis, Universitat de Barcelona, 2000.

86 FOLCH, R., CASADEMUNT, J., HERNÁNDEZ-MACHADO, A., AND RAMÍREZ-PISCINA, L. Phase-field model for Hele-Shaw flows with arbitrary viscosity contrast. I. Theoretical approach. *Phys. Rev. E 60*, 2 (1999), 1724–1733.

87 FOLCH, R., CASADEMUNT, J., HERNÁNDEZ-MACHADO, A., AND RAMÍREZ-PISCINA, L. Phase-field model for Hele-Shaw flows with arbitrary viscosity contrast. II. Numerical study. *Phys. Rev. E 60*, 2 (1999), 1734–1740.

88 FOLTIN, G. Dynamics of incompressible fluid membranes. *Phys. Rev. E 49* (1994), 5243–5248.

89 FORD, M. G. J., MILLS, I. G., PETER, B. J., VALLIS, Y., PRAEFCKE, G. J. K., EVANS, P. R., AND MCMAHON, H. T. Curvature of clathrin-coated pits driven by epsin. *Nature 419* (2002), 361–366.

90 FOTIN, A., CHENG, Y., SLIZ, P., GRIGORIEFF, N., HARRISON, S. C., KIRCHHAUSEN, T., AND WALZ, T. Molecular model for a complete clathrin lattice from electron cryomicroscopy. *Nature 432* (2004), 573–579.

91 FOURNIER, J. B. Microscopic membrane elasticity and interactions among membrane inclusions: interplay between the shape, dilation, tilt and tilt-difference modes. *Eur. Phys. J. B 11*, 2 (1999), 261–272.

92 FRANK, F. C. I. Liquid crystals. On the theory of liquid crystals. *Faraday Discuss. 25* (1958), 19–28.

93 FROST, A., DE CAMILLI, P., AND UNGER, V. M. F-BAR Proteins Join the BAR Family Fold. *Structure 15*, 7 (2007), 751–753.

94 FROST, A., PERERA, R., ROUX, A., SPASOV, K., DESTAING, O., EGELMAN,

E. H., DE CAMILLI, P., AND UNGER, V. M. Structural basis of membrane invagination by F-BAR domains. *Cell 132*, 5 (2008), 807–817.

95 FULLER, N., BENATTI, C. R., AND RAND, R. P. Curvature and bending constants for phosphatidylserine-containing membranes. *Biophys. J. 85*, 3 (2003), 1667–1674.

96 FULLER, N., AND RAND, R. P. The influence of lysolipids on the spontaneous curvature and bending elasticity of phospholipid membranes. *Biophys. J. 81*, 1 (2001), 243–254.

97 FYGENSON, D. K., MARKO, J. F., AND LIBCHABER, A. Mechanics of microtubule-based membrane extension. *Phys. Rev. Lett. 79*, 22 (1997), 4497–4500.

98 GALLOP, J. L., JAO, C. C., KENT, H. M., BUTLER, P. J. G., EVANS, P. R., LANGEN, R., AND MCMAHON, H. T. Mechanism of endophilin N-BAR domain-mediated membrane curvature. *EMBO J. 25* (2006), 2898–2910.

99 GELFAND, I. M., AND FOMIN, S. V. *Calculus of variations*. Courier Dover Publications, 2000.

100 GIBBS, J. W. On the equilibrium of heterogeneous substances (1876). The Collected Papers of J. Willard Gibbs. Vol. I, 1957.

101 GOETZ, A. *Introduction to differential geometry*. Addison-Wesley. Reading, MA, 1970.

102 GOLDBERG, J. Structural basis for activation of ARF GTPase: mechanisms of guanine nucleotide exchange and GTP-Myristoyl switching. *Cell 95* (1998), 237–248.

103 GOLDSTEIN, H., POOLE, C., AND SAFKO, J. *Classical Mechanics*, third ed. Addison–Wesley, 2002.

104 GOLDSTEIN, R. E., NELSON, P., POWERS, T., AND SEIFERT, U. Front propagation in the pearling instability of tubular vesicles. *J. Phys. II 6* (1996), 767–796.

105 GOMPPER, G., AND SCHICK, M. *Self-assembling amphiphilic system*. No. 16 in Phase Transitions and Critical Phenomena. Academic Press, London, 1994.

106 GONZÁLEZ-CINCA, R., FOLCH, R., BENÍTEZ, R., RAMIREZ-PISCINA, L., CASADEMUNT, J., AND HERNÁNDEZ-MACHADO, A. Phase-field models in interfacial pattern formation out of equilibrium. In *Advances in Condensed Matter and Statistical Physics*, E. Korutcheva and R. Cuerno, Eds. Nova Science Publishers, New York, 2004, pp. 203–236.

107 HALSTENBERG, S., HEIMBURG, T., HIANIK, T., KAATZE, U., AND KRIVANEK, R. Cholesterol-induced variations in the volume and enthalpy Fluctuations of lipid bilayers. *Biophys. J. 75*, 1 (1998), 264–271.

108 HAMM, M., AND KOZLOV, M. M. Tilt model of inverted amphiphilic mesophases. *Eur. Phys. J. B 6*, 4 (1998), 519–528.

109 HELFRICH, W. Elastic properties of lipid bilayers: theory and possible experiments. *Z. Naturforsch. C 28* (1973), 693–703.

110 HELFRICH, W. Amphiphilic mesophases made of defects. In *Physics of defects* (1981), R. Balian, M. Kléman, and J. Poirier, Eds., Les Houches, Session XXXV, 1988, North-Holland, Amsterdam, pp. 713–755.

111 HELFRICH, W. Elasticity and thermal undulations of fluid films of amphiphiles. In *Liquids at Interfaces* (1990), J. Charvolin, J.-F. Joanny, and J. Zinn-Justin, Eds., Les Houches, Session XLVIII, 1988, Elsevier Science, Amsterdam, pp. 212–237.

112 HENNE, W. M., KENT, H. M., FORD, M. G. J., HEGDE, B. G., DAUMKE, O., BUTLER, P. J. G., MITTAL, R., LANGEN, R., EVANS, P. R., AND MCMAHON, H. T. Structure and analysis of FCHo2 F-BAR domain: a dimerizing and membrane recruitment module that effects membrane curvature. *Structure 15*, 7 (2007), 839–852.

113 HERNÁNDEZ-MACHADO, A., LACASTA, A. M., MAYORAL, E., AND CORVERA POIRÉ, E. Phase-field model of Hele-Shaw flows in the high-viscosity contrast regime. *Phys. Rev. E 68*, 4 (2003), 46310.

114 HERRICK, D. Z., STERBLING, S., RASCH, K. A., HINDERLITER, A., AND CAFISO, D. S. Position of synaptotagmin I at the membrane interface: cooperative interactions of tandem C2 domains. *Biochemistry 45*, 32 (2006), 9668–9674.

115 HINSHAW, J. E. Dynamin and its role in membrane fission. *Ann. Rev. Cell Develop. Biol. 16* (2000), 483–519.

116 HOFFMAN, J. F., Ed. *Membrane transport processes*, vol. 1. Raven Press, 1977.

117 HOHENBERG, P., AND HALPERIN, B. Theory of dynamic critical phenomena. *Rev. Mod. Phys. 49* (1977), 435.

118 HÖRGER, I., VELASCO, E., MINGORANCE, J., RIVAS, G., TARAZONA, P., AND VÉLEZ, M. Langevin computer simulations of bacterial protein filaments and the force-generating mechanism during cell division. *Phys. Rev. E 77*, 1 (2008), 11902.

119 HOWARD, J. *Mechanics of motor proteins and the cytoskeleton*. Sinauer Press, 2001.

120 HUA, Z., AND GRAHAM, T. R. Requirement for Neo1p in retrograde transport from the Golgi complex to the endoplasmic reticulum. *Mol. Biol. Cell 14*, 12 (2003), 4971–4983.

121 HUANG, K. *Statistical mechanics*, second ed. John Wiley & Sons, 1963.

122 ILLYA, G., LIPOWSKY, R., AND SHILLCOCK, J. C. Effect of chain length and asymmetry on material properties of bilayer membranes. *J. Chem. Phys. 122* (2005), 244901.

123 ISRAELACHVILI, J. *Intermolecular and surface forces*, 2nd ed. Academic Press, 1992.

124 ISRAELACHVILI, J. N., MITCHELL, D. J., AND NINHAM, B. W. Theory of self-assembly of hydrocarbon amphiphiles into micelles and bilayers. *J. Chem. Soc., Faraday Trans. 72* (1976), 1525–1568.

125 IWAMOTO, M., AND OU-YANG, Z. Shape deformation and circle instability in two-dimensional lipid domains by dipolar force: a shape- and size-dependent line tension model. *Phys. Rev. Lett. 93*, 20 (2004), 206101.

126 JIAN-GUO, H., AND ZHONG-CAN, O. Y. Shape equations of the axisymmetric vesicles. *Phys. Rev. E 47*, 1 (1993), 461–467.

127 JÜLICHER, F., AND LIPOWSKY, R. Shape transformations of vesicles with intramembrane domains. *Phys. Rev. E 53*, 3 (1996), 2670–2683.

128 JÜLICHER, F., AND SEIFERT, U. Shape equations for axisymmetric vesicles: a clarification. *Phys. Rev. E 49*, 5 (1994), 4728–4731.

129 JÜLICHER, F., SEIFERT, U., AND LIPOWSKY, R. Phase diagrams and shape transformations of toroidal vesicles. *J. Phys. II 3* (1993), 1681.

130 KAMIEN, R. D. The geometry of soft materials: a primer. *Rev. Mod. Phys. 74* (2002), 953–971.

131 KELLER, D. J., KORB, J. P., AND MCCONNELL, H. M. Theory of shape transitions in two-dimensional phospholipid domains. *J. Phys. Chem. 91*, 25 (1987), 6417–6422.

132 KENWORTHY, A. K., NICHOLS, B. J., REMMERT, C. L., HENDRIX, G. M., KUMAR, M., ZIMMERBERG, J., AND LIPPINCOTT-SCHWARTZ, J. Dynamics of putative raft-associated proteins at the cell surface. *J. Cell Biol. 165*, 5 (2004), 735.

133 KIRCHHAUSEN, T. Three ways to make a vesicle. *Nat. Rev. Mol. Cell Biol. 1*, 3 (2000), 187.

134 KIRCHHAUSEN, T. Making COPII coats. *Cell 129*, 7 (2007), 1251–1252.

135 KOMURA, S., SHIROTORI, H., OLMSTED, P. D., AND ANDELMAN, D. Lateral phase separation in mixtures of lipids and cholesterol systems. *Europhys. Lett. 67*, 2 (2004), 321–327.

136 KOOIJMAN, E. E., CHUPIN, V., DE KRUIJFF, B., AND BURGER, K. N. J. Modulation of membrane curvature by phosphatidic acid and lysophosphatidic acid. *Traffic 4*, 3 (2003), 162–174.

137 KORLACH, J., SCHWILLE, P., WEBB, W. W., AND FEIGENSON, G. W. Characterization of lipid bilayer phases by confocal microscopy and fluorescence correlation spectroscopy. *Proc. Nat. Acad. Sci. U.S.A. 96*, 15 (1999), 8461.

138 KOSTER, G., CACCIUTO, A., DERÉNYI, I., FRENKEL, D., AND DOGTEROM, M. Force barriers for membrane tube formation. *Phys. Rev. Lett. 94* (2005), 068101.

139 KOYNOVA, R., AND CAFFREY, M. Phases and phase transitions of the phosphatidylcholines. *Biochim. Biophys. Acta, Rev. Biomembr. 1376*, 1 (1998), 91–145.

140 KOZLOV, M. M. Membrane shape equations. *J. Phys.: Condens. Matter 18*, 28 (2006), S1177–S1190.

141 KOZLOV, M. M. *Soft condensed matter physics in molecular and cell biology*. Taylor & Francis Group, 2006, ch. Some aspects of membrane elasticity.

142 KOZLOV, M. M., LEIKIN, S., AND RAND, R. P. Bending, hydration and interstitial energies quantitatively account for the hexagonal-lamellar-hexagonal reentrant phase transition in dioleoylphosphatidylethanolamine. *Biophys. J. 67*, 4 (1994), 1603–1611.

143 KOZLOV, M. M., AND WINTERHALTER, M. Elastic moduli and neutral surface for strongly curved monolayers. Analysis of experimental results. *J. Phys. II 1* (1991), 1085–1100.

144 KOZLOVSKY, Y., ZIMMERBERG, J., AND KOZLOV, M. M. Orientation and interaction of oblique cylindrical inclusions embedded in a lipid monolayer: a theoretical model for viral fusion peptides. *Biophys. J. 87*, 2 (2004), 999–1012.

145 LANDAU, L., AND LIFCHITZ, E. *Physique statistique*. Éditions de Moscou, 1967.

146 LANDAU, L. D., AND LIFSHITZ, E. M. *Theory of elasticity*, 3rd ed. Pergamon Press, 1986.

147 LANG, S. *Algebra*. Springer, 2002.

148 LANGER, J. Models of pattern formation in first-order phase transitions. In *Directions in Condensed Matter Physics*, G. Grinstein and G. Mazenko, Eds. World Scientific, 1986, p. 165.

149 LAURILA, T., PRADAS, M., HERNANDEZ-MACHADO, A., AND ALA-NISSILA, T. Influence of disorder strength on phase field models of interfacial growth. *Phys. Rev. E 78* (2008), 031603.

150 LEDESMA-AGUILAR, R., QUEVEDO-REYES, M., CORVERA POIRÉ, E., AND HERNÁNDEZ-MACHADO, A. Lateral instability in normal viscous fingers. *Phys. Rev. E 71*, 1 (2005), 16312.

151 LEDUC, C., CAMPAS, O., ZELDOVICH, K. B., ROUX, A., JOLIMAITRE, P., BOUREL-BONNET, L., GOUD, B., JOANNY, J.-F., BASSEREAU, P., AND PROST, J. Cooperative extraction of membrane nanotubes by molecular motors. *Proc. Nat. Acad. Sci. U.S.A. 101*, 49 (2004), 17096.

152 LEE, K. Y. C., AND MCCONNELL, H. M. Quantized symmetry of liquid monolayer domains. *J. Phys. Chem. 97*, 37 (1993), 9532–9539.

153 LEE, M. C. S., MILLER, E. A., GOLDBERG, J., ORCI, L., AND SCHEKMAN, R. Bidirectional protein transport between the ER and Golgi. *Annu. Rev. Cell Dev. Biol. 20*, 1 (2004), 87–123.

154 LEE, M. C. S., ORCI, L., HAMAMOTO, S., FUTAI, E., RAVAZZOLA, M., AND SCHEKMAN, R. Sar1p N-terminal helix initiates membrane curvature and completes the fission of a COPII vesicle. *Cell 122*, 4 (2005), 605–617.

155 LEHNINGER, A. L., NELSON, D. L., AND COX, M. M. *Principles of biochemistry*. WH Freeman, New York, 1993.

156 LEIBLER, S. Curvature instability in membranes. *J. Phys. 47*, 3 (1986), 507–516.

157 LEIKIN, S., KOZLOV, M. M., FULLER, N. L., AND RAND, R. P. Measured effects of diacylglycerol on structural and elastic properties of phospholipid membranes. *Biophys. J. 71*, 5 (1996), 2623–2632.

158 LI, H. B., YI, H. H., SHAN, X. W., AND FANG, H. P. Shape changes and motion of a vesicle in a fluid using a lattice Boltzmann model. *Europhys. Lett. 81* (2008), 54002.

159 LIM H. W., G., WORTIS, M., AND MUKHOPADHYAY, R. Stomatocyte-discocyte-echinocyte sequence of the human red blood cell: evidence for the bilayer-couple hypothesis from membrane mechanics. *Proc. Nat. Acad. Sci. U.S.A. 99*, 26 (2002), 16766.

160 LIPOWSKY, R., AND SACKMANN, E., Eds. *Structure and dynamics of membranes*. Handbook of Biological Physics. Elsevier Science, 1995.

161 LIU, Q. H., HAIJUN, Z., LIU, J. X., AND ZHONG-CAN, O. Y. Spheres and prolate and oblate ellipsoids from an analytical solution of the spontaneous-curvature fluid-membrane model. *Phys. Rev. E 60*, 3 (1999), 3227–3233.

162 MACKINNON, R. Structural biology: voltage sensor meets lipid membrane. *Science 306*, 5700 (2004), 1304–1305.

163 MANDELBROT, B. B. *The fractal geometry of nature*. WH Freeman, 1982.

164 MARGOLIN, W. FtsZ and the division of prokaryotic cells and organelles. *Nat. Rev. Mol. Cell Biol. 6*, 11 (2005), 862.

165 MARSH, D. *Handbook of lipid bilayers*. CRC Press Boca Raton, FL, 1990.

166 MARSH, D. Lateral pressure profile, spontaneous curvature frustration, and the incorporation and conformation of proteins in membranes. *Biophys. J. 93*, 11 (2007), 3884.

167 MARTENS, S., KOZLOV, M. M., AND MCMAHON, H. T. How synaptotagmin promotes membrane fusion. *Science 316*, 5828 (2007), 1205.

168 MAXFIELD, F. R. Plasma membrane microdomains. *Curr. Opin. Cell Biol. 14*, 4 (2002), 483–487.

169 MAY, S., KOZLOVSKY, Y., BEN-SHAUL, A., AND KOZLOV, M. M. Tilt modulus of a lipid monolayer. *Eur. Phys. J. E 14*, 3 (2004), 299–308.

170 MCCONNELL, H. M. Structures and transitions in lipid monolayers at the air-water interface. *Annu. Rev. Phys. Chem. 42*, 1 (1991), 171–195.

171 MCMAHON, H. T., AND GALLOP, J. L. Membrane curvature and mechanisms of dynamic cell membrane remodelling. *Nature 438*, 7068 (2005), 590–596.

172 MCMAHON, H. T., AND MILLS, I. G. COP and clathrin-coated vesicle budding: different pathways, common approaches. *Curr. Opin. Cell Biol. 16*, 4 (2004), 379–391.

173 MCNIVEN, M. A., CAO, H., PITTS, K. R., AND YOON, Y. The dynamin family of mechanoenzymes: pinching in new places. *Trends Biochem. Sci. 25*, 3 (2000), 115–120.

174 MEARS, J. A., RAY, P., AND HINSHAW, J. E. A corkscrew model for dynamin constriction. *Structure 15*, 10 (2007), 1190–1202.

175 MESMIN, B., DRIN, G., LEVI, S., RAWET, M., CASSEL, D., BIGAY, J., AND ANTONNY, B. Two lipid-packing sensor motifs contribute to the sensitivity of ArfGAP1 to membrane curvature. *Biochemistry 46*, 7 (2007), 1779–1790.

176 MIAO, L., FOURCADE, B., RAO, M., WORTIS, M., AND ZIA, R. K. P. Equilibrium budding and vesiculation in the curvature model of fluid lipid vesicles. *Phys. Rev. A 43*, 12 (1991), 6843–6856.

177 MITOV, M. D. Third and fourth order curvature elasticity of lipid bilayers. *C. R. Acad. Bulg. Sci. 31* (1978), 513–515.

178 MUKHOPADHYAY, R., LIM H. W., G., AND WORTIS, M. Echinocyte shapes: bending, stretching, and shear determine spicule shape and spacing. *Biophys. J. 82*, 4 (2002), 1756–1772.

179 NAITO, H., OKUDA, M., AND ZHONG-CAN, O. Y. New solutions to the Helfrich variation problem for the shapes of lipid bilayer vesicles: beyond Delaunay's surfaces. *Phys. Rev. Lett. 74*, 21 (1995), 4345–4348.

180 NAKAHARA, M. *Geometry, topology and physics*. Institute of Physics Publishing, 2003.

181 NELSON, P., POWERS, T., AND SEIFERT, U. Dynamical theory of the pearling instability in cylindrical vesicles. *Phys. Rev. Lett. 74*, 17 (1995), 3384–3387.

182 NGUYEN, T. T., GOPAL, A., LEE, K. Y. C., AND WITTEN, T. A. Surface charge relaxation and the pearling instability of charged surfactant tubes. *Phys. Rev. E 72*, 5 (2005), 51930.

183 NIELSEN, M., MIAO, L., IPSEN, J. H., ZUCKERMANN, M. J., AND MOURITSEN, O. G. Off-lattice model for the phase behavior of lipid-cholesterol bilayers. *Phys. Rev. E 59*, 5 (1999), 5790–5803.

184 NIGGEMANN, G., KUMMROW, M., AND HELFRICH, W. The bending rigidity of phosphatidylcholine bilayers: dependences on experimental method, sample cell sealing and temperature. *J. Phys. II 5* (1995), 413–425.

185 NITSCHE, J. C. C. *Vorlesungen über minimalflächen*. Die Grundlehren der mathematische Wissenschaften. Springer–Verlag, 1975.

186 NOGEE, L. M., GARNIER, G., DIETZ, H. C., SINGER, L., MURPHY, A. M., DEMELLO, D. E., AND COLTEN, H. R.

A mutation in the surfactant protein B gene responsible for fatal neonatal respiratory disease in multiple kindreds. *J. Clin. Invest. 93*, 4 (1994), 1860.

187 NOGUCHI, H., AND GOMPPER, G. Fluid vesicles with viscous membranes in shear flow. *Phys. Rev. Lett. 93* (2004), 258102.

188 NOGUCHI, H., AND GOMPPER, G. Dynamics of fluid vesicles in shear flow: effect of membrane viscosity and thermal fluctuations. *Phys. Rev. E 72*, 1 (2005), 11901.

189 NOGUCHI, H., AND GOMPPER, G. Shape transitions of fluid vesicles and red blood cells in capillary flows. *Proc. Nat. Acad. Sci. U.S.A. 102*, 40 (2005), 14159–14164.

190 OSHER, S., AND FEDKIW, R. *Level set methods and dynamic implicit surfaces*. No. 153 in Applied mathematical Sciences. Springer, 2003.

191 OSHER, S. J., AND SETHIAN, J. A. Fronts propagation with curvature dependent speed: algorithms based on Hamilton-Jacobi formulations. *J. Comput. Phys. 79*, 1 (1988), 12–49.

192 PARASASSI, T., LOIERO, M., RAIMONDI, M., RAVAGNAN, G., AND GRATTON, E. Absence of lipid gel-phase domains in seven mammalian cell lines and in four primary cell types. *Biochim. Biophys. Acta 1153*, 2 (1993), 143–54.

193 PARSEGIAN, V. A. Theory of liquid-crystal phase transitions in lipid + water systems. *Trans. Faraday Soc. 62* (1966), 848–860.

194 PEARSON, K. Mathematics and biology. *Nature 63* (1901), 274.

195 PETER, B. J., KENT, H. M., MILLS, I. G., VALLIS, Y., BUTLER, P. J. G., EVANS, P. R., AND MCMAHON, H. T. BAR domains as sensors of membrane curvature: the amphiphysin BAR structure. *Science 303*, 5657 (2004), 495.

196 PETRACHE, H. I., DODD, S. W., AND BROWN, M. F. Area per lipid and acyl length distributions in fluid phosphatidylcholines determined by ^2H NMR spectroscopy. *Biophys. J. 79*, 6 (2000), 3172–3192.

197 PICARD, M.-E. Discours. *Bulletin de la Société mathématique de France 52* (1924), 27–32.

198 PLATEAU, J. *Statique expérimentale et théorique des liquides soumis aux seules forces moléculaires*. Gauthier-Villars, 1873.

199 POMORSKI, T., HOLTHUIS, J. C. M., HERMANN, A., AND VAN MEER, G. Tracking down lipid flippases and their biological functions. *J. Cell Sci. 117*, 6 (2004), 805–813.

200 POWERS, T. R., HUBER, G., AND GOLDSTEIN, R. E. Fluid-membrane tethers: minimal surfaces and elastic boundary layers. *Phys. Rev. E 65* (2002), 041901.

201 PRADAS, M., AND HERNÁNDEZ-MACHADO, A. Intrinsic versus super-rough anomalous scaling in spontaneous imbibition. *Phys. Rev. E 74*, 4 (2006), 41608.

202 PRADAS, M., HERNÁNDEZ-MACHADO, A., AND RODRÍGUEZ, M. A. Dynamical scaling of imbibition in columnar geometries. *Phys. Rev. E 77*, 5 (2008), 56305.

203 PRAEFCKE, G. J. K., AND MCMAHON, H. T. The dynamin superfamily: universal membrane tubulation and fission molecules? *Nat. Rev. Mol. Cell Biol. 5*, 2 (2004), 133–147.

204 PRESS, W. H., ET AL. *Numerical recipes in Fortran 77*, second ed. Cambridge U.P., 1992.

205 RAMACHANDRAN, R., AND SCHMID, S. L. Real-time detection reveals that effectors couple dynamin's GTP-dependent conformational changes to the membrane. *EMBO J. 27* (2008), 27–37.

206 RAWICZ, W., OLBRICH, K. C., MCINTOSH, T., NEEDHAM, D., AND EVANS, E. Effect of chain length and unsaturation on elasticity of lipid bilayers. *Biophys. J. 79*, 1 (2000), 328–339.

207 RAYLEIGH, L. On the stability of liquid jets. *Proc. London Math. Soc 10*, 4 (1878).

208 RAYLEIGH, L. Investigations in capillarity. *Phil. Mag. 48*, 321-330 (1899), 222.

209 RICHARDS, I., AND YOUN, H. *Theory of distributions: a non-technical introduction*. Cambridge University Press, 1990.

210 RINGSDORF, H., SCHLARB, B., AND VENZMER, J. Molecular architecture and function of polymeric oriented systems: models for the study of organization, surface recognition, and dynamics

of biomembranes. *Angew. Chem. Int. Ed. Engl. 27* (1988), 113–158.

211 RINGSDORF, H., VENZMER, J., AND WINNIK, F. M. Interaction of hydrophobically-modified poly-N-isopropylacrylamides with model membranes –or playing a molecular accordion. *Angew. Chem. Int. Ed. 30*, 3 (1991), 315–318.

212 RISKEN, H. *The Fokker-Planck equation: methods of solution and applications*. Springer-Verlag Berlin and Heidelberg GmbH & Co. K, 1989.

213 ROSSIER, O., CUVELIER, D., BORGHI, N., PUECH, P. H., DERENYI, I., BUGUIN, A., NASSOY, P., AND BROCHARD-WYART, F. Giant vesicles under flows: extrusion and retraction of tubes. *Langmuir 19*, 3 (2003), 575–584.

214 ROUX, A., CAPPELLO, G., CARTAUD, J., PROST, J., GOUD, B., AND BASSEREAU, P. A minimal system allowing tubulation with molecular motors pulling on giant liposomes. *Proc. Nat. Acad. Sci. U.S.A. 99*, 8 (2002), 5394–5399.

215 ROUX, A., CUVELIER, D., NASSOY, P., PROST, J., BASSEREAU, P., AND GOUD, B. Role of curvature and phase transition in lipid sorting and fission of membrane tubules. *EMBO J. 24* (2005), 1537–1545.

216 ROUX, A., UYHAZI, K., FROST, A., AND DE CAMILLI, P. Gtp-dependent twisting of dynamin implicates constriction and tension in membrane fission. *Nature 441* (2006), 528–531.

217 RUSTOM, A., SADDRICH, R., MARKOVIC, I., WALTHER, P., AND GERDES, H.-H. Nanotubular highways for intercellular organelle transport. *Science 303* (2004), 1007–1010.

218 SAFRAN, S. A. *Statistical thermodynamics of surfaces, interfaces, and membranes*. No. 90 in Frontiers in Physics. Addison-Wesley, 1994.

219 SCHMID, S. L. Clathrin-coated vesicle formation and protein sorting: An integrated process. *Annu. Rev. Biochem. 66*, 1 (1997), 511–548.

220 SCHNEIDER, M. F., AND TANAKA, M. Physics of glycolipid monolayers – a model of glycocalix. *Biophys. J. 82*, 1 (2002), 32–32.

221 SCHUTZ, B. F. *Geometrical methods of mathematical physics*. Cambridge University Press, 1980.

222 SEIFERT, R. Ion channels and pumps. In *35th Spring School. Physics meets Biology* (2004), Forschungszentrum Jülich.

223 SEIFERT, U. Vesicles of toroidal topology. *Phys. Rev. Lett. 66*, 18 (1991), 2404–2407.

224 SEIFERT, U. Configurations of fluid membranes and vesicles. *Adv. Phys. 46*, 1 (1997), 13–137.

225 SEIFERT, U., BERNDL, K., AND LIPOWSKY, R. Shape transformations od vesicles: phase diagram for spontaneous-curvature and bilayer-coupling models. *Phys. Rev. A 44*, 2 (1991), 1182–1202.

226 SEIFERT, U., MIAO, L., DÖBEREINER, H.-G., AND WORTIS, M. *The structure and conformation of amphiphilic membranes*. Springer, Berlin.

227 SEVER, S., DAMKE, H., AND SCHMID, S. L. Garrotes, springs, ratchets, and whips: putting dynamin models to the test. *Traffic 1*, 5 (2000), 385–392.

228 SHEETZ, M. P. Cell control by membrane-cytoskeleton adhesion. *Nat. Rev. Mol. Cell Biol. 2*, 5 (2001), 392–6.

229 SHEETZ, M. P., AND SINGER, S. J. Biological membranes as bilayer couples. A molecular mechanism of drug-erythrocyte interactions. *Proc. Nat. Acad. Sci. U.S.A. 71*, 11 (1974), 4457–4461.

230 SHEMESH, T., LUINI, A., MALHOTRA, V., BURGER, K. N. J., AND KOZLOV, M. M. Prefission constriction of golgi tubular carriers driven by local lipid metabolism: a theoretical model. *Biophys. J. 85* (2003), 3813–3827.

231 SHIBATA, Y., VOELTZ, G. K., AND RAPOPORT, T. A. Rough sheets and smooth tubules. *Cell 126*, 3 (2006), 435–439.

232 SIEGEL, D. P., AND KOZLOV, M. M. The gaussian curvature elastic modulus of n-monomethylated dioleoylphosphatidylethanolamine: relevance to membrane fusion and lipid phase behavior. *Biophys. J. 87* (2004), 366.

233 SIMONS, K., AND EHEHALT, R. Cholesterol, lipid rafts, and disease. *J. Clin. Invest. 110*, 5 (2002), 597.

234 SIMONS, K., AND IKONEN, E. Functional rafts in cell membranes. *Nature 387* (June 1997), 569–572.

235 SIMONS, K., AND TOOMRE, D. Lipid rafts and signal transduction. *Nat. Rev. Mol. Cell Biol. 1*, 1 (2000), 31–39.

236 SONG, B. D., AND SCHMID, S. L. A molecular motor or a regulator? Dynamin's in a class of its owns. *Biochemistry 42*, 6 (2003), 1369–1376.

237 STELITANO, D., AND ROTHMAN, D. H. Fluctuations of elastic interfaces in fluids: theory, lattice-Boltzmann model, and simulation. *Phys. Rev. E 62*, 5 (2000), 6667–6680.

238 STRIKWERDA, J. C. *Finite difference schemes and partial differential equations*. Wadsworth & Brooks, 1989.

239 SVETINA, S., OTTOVA-LEITMANNOVA, A., AND GLASER, R. Membrane bending energy in relation to bilayer couples concept of red blood cell shape transformations. *J. Theor. Biol. 94*, 1 (1982), 13–23.

240 SVETINA, S., AND ZEKS, B. Bilayer couple hypothesis of red cell shape transformations and osmotic hemolysis. *Biomed. Biochim. Acta 42*, 11-12 (1983), S86–90.

241 SVETINA, S., AND ŽEKŠ, B. Membrane bending energy and shape determination of phospholipid vesicles and red blood cells. *Eur. Biophys. J. 17*, 2 (1989), 101–111.

242 SZULE, J. A., FULLER, N. L., AND RAND, R. P. The effects of acyl chain length and saturation of diacylglycerols and phosphatidylcholines on membrane monolayer curvature. *Biophys. J. 83*, 2 (2002), 977–984.

243 TAKAMORI, S., HOLT, M., STENIUS, K., LEMKE, E. A., GRØNBORG, M., RIEDEL, D., URLAUB, H., SCHENCK, S., BRÜGGER, B., RINGLER, P., ET AL. Molecular anatomy of a trafficking organelle. *Cell 127*, 4 (2006), 831–846.

244 TANFORD, C. The hydrophobic effect and the organization of living matter. *Science 200*, 4345 (1978), 1012–1018.

245 TANFORD, C. *The hydrophobic effect*. Wiley, New York, 1980.

246 TANIGUCHI, T. Shape deformation and phase separation dynamics of two-component vesicles. *Phys. Rev. Lett. 76*, 23 (1996), 4444–4447.

247 THOMPSON, D. W. *On Growth and form: the complete revised edition*. 1992.

248 THORNE, K. S., AND PRICE, R. H. *Black holes: the membrane paradigm*. Yale University Press, 1986.

249 TSAFRIR, I. *Shape instabilities of membranes with anchored polymers under geometric constraints*. PhD thesis, Weizmann Institute of Science, 2003.

250 TSAFRIR, I., CASPI, Y., GUEDEAU-BOUDEVILLE, M. A., ARZI, T., AND STAVANS, J. Budding and tubulation in highly oblate vesicles by anchored amphiphilic molecules. *Phys. Rev. Lett. 91* (2003), 138102.

251 TSAFRIR, I., SAGI, D., ARZI, T., GUEDEAU-BOUDEVILLE, M. A., FRETTE, V., KANDEL, D., AND STAVANS, J. Pearling instabilities of membrane tubes with anchored polymers. *Phys. Rev. Lett. 86* (2001), 1138–1141.

252 VOELTZ, G. K., PRINZ, W. A., SHIBATA, Y., RIST, J. M., AND RAPOPORT, T. A. A class of membrane proteins shaping the tubular endoplasmic reticulum. *Cell 124*, 3 (2006), 573–586.

253 WAGENSBERG, J. *La rebelión de las formas: o cómo perseverar cuando la incertidumbre aprieta*. Tusquets Editores, 2005.

254 WANG, X. *Phase field models and simulations of vesicle bio-membranes*. PhD thesis, Department of Mathematics. The Pennsylvania State University., 2005.

255 WATERMAN-STORER, C. M., AND SALMON, E. D. Endoplasmic reticulum membrane tubules are distributed by microtubules in living cells using three distinct mechanisms. *Curr. Biol 8* (1998), 798–806.

256 WEIGERT, R., SILLETTA, M. G., SPANÒ, S., TURACCHIO, G., CERICOLA, C., COLANZI, A., SENATORE, S., MANCINI, R., POLISHCHUK, E. V., SALMONA, M., FACCHIANO, F., BURGER, K. N., MIRONOV, A., LUINI, A., AND CORDA, D. Ctbp/bars induced fission of golgi membranes by acylating lysophosphatidic acid. *Nature 402* (1999), 429–433.

257 WIDOM, B., BHIMALAPURAM, P., AND KOGA, K. The hydrophobic effect. *PCCP 5*, 15 (2003), 3085–3093.

258 WIESE, W., HARBICH, W., AND HELFRICH, W. Budding of lipid bilayer vesicles and flat membranes. *J. Phys. Condens. Matter 4* (1992), 1647–1657.

259 WINTZ, W., DOEBEREINER, H. G., AND SEIFERT, U. Starfish vesicles. *Europhys. Lett. 33*, 5 (1996), 403–408.

260 ZHANG, P., AND HINSHAW, J. E. Three-dimensional reconstruction of dynamin in the constricted state. *Nat. Cell Biol. 3*, 10 (2001), 922–926.

261 ZHENG, W. M., AND LIU, J. Helfrich shape equation for axisymmetric vesicles as a first integral. *Phys. Rev. E 48*, 4 (1993), 2856–2860.

262 ZHONG-CAN, O. Y., AND HELFRICH, W. Bending energy of vesicle membranes: general expressions for the first, second, and third variation of the shape energy and applications to spheres and cylinders. *Phys. Rev. A 39*, 10 (1989), 5280–5288.

263 ZIMMERBERG, J., AND KOZLOV, M. M. How proteins produce cellular membrane curvature. *Nat. Rev. Mol. Cell Biol. 7* (2006), 9–19.

264 ZIMMERBERG, J., AND MCLAUGHLIN, S. Membrane curvature: how BAR domains bend bilayers. *Curr. Biol. 14*, 6 (2004), 250–252.